

DISS ETH NO. 29655

Severe Convective Storms Over the Alpine-Adriatic Region in Kilometer-Scale Climate Simulations

A thesis submitted to attain the degree of
DOCTOR OF SCIENCES OF ETH ZURICH
(DR. SC. ETH ZURICH)

presented by

RUOYI CUI

M.Sc. in Atmospheric and Climate Science, ETH Zurich

born on 7 October, 1994

citizen of China

accepted on the recommendation of

Prof. Dr. Christoph Schär, examiner
Prof. Dr. Nikolina Ban, co-examiner
Dr. Marie-Estelle Demory, co-examiner
Prof. Dr. Olivia Martius, co-examiner

2023

Contents

Abstract	iii
Résumé	v
1 Background and introduction	1
1.1 Weather and climate extremes	1
1.2 Physical background	3
1.2.1 Severe convective storms	3
1.2.2 Hail	4
1.2.3 Lightning	5
1.3 Observations	8
1.3.1 Hail	8
1.3.2 Lightning	8
1.4 Kilometer-scale modeling	9
1.5 Early Alpine hail research	10
1.6 Effects of climate change on severe convective storms	11
1.6.1 Hail	11
1.6.2 Lightning	12
1.7 Objectives and thesis outline	13
2 Exploring hail and lightning diagnostics over the Alpine-Adriatic region in a km-scale climate model	15
2.1 Introduction	16
2.2 Data and methods	18
2.2.1 Model description	18
2.2.2 HAILCAST – hail growth model	19
2.2.3 LPI – lightning potential index	20
2.2.4 Observational datasets	21
2.2.5 Analysis methods	23
2.3 Results	24
2.3.1 Synoptic overview of selected cases	24
2.3.2 Evaluation of precipitation, hail, and lightning	25
2.3.3 Evaluation of precipitation, hail, and lightning	26

2.3.4	Assessment of model internal variability	32
2.3.5	Analysis of three specific cases	34
2.3.6	Conclusions	40
3	Simulating hail and lightning over the Alpine-Adriatic region – a model comparison study	43
3.1	Introduction	44
3.2	Selected hailstorms and observational data	47
3.3	Modeling setup and evaluation approach	48
3.4	COSMO and WRF setups	48
3.5	Evaluation approach	49
3.6	Results and discussion	51
3.6.1	Precipitation	51
3.6.2	Lightning potential index results	54
3.6.3	HAILCAST results	55
3.6.4	Differences between models and model internal variability	62
3.7	Conclusions	68
4	Evaluation of decade-long hail and lightning simulation over the Alpine-Adriatic region using a km-scale climate model	71
4.1	Introduction	72
4.2	Data and methods	74
4.2.1	Model setup	74
4.2.2	Hail and lightning diagnostics	76
4.2.3	Observations	78
4.2.4	Analysis methods	80
4.3	Results	81
4.3.1	Evaluation of temperature and precipitation	81
4.3.2	Evaluation of hail and lightning	84
4.3.3	Comparison of different proxies	90
4.4	Conclusions	95
5	Conclusions and outlook	97
5.1	Conclusions	97
5.2	Outlook	98
A	Simulation documentation	101
B	Supporting information for Chapter 4	105
	Acknowledgements	109
	References	109
	Curriculum Vitae	129

Abstract

Severe convective storms are often associated with local-scale hazardous phenomena such as hail, lightning, wind gusts, and flash floods. Despite their rarity, these events can lead to considerable damage and profound socioeconomic impacts. Currently, the scientific community is directing significant efforts toward enhancing the comprehension of these phenomena, refining the existing climatological knowledge, and improving the predictive power of weather and climate models. Understanding the past trends, present climatology, and future projections of hail and lightning requires an approach across weather and climate scales. With the development of high-performance computing, kilometer-scale models can explicitly represent deep convection with grid spacings less than about 4 km. Recent studies reveal that these models improve the representation of topography and heavy precipitation, while their application for hail and lightning has been very limited so far.

This thesis is a part of the Croatian-Swiss research project titled “Severe Weather over the Alpine-Adriatic region in a Changing Climate (SWALDRIC)”, with a specific focus on modeling and observations. The main objective of the SWALDRIC project is to assess the representation of hail and lightning using kilometer-scale models over the Alpine-Adriatic region. Simultaneously, it aims to exploit unique hailpad and hail polygon datasets, as well as to leverage and explore a newly digitized hail dataset from station records in Croatia. In addition, the evaluation benefits from the utilization of radar-based hail detection algorithms operated by MeteoSwiss over the Alpine region. In this thesis, several real-case and climate simulations are conducted using the Consortium for Small-scale Modeling (COSMO) model over the Alpine-Adriatic region at a horizontal grid spacing of 2.2 km ($800 \times 600 \times 60$ grid points) driven by ERA5 reanalysis. The recently developed hail growth model (HAILCAST) and lightning potential index (LPI) are embedded within COSMO as diagnostic tools for hail and lightning. These simulations are compared against the above-listed observations, and the results are organized as follows.

The initial phase of this thesis (Chapter 2) involves the simulation of eight real cases under different synoptic situations to understand the representation of hail and lightning using kilometer-scale simulations. Comparison against available high-resolution observations reveals that COSMO with HAILCAST and LPI captured the main spatial distributions, including whether they exhibit elongated swaths, localized patterns, and instances with no or very little hail and lightning alongside heavy precipitation. The model is able to reproduce various storm environments, encompassing a capping layer that serves to accumulate humidity and energy, a “back building process” that con-

tributes to quasi-stationary convective cells near the elevated terrains, and an upper-level trough or cold front that triggers and promotes upward motion. Despite HAILCAST's limitations in generating extra-large hailstones due to broader convective clouds and weaker updrafts in the model compared to the real world, both diagnostics are proven to be successful and promising tools for simulating hail and lightning.

Subsequently, in the second part of the thesis (Chapter 3), a comprehensive model intercomparison is conducted between the COSMO and the Weather Research and Forecasting (WRF) models, utilizing the same HAILCAST and LPI diagnostics. Ensemble simulations are performed to gain a more robust insight into the sources of the differences and to account for the model internal variability. The analysis reveals that WRF tends to yield less precipitation and smaller hail swaths, while exhibiting higher values of LPI and more large hailstones compared to COSMO. This could be attributed to differences in vertical profiles of updraft strength and microphysical properties inside the thunderclouds. Specifically, WRF simulates stronger updrafts, with the updraft core located exactly where solid and liquid hydrometeors are nearly equal, thus promoting more intense lightning activity. Furthermore, this study systematically and quantitatively evaluates hail and lightning against the observations. Overall, both models, coupled with HAILCAST and LPI, successfully reproduce the characteristics of hail and lightning, underscoring their potential for climatological assessments of these phenomena.

Motivated by the encouraging results from case studies, the third part of the thesis (Chapter 4) is dedicated to 10 years (2009–2018) of multi-seasonal (April–September) climate simulations. In addition to observations, HAILCAST and LPI are compared to several widely used surrogate proxies for hail and lightning. Both diagnostics can reproduce the hail and lightning hotspots: the northern and southern foothills of the Alps, the vicinity of the Massif Central in France, along the Appennine Mountains and the east coast of the Adriatic Sea, and over the Carpathians in the Panonian Basin. Furthermore, characteristics over different topographic subdomains are compared against radar-based estimates over the Alpine region and station records over the Adriatic region. The south of the Alps exhibits an earlier onset of the hail season and an extended diurnal cycle towards the late evening compared to the north. Over the Adriatic region, the seasonal and diurnal cycles behave differently across the coastal, plains, and mountain regions. The frequency distribution of hail sizes in different seasons aligns with previous observations, with the highest frequency of very large hailstones occurring in June.

In summary, this thesis delves into the hail and lightning characteristics over the Alpine-Adriatic region using kilometer-scale climate simulations. This is the first long-term simulation at the subcontinental scale with hail and lightning diagnostics applied to a regional climate model. Comparison of HAILCAST and LPI diagnostics with available observations yields promising results. These findings could have important implications for stakeholders to make more informed decisions. As our climate continues to evolve under global warming, the analyses presented herein lay the groundwork for future research — changes in severe convective storms under future climate.

Résumé

Les tempêtes convectives sévères sont souvent associés à des phénomènes dangereux à l'échelle locale tels que la grêle, la foudre, les rafales de vent et les crues soudaines. Malgré leur rareté, ces événements peuvent provoquer des dégâts considérables et avoir de profondes répercussions socio-économiques. Actuellement, la communauté scientifique déploie des efforts considérables pour améliorer la compréhension de ces phénomènes, affiner les connaissances climatologiques existantes et renforcer la capacité prédictive des modèles météorologiques et climatiques. Comprendre les tendances passées, la climatologie actuelle et les projections futures de la grêle et de la foudre nécessite une approche à différentes échelles météorologiques et climatiques. Grâce au développement de l'informatique haute performance, les modèles à l'échelle du kilomètre peuvent représenter explicitement la convection profonde avec des espacements de grille inférieurs à environ 4 km. Des études récentes révèlent que ces modèles améliorent la représentation de la topographie et des fortes précipitations, bien que leur application à la grêle et à la foudre a été très limitée jusqu'à présent.

Cette thèse fait partie du projet de recherche croato-suisse intitulé "Severe Weather over the Alpine-Adriatic region in a Changing Climate (SWALDRIC)", avec un accent particulier sur la modélisation et les observations. L'objectif principal du projet SWALDRIC est d'évaluer la représentation de la grêle et de la foudre à l'aide de modèles à l'échelle du kilomètre dans la région alpine-adriatique. Simultanément, il vise à exploiter des ensembles de données uniques sur les hailpads et les polygones de grêle, ainsi qu'à tirer parti et à explorer un nouvel ensemble de données de grêle numérisé à partir des relevés de stations en Croatie. En outre, l'évaluation bénéficie de l'utilisation d'algorithmes de détection de grêle par radar exploités par MétéoSuisse sur la région alpine. Dans cette thèse, plusieurs simulations climatiques et de cas réels sont réalisées à l'aide du modèle du Consortium for Small-scale Modeling (COSMO) sur la région alpine et adriatique avec un espacement de grille horizontal de 2.2 km (800×600×60 points de grille) piloté par la réanalyse ERA5. Le modèle de croissance de grêle (HAILCAST) et l'indice de potentiel de foudre (LPI) récemment développés sont intégrés dans COSMO en tant qu'outils de diagnostic pour la grêle et la foudre. Ces simulations sont comparées aux observations susmentionnées, et les résultats sont organisés comme suit.

La phase initiale de l'étude (Chapitre 2) implique la simulation de huit cas réels dans différentes situations synoptiques pour comprendre la représentation de la grêle et de la foudre à l'aide de simulations à l'échelle kilométrique. La comparaison avec les observations à haute résolution disponibles révèle que COSMO avec HAILCAST et

LPI a capturé les principales distributions spatiales, y compris si elles présentent des bandes allongées, des configurations localisées, et des cas avec pas ou très peu de grêle et de foudre mais de fortes précipitations. Le modèle est capable de reproduire divers environnements de tempête, englobant une couche de recouvrement qui sert à accumuler l'humidité et l'énergie, un "processus de construction arrière" qui contribue à des cellules convectives quasi-stationnaires près des terrains élevés, et un creux de niveau supérieur ou front froid qui déclenche et favorise le mouvement ascendant. Malgré les limites de HAILCAST à générer des grêlons extra-larges en raison de nuages convectifs plus larges et de courants ascendants plus faibles dans le modèle par rapport au monde réel, les deux diagnostics se sont avérés être des outils appropriés et prometteurs pour simuler la grêle et la foudre.

Par la suite, dans la deuxième partie de la thèse (Chapitre 3), une intercomparaison complète des modèles est effectuée entre les modèles COSMO et Weather Research and Forecasting (WRF), en utilisant les mêmes diagnostics HAILCAST et LPI. Des simulations d'ensemble sont effectuées pour obtenir un aperçu plus solide des sources de différences et pour tenir compte de la variabilité interne du modèle. L'analyse révèle que WRF tend à produire moins de précipitations et de plus petites bandes de grêle, tout en présentant des valeurs plus élevées de LPI et plus de gros grêlons par rapport à COSMO. Cela pourrait être attribué aux différences dans les profils verticaux de la force du courant ascendant et des propriétés microphysiques à l'intérieur des nuages d'orage. Plus précisément, WRF simule des ascendances plus fortes, avec le noyau d'ascendance situé exactement là où les hydrométéores solides et liquides sont presque égaux, ce qui favorise ainsi une activité de foudre plus intense. En outre, cette étude évalue systématiquement et quantitativement la grêle et la foudre par rapport aux observations. Dans l'ensemble, les deux modèles, associés à HAILCAST et LPI, reproduisent avec succès les caractéristiques de la grêle et de la foudre, soulignant leur potentiel pour les évaluations climatologiques de ces phénomènes.

Motivée par les résultats encourageants des études de cas, la troisième partie de la thèse (Chapitre 4) est dédiée à dix années (2009–2018) de simulations climatiques multi-saisonniers (d'avril à septembre). En plus des observations, HAILCAST et LPI sont comparés à plusieurs proxys de substitution largement utilisés pour la grêle et la foudre. Les deux diagnostics peuvent reproduire les zones à risque de grêle et de foudre: les contreforts nord et sud des Alpes, les environs du Massif Central en France, le long des montagnes des Apennins et la côte est de la mer Adriatique, et sur les Carpates dans le bassin panonien. De plus, les caractéristiques de différents sous-domaines topographiques sont comparées aux estimations basées sur les radars dans la région alpine et aux relevés de stations dans la région adriatique. Le sud des Alpes présente un début de saison de grêle plus précoce et un cycle diurne prolongé jusqu'au soir par rapport au nord. Dans la région adriatique, les cycles saisonniers et diurnes se comportent différemment le long des zones côtières, des plaines et des régions montagneuses. La distribution fréquentielle des tailles de grêlons durant différentes saisons est conforme aux observations précédentes, la fréquence la plus élevée de très gros grêlons se produisant en juin.

En résumé, cette thèse se penche sur les caractéristiques de la grêle et de la foudre sur la région alpine-adriatique en utilisant des simulations climatiques à l'échelle du

kilomètre. Il s'agit de la première simulation à long terme à l'échelle subcontinentale avec des diagnostics de grêle et de foudre appliqués à un modèle climatique régional. La comparaison des diagnostics HAILCAST et LPI avec les observations disponibles donne des résultats prometteurs. Ces découvertes pourraient avoir des implications importantes pour les parties prenantes afin de prendre des décisions plus éclairées. Alors que notre climat continue d'évoluer sous l'effet du réchauffement global, les analyses présentées ici établissent les fondements de recherches futures — changements dans les tempêtes convectives sévères sous le climat futur.

Chapter 1

Background and introduction

Just as Johann Strauss eloquently portrayed the fury and grandeur of a summer thunderstorm in his symphonic poem “*Unter Donner und Blitz*, Op. 324” (Under thunder and lightning), nature’s tempestuous ensemble remains a subject of enduring fascination for humans. In the symphony of Earth’s ever-evolving climate, severe convective storms stand as awe-inspiring crescendos, and have emerged as a growing field of climate research.

However, as indicated in the most recent Intergovernmental Panel on Climate Change (IPCC) Assessment Report (AR) 6 (Seneviratne et al., 2021), the observed and human contribution to the trends of severe convective storms (SCSs) since 1950 is assessed as *low confidence*, and the projected trends also as *low confidence*. Severe convective storms are always associated with extreme phenomena such as tornadoes, hail, heavy precipitation, strong winds, and lightning. Quantifying and understanding the past trends and future projections of SCSs is challenging, due to several reasons: (1) hailstorms and thunderstorms are rare, local and short-lived, therefore lack homogeneous long-term high-quality observations; (2) incomplete understanding of the microphysical and dynamical processes; (3) the model’s limited ability to represent the complex topography and unresolved processes; (4) modeling study show different signals across models and proxies in future climate projection and several competing effects exist. These challenges lead to the *low confidence* assessment and are elaborated in the subsequent sections. Finally, the objectives of this thesis are outlined at the end of this chapter.

1.1 Weather and climate extremes

At the global scale, anthropogenic increases in the emission of greenhouse gases (GHG) are expected to raise the global mean temperature. According to the Clausius-Clapeyron (CC) relation, the atmospheric water holding capacity increases by approximately 6 to 7% per degree of atmospheric warming (Allen and Ingram, 2002). This leads to the intensification of the hydrological cycle, which is confirmed in observations and models (see e.g., Fischer and Knutti (2016); Fowler et al. (2021)). In addition to thermodynamic changes, the dynamic contribution modulates the regional responses. For example, the poleward expansion of the Hadley cell (Brogli et al., 2019), the poleward

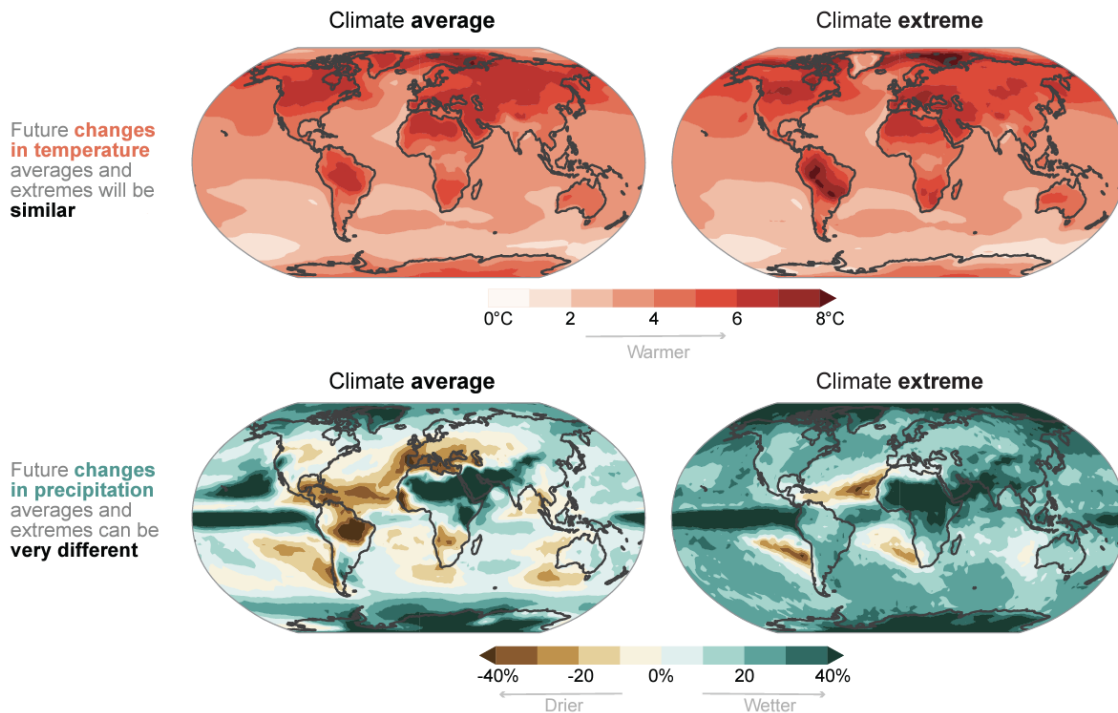


Figure 1.1: Global maps of future changes in surface temperature (top panels) and precipitation (bottom panels) for long-term average (left) and extreme conditions (right). Changes are estimated using Coupled Model Intercomparison Project Phase 6 ensemble median with global warming of 4 °C relative to 1850–1900 temperatures. Average surface temperature refers to the warmest three-month season and extreme temperature refers to the hottest day in a year. Average precipitation refers to changes in rainfall and snowfall and extreme precipitation refers to changes in largest daily precipitation in a year, shown as a percentage relative 1850–1900 values. Adopted from IPCC AR6 Chapter 11 (Seneviratne et al., 2021).

migration of storm tracks (Barnes and Polvani, 2013; Shaw et al., 2016), and extra latent heat released from the thermodynamic increase in moisture can potentially result in an increase in moisture and strength of convective updrafts (Trapp et al., 2009).

Climate change includes not only changes in mean climate, but also in weather extremes. Compared to temperature extremes, the projected changes in precipitation extremes show regional patterns (Fig. 1.1). Relative changes in extreme precipitation exhibit little geographical structure, despite the presence of complex topography and pronounced patterns in absolute precipitation (Ban et al., 2015). Giorgi (2006) demonstrates the Mediterranean and northeastern Europe are two hotspots that are the most responsive regions to global change.

Climate change exerts various influences on weather extremes, encompassing the change in intensity, frequency, duration, timing, and spatial extent. Weather and climate extremes can be generally quantified based on different metrics, such as percentile indices (e.g., Schär et al. (2016)), thresholds (e.g., hailstone exceeding a certain diameter (Trapp et al., 2019)), and return periods (e.g., return periods of large hail (Ni et al.,

2020)). Research on hail using reanalysis over past decades and simulations of future climate in the US suggests climate change may have an impact on hail characteristics, including hail size, frequency of hail days, duration and shift in hail seasons, and spatial extent of large hail reports (Trapp et al., 2019; Tang et al., 2019). Information on the characteristics of hail and lightning can help stakeholders build resilience for agriculture, vehicles, transportation infrastructure, and buildings under current and future climate conditions.

1.2 Physical background

1.2.1 Severe convective storms

The fundamental building block of convective storms, is the “cell” (Browning, 1977), and can be categorized as ordinary cells or supercells; or alternatively, single-cell (an ordinary cell), multi-cell (multiple ordinary cells), and supercell. The lifetime of an ordinary cell can be identified as three stages: the cumulus stage, the mature stage, and the dissipating stage (Byers and Braham, 1949).

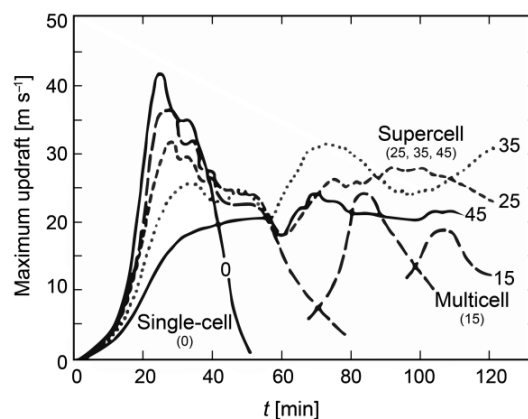


Figure 1.2: Lifetime of single-cell, multicell and supercell thunderstorms in terms of maximum updraft velocity. Adopted from Weisman and Klemp (1982).

As illustrated in Fig. 1.2, a *single-cell* thunderstorm that consists of only one updraft is short-lived because new cells are usually not initiated. This usually happens in weak shear environments and only occasionally produces hail. For *Multi-cell* thunderstorms, the gust front initiates new cells repeatedly, therefore – while individual cells last for 30-60 minutes – severe multicell storms can persist for hours and produce hail up to the size of golf balls (e.g., Marwitz (1972)). *Supercell* is characterized by the presence of a deep mesocyclone within the updraft, typically persisting for a duration of 1-4 hours. *Mesocyclone* is a region of vertically connected rotating updraft with 3-8 km in diameter (Houze, 2014), as often observed by radar (e.g., Feldmann et al. (2021)). Despite being less common, supercell storms are responsible for a large fraction of severe weather reports (e.g., Kunz et al. (2017)).

Mesoscale convective systems (MCSs) are organized groups of convective storms (Markowski and Richardson, 2010). Numerous case studies have been done on under-

standing the morphologies related to MCSs, such as quasi-linear convective systems (QLCS), squall lines (Thompson et al., 2012) and bow echoes (Fujita, 1978).

The ingredients required for severe convective storms include conditional instability, sufficient low-level moisture, a triggering mechanism, and vertical wind shear (Taszarek et al., 2021). Instability can be described using convective available potential energy (CAPE), which is an estimation of vertically integrated buoyancy for a rising air parcel. Higher values of CAPE indicate the atmosphere is more unstable and would therefore produce a stronger updraft. Positive CAPE is necessary but insufficient condition for severe storms (Lock and Houston, 2014). Contrarily, convective inhibition (CIN) quantifies the amount of energy required to overcome the negatively buoyant air parcel before it reaches the level of free convection (LFC). Less CIN is therefore expected when convective storms occur.

Furthermore, strong vertical wind shear can enhance the intensity and longevity by separating the updraft and downdraft regions of the storm. Thus, 0–6 km bulk wind shear (Trapp et al., 2007; Markowski and Richardson, 2010), i.e., the difference of the wind vector between the surface and 6 km above the surface, can discriminate the supercell and nonsupercell thunderstorm environments.

1.2.2 Hail

Hail is a form of solid precipitation, and thunderstorms that produce hail are considered as hailstorms. To distinguish hail from graupel or freezing rain, the World Meteorological Organization (WMO) recommends that ice crystals with a diameter larger than 5 mm be referred as hailstone. Despite large natural variability, hailstones can be better represented as triaxial ellipsoid shapes (Shedd et al., 2021), and generally 5–50 mm in diameter. The very large hailstone can reach 160 mm in diameter, according to the European Severe Weather Database. Hail can cause damage, such as broken windows and roofs, dented vehicles, crops, and injury to humans and livestock (Půček et al., 2019).

Growth and life cycle of a hailstone

As shown schematically in Fig. 1.3, the formation and growth of a hailstone is a complex process. The raindrop is lifted above 0 °C and gradually freezes and forms the core of a hailstone (point 2 in Fig. 1.3). It grows further by accretion with cloud droplets and ice crystals in the updraft until it becomes sufficiently heavy and falls down. There are two different regimes of hail growth. Cloud droplets or raindrops colliding with the hailstone that forms a water sphere around the frozen core is called *wet growth*. In contrast, if accretion of the hailstone with supercooled water droplets occurs while the temperature remains below the freezing point, it is called *dry growth*. The hailstone layers do not simply due to the hailstone's up-and-down excursions (Ziegler et al., 1983). Rather, it is because of the contribution of wet and dry growth regimes when hailstone encounters different temperatures and liquid water content distributions. The maximizing residence time in the updraft is a balance between the hailstone fall speed and the updraft speed. Therefore, supercells with strong updrafts could be beneficial for large hailstones. When the hailstone becomes large enough or the updraft weakens, it may fall out of the hail growth region. Hailstone then enters a melting process before it

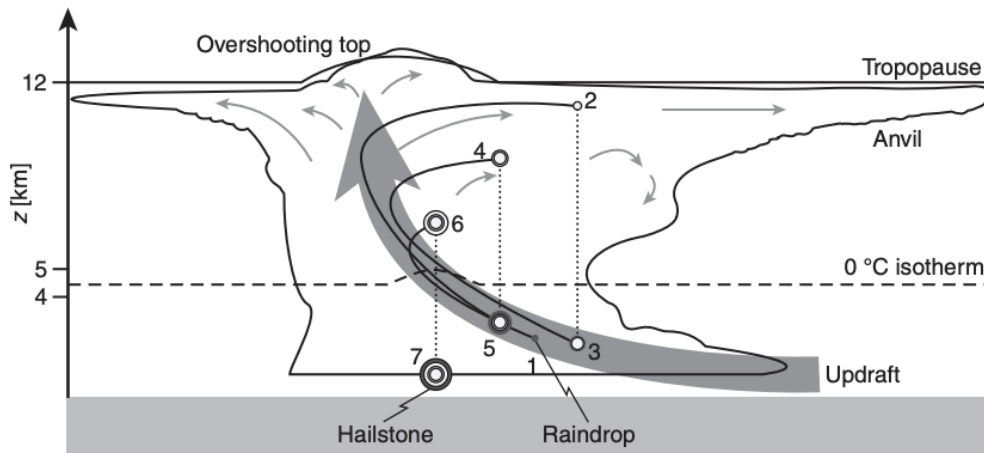


Figure 1.3: Schematic diagram of hail formation. Black circles denote wet growth and white circles dry growth. Upward-directed motions of the hailstone are denoted by solid lines and downward motions by dotted lines. Adapted from Lohmann et al. (2016).

reaches the ground.

In reality, the growth and lifecycle of a hailstone can vary differently depending on the conditions in the atmosphere. Some hailstones can be as small as a pea, while others can grow to be as large as a grapefruit.

Hail proxies and hail growth models

Hail proxies use several parameters to provide information of hail, among them mostly used are Hail Size Index (HSI), Large Hail Parameter (LGHAIL), and Significant Hail Parameter (SHIP, http://www.spc.noaa.gov/exper/mesoanalysis/help/help_sigh.html). However, hail proxies suffer from several drawbacks. Firstly, the proxy approach does not consider storm triggers. Secondly, it usually provides whether the environment is “hail prone” or “not hail prone”. However, not every favorable environment produces a severe thunderstorm or thunderstorm at all (Taszarek et al., 2021; Raupach et al., 2022). Thirdly, those indices represent empirical relationships from a regional scale, the performance of proxies may vary by the region and the time of the year. And it can be difficult to provide an estimation on a global scale.

With the development of the km-scale model, the research approach starts using physical-based hail diagnostics such as HAILCAST (Fig 1.4, Adams-Selin and Ziegler (2016)) that is able to be embedded in high-resolution models and calculate the hailstone size at the ground.

1.2.3 Lightning

A storm that exhibits lightning and thunder is called a thunderstorm. In 1752, Benjamin Franklin proposed that lightning is electricity through the famous but dangerous kit experiment. Actually, electricity in the atmosphere is not limited to stormy weather. On a clear day, a downward-pointing electric field is about 100 V m^{-1} near the Earth’s surface, meaning the fair-weather electric field tends to drive positive charges to the

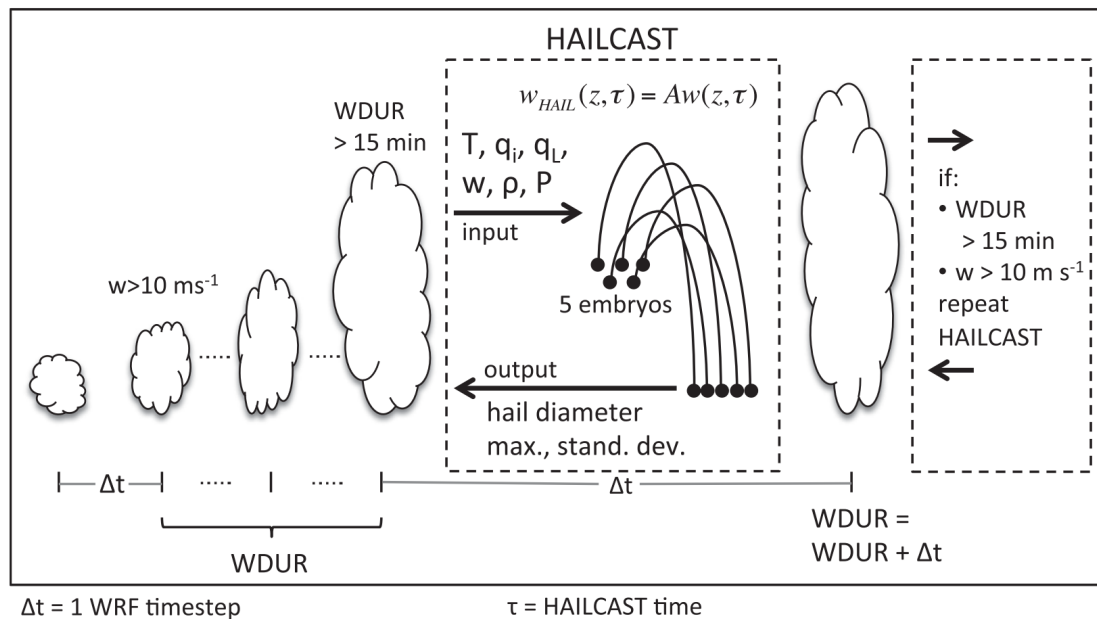


Figure 1.4: A conceptual diagram of HAILCAST integrated with high-resolution model. Adapted from Adams-Selin and Ziegler (2016).

negatively charged surface (Wang, 2013). The electric charges in the atmosphere mainly come from the radioactive emanation from the Earth's surface and cosmic rays from space.

As proposed by Wilson (1921), in the global electrical circuit, the atmosphere is an imperfect insulator between the Earth's surface and the ionosphere. And electrified thunderstorm clouds act as generators that replenish the Earth's surface with negative charges of 1500 A to balance the fair weather electric field and positive charges carried by falling precipitation particles. Lightning is to the global electrical circuit as precipitation to the general circulation (Williams, 2005).

Lightning is important for atmospheric chemistry as one of the primary sources of nitrogen oxides (Schumann and Huntrieser, 2007; Banerjee et al., 2014). It also influences the frequency of natural wildfires (Krause et al., 2014) and damage to infrastructure.

Charge distribution in thunderclouds

As illustrated in Fig. 1.5a, previous studies found most thunderstorm clouds have a tripolar structure (Williams, 1989). In the mature stage of the convective clouds (left, updraft dominate), the upper layer mostly carries positive charges where cloud ice and snow exist. In the middle level, a thin negative layer is located between -10 and -20 °C, which may contain both raindrops and graupel/hail. Near the cloud base is often a smaller positive charge region. At the very top of the cloud, there is another thin layer of negative charge that might be due to cosmic rays. While in the dissipating stage (Fig. 1.5b), the positive charges in the lower region precipitate out with downdrafts.

Charge separation mechanisms

Mechanisms responsible for charge separation that lead to lightning are not fully

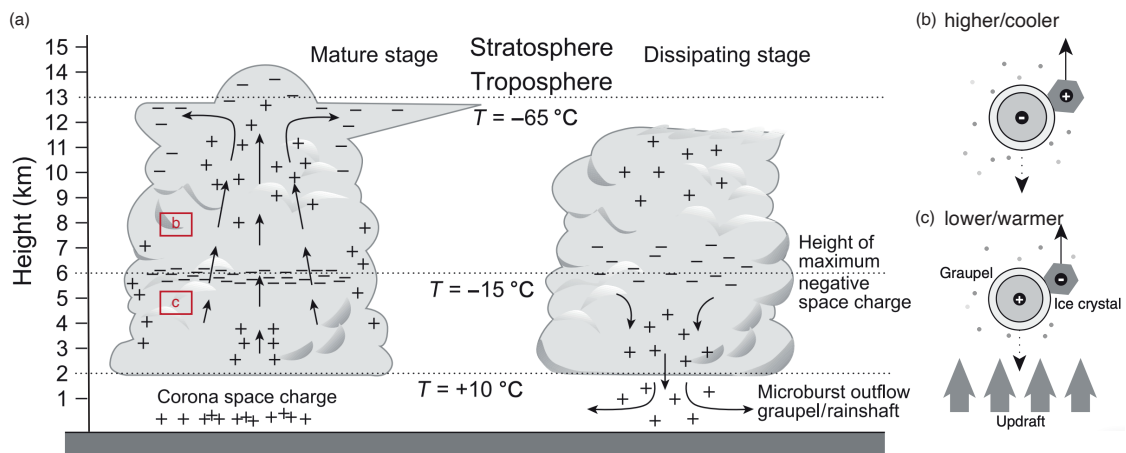


Figure 1.5: (a) Schematic of the electrical structure of a convective cloud in mature and dissipating stages. Adapted from Houze (2014). (b) and (c) Collisions between graupel particles (circles) and small ice crystals (hexagons) in the presence of supercooled liquid droplets (dots). Adapted from Lohmann et al. (2016).

understood, and many hypotheses exist and are under debate at present. During the development of the convection, the updraft motion will have an impact on charge distribution in the cloud. But there are discrepancies between this convection hypothesis and observations, so it is not considered as a viable initiation mechanism for electrification.

The non-inductive mechanisms (Reynolds et al., 1957) are considered to be the main cause of thundercloud electrification, which leads to charge separation without the need for an external electric field. Laboratory experiments have shown that rebounding collisions of riming graupel with ice crystal in the presence of supercooled liquid water is likely the most important process (Takahashi, 1978). As depicted in Fig. 1.5, the charge reversal temperature (T_R) at about 15°C , where graupel charged positively (negatively) when temperature above (below) T_R . This explains the observed tripole structure of the electrified clouds. On the other hand, inductive mechanisms refer to the charges induced in a pre-existing electric field. However, the effectiveness and efficiency of the processes to produce lightning are questionable and unrealistic.

Lightning parameterizations

A widely used modeling proxy for lightning flash is the use of the convective cloud-top height (CTH) proposed by Price and Rind (1992). As maritime thunderstorms produce less lightning than over continental with similar cloud top heights, they use different formulations over land and ocean. Romps et al. (2014) proposed that the lightning flash rate is proportional to the CAPE times the precipitation rate (hereafter “CAPEXP”).

As theory suggests that charging occurs in the mixed-phase region, atmospheric quantities such as updraft velocity, updraft volume (Deierling and Petersen, 2008), convective precipitation (Allen and Pickering, 2002), and cloud ice flux (McCaul et al., 2009; Finney et al., 2014) are considered as indicators of lightning activity. Lightning potential index (LPI, Yair et al. (2010)), using the updraft velocity in the developing thundercloud

scaled by the potential of charge separation based on the ratio of total ice and liquid water within the “main charging zone” (0 to -20°C). Recently, [Fierro et al. \(2013\)](#) implemented the explicit treatment of charging and discharging of lightning within the Weather Research and Forecasting (WRF) model.

1.3 Observations

1.3.1 Hail

The primary challenge in investigating hail climatology is the lack of homogeneous, long-term, and high-quality observations. Due to the highly localized nature of hail events, data access from meteorological stations is often limited and only a few countries have long-term records (e.g., China ([Li et al., 2016](#)), Croatia ([Blašković et al., 2023](#)), Romania ([Burcea et al., 2016](#)), and Serbia ([Ćurić and Janc, 2015](#))). Hailpad networks can provide more detailed information but cover limited areas (e.g., Italy ([Giaiotti et al., 2003](#); [Manzato et al., 2022a](#)), France ([Berthet et al., 2011, 2013](#)) Croatia ([Počakal et al., 2018](#))). Insurance damage data provides hail occurrence and the severity of hail damage ([Kunz et al., 2009](#)). However, it might be affected by variable exposure, vulnerability and other factors ([Punge and Kunz, 2016](#)). Hail information can be gained from crowd-sourced reports, such as newspapers ([Piani et al., 2005](#)), Internet sources ([Kahraman et al., 2015](#)), and public users collected from smartphone applications ([Barras et al., 2019](#)). The European Severe Weather Database (ESWD, [Dotzek et al. \(2009\)](#)) maintained by the European Severe Storms Laboratory (ESSL, [Groenemeijer et al. \(2017\)](#)) is by far the first and largest archive for pan-European hail reports. However, those reports suffer from unequal reporting efficiency and population density ([Taszarek et al., 2019](#)).

Besides direct observations, hail information can be indirectly retrieved from national radar networks with high spatial and temporal resolution (e.g., Germany, France, Belgium and Luxembourg ([Fluck et al., 2021](#)), Switzerland ([Nisi et al., 2016, 2018](#)) and the contiguous United States ([Cintineo et al., 2012](#))). Also, satellite detection of overshooting cloud tops can provide hail occurrence on continental scales ([Bedka, 2011](#); [Punge et al., 2017](#)). A summary of hail observations in Europe can be found in [Punge and Kunz \(2016\)](#).

1.3.2 Lightning

Over the past decades, numerous ground-based lightning location systems (LLSs) have been developed and deployed. The lightning data over broader areas is obtained by long-range detection systems that operate at very low frequencies (VLF), for example, the Worldwide Lightning Location Network (WWLLN, [Rodger et al. \(2006\)](#)), the Global Lightning Dataset 360 (GLD360, [Said et al. \(2010\)](#)), the National Lightning Detection Network (NLDN, [Orville and Huffines \(2001\)](#)), the National Observatory of Athens (ZEUS, [Kotroni and Lagouvardos \(2016\)](#)) and the UK Meteorological Office Arrival Time Difference system (ATDnet, [Anderson and Klugmann \(2014\)](#)). However, these systems are limited in location accuracy and detection efficiency. Another type of sensor that detects radiation from lightning discharges at very high frequency (VHF) is used in

lightning mapping array (LMA, [Rison et al. \(1999\)](#)) and provides detailed information on 3D characteristics of flashes, but over limited domains. The European Cooperation for Lightning Detection (EUCLID, [Poelman et al. \(2016\)](#)) established in 2001 is a collaborative network that receives sensor data from several national networks to provide European-wide lightning observations.

Alternatively, lightning can be obtained using satellite imagers that measure the radiation emitted from both IC and CG lightning flashes (e.g., Optical Transient Detector (OTD, operated between 1995 to 2000) and the successor Lightning Imaging Sensor (LIS) ([Christian, 2003](#); [Cecil et al., 2014](#))). However, these instruments cannot detect lightning at very high latitudes (e.g., LIS can only detect as far north as the southern Mediterranean). The Meteosat Third Generation (MTG) geostationary satellite carried with Lightning Image was just launched in 2019 and is able to detect lightning over Europe and Africa. The new platforms can provide unprecedented spatial coverage at high resolution and can be used as complements to the existing ground-based networks in the future.

1.4 Kilometer-scale modeling

As shown in Fig. 1.6, individual thunderstorms have a spatial scale of several kilometers, and a temporal scale as short as hours. Consequently, they are unresolved in a typical global climate model (GCM). Simulating hail and lightning can be challenging. Firstly, the complicated processes of convection and microphysics are involved in severe convective storms. For example, hail and lightning require a sufficiently high vertical velocity, and the relevant convective velocities are not resolved in GCMs. Secondly, the triggering depends on small-scale factors, such as local winds, topography, and pre-existing outflows from nearby convective cells ([Kahraman et al., 2022](#)). The hail and lightning proxies used in previous studies (e.g., [Romps et al. \(2014\)](#); [Rädler et al. \(2019\)](#); [Raupach et al. \(2022\)](#)) are a source of uncertainties in the understanding of future thunderstorms ([Seeley and Romps, 2015](#); [Finney et al., 2018](#)).

With the advent of emerging supercomputing platforms, and with the progress in high-resolution climate modeling, climate models can explicitly resolve the convective process by reducing the horizontal grid spacing to less than 4 km ([Prein et al., 2015](#); [Schär et al., 2020](#)). It is able to simulate extreme precipitation at high percentiles at hourly and sub-hourly time scales ([Vergara-Temprado et al., 2021](#)). In the meantime, using the km-scale model improves the representation of fine-scale topography, which is especially beneficial in mountainous regions (e.g., [Heim et al. \(2020\)](#)).

The explicit treatment of deep convection used in the km-scale climate model can be attractive to understanding the projection of SCSs. The recent IPCC AR6 report ([Seneviratne et al., 2021](#)) highlights that the significant uncertainty in projected regional changes in hail and lightning stems from the limited analysis of simulations using convection-permitting models. So far, there are only a handful of high-resolution climate simulations to study hail and lightning ([Trapp et al., 2019](#); [Kahraman et al., 2022](#)), leaving ample room for further investigation.

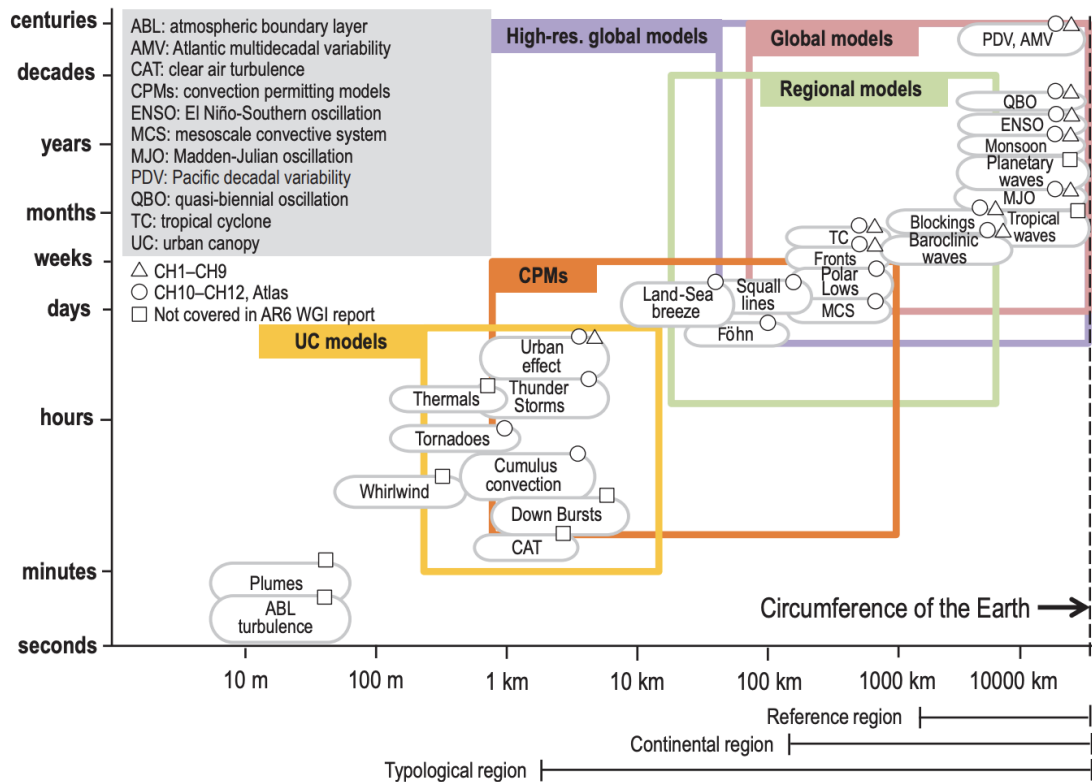


Figure 1.6: Schematic diagram to display interacting spatial and temporal scales relevant to regional climate change information. Adapted from IPCC AR6 Chapter 10 (Doblas-Reyes et al., 2021).

1.5 Early Alpine hail research

The hail research is important, as the Alpine region is the hotspot of initiation of thunderstorms in Europe (Manzato et al., 2022b). In the 1970s, the early hail research efforts and field campaigns were motivated by the pursuit of cloud seeding experiments aimed at hail prevention or suppression (e.g., Grossversuch IV, Federer et al. (1986)). Later, the research interests shifted towards detecting, forecasting, and mitigating hailstorms through improved property resiliency (Allen et al., 2020). Storms in the Alpine region exhibit a different storm environment than classic prototypes (Houze et al., 1993) and the United States (Taszarek et al., 2020b). Huntrieser et al. (1997) developed an environmental-based “SWISS index” that adjusted to the conditions in northern Switzerland. At that time, the best observational set available on the climatological distribution of severe hailstorms was hail damage claims collected by the Swiss crop-hail insurance data (Willemse, 1995). Later on, the era of meteorological radar measurements unlocked vast potential for in-depth research into severe convective storms. Dealing with the shielding of the radar beam by mountain ranges (Germann et al., 2006) has shown improved quantitative precipitation information. In 2016, Nisi et al. (2016) filled in the gap in hail climatology for Switzerland and developed radar-based hail detection algorithms combined with the information extracted from high-resolution simulations using the Consortium for Small-scale Modeling (COSMO) model.

1.6 Effects of climate change on severe convective storms

1.6.1 Hail

Past trends

As reviewed by [Punge and Kunz \(2016\)](#), insufficient monitoring of hail events over a long-term period, as well as national borders and different observation systems, hamper the trend analysis of hail changes in the past. In Europe, the number of hail days from coarsely spaced weather stations shows different trends. In Romania, for the period of 1961–2014, only half of the stations show a positive trend ([Burcea et al., 2016](#)), while the positive trend is significant only for high-impact events in Catalonia (Spain) for the period of 1994–2009 ([Aran et al., 2011](#)). In Croatia, [Blašković et al. \(2023\)](#) found a negative and significant trend of hail days for very long periods (1900–2020), and a stagnation of negative trend in recent period (1995–2019). Several hailpad networks provide the probability to study long-term hail trends. [Manzato et al. \(2022a\)](#) found no significant trend from hailpad observations (1988–2016) in northeastern Italy, except for an increase in mean hail diameter with a lower number of hailstones in the recent period (1995–2016). Another study by [Eccel et al. \(2011\)](#) using hailpad observations in Italy (1975–2009) found the number of hail days remained unchanged while there is a positive trend for the 90th percentile of hailstone diameter. These hailpad results reveal a general increase in hail severity ([Raupach et al., 2021](#)).

Insurance hail losses in Europe have dramatically grown since 2008, though the trend can be affected by economic growth, inflation and change in exposure ([SwissRe, 2021](#)). Notably, severe hail damage in France set a new event loss benchmark in 2022, underscoring the shift of risk management ([SwissRe, 2023](#)).

Future projections

More low-level moisture indicates an increase in instability and therefore stronger updraft (Fig. 1.7(1)). However, [Taszarek et al. \(2021\)](#) pointed out the positive trend in instability may not necessarily result in a higher number of storms, particularly accompanied by a considerable increase in CIN.

An increase in melting level height due to climate warming also affects the hailstones (Fig. 1.7(2)), despite more intense storms and larger amounts of hail generated in-cloud ([Mahoney et al., 2012](#); [Brimelow et al., 2017](#); [Prein and Heymsfield, 2020](#)). This is due to the enhanced melting of hailstones when they fall through a deeper and warmer layer before they reach the surface. Using hailpad observation in France, [Dessens et al. \(2015\)](#) found this can be more detrimental to smaller hailstones compared to larger ones. Therefore, the hailstone size distribution will probably shift towards larger hailstones ([Mahoney et al., 2012](#)).

Another fact that adds to the complexity is the change in vertical wind shear (Fig. 1.7(3)). While wind shear plays an important role in amplifying and sustaining the updraft through storm organization ([Dennis and Kumjian, 2017](#)), previous studies have found that its impact on hailstorms is smaller compared to the instability ([Genio et al., 2007](#)) or melting level height. Though it is expected to decrease owing to the projected weakening of the meridional gradient of temperature as a result of polar am-

plification, suggesting an increased likelihood of more severe events. However, from regional simulations of the US, [Diffenbaugh et al. \(2013\)](#) found it mostly happened in days under low CAPE. To incorporate the effect of wind shear, tracking the position of hailstone and velocity over time can be very computationally intensive for climate studies. Thus, it is difficult to quantify how wind shear affects the projection of hailstorms under future climate.

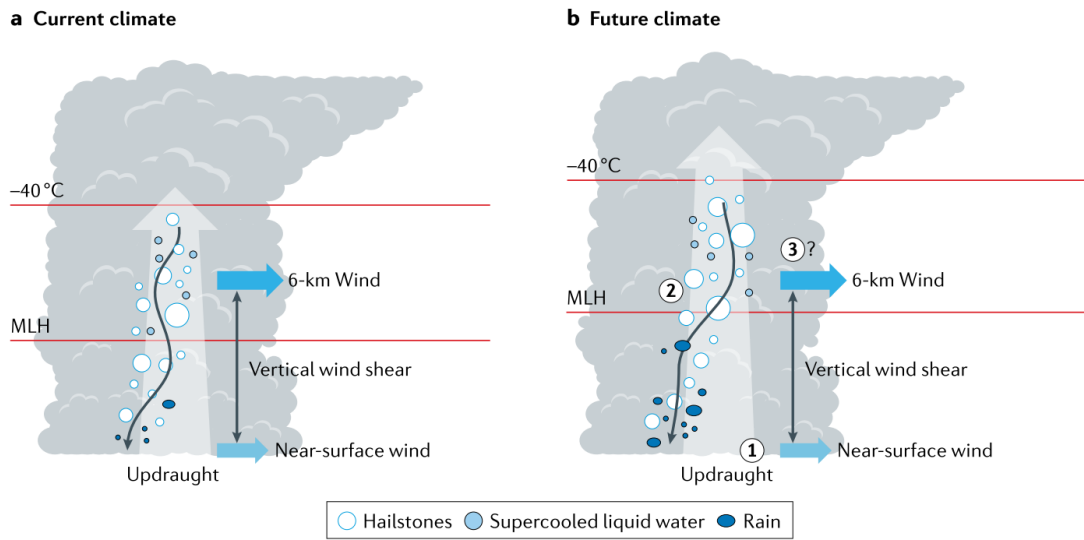


Figure 1.7: The expected environments in hail-relevant atmospheric phenomena in the (a) current and (b) future climate conditions. The numbered points in (b) correspond to the (1) increased low-level moisture which leads to the increased convective instability and updraught strength; (2) increased hailstone sizes which leads towards larger hailstones; and (3) changes in vertical wind shear which may affect storm structure and hailstone trajectories, but this is generally overshadowed by instability changes. Adapted from ([Raupach et al., 2021](#)).

1.6.2 Lightning

Past trends

Trends in lightning are a challenging problem since using lightning observations over a decade would be too short to access climate trends. [Taszarek et al. \(2019\)](#) indicates an increased number of days with thunderstorms over the Alps and central, southeastern, and eastern Europe, while with a decrease over the southwest since 1979. Applying the statistical method to reconstruct lightning climatology over 40 years (1980–2019), [Simon et al. \(2023\)](#) suggests the most intense increase happened over the high Alps, where lightning activity doubled in the 2010s compared to the 1980s. Also, the signals along the southern and northern Alpine rim are similar but weaker, whereas the flatlands surrounding the Alps have no significant trend. In contrast, by applying empirical proxies for lightning, there is a robust negative trend for thunderstorms over the majority of southern and western parts of the US. Based on NLDN observations (1989–2018), [Taszarek et al. \(2021\)](#) found the largest decreases of observed CG lightning

hours during summer over the south Great Plain. These studies highlight the divergent lightning trends over Europe and the US, underlying environment driving thunderstorms are very different (Taszarek et al., 2020a,b).

Future projections

How climate change affects lightning in the future is even more uncertain, and previous studies have shown that different regions have contrasting stories of lightning using different parameterizations (Clark et al., 2017; Finney et al., 2018; Romps, 2019; Brisson et al., 2021; Charn and Parishani, 2021; Kahraman et al., 2022; Haberlie et al., 2022).

CAPE responds positively to temperature, thus CAPE-based proxies suggest an increase (Romps, 2019). However, when including the cloud ice, Brisson et al. (2021) shows contrasting projections over Germany. Thus, using CAPE_{EXP}, cloud-top height, or similar proxies without the presence of cloud ice cannot identify most of the decreasing lightning patterns in a warming climate (Kahraman et al., 2022). Several studies (Singh and O’Gorman, 2014; Mortelmans et al., 2022) suggest that microphysics play an important role in determining the response of convective precipitation extremes to warming, particularly when ice- and mixed-phase processes are important. Thus, it remains uncertain which proxy is well suited to predicting the change in lightning rates and patterns.

Another effect is the change of surface characteristics and aerosols (Thornton et al., 2017). A drier surface allows for a higher cloud base height and a suppression of warm rain coalescence beneath the 0°C isotherm. A more polluted boundary layer leads to the reduced mean droplet size, suppresses the warm-rain coalescence, and allows for more liquid water to enter the mixed phase region where it can invigorate the ice-based electrification process (Williams, 2005). However, the relative importance of these factors has not been resolved yet.

1.7 Objectives and thesis outline

This doctoral thesis is a part of the Croatian-Swiss Research Programme titled “Severe Weather over the Alpine-Adriatic region in a Changing Climate (SWALDRIC)”, specifically focusing on modeling hail and lightning using kilometer-scale climate simulations. The overarching goals of the thesis are:

- How well are severe convective storms simulated by km-scale models?
- What are the main characteristics of hail and lightning over the Alpine-Adriatic region?

To achieve the objectives, several real-case and long-term simulations under present conditions are conducted with hail and lightning diagnostics. Apart from the introduction chapter, the research questions are addressed in the following chapters:

Chapter 2: Exploring hail and lightning diagnostics over the Alpine-Adriatic region in a km-scale climate model. [Cui et al. (2023)] This chapter focuses on eight real cases of severe convective storms (including moderate to severe hailstorms and one no-hail storm) over the Alpine region that occurred in the period of 2009 to 2018

under different conditions. The simulations are performed with the climate version of the COSMO model with HAILCAST and LPI diagnostics. Overall, the model did a good job of simulating total precipitation, hail, and lightning compared to available high-resolution observations. At the same time, a detailed analysis of three cases is conducted to evaluate how the model reproduces heavy thunderstorm environments.

Chapter 3: Simulating hail and lightning over the Alpine-Adriatic region – A model comparison study. [Malečić et al. (2023)] In this chapter, eight hailstorms that occurred over the Alpine-Adriatic region are analyzed using simulations with the WRF and the COSMO models. A model comparison study is performed to systematically and quantitatively evaluate the ability of HAILCAST and LPI to reproduce the occurrence of hail and lightning. Overall, the two models yield similar results, but some systematic differences are found and tied to differences in model structure.

Chapter 4: Evaluation of decade-long hail and lightning simulation over the Alpine-Adriatic region using a km-scale climate model. How can we increase confidence in our future projections? This chapter focuses on the multi-seasonal (April–September) simulations of hail and lightning characteristics under the current climate (2009–2018). Alongside the HAILCAST and LPI diagnostics, we compared several widely used hail and lightning proxies against available observations. Such comprehensive approaches enable us to examine and compare the inter-annual, sub-seasonal, and diurnal variations across different topographical regions.

Chapter 5: Conclusions and outlook. The final chapter summarizes the main results of this thesis and provides an outlook for future research.

Chapter 2

Exploring hail and lightning diagnostics over the Alpine-Adriatic region in a km-scale climate model

Ruoyi Cui¹, Nikolina Ban², Marie-Estelle Demory^{1,3,4,5}, Rafael Aellig^{1,6}, Oliver Fuhrer⁶, Jonas Jucker¹, Xavier Lapillonne⁶, Christoph Schär¹

This chapter has been published in *Weather and Climate Dynamics*: <https://doi.org/10.5194/wcd-4-905-2023>

Abstract The north and south of the Alps, as well as the eastern shores of the Adriatic Sea, are hot spots of severe convective storms, including hail and lightning associated with deep convection. With advancements in computing power, it has become feasible to simulate deep convection explicitly in climate models by decreasing the horizontal grid spacing to less than 4 km. These kilometer-scale models improve the representation of orography and reduce uncertainties associated with the use of deep convection parameterizations.

In this study, we perform km-scale simulations for eight observed cases of severe convective storms (seven with and one without observed hail) over the Alpine-Adriatic region. The simulations are performed with the climate version of the regional model Consortium for Small-scale Modeling (COSMO) that runs on graphics processing units (GPUs) at a horizontal grid spacing of 2.2 km. To analyze hail and lightning we have explored the hail growth model (HAILCAST) and lightning potential index (LPI) diagnostics integrated with the COSMO-crCLIM model.

¹Institute for Atmospheric and Climate Science, ETH Zurich, Zurich, Switzerland

²Department of Atmospheric and Cryospheric Sciences, University of Innsbruck, Innsbruck, Austria

³Wyss Academy for Nature, University of Bern, Bern, Switzerland

⁴Climate and Environmental Physics, Physics Institute, University of Bern, Bern, Switzerland

⁵Oeschger Centre for Climate Change Research, University of Bern, Bern, Switzerland

⁶Federal Office for Meteorology and Climatology (MeteoSwiss), Zurich, Switzerland

Comparison with available high-resolution observations reveals good performance of the model in simulating total precipitation, hail, and lightning. By performing a detailed analysis of three of the case studies, we identified the importance of significant meteorological factors for heavy thunderstorms that were reproduced by the model. Among these are the moist unstable boundary layer and dry mid-level air, the topographic barrier, as well as an approaching upper-level trough and cold front. Although COSMO HAILCAST tends to underestimate the hail size on the ground, the results indicate that both HAILCAST and LPI are promising candidates for future climate research.

2.1 Introduction

Deep convective storms are ubiquitous worldwide, and severe convective events may be accompanied by hailstorms, lightning, wind gusts, and flash floods that lead to significant damage. For example, small hailstones can damage crops and vineyards, while larger hailstones can damage roofs and buildings, resulting in considerable economic and (re-)insured losses (e.g., [Punge and Kunz \(2016\)](#)). The damage from individual hailstorms in Europe and the United States can exceed USD 1 billion ([Půčik et al., 2019](#)). Therefore, it is essential to understand the spatial and temporal characteristics and associated mechanisms of such severe convective storms and their potential change with the further warming of the atmosphere.

The Alpine-Adriatic region encompasses the Alps, including their southeastern extension along the Adriatic Sea. It is recognized as one of the regions at high risk of experiencing thunderstorms in Europe due to its notable topography and proximity to the Mediterranean Sea ([Punge and Kunz, 2016](#)). Using 15 years of radar-based observations between 2002 and 2016, [Nisi et al. \(2016, 2018\)](#) identified enhanced frequency of hail days along the foothills of the Alps in the northern and southern pre-Alpine region, the Jura mountains, southern Germany, and the Bavarian Alps. In contrast, over the highest part of the Alps, severe hailstorms rarely occur ([Punge and Kunz, 2016](#)). Situated over the eastern shore of the Adriatic Sea, Croatia is also exposed to frequent hail events. Using 11 000 reports from hail stations in the period of 1981–2006, [Počakal et al. \(2009\)](#) identified the highest average number of hail days over the northern region in the continental part of Croatia, which is located between several mountains. Also, longer hail fall duration and larger hail diameters were found in the areas around the mountains compared to the flat eastern part of Croatia. However, owing to difficulties in observing and modeling such events, it remains a challenge to understand the characteristics and mechanisms of such severe convective storms.

Due to the rarity, the local-scale of hail events and the sparseness of stations, hailstorms are not well captured by ground-based observations. Hailpad networks are one of the options that provide information about hail size, mass, and kinetic energy, but they are only available in limited hail-prone areas ([Schmid et al., 1992](#); [Počakal et al., 2009](#); [Jelić et al., 2020](#)). Another option to retrieve information on hailstones is the use of weather radars. Algorithms based on radar reflectivity have successfully quantified precipitation amounts and the occurrence and properties of hail ([Germann et al., 2022](#)). Radar provides continuous information about the spatial and temporal distributions of

hail on a national scale, for example, over the contiguous United States (Cintineo et al., 2012) and the Alpine region (Nisi et al., 2016, 2018; Barras et al., 2021). These studies indicate that the combination of ground-based hailpads and radar-based products can provide valuable information for hail analysis on weather and climate time scales and support the evaluation of models.

Although severe convective storms can cause catastrophic damage, important processes, such as hail growth (Adams-Selin, 2023) and lightning processes (Fierro et al., 2013), for predicting hail and lightning are insufficiently represented in weather and climate models. The key ingredients of severe thunderstorms are conditional instability often associated with high convective available potential energy (CAPE), sufficient low-level moisture, lifting mechanisms that trigger the development of storms, and wind shear that can promote the storm organization and intensification of updrafts (e.g., Markowski and Richardson (2010)). The combination of CAPE with other parameters, such as precipitation rate (Romps et al., 2014) or a 0–6 km deep wind shear (e.g., Seeley and Romps (2015)), has been used to identify atmospheric conditions prone to severe convective storms. Furthermore, over complex topography, additional thermodynamic and kinematic mechanisms may also affect the initiation and development of convection. For example, Kalthoff et al. (2009) used sodar, lidar, and aircraft data to investigate the 15 July 2007 storm that occurred east of the Black Forest in Germany and identified several triggering mechanisms. High insolation during the day contributed to large latent heat fluxes, resulting in moisture accumulation within the valley. This moisture was subsequently transported to the mountain crest via upvalley winds. Strong updrafts nearly reached the level of free convection when a mesoscale convergence zone arrived and superposed with the stationary thermally induced convergence. Trefalt et al. (2018) found that the convection initiation on 6 June 2015 in the northern Swiss Prealps was associated with strong convergence at mountain tops that propagated via cold air outflow downslope to the valley. Convergence areas commonly have a width of about 1–2 km (Baldauf et al., 2011), so a fine and adequate representation of the convergence strength and updrafts is required to simulate a severe convective storm and investigate the driving mechanisms. At the same time, convection can be influenced and modulated by fronts, upper-level troughs, cold pools, and terrain effects. Therefore, the processes involved in each convective storm that occurs in different regions and under different synoptic situations can be very different and require specific case studies (Luo et al., 2020).

In the past decade, climate simulations at the kilometer-scale grid spacing started to emerge. The main advantages of running a model at such a high resolution are a better representation of orography and that there is no need for a deep convection parameterization, which is often associated with large uncertainties in climate simulations (Prein et al., 2015; Leutwyler et al., 2016; Ban et al., 2021). Such km-scale simulations lead to improved representation of the diurnal cycle of precipitation, heavy precipitation, clouds, snow, and local winds (Ban et al., 2021; Pichelli et al., 2021; Hentgen et al., 2019; Lüthi et al., 2019; Belušić et al., 2017). Still, hail and lightning are commonly not resolved or diagnosed in such models because of the complicated hail growth processes and electrification mechanisms that would make the models too expensive for climate simulations. The need to understand, predict, and project hail and lightning

have led to the development of diagnostic tools such as the hail growth model HAILCAST (Adams-Selin and Ziegler, 2016) and the lightning potential index (LPI) (Lynn and Yair, 2010). Such diagnostics implemented in km-scale models take advantage of a more realistic representation of convection and micro-physical processes and provide information on hail and lightning without a significant increase in the computational cost of simulations. Comparison with observations shows that the HAILCAST diagnostic is a good indicator of the hailstone sizes at the ground (Adams-Selin et al., 2019; Malečić et al., 2022), and LPI is highly correlated with the observed lightning flashes (Yair et al., 2010) when the convection is well simulated. There are some models that include a more sophisticated treatment of hail and lightning processes. For instance, Meso-NH supports an explicit treatment of lightning, which represents the life cycle of the electric charges from generation to neutralization via lightning flashes, and a two-moment aerosol-coupled-microphysics scheme (Lac et al., 2018). Such simulations are far more expensive and currently not yet suited for simulations over climate time scales in large computational domains.

In this study, we use the Consortium for Small-scale Modeling (COSMO) model with HAILCAST and LPI diagnostics and available observations to explore severe convective storms over the Alpine Adriatic region. The specific objectives of the study are:

- Evaluate the performance of the COSMO model at km-scale grid spacing in simulating hail and lightning.
- Explore how the COSMO model represents storm environments through case studies.

To address the above objectives, we simulate eight cases of severe convective storms (including moderate to severe hailstorms and one no-hail storm) over the Alpine-Adriatic region that occurred in the period from 2009 to 2018 under different synoptic conditions.

This chapter is structured as follows. Section 2.2 describes the model configurations and diagnostics together with the available observations and validation methods. Section 2.3.1 presents the eight selected cases with observed severe weather over the Alpine-Adriatic region. Section 2.3.3 evaluates the performance of HAILCAST and LPI. Section 2.3.5 analyzes the results for three selected cases to understand the drivers of such events and how they are represented in the model. Finally, Section 2.3.6 presents a summary of the results with a discussion of the potential use of HAILCAST and LPI diagnostics in future climate simulations.

2.2 Data and methods

2.2.1 Model description

The simulations are performed with the climate version of the non-hydrostatic COSMO model (Baldauf et al., 2011). More specifically, we use COSMO-crCLIM, a version of COSMO that is able to run on hybrid CPU-GPU architectures (Leutwyler et al., 2017; Schär et al., 2020). Hereafter, we refer to COSMO-crCLIM as COSMO for simplicity. The simulations are conducted following a two-step, one-way nesting ap-

proach with a horizontal grid spacing of 12 km for the first nest and 2.2 km for the second nest (Fig. 2.1a). The simulations are driven by the ERA5 reanalysis (Hersbach et al., 2020) with a boundary updating interval of 1 h. Both domains are discretized with 60 terrain-following hybrid vertical levels, where vertical spacing ranges from 20 m near the surface to about 1.2 km at the model top are located at around 23.5 km above mean sea level.

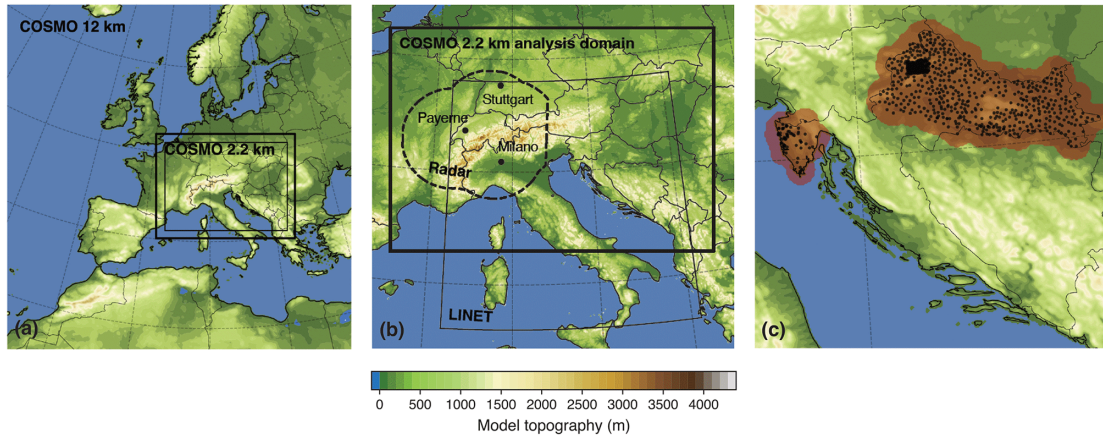


Figure 2.1: COSMO model topography, analysis domains, and observational coverage. (a) Computational domains for the simulations with 12 and 2.2 km grid spacing. The innermost box denotes the analysis domain. (b) COSMO 2.2 km analysis domain (thick solid line), LINET lightning observations (thin line), radar-based hail observations (dashed line). Black dots represent the three sounding stations used in this study: Payerne, Milan, and Stuttgart. (c) Available hailpad measurements over Croatia (black dots). A dense hailpad polygon (150 hailpads aligned with a distance of around 2 km between hailpads) is located in the northwestern part of Croatia. The red-shaded area indicates the region used to evaluate hail simulated by COSMO HAILCAST.

From the parameterization packages, we apply a single-moment bulk microphysics scheme with prognostic cloud water, cloud ice, graupel, rain, and snow (Reinhardt and Seifert, 2006), and a radiation scheme with a δ -two-stream approach (Ritter and Geleyn, 1992). For the outer 12 km domain, the Tiedtke (1989) convection scheme is turned on for shallow convection and switched off for deep and mid-level convection following Vergara-Temprado et al. (2020). For the inner 2.2 km domain, the convection parameterization scheme is switched off entirely to resolve the convection processes explicitly as far as feasible.

2.2.2 HAILCAST – hail growth model

The COSMO model is run with the HAILCAST module, a diagnostic hail growth model that predicts the size of hailstones falling to the ground. It was originally a 1D coupled cloud and hail model developed by Poolman (1992) and further improved by Brimelow et al. (2002) and Adams-Selin and Ziegler (2016). The HAILCAST version used in this study is adopted from WRF-HAILCAST (Adams-Selin and Ziegler, 2016). If the grid column or any adjacent grid columns has a maximum updraft exceeding

10 m s^{-1} between the previous and current model time steps, the updraft duration field is incremented by one model time step. This field is used to track the convective cells and limit the maximum updraft time in the hail model. HAILCAST activates when the updraft velocity is larger than 10 m s^{-1} and the updraft duration is more than 15 min. At that point, the vertical profile at the given model time step is passed to HAILCAST, which then calculates the evolution of five hail embryos selected based on microphysical considerations. Two embryos of 5 and 7.5 mm in diameter are initialized at -8°C level and three embryos of 5, 7.5, and 10 mm in diameter are initialized at -13°C . HAILCAST is activated every 5 min in the inner COSMO 2.2 km domain. The hourly maximum hailstone diameter among the five prescribed hail embryos is stored at hourly output intervals, providing information on hail swaths and the maximum expected hail size over an hour.

2.2.3 LPI – lightning potential index

The lightning potential index (LPI, J kg^{-1}) is a measure of the potential for charge generation and separation that leads to lightning flashes in thunderstorms (Lynn and Yair, 2010; Yair et al., 2010). It considers the separation region of clouds within the main charging zone (0 to -20°C), where the contribution of non-inductive mechanisms is the most efficient. Non-inductive mechanisms refer to the rebounding collisions between cloud ice crystals and graupel particles under the presence of supercooled liquid water (Takahashi, 1978). We use the updated LPI version after Brisson et al. (2021):

$$LPI = f_1 f_2 \frac{1}{H_{-20^\circ\text{C}} - H_{0^\circ\text{C}}} \int_{H_{0^\circ\text{C}}}^{H_{-20^\circ\text{C}}} \varepsilon w^2 g_{(w)} dz \quad (2.1)$$

with

$$\varepsilon = \frac{2(q_L q_F)^{0.5}}{q_L + q_F} \quad (2.2)$$

and

$$q_L = q_c + q_r, \quad (2.3)$$

$$q_F = q_g \left(\frac{(q_i q_g)^{0.5}}{q_i + q_g} + \frac{(q_s q_g)^{0.5}}{q_s + q_g} \right) \quad (2.4)$$

where q_c , q_r , q_i , q_s , and q_g are the mixing ratios of cloud water, rain water, cloud ice, snow, and graupel, respectively. $g_{(w)}$ is a boolean function equal to 1 when vertical velocity $w \geq 0.5 \text{ m s}^{-1}$, and 0 otherwise. ε is a dimensionless number that has a value between 0 and 1, and it scales the cloud updrafts and reaches the maximum when the vertically averaged mixing ratios of liquid (q_L) and combined ice (q_F) species are equal. Thus, the LPI is non-zero when liquid water and ice species co-exist in the grid boxes with updraft velocity above 0.5 m s^{-1} , a threshold that identifies the growth phase of the thunderstorm. However, this chosen threshold generates many LPI signals. To overcome this issue two Boolean functions f_1 and f_2 are included to filter out weak and noisy

LPI signals caused by isolated single-grid-column updrafts (f_1) and to filter out false LPI signals in strong orographic gravity wave clouds (f_2) following [Brisson et al. \(2021\)](#). f_1 is TRUE if more than 50% of grid boxes in a surrounding area of $10 \times 10 \text{ km}^2$ have an updraft larger than (or equal to) a threshold w_{max} . The threshold w_{max} is somehow arbitrary (see [Brisson et al. \(2021\)](#)) and depends on the grid spacing used. In our application, we have set it to 2 m s^{-1} , which showed a reasonable distribution of LPI. However, this threshold is slightly different from 1.1 m s^{-1} used by [Brisson et al. \(2021\)](#) with a grid spacing of 2.8 km. Note that these values are much lower than what is observed in the real world due to the simulated wider convective clouds and weaker updrafts, given that the 2.2 km grid spacing is high but not to a level that matches reality. f_2 is TRUE if a column integrated buoyancy (see Eq. 16 in [Brisson et al. \(2021\)](#)) in a surrounding area of $20 \times 20 \text{ km}^2$ is larger than (or equal to) -1500 J kg^{-2} . As for w_{max} , this threshold is also arbitrary, but in this case, we did not do any additional test and simply used the one recommended by [Brisson et al. \(2021\)](#). Thus, for more detail on these functions and choices, please see [Brisson et al. \(2021\)](#). LPI is calculated every 15 min in the COSMO 2.2 km simulations, and it is saved as an hourly maximum.

2.2.4 Observational datasets

Precipitation observations. The Integrated Multi-satellitE Retrievals for Global Precipitation Measurement (IMERG, [Huffman et al. \(2019\)](#)) dataset is used to validate the simulated total precipitation. It has a grid spacing of 0.1° ($\approx 10 \text{ km}$) and is available at half hourly time frequency. The IMERG data covers our entire analysis domain, including oceans that lack in-situ precipitation measuring instruments.

In addition to IMERG, we use a gridded precipitation dataset, RhiresD, available over Switzerland only ([Wüest et al., 2009](#)). It provides daily accumulated precipitation based on a high-density rain gauge network – including 430 gauges in Switzerland. The data is available at a horizontal grid spacing of 2 km. The dataset suffers from a general tendency to overestimate light precipitation and underestimate intense precipitation due to interpolation uncertainty. The uncertainty is higher in data-sparse areas and in cases of high spatial variations (e.g., convective precipitation).

Hail observations. Simulated hail is evaluated against in-situ and remote radar-based observations. In-situ observations include crowd-sourced hail reports collected from the MeteoSwiss weather app (2015 to present, [Barras et al., 2019](#)) and hailpad observations retrieved from three networks located in Croatia (Fig. 2.1c; [Počakal et al., 2009](#); [Malečić et al., 2022](#)). MeteoSwiss crowd-sourced data provides information on the time, location, and size of the observed hail collected by the users of the MeteoSwiss App. The user can choose the hail size from predefined hailstone size categories: “coffee bean (0–15 mm)”, “1 Swiss Franc (CHF) coin (15–27 mm)”, “5 CHF coin (27–32 mm)”, and “> 5 CHF coin (> 32 mm)”. The size category was updated in September 2017 to include a “< coffee bean (0–5 mm)” category (to differentiate between graupel and hail), updated “coffee bean (5–15 mm)”, and “5 CHF coin (27–37 mm)”, and added two new categories “golf ball (37–55 mm)” and “tennis ball (> 55 mm)”. More details can be found in Table 1 of [Barras et al. \(2019\)](#).

Hailpads provide information about the number and diameters of hailstones that

hit the measuring plate. The hailpad networks in Croatia include (i) stations in the continental part of Croatia (590 hail stations with a mean distance of about 5.5 km between hailpads), (ii) the hailpad polygon in the western part of Zagorje (150 hailpads with an equidistant spacing of 2 km), and (iii) the hailpad network installed in Istria (67 hailpads) (Fig. 2.1c). It should be noted that hailpad observations do not report hail sizes smaller than 5 mm.

Two radar-based hail products are used to analyze hail swaths over the complex topography of the Alpine region (Fig. 2.1b): probability of hail (POH) and maximum expected severe hail size (MESHS) (Nisi et al., 2016). POH is a measure of the likelihood of hail occurrence and ranges from 0 % to 100 %. Using insurance loss reports, Nisi et al. (2016) found that when POH equals or exceeds 80 %, a day can be considered as hail day. The same threshold is used by Meteoswiss Swiss Hail Climatology Project and in the current study. MESHS estimates the largest expected hail diameter starting at 20 mm (Nisi et al., 2016). Both products are available on a spatial grid of $1 \times 1 \text{ km}^2$ and every 5 min and cover the area of Switzerland and the surrounding area. They rely on the third-generation C-band radars in operation since 2002 and were later replaced with dual-polarization radars between 2011 and 2012 (Nisi et al., 2018). The algorithms require information on the freezing-level height ($H_{0^\circ\text{C}}$) provided by the MeteoSwiss weather forecasts using COSMO. POH considers the vertical distance between the highest radar reflectivity of at least 45 dBZ and $H_{0^\circ\text{C}}$ (Waldvogel et al., 1979; Foote et al., 2005), while MESHS considers the vertical distance between 50 dBZ and $H_{0^\circ\text{C}}$ (Treloar, 1998; Joe et al., 2004). The availability of the hail data differs between the analyzed cases, so we list which hail observations are considered for each of the cases in Table 2.1.

Lightning flashes. Simulated LPI is validated against a lightning detection network (LINET) that covers large parts of Europe (Fig. 2.1b; Betz et al., 2009). It has the capability to detect the total number and location of lightning strikes, where cloud-to-ground strokes, in-cloud, and cloud-to-cloud discharges are included. LINET has an average location accuracy of approximately 150 m (Betz et al., 2009). The LINET data used here is taken from Jelić et al. (2021), in which the total lightning is gridded at 3 km grid spacing with a temporal resolution of 2 min. Higher temporal resolution and spatial resolutions are possible, but due to high computational and storage demands, we use this 2D database. Nonetheless, it still provides sufficient information to discern local characteristics. Later, we aggregated the LINET lightning flashes every hour to compare against the simulated hourly maximum LPI.

Diagnostic radar reflectivity. The COSMO model provides a diagnostic forward operator to derive an estimate of radar reflectivity. This tool will be used in some diagrams to visualize the thunderstorm development. However, it should be noted that this tool does not account for all aspects that contribute to radar reflectivity; for instance, it does not generate the bright band near the melting level. For these reasons, we have not used it as a validation product.

Atmospheric soundings. To further explore the atmospheric environments, we use data from three sounding stations (Fig. 2.1b) located at Payerne (Switzerland), Milan (Italy), and Stuttgart (Germany). Data is obtained from the University of Wyoming's online archive (<https://weather.uwyo.edu/upperair/sounding.html>). The soundings

are available at 00:00 and 12:00 UTC.

2.2.5 Analysis methods

We evaluate daily accumulated total precipitation against IMERG using an object-based verification method. For a fair comparison, both observations and model outputs are interpolated to the same grid spacing of 12 km (Fig. 2.1b). We use the SAL (structure-amplitude-location) method proposed by [Wernli et al. \(2008\)](#) to evaluate the model performance. The *A* component is calculated as the normalized difference between the domain-averaged observed and simulated fields. A positive (negative) *A* component indicates an overestimation (underestimation) by the model. The *L* component considers the displacement of the center of mass between the observed and simulated fields, as well as the weighted average distance between individual objects and the mass center of the total field. Lower *L* values indicate a more accurate placement of the simulated field. The *S* component accounts for the size and shape of the objects. Positive (negative) *S* values suggest a more widespread (peaked) simulated field. The computation requires the identification of precipitation objects within the analysis domain, separately for the observed and simulated fields. An object is defined as the grid points above the threshold of 1/15 of the maximum value of precipitation within the domain as suggested in [Wernli et al. \(2008\)](#). As a result, the influence of interpolation on the result is rather small.

For each case, we have estimated whether the atmospheric instability was generated by local conditions or synoptic atmospheric processes. This classification depends on the convection adjustment scale τ , which is derived using the precipitation rate P ($\text{kg m}^{-2} \text{s}^{-1}$) and CAPE according to the following equation ([Keil et al., 2013](#)):

$$\tau \sim \frac{\text{CAPE}}{d\text{CAPE}/dt} \sim \frac{1}{2} \frac{c_p \rho T_0}{L_v g} \frac{\text{CAPE}}{P} \quad (2.5)$$

where the change of CAPE due to the release of latent heat $d\text{CAPE}/dt$ is estimated from precipitation rate P . Reference values of density ($\rho = 1.292 \text{ kg m}^{-3}$), temperature ($T_0 = 273.15 \text{ K}$), specific heat of air at constant pressure (c_p), latent heat of vaporization (L_v), and acceleration due to gravity (g) are taken. τ considers the timescale within which CAPE is removed by convection. For the calculation of τ , we use the hourly domain-averaged CAPE and total precipitation from ERA5 (same domain as in Fig. 2.2) and calculate the daily maximum τ for each case, as it must be calculated over a region large enough to smooth the variability from individual clouds. [Keil et al. \(2013\)](#) suggests that if τ is shorter than 12 h, the atmospheric instability is governed by the synoptic conditions, and the event is then classified as strong synoptic forcing. A larger τ ($> 12 \text{ h}$), however, indicates that the convection is driven by high local CAPE values, in which case the event is classified as weak synoptic forcing. We should note that the threshold between weak and strong synoptic forcing varies in the literature (see, e.g., [Zimmer et al., 2011](#)), and should thus not be taken strictly, especially for the cases close to it. Here, we just use it as an indication of prevailing conditions.

2.3 Results

2.3.1 Synoptic overview of selected cases

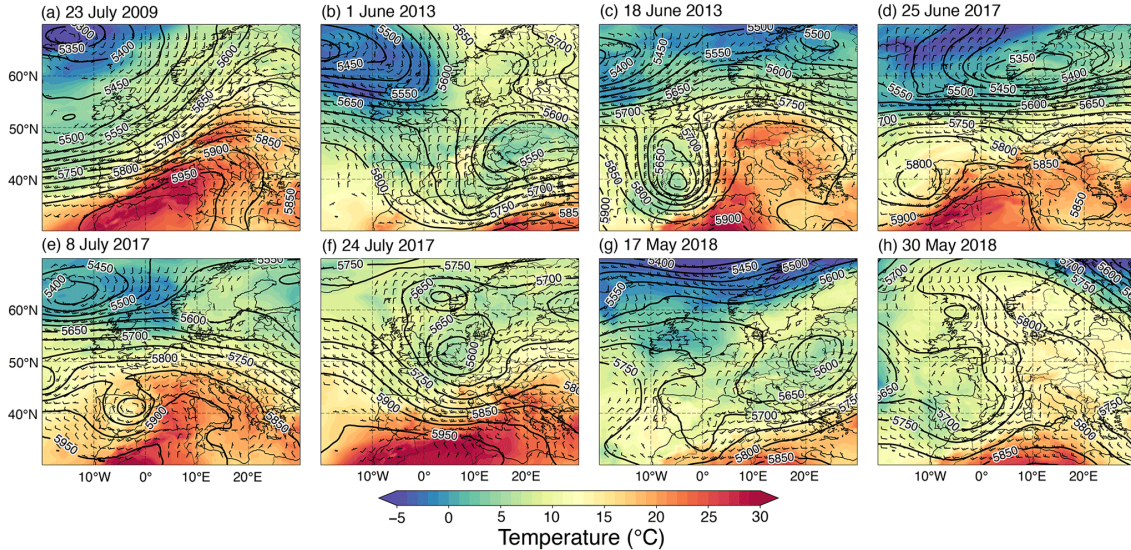


Figure 2.2: Synoptic overview of the eight cases analyzed in this study. Panels show geopotential height at 500 hPa (m, black contours), temperature at 850 hPa (°C, shaded) and wind barbs at 500 hPa obtained from ERA5 reanalysis at 12 UTC on the day when the respective case was observed.

In this study, we simulate and analyze eight cases of observed severe convective storms covering different synoptic situations (Fig. 2.2). The following cases are selected according to the severity of their impacts (e.g., the size of hailstones, number of lightning strikes, and cost of damages):

- **23 July 2009.** Severe hailstorms occurred over eastern and central Switzerland and caused damage to buildings amounting to around CHF 261 million in Switzerland (NCCS, 2021). The weather over Central Europe was dominated by a southwesterly flow and large temperature contrasts (Fig. 2.2a). Strong lifting associated with a cold front resulted in severe thunderstorms, leading to several long hail swaths that can be seen in radar observations (Fig. 2.5a).
- **1 June 2013.** Warm and humid air transported from the northeast towards the Alps encountered cool air from the west (Fig. 2.2b). The event produced heavy rain (without hail) in a very narrow band near the foothills of the Alps and caused water discharges with return periods of 10 to 30 years reported from several weather stations in central and eastern Switzerland (FEON, 2013; Grams et al., 2014). We selected this event to evaluate the ability of the model to simulate heavy rain without hail.
- **18 June 2013.** A low-pressure system was situated over the Bay of Biscay (Fig. 2.2c) and brought warm and moist unstable air masses to central Europe with very large CAPE (not shown). Several localized and short-lived thunderstorm cells

developed in the afternoon to the east of this system. Hailstones observed near Zurich caused massive localized damage estimated at CHF 15 million according to the building insurance of the Canton of Zürich (Gebäudeversicherung Kanton Zürich, [GVZ, 2013](#)).

- **25 June 2017.** This event is characterized by heavy precipitation which occurred south of the Alps. A thunderstorm that hit the city of Lugano in the early morning produced 81.5 mm of rainfall within an hour, which is expected over a long period of time less frequently than every 100 years ([MeteoSwiss, 2017](#)). It was the second hottest June since measurements began in 1864 ([MeteoSwiss, 2017](#)). Prior to this event, the high temperatures above 30 °C recorded in the Po Valley lasted for more than 3 d. A surface front was not present, but a short-wave upper-level trough moving over Switzerland can be seen from the geopotential field at 500 hPa (Fig. 2.2d).
- **8 July 2017.** This event was embedded into the strong westerlies with high surface temperature ahead of a pronounced upper-level cut-off low in Spain (Fig. 2.2e). Several convective cells developed to the east of the Black Forest and moved towards Lake Constance. Later in the afternoon, multiple convective cells were triggered successively near the southern edge of the Jura mountains and north of the Alps.
- **24 July 2017.** A slow-moving cut-off low passed over the northern side of the Alps. On the western side of the low, upper-level cold air advection occurred and led to an unstable environment (Fig. 2.2f). With the deepening of the system, low-level convergence and ascending motion initiated several thunderstorm cells to the south of the Alps, which later shifted northeastward with the prevailing flow.
- **17 May 2018.** Under the influence of the upper-level low over Poland (Fig. 2.2g), several isolated and local thunderstorms developed in the afternoon over the eastern shores of the Adriatic Sea. Hail was observed over the northern part of Istria (Croatia) according to hailpad observations. Affected by the Bise (a northeasterly wind that blows across the Swiss plateau to the north of the Alps), local rain showers developed over Switzerland without hail and lightning.
- **30 May 2018.** Scattered and widespread thunderstorms were initiated near eastern France and the southern flank of the Alps. The slow-moving storms caused significant damage across a large area. The surface pressure distribution was relatively flat (not shown), characterized by a “fair-weather” situation with weak temperature gradients over the eastern Alps. The Alpine region was affected by the southerly upper-level flow (Fig. 2.2h), where a trough extended over the Mediterranean and an anticyclonic curvature north of the trough axis. During the day, the southerly flow started to affect the weather in the Alpine region. A similar situation continued the next day.

2.3.2 Evaluation of precipitation, hail, and lightning

In this section, we assess how COSMO, with a 2.2 km grid spacing, performs in simulating total precipitation, hail, and lightning. To do so we look into the model

performance with SAL diagrams (explained in section 2.2.5) shown in Fig. 2.3, and spatial distribution of total precipitation, hail, and lightning obtained from the model and observations for all eight cases shown in Figs. 2.4–2.8.

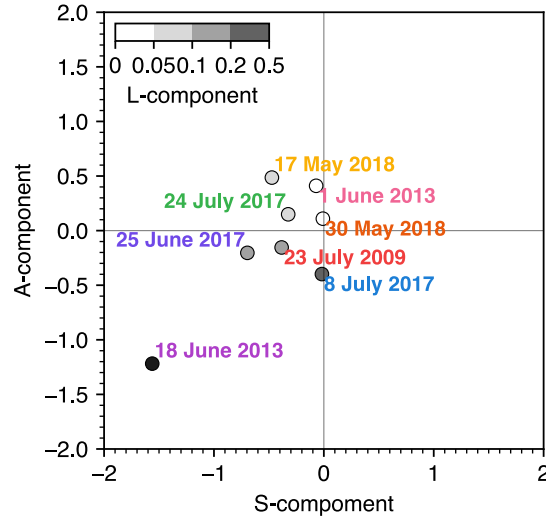


Figure 2.3: SAL diagram of daily accumulated total precipitation in COSMO simulations compared to IMERG observations over the analysis domain for all eight analyzed cases. The S, A, L components evaluate the differences in structure, amplitude, and location of the events, respectively. Values near zero signal a perfect match with observations.

Table 2.1: List of eight selected cases and their characteristics. The convection adjustment time τ is calculated according to the Eq. (2.2.5) and indicates cases with stronger (small τ) or weaker (large τ) synoptic forcing.

Date	Hail observations	τ (hours)
23 July 2009	Radar	10
1 June 2013	Radar	2
18 June 2013	Radar	28
25 June 2017	Radar, crowd-sourced, hailpad	25
8 July 2017	Radar, crowd-sourced	15
24 July 2017	Radar, hailpad	18
17 May 2018	Radar, hailpad	3
30 May 2018	Radar, crowd-sourced	18

2.3.3 Evaluation of precipitation, hail, and lightning

In this section, we assess how COSMO, with a 2.2 km grid spacing, performs in simulating precipitation, hail, and lightning. To do so, we look into the model performance with SAL diagrams (explained in Section 2.2.5) shown in Fig. 2.3, and spatial distribution of precipitation, hail, and lightning obtained from model and observations for all eight cases shown in Fig. 2.4–2.8.

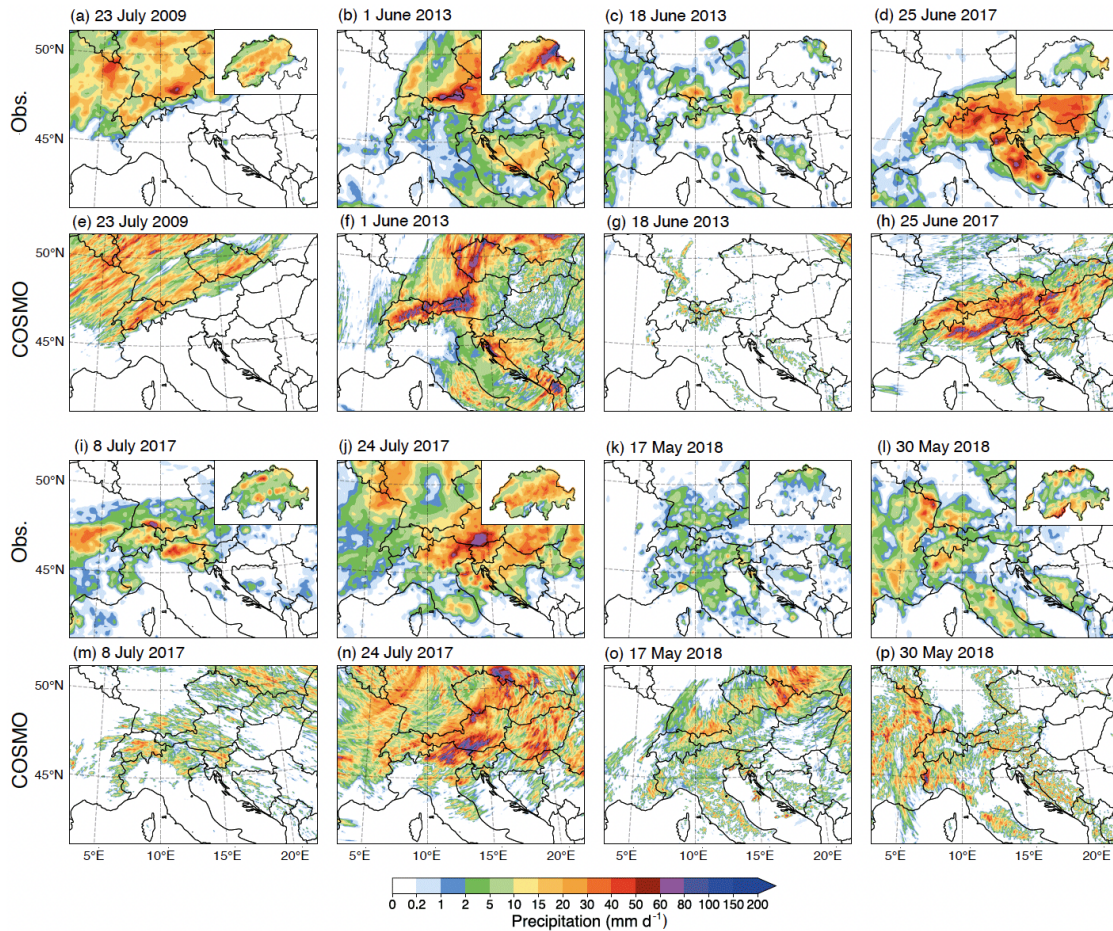


Figure 2.4: Daily accumulated total precipitation (mm d^{-1}) for all eight cases obtained from observations (first and third rows) and COSMO simulations (second and fourth rows). The IMERG observations cover the entire analysis domain, while high-resolution RhiresD gridded rain gauge observations (shown in the upper right corners) cover Switzerland only.

The SAL diagram of daily accumulated total precipitation is shown in Fig. 2.3. The amplitude (i.e., intensity) of precipitation is overestimated for 1 June 2013 and 17 May 2018 and underestimated for 18 June 2013 and 8 July 2017. The structure component is captured relatively well for most of the cases except for 2 cases – 18 June 2013 and 25 June 2017 – for which the precipitation objects are too small and peaked compared to observations. For the case of 17 May 2018, the simulated precipitation is more scattered (Fig. 2.4k,o). Finally, the location component is particularly large in two cases – 8 July 2017 and 18 June 2013. The bias shown for the 8 July 2017 case is partially due to the southerly shift of the convective system (Fig. 2.4i,m). On 18 June 2013, COSMO fails to simulate precipitation over eastern France and overestimates peak precipitation over the Black Forest (Fig. 2.4c,g), which results in a large location error together with the largest negative bias for amplitude and structure components.

Comparison against IMERG and high-resolution RhiresD observations reveals that

COSMO can capture the main spatial distribution of daily accumulated total precipitation (Fig. 2.4). The best performance is seen for the case of 23 July 2009 (Figs. 2.3 and 2.4a, e), characterized by stronger synoptic forcing and convection ahead of the cold front. The worst performance is seen in Figs. 2.3 and 2.4c and g for the case of 18 June 2013. The inability of the model to simulate this event properly is attributed to the local processes involved. The event is associated with weak synoptic forcing, with the largest convective timescale of all cases (Table 2.1). Thus, due to its more chaotic nature, this event has small predictability. We should note, however, that the SAL components of precipitation are computed against IMERG, which has a much coarser resolution than the model. Therefore, some of the biases can be attributed to the rather smooth precipitation distribution (larger precipitation objects of lower intensity) shown by the observations (Fig. 2.4). It is also interesting to note that none of the precipitation observations used, neither IMERG nor RhiresD, captured the record-breaking hourly precipitation amount of 82 mm as observed at the rain gauge station in Lugano (southern Switzerland) on 25 June 2017. However, such a high precipitation intensity is simulated by the model, even though it is slightly misplaced.

To evaluate the hail produced by COSMO HAILCAST, we first compare the model output against radar-based observations available over Switzerland and its surrounding areas (Fig. 2.5a–h). We first show the simulation against the POH data in terms of the hail footprint and coverage, but the comparison against MESHS data looks qualitatively similar. In general, the occurrence of hail is simulated well, but the placement and coverage are not captured very well in some cases (e.g., 8 July 2017). The case of 1 June 2013 with heavy rain but no hail over Switzerland is well reproduced, even though a very small number of grid cells produced small hail (Fig. 2.6b). Among the best-simulated cases, the same as for total precipitation, we can again consider the case of 23 July 2009 characterized by stronger synoptic forcing and elongated hail swaths reproduced by the model (Fig. 2.5a). The record-breaking rainfall event of 25 June 2017 also produced hail south of the Alps, as observed by radar and crowd-sourced reports and over the Adriatic region, including the continental part of Croatia as observed by hailpads (Fig. 2.5d,i,l). The widespread occurrence of hail in this case is reproduced by the model, even though the spatial extent is overestimated. The case of 17 May 2018 is characterized by hail recorded on the Istrian peninsula in Croatia and was well reproduced by the model. However, the model produced very light and scattered hail over both Adriatic and Alpine regions where it was not observed (Fig. 2.5g,n). Another case with poorer model performance is 18 June 2013, when the model overestimates the spatial extent of hail swaths, especially over the Black Forest (Fig. 2.5c). Overall, we can see that the performance in the simulation of hail aligns with the performance in the simulation of total precipitation. However, we should note many difficulties in comparing model output with available hail observations. As described earlier, MESHS data provides information on hailstone diameters above 20 mm only, which can potentially lead to underestimating the hail frequency and spatial coverage. POH only provides the probability of hail but does not indicate whether or not hail has occurred. Furthermore, both MESHS and POH detect hail at higher altitudes and not on the ground, and melting may influence hailstones (Nisi et al., 2016). Last but not least, even though the hailpad network consists of many hailpad stations, many areas are not well covered and,

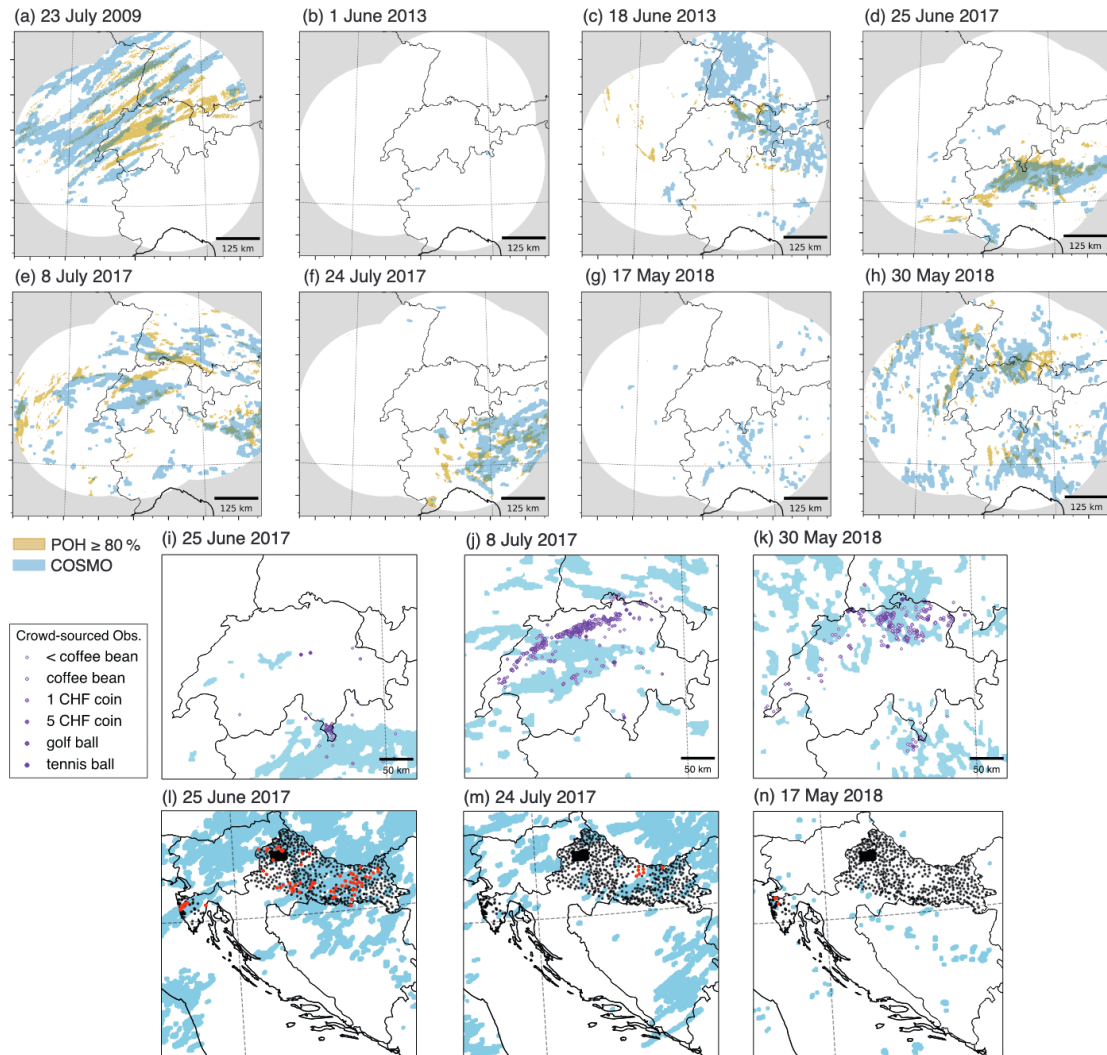


Figure 2.5: Observed and simulated daily hail footprints for all eight cases analyzed in this study. COSMO hail footprint is shown in blue shading and compared against different observations over different regions. (a–h) COSMO against radar-based POH observations, shown in orange shading for the radar-covered area. A grid point with POH larger than 80 % is considered a grid point with hail. (i–k) COSMO against crowd-sourced reports collected within Switzerland, indicated with purple dots and classified according to various categories of hail sizes. Note that after 2018, there was a change in the definition of hail sizes. (l–n) COSMO against hailpad measurements. Available hailpads are indicated with black dots, and hailpads recording hail during the events are indicated in red for the three cases where hail occurred in Croatia.

thus, are prone to miss recording very localized events such as thunderstorms and hail associated with them.

To further explore the performance of the COSMO HAILCAST, we compare the simulated hail against available observations for different cases as listed in Table 2.1. We compared the area affected by hail using COSMO HAILCAST against MESHS over

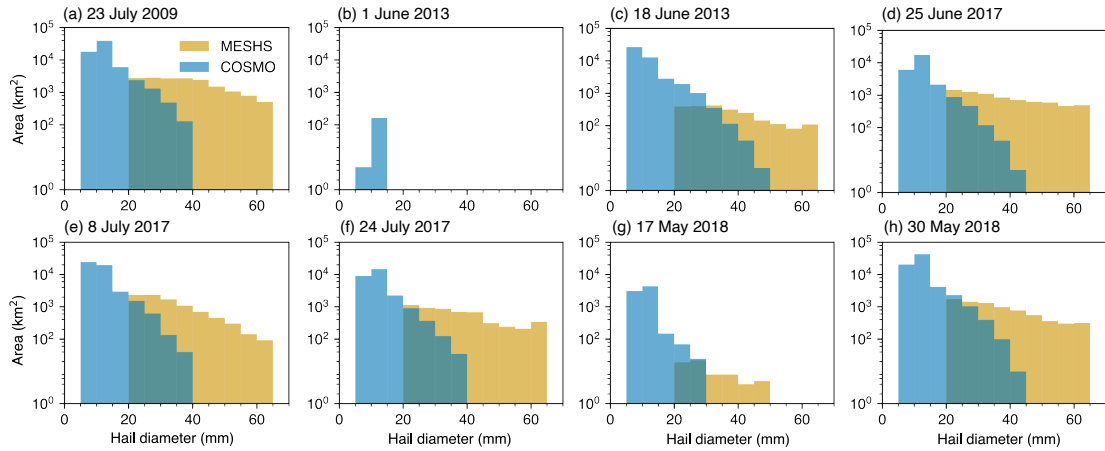


Figure 2.6: Area affected by hail obtained in radar-based MESHs observations (orange) and COSMO HAILCAST (blue) for all eight cases analyzed over the radar domain (Fig. 2.1). Note that MESHs estimates are only available for diameters > 20 mm.

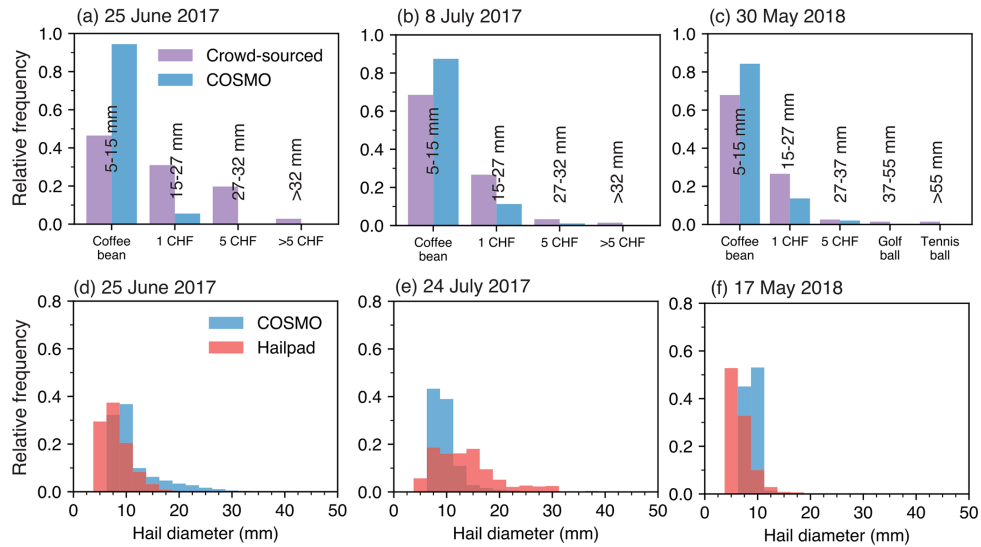


Figure 2.7: Relative frequency of hail diameter obtained from (a–c) crowd-sourced observations (purple) and COSMO HAILCAST (blue) in Switzerland, and (d–f) hailpad observations (red) and COSMO HAILCAST (blue) over hailpad-covered areas in Croatia (Fig. 2.1c). The histograms show the frequency of hail size for each bin relative to the number of observed or modeled hail events.

the radar-covered area (Fig. 2.6), frequency of simulated hail diameter against crowd-sourced data over Switzerland (hailstones larger than coffee beans – 5 mm – are shown; Fig. 2.7a–c), and hailpad observations over the hailpad-covered area (Fig. 2.7d–f). When compared to MESHs, the results show a large difference between the observed and simulated area. We see that, while MESHs observation only estimates hail diameter above 20 mm, the model produces hail diameter below 20 mm.

According to [Barras et al. \(2019\)](#), considering the 23 and 32 mm reports, MESHs

tends to exceed the crowd-sourced reported hailstone size by 10–15 mm on average. Yet, compared to crowd-sourced data over Switzerland (Fig. 2.7a–c), the model shows a reasonable hail size distribution, although it still tends to overestimate small hailstones and underestimate large hailstones. Moreover, when compared to hailpad observations over Croatia (Fig. 2.7d–f), the model exhibits a distribution that closely aligns with the observed data, particularly for the two cases of 25 June 2017 and 17 May 2018. For the case of 24 July 2017, an event relatively well captured by the model, the simulated hailstones above 15 mm are underestimated. Therefore, the comparisons against radar-based MESHs should be considered with caution. They show that there is a need to improve radar-based hail algorithms, although comparisons with other observations show that COSMO in general tends to overestimate small hailstones and underestimate large ones.

It is clear that HAILCAST underestimates the frequency of larger hail sizes, i.e., does not produce many hailstones larger than 30 mm. As noted by Adams-Selin and Ziegler (2016); Adams-Selin et al. (2019), the hail size strongly depends on the initial hail size embryo – the larger the initial embryo, the larger the output hail size. However, the size also depends on the model micro-physics, the strength of the updrafts that hail has to overcome to fall to the surface, and the initial temperature level. For example, if updrafts are weaker, larger hail falls down faster and does not have enough time to grow further, while smaller hail has more time to grow but does not reach sizes above 20 mm. In a parallel study, in which the same eight cases are simulated with the WRF model (Malečić et al., 2023), larger hailstones are obtained with the WRF model than with COSMO. This result indicates that the simulated hail size strongly depends upon the model formulation.

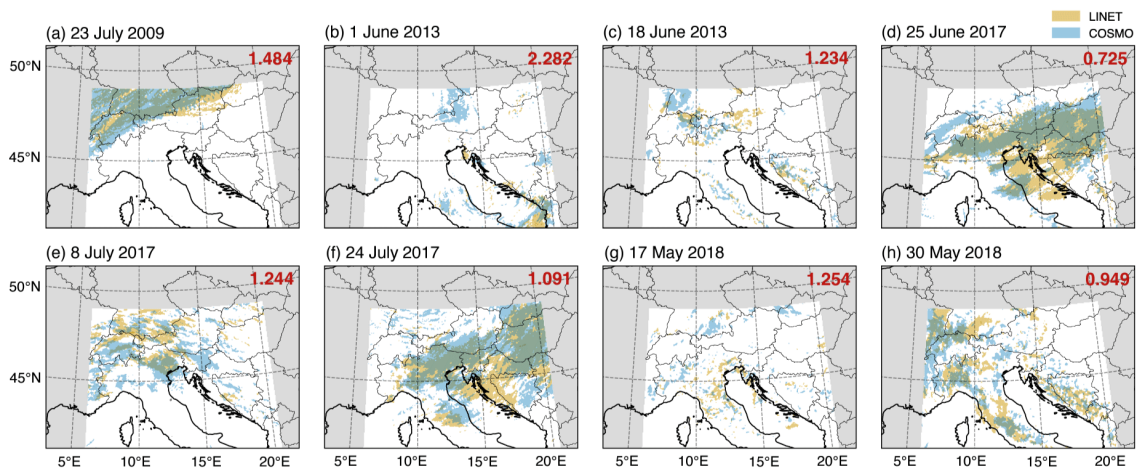


Figure 2.8: Foot prints of daily LINET lightning flashes (> 0 , orange) and COSMO LPI ($> 0 \text{ J kg}^{-1}$, blue) for all eight cases. The number in the upper-right corner of each panel displays a coverage bias, defined as the ratio of grid points with lightning in model and observations. Values larger and smaller than 1 indicate model overestimation and underestimation of spatial coverage, respectively.

Next, we turn our attention to the evaluation of lightning. A comparison of light-

ning patterns between the model and LINET observations for each of the cases is shown in Fig. 2.8. In addition, to overcome difficulties related to different variables represented by observations and model (lightning flashes versus lightning potential), we calculate and display a coverage bias in the figure (red number). It is defined as the ratio of the number of gridpoints with lightning in the model and observations, respectively. Note that the coverage bias does not provide any information on the overlap of simulated and modeled lightning, but this is qualitatively assessed from the spatial representation. Overall, the model using LPI diagnostics is able to capture the lightning patterns for each case, although it tends to slightly overestimate the spatial patterns of the signal (as for total precipitation and hail). The largest overestimation of spatial patterns, and, thus the coverage bias, is found in the case of 1 June 2013, when very little lightning was observed over the Adriatic and no lightning over the Alpine region. However, the model diagnostics produced lightning over the eastern Alps, which coincides with the area of very intense precipitation. The case of 1 June 2013 is the case without hail over the Alpine region, which was successfully reproduced by the model. Differences in representing hail and lightning can be related to different updraft thresholds used by LPI and HAILCAST, which is lower for LPI: 0.5 m s^{-1} for LPI (Section 2.2.3) versus 10 m^{-1} for HAILCAST (Section 2.2.2). The smallest coverage bias is obtained for the case of 24 July 2017 and 30 May 2018, even though there is a slight shift between the observations and the model. We should also note that both of these cases are characterized by weaker synoptic forcing and more locally driven convection, which is well reproduced by the model. The largest underestimation of the spatial coverage of lightning is found in the case of 25 June 2017. A large part of this bias is visible over the Adriatic Sea – the area over which the model fails in reproducing total precipitation as well.

Overall and not surprisingly, we can see that the performance of both hail and lightning diagnostics strongly depends on simulated total precipitation, since both hail and lightning diagnostics depend on the same ingredients as precipitation.

2.3.4 Assessment of model internal variability

A central element of the simulation strategy is the use of ERA5 lateral boundary conditions, with the initialization taking place at 12:00 UTC on the day before the event to account for the spin-up of the storms. The simulation is thus guided along the re-analysis, and the predictability in our simulations is much higher than in a numerical weather prediction (NWP) forecast. The strategy is ideal for testing diagnostic tools that require adequate synoptic forcing. Despite the enhanced predictability due to the use of ERA5 lateral boundaries, there is some remaining internal variability. To test the effect of model internal variability on our results, we conducted a small ensemble of simulations for three of the eight cases, by shifting the initialization by +6 and –6 h. The ensemble simulations are initialized at 06:00, 12:00, and 18:00 UTC on the day before the storms occurred. Consideration is given to the whole modeling chain with nested simulations at 12 and 2 km resolutions.

Results show that even for localized deep convective storms, the predictability of precipitation and hail is overall quite high (Fig. 2.9). However, there are significant differences in detail, due to the chaotic nature of the nonlinear flow evolution. For

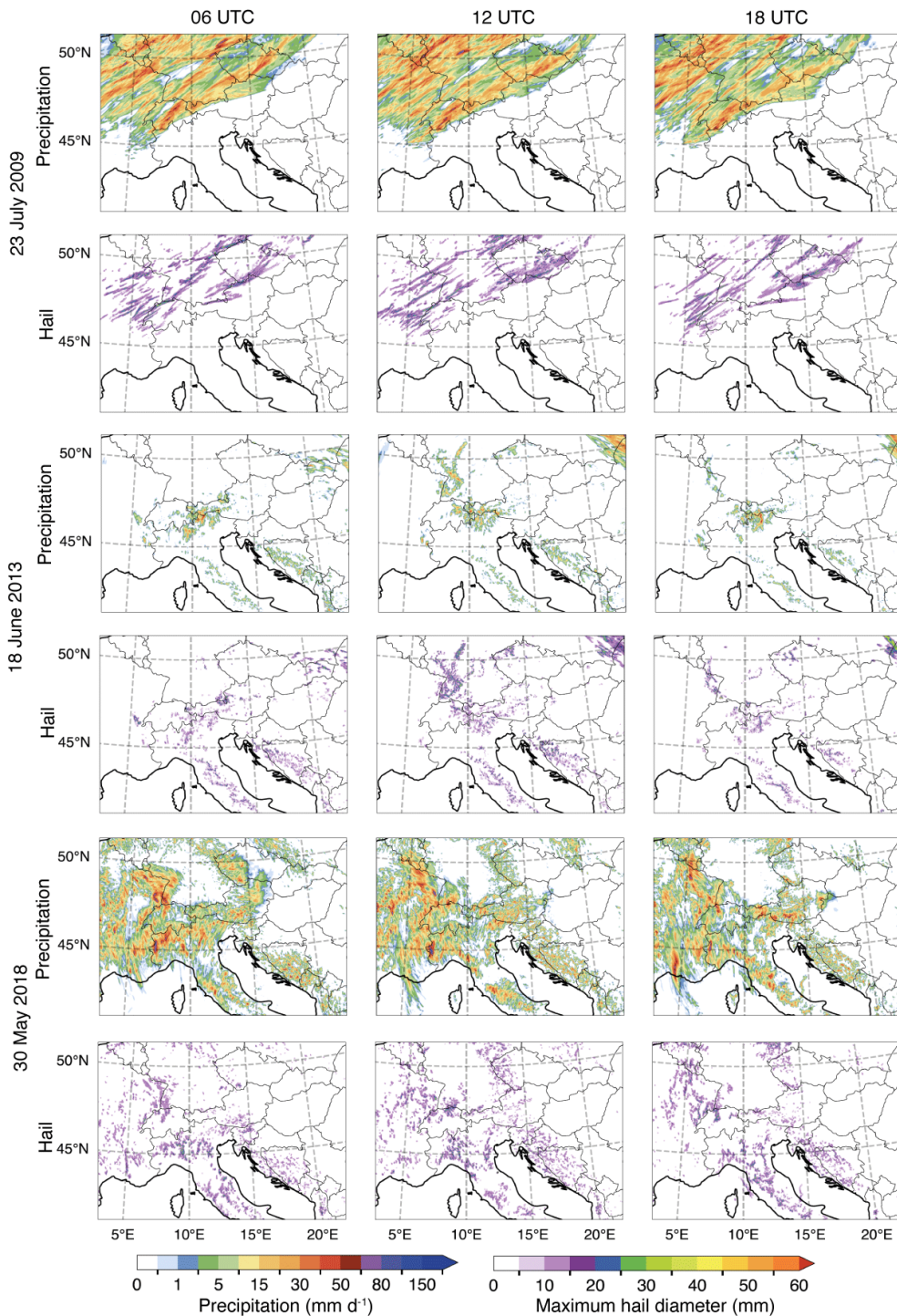


Figure 2.9: Small ensemble of simulations to explore the internal variability of the simulation strategy. Daily accumulated total precipitation and maximum hail diameter in simulations initiated at 06:00 (left), 12:00 (middle), and 18:00 (right) UTC on the day before the event occurred. All ensemble members are driven by ERA5 at the lateral boundary of the 12 km domain using hourly resolution. The results are obtained for the case of 23 July 2009 (two upper rows), 18 June 2013 (two middle rows), and 30 May 2018 (two lower rows).

example, in the case of July 2009 (top two rows of Fig. 2.9), there are considerable differences in the length and location of the hail swaths. Likewise, in the case of 18 June 2013, precipitation is simulated over the Black Forest when initialized at 12:00 UTC but not when initialized at 06:00 and 18:00 UTC. Similarly, in the case of 30 May 2018, there are pronounced differences in the precipitation fields with concomitant differences in hail. Overall, however, the internal variability is rather small, and, hence, the simulations confirm the suitability of the selected modeling strategy for assessing the performance of the modeling approach for case studies of severe convection. A comparison of the cases shown in Fig. 2.9 suggests that synoptically driven convective storms have a higher predictability.

2.3.5 Analysis of three specific cases

To further investigate the environmental conditions and the mechanisms that are favorable for the development of thunderstorms over the Alpine-Adriatic region we present a more detailed analysis of three specific cases, which affected different areas under different synoptic situations.

The case of 23 July 2009 – Severe thunderstorms with elongated hail swaths over Switzerland

As shown above, the case of 23 July 2009 is one of the best-simulated cases with very good performance in simulating total precipitation, hail, and lightning despite overestimating the spatial extent of hail and lightning. The good performance is most likely due to the nature of this event, which was characterized by thunderstorms ahead of a cold front and is thus classified as an event under stronger synoptic forcing. On that day, central Europe was dominated by a large trough stretched from Scandinavia and its upper low-pressure system positioned north of Iceland. The associated cold front approached the Alps at around 12:00 UTC. The propagation of the front was slow due to the distortion of the flow field around the Alps (Schumann, 1987), while the convergence along the front resulted in a fast storm movement. According to Schemm et al. (2016), up to 45 % of detected hail events in northeastern and southern Switzerland form in this kind of pre-frontal zone.

Figure 2.10a and b shows the observed and modeled Skew-T log-p thermodynamic diagram from Payerne (see Fig. 2.1b) at 00:00 and 12:00 UTC on 23 July 2009, which provides information in Switzerland before and during the passage of the cold front. During the night, a moist and stable layer below 800 hPa was located underneath a warm and dry mid-level layer. This constellation with high observed convective inhibition (CIN) of -634 J kg^{-1} (Fig. 2.10a) acted to suppress convection. The dry capping layer trapped humidity in the boundary layer and accumulated energy prior to the triggering of the thunderstorms later in the afternoon. Around noon, this profile changed significantly below 600 hPa where temperature decreased due to the approaching cold front (Fig. 2.10e), while dew-point temperatures increased prominently at 800 hPa as the moisture in the warm air mass was lifted ahead of the cold front. The resulting convective cells moved northeastward (Fig. 2.10f) and weakened in the middle of the night. At 00:00 UTC on 24 July 2009, CIN was completely depleted (not shown). A comparison

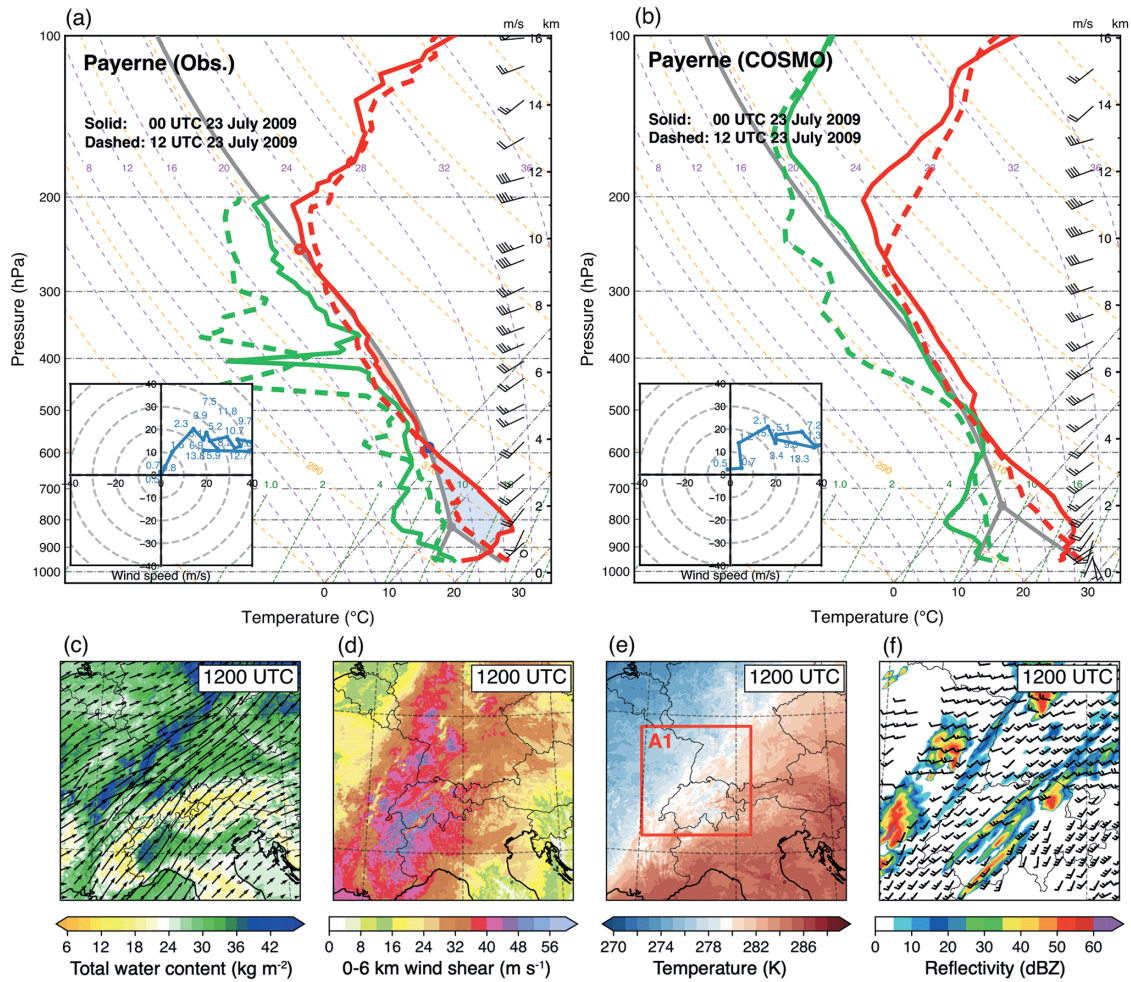


Figure 2.10: Detailed characteristics of the case 23 July 2009. Thermodynamic skew-T log-p diagrams of (a) sounding observations and (b) COSMO extracted profiles at Payerne station at 00:00 (solid) and 12:00 UTC (dashed). Red and green lines represent the temperature and dew-point temperature profiles, respectively. Corresponding wind hodographs, shown in the bottom left corner, were obtained for 12:00 UTC on 23 July 2009. COSMO simulated (c) total water content and vertically integrated water flux vectors, (d) 0–6 km bulk wind shear, (e) temperature at 700 hPa, and (f) simulated reflectivity and wind barbs at 1 km above ground level at 12:00 UTC on 23 July 2009. The red box A1 indicates the zoomed subdomain shown in (f).

of the model simulation against observations at Payerne station reveals that COSMO reproduces this environment very well (Fig. 2.10b). This relatively good simulation of the storm environment leads to a good overall performance of the model in simulating total precipitation, hail, and lightning during that event.

Further analysis of the case based on the model output reveals that the southwesterly flow transported warm and moist air from the Mediterranean with an abundant water content of 35 kg m^{-2} (Fig. 2.10c). This warm and moist air, together with extremely large 0–6 km bulk wind shear defined as the difference in horizontal velocity

between 6 km and the surface (exceeding 40 m s^{-1} in some areas; Fig. 2.10d), created favorable conditions for strong rotating updrafts. At around 05:00 UTC, a line of convection developed in northeastern France and moved to the Black Forest (not shown). Hail was first observed in radar-based observations at around 09:00 UTC over northeastern France and the Jura mountains. Later in the afternoon, a supercell developed near Lyon (in France), moving northeastward and gradually splitting into several elongated convection cells accompanied by observed and simulated long hail swaths extending for hundreds of kilometers over Switzerland (Fig. 2.10f).

The case of 25 June 2017 – A record-breaking precipitation event in Lugano

The case of 25 June 2017 is associated with the record-breaking precipitation rate in Lugano during the measurement period (see Section 2.3.1 above). We chose this event for detailed analysis since interesting conditions triggered the event as explained below. The COSMO model shows a good performance in simulating total precipitation, hail, and lightning over the Alpine region. However, at the same time, it underestimates total precipitation and lightning over the Adriatic Sea. As for the previous case, we first look at the structure and evolution of the pre-storm environments using radiosonde profiles, but this time at the Milano station (since it is closer to the event) in the northwestern section of the Po Valley in Italy (Fig. 2.11a,b). At 12:00 UTC on 24 June 2017, a typical “loaded gun” structure can be identified with a temperature inversion at 850 hPa and dry air located above warm and moist air. Such a profile is known as an elevated mixed layer (EML, Carlson et al., 1983), and it can also be identified as the “capping” layer (Lanicci and Warner, 1991), which is an indication of a severe storm environment. The cap or lid prevents deep vertical mixing and inhibits the premature release of the convective instability with observed CIN of -144 J kg^{-1} and CAPE as high as 2723 J kg^{-1} . The CIN gradually decreased in the following hours without much change in CAPE (not shown). At 00:00 UTC on 25 June 2017, the air below 900 hPa became cooler and the lid was higher, indicating that the capping inversion was penetrated by updrafts. Together with the potential instability ahead of an upper-level trough, the buoyant air was lifted and released the accumulated energy. This led to a burst of thunderstorms that hit this area in the early morning, where hail was first observed at around 00:30 UTC.

A comparison of the simulated profile at the Milano station (Fig. 2.11b) with the observed and above-discussed profile (Fig. 2.11a) reveals a good performance of the model in capturing the vertical profile and thus the triggering mechanisms of the event. The model reproduced the “capping” layer on the day before the event occurred and the deepening of the moist and warm air several hours before the event occurred.

Analysis of the model output shows a warm and moist layer over the Po Valley with simulated total water content larger than 45 kg m^{-2} (Fig. 2.11c,d). As shown in Fig. 2.2b, due to the presence of an upper-level trough, the Po Valley was influenced by south-westerly flow. A line of organized convection gradually formed along the northwest-southeast oriented mountain edge at around 02:30 UTC (not shown). Subsequently, the convective cells continuously developed over the elevated terrain and propagated upwind. Heavy precipitation associated with hail, and lightning was localized and became most intense between 03:00 and 04:00 UTC (Fig. 2.11e). This back-building process (e.g.,

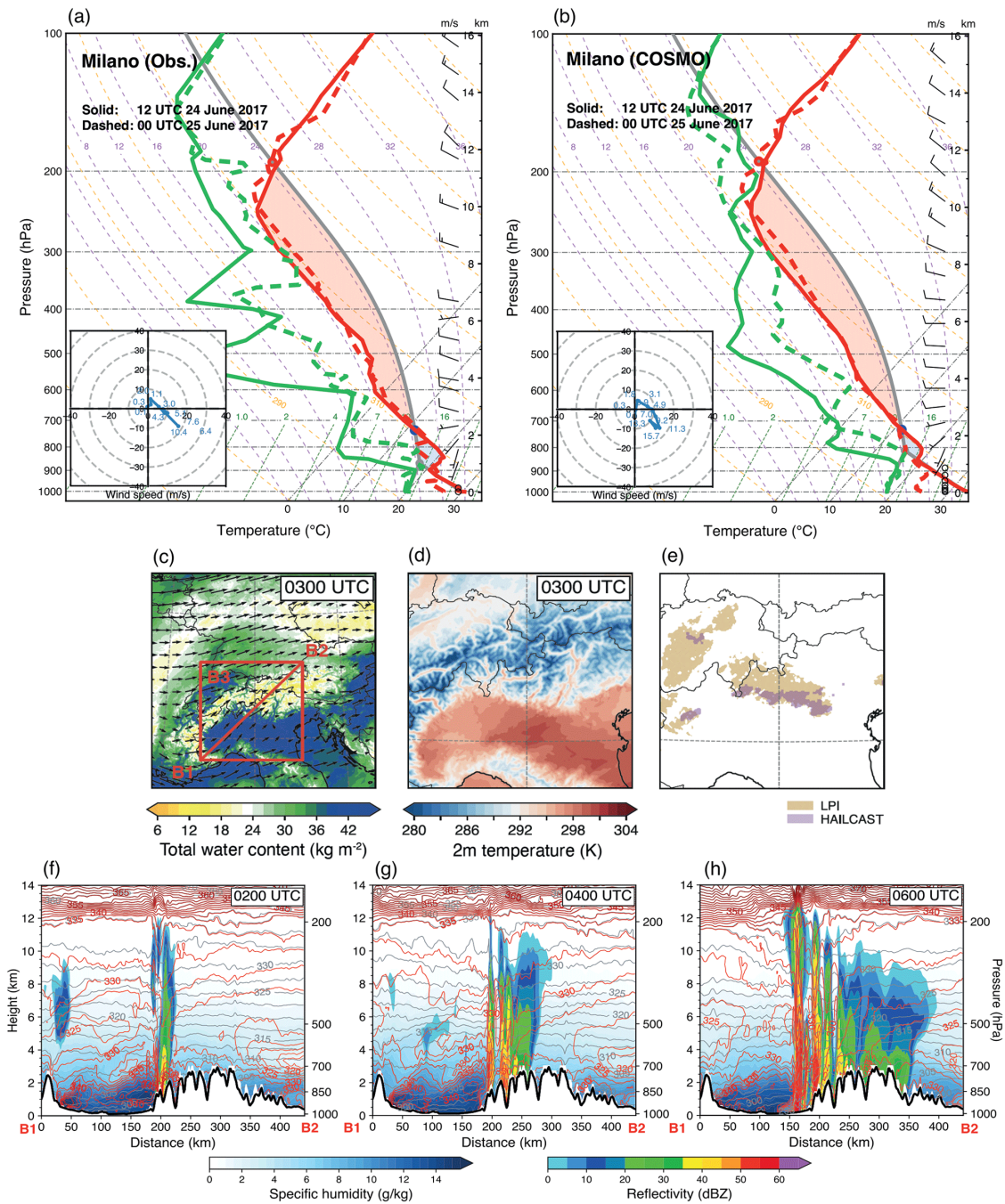


Figure 2.11: As in Fig. 2.10, but for the case of 25 June 2017. (a) Sounding observations and (b) COSMO extracted profiles at Milano at 12:00 UTC on 24 June 2017 (solid lines) and 00:00 UTC on 25 June 2017 (dashed lines). (c) COSMO simulated total water content and vertically integrated water flux vectors, (d) 2m temperature at 03:00 UTC on 25 June 2017, and (e) footprints of LPI and HAILCAST obtained between 03:00 and 04:00 UTC are shaded in yellow and purple, respectively. The red box B3 in (c) indicates the zoomed subdomain shown in (d,e). (f–h) Vertical cross sections of potential temperature (gray contours), equivalent potential temperature (red contours), specific humidity (blue shaded), and simulated reflectivity (color shaded) along the red transect B1–B2 at 02:00, 04:00, and 06:00 UTC on 25 June 2017.

Lagasio et al., 2017) is shown with cross sections normal to the squall line (Fig. 2.11f–h), where the convection developed upwind over the foothills. The triggered cells remain nearly stationary and the intensity significantly weakened when it moved to the north-east due to the loss of low-level warm and humid air over the Po Valley. The topography of the Po Valley offers a favorable environment for the initiation of new cells, which consequently explains the hot spot of hail occurrence over this region.

The case of 8 July 2017 – Thunderstorms near the Jura mountain

The case of 8 July 2017 is characterized by multiple thunderstorms over the Alps. Overall, the precipitation structure for this case is well reproduced, while the intensity is slightly underestimated with a large location error, which is most likely due to the southerly shift or the underestimation of the total precipitation. We again start with a look into the thermodynamic environment with the help of sounding observations at Stuttgart (Germany) near the location of hail occurrence (Fig. 2.12a,b). At 00:00 UTC, the profile shows a dry layer below 800 hPa and a moist layer probably associated with a cloud at around 850 hPa, and capped by a dry layer above 700 to 500 hPa (Fig. 2.12a). The observed CIN amounted to -130 J kg^{-1} and CAPE to only 70 J kg^{-1} , which is not a favorable environment for thunderstorm development. In the morning hours, the stable layer was eroded due to the warming of the near-surface air in the morning hours, making the conditions more favorable for the development of convection. At 12:00 UTC, a deep and well-mixed boundary layer was observed up to 800 hPa, nearly following the dry adiabatic profile. Comparison with the model (Fig. 2.12b) reveals that the model captures the vertical profile, even though temperature and dew-point temperature do not come as close as in observations at around 800 hPa level. Figure 2.12d shows a band of very low relative humidity at the 500 hPa level, consistent with a stratospheric intrusion embedded in the strong upper-level westerly flow (Fig. 2.2e). This band is near the Stuttgart sounding, but slightly to the south of it.

Further analysis based on the model output, reveals that the westerly flow affected the northern pre-Alpine region (Fig. 2.12c), eroded the stable layer near the surface, and brought moisture to the northern Alpine foreland. Vertical cross sections across this area at 05:00 UTC show that this dry and cold air was superimposed above the warm and moist layer near the surface (Fig. 2.12g). With significant instability, hail was initially observed at around 12:00 UTC to the east of the Black Forest when the cold upper-level was advected over the warm near-surface air (Fig. 2.12h). Subsequently, convective cells associated with hail moved towards Lake Constance. Due to the dry and cold air aloft, evaporative cooling and melting of hydrometeors could lead to stronger and colder downdrafts (Johns and Doswell, 1992). While updrafts also experience entrainment, the overall effect tends to be less evaporative cooling (James and Markowski, 2010). Several isolated cold pools that spread radially away with temperature depressions of 4 K can be identified from the subdomain C3 at 925 hPa level (Fig. 2.12e). The cold pool induced a large updraft velocity at the leading edge, which is favorable for convective intensification and new cell formation (Fig. 2.12f). Previous studies showed that the modeling framework is able to capture such developments (Leutwyler et al., 2016). Convective cells associated with observed hail and lightning formed on the southern

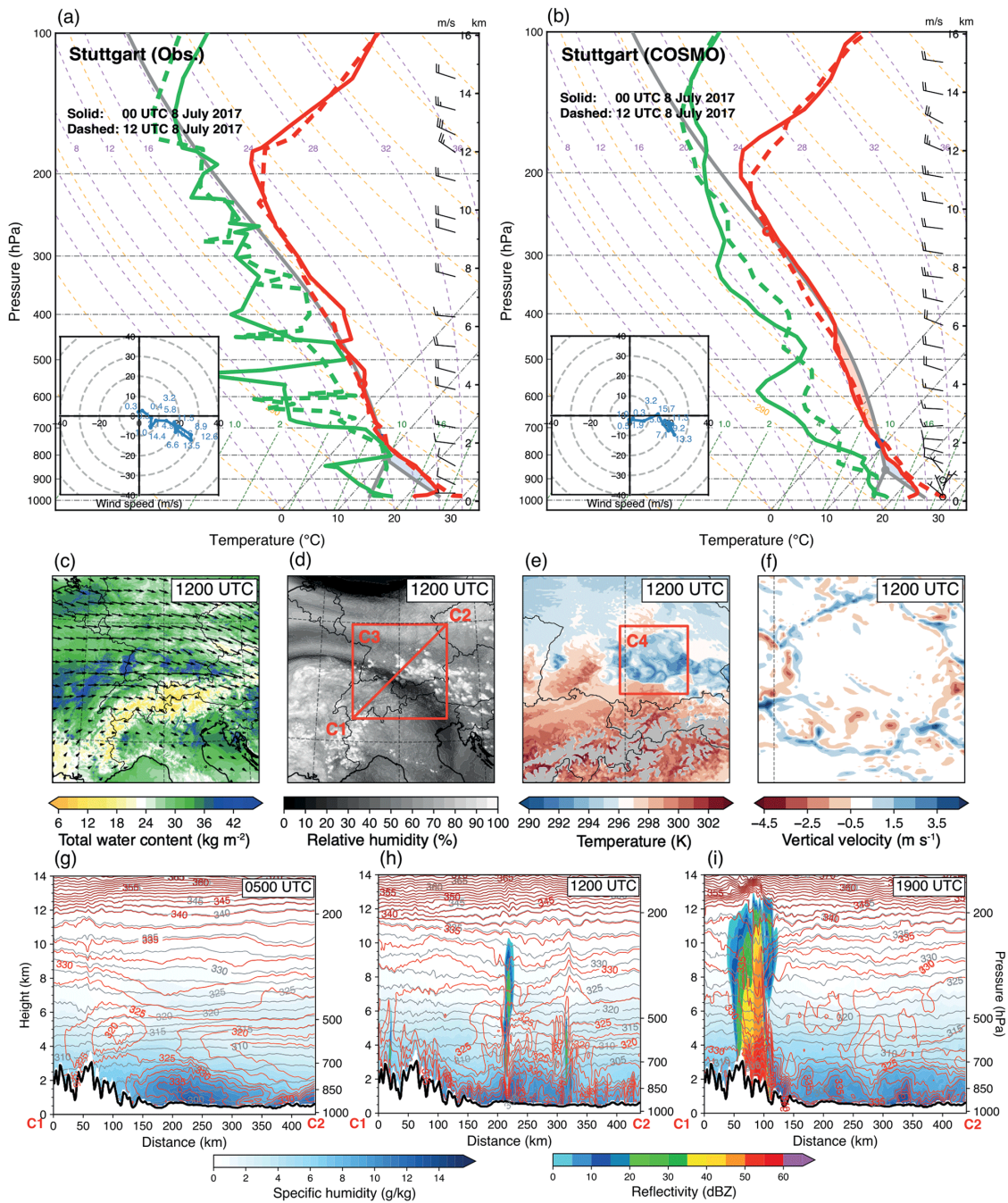


Figure 2.12: As in Fig. 2.10, but for the case of 8 July 2017. (a) Sounding observations and (b) COSMO extracted profiles at Stuttgart at 00:00 (solid lines) and 12:00 UTC (dashed lines). (c) COSMO simulated total water content, (d) relative humidity at 500 hPa, (e) temperature at 925 hPa, and (f) vertical velocity at 850 hPa at 12:00 UTC on 8 July 2017. The red box C3 in (c) indicates the zoomed subdomain shown in (e), and the box C4 in (d) indicates the zoomed subdomain shown in (f). (g–i) Vertical cross sections of humidity, temperature (red isolines), and simulated radar reflectivity along the red transect C1–C2 in (d).

flank of the Jura mountains at around 13:00 UTC, and later, on the northern flank of the Alps at around 15:00 UTC (Fig. 2.12i). Several wet downbursts were confirmed by reliable sources (<http://www.sturmarchiv.ch/index.php/Hagel>, last access: 20 October 2023) in central Switzerland (canton of Bern over Roggwil, around 14:00 UTC, and Wilderswil, around 15:00 UTC) with wind gusts above 90 km h^{-1} .

2.3.6 Conclusions

In this study, we analyzed the simulations of eight observed cases of severe convection. The simulations were performed using a regional climate model, COSMO, at 2.2 km horizontal grid spacing, integrated with HAILCAST and LPI diagnostics over the Alpine-Adriatic region. The performance of the model in simulating total precipitation, hail, and lightning was evaluated against available observations. The main findings are summarized as follows.

Overall, the COSMO model together with HAILCAST and LPI diagnostics performed well in simulating total precipitation, hail, and lightning. In particular, the case-study simulations captured the main characteristics of the cases considered, such as the large-scale precipitation distributions, or the occurrence of elongated hail swaths versus localized hail events controlled by topography (Figs. 2.4–2.8). The best performance was obtained for the cases with strong synoptic forcing. This is to some extent associated with the chaotic nature of the underlying dynamics and the lower predictability of localized events. The two cases with the strongest synoptic forcing (1 June 2013 and 17 May 2018) are associated with heavy precipitation (especially 1 June 2013), but with no or very little hail and lightning. Even though the model overestimated the precipitation intensity for these two cases, it produced no or very little hail, which is in accordance with the observations. Overall, we see that the performance in the simulation of hail and lightning is consistent with the model performance for convection. Comparison of the model with radar-based hail estimates revealed that COSMO with HAILCAST tends to underestimate the frequency of large hailstones and fails to produce extra-large hailstones (larger than 40 mm). However, when compared to crowd-sourced and hailpad observations, COSMO shows a good hail size distribution. It is possible that some of the biases could be addressed by tuning the diagnostic computations of hail and lightning.

The ability of COSMO to simulate severe convective storms associated with hail and lightning enables further exploration of the mechanisms that drive such events. By investigating three cases that were selected according to their impacts in different synoptic situations over hot spots of the Alpine-Adriatic region, we identified several storm environments that contribute to the heavy precipitation associated with hail and lightning. These mechanisms include a capping layer that serves to accumulate humidity and energy below this layer (23 July 2009, 25 June 2017), a “back-building process” that contributes to convective cells that remain quasi-stationary near elevated terrain (25 June 2017), dry air above a warm and moist surface that leads to higher instability and stronger downdrafts (8 July 2017), and an upper-level trough that promotes ascent (25 June 2017). The results show that, although the simulations are not designed to simulate the detailed structure, amplitude and location of the events in terms of total precipitation, hail, and lightning, COSMO is generally able to credibly replicate key pro-

cesses of severe thunderstorms and create the related favorable environments for storm development.

Our findings show that HAILCAST and LPI integrated with COSMO are promising tools to diagnose hail and lightning over the Alpine Adriatic region (as also shown by [Malečić et al., 2023](#)). However, a couple of shortcomings are revealed: (i) Comparison of the model to available hail observations reveals that COSMO HAILCAST fails to reproduce extra-large hailstones. The most likely cause for the lack of large hailstones is the underestimation of strong updrafts in COSMO. Such an underestimation is plausible, as with a computational resolution of 2 km, simulations of heavy convection exhibit signs of bulk converge, but not yet structural convergence ([Panosetti et al., 2018](#)). In other words, the horizontal scales of the thunderstorm are overestimated, and peak updrafts are underestimated. (ii) The spatial extent of large hailstones is underestimated in COSMO HAILCAST compared to the radar-based observations. We should note the fact that MESHS only provides the estimation of hailstones larger than 20 mm, while POH only provides the probability of hail. (iii) The output of HAILCAST is sensitive to the initial hail embryo size (e.g., the maximum hail diameter always comes from the largest hail embryo) as shown by [Adams-Selin and Ziegler \(2016\)](#); [Adams-Selin et al. \(2019\)](#). (iv) For the LPI, the threshold of vertical velocity should be resolution dependent ([Brisson et al., 2021](#)), and thus a comprehensive analysis against observations is required before application. The LPI provides the potential of lightning, not the exact number of lightning flashes, which makes it difficult to evaluate against observations. Thus our analysis was only focused on the coverage or footprints of the lightning.

The promising results of these case studies reveal that kilometer-scale atmospheric models are not only able to simulate thunderstorms and their associated heavy precipitation, but also critical impacts of severe convective storms such as hail and lightning. This gives us confidence in future applications of hail and lightning diagnostics for climate simulations and analyses of potential changes with further warming of the atmosphere, which is part of a parallel ongoing study.

Author contributions. RC performed the simulations and analysed the model output and observations. RC, NB, MED and CS wrote the manuscript. NB, MED and CS provided scientific advice throughout the project. RA, OF, JJ, and XL ported the GPU version of HAILCAST and LPI in COSMO. All authors read and commented the paper.

Chapter 3

Simulating hail and lightning over the Alpine-Adriatic region – a model comparison study

Barbara Malečić¹, Ruoyi Cui², Marie-Estelle Demory^{2,3,4,5}, Kristian Horvath⁶, Damjan Jelić¹, Christoph Schär², Maja Telišman Prtenjak⁶, Patricio Velasquez², Nikolina Ban⁷

This chapter has been published in *Journal of Geophysical Research: Atmospheres*: <https://doi.org/10.1029/2022JD037989>

Abstract Hail is a significant convective weather hazard, often causing considerable crop and property damage across the world. Although extremely damaging, hail still remains a challenging phenomenon to model and forecast, given the limited computational resolution and the gaps in understanding the processes involved in hail formation. Here, eight hailstorms occurring over the Alpine-Adriatic region are analyzed using simulations with the Weather Research and Forecasting (WRF) and the Consortium for Small Scale Modeling (COSMO) models, with embedded HAILCAST and Lightning Potential Index (LPI) diagnostics at kilometer-scale grid spacing (~2.2 km). In addition, a systematic model intercomparison study is performed to investigate the ability of the different modeling systems in reproducing such convective extremes, and to further assess the uncertainties associated with simulations of such localized phenomena. The results are verified by hailpad observations over Croatia, radar estimates of hail over Switzerland, and lightning measurements from the LINET network. The analysis reveals that both HAILCAST and LPI are able to reproduce the affected area and intensities of

¹Faculty of Science, Department of Geophysics, University of Zagreb, Zagreb, Croatia

²Institute for Atmospheric and Climate Science, ETH Zurich, Zurich, Switzerland

³Wyss Academy for Nature, University of Bern, Bern, Switzerland

⁴Climate and Environmental Physics, Physics Institute, University of Bern, Bern, Switzerland

⁵Oeschger Centre for Climate Change Research, University of Bern, Bern, Switzerland

⁶Croatian Meteorological and Hydrological Service, Zagreb, Croatia

⁷Department of Atmospheric and Cryospheric Sciences, University of Innsbruck, Innsbruck, Austria

hail and lightning. Moreover, hail and lightning fields produced by both models are similar, although a slight tendency of WRF to produce smaller hail swaths with larger hailstones and higher LPI compared to COSMO is visible. It is found that these differences can be explained by systematic differences in vertical profiles of microphysical properties and updraft strength between the models. Overall, results are promising and indicate that both HAILCAST and LPI could be valuable tools for real-time forecasting and climatological assessment of hail and lightning in current and changing climate.

3.1 Introduction

Hail is a severe weather hazard that can produce significant crop and property damage across the world (Allen et al., 2020), especially when it occurs over highly populated areas with high-density assets (Kunz et al., 2017). In the literature, a large number of hailstorms causing more than US\$1 billion in damage is reported across the world (Schuster et al., 2005; Changnon, 2009; Brown et al., 2015; Kunz et al., 2017; Púčik et al., 2019). Punge and Kunz (2016) and Púčik et al. (2019) describe several hail hotspots in Europe, including the pre-Alpine and Adriatic areas. Although large hail occurs less often over the highest mountain peaks in the central Alps, severe hailstorms frequently affect Switzerland with up to 4 large hail days per year (Nisi et al., 2016; Púčik et al., 2019). In this area, the maximum hail diameter can sometimes exceed 10 cm (e.g., see Fig. 8 from Púčik et al. (2019)). Furthermore, parts of Croatia (Počakal et al., 2018; Jelić et al., 2020) and broader northern Adriatic region (Manzato et al., 2020) have similar statistics of hail frequency as southern Germany or southeastern Austria (Punge and Kunz, 2016). Therefore, considering the high economic losses associated with (severe) hailstorms, and high frequencies of hail occurrence, it is very important to have reliable hail models, both for short-term numerical weather prediction (NWP) and long-term climate-change adaptation strategies.

One of the largest limitations in understanding processes involved in hail formation is the lack of dense and direct measurements of hail properties on the ground. Hailpads, which are simple meteorological devices consisting of a stand and a measuring plate, represent one of the few methods to detect and measure hailstones directly on the ground. Besides the number of falling hailstones and their diameters, hailpads can also detect the intensity (i.e., kinetic energy) of hail (Smith and Waldvogel, 1989). In Europe, hailpad networks exist in several regions, including parts of Spain, France (Dessens, 1998; Berthet et al., 2011), Greece (Sioutas et al., 2009), northern Italy (Giajotti et al., 2003), eastern Austria (Svabik, 1989) and parts of Croatia (Počakal et al., 2009; Počakal, 2011) and have also been used in randomized hail suppression experiments in Switzerland (Federer et al., 1978). Although hailpads are one of the few sources of direct information on hail occurrence, they provide spatially discrete (but unique) information on hail occurrence as they only record hail at the point where they are installed.

Another source of information on hail occurrence is related to weather radars. As the abilities of weather radars to detect different kinds of hydrometeors such as rain, snow and hail progressed over the years, several hail detection algorithms have been developed (Waldvogel et al., 1979; Witt et al., 1998). At present, hail detection algo-

rithms are widely used as hail proxies and can provide spatially continuous information on various hail properties, for example, probability of hail occurrence or maximum expected hailstone size. In Switzerland, two hail detection algorithms are operational in real-time, namely, Probability of Hail (POH, [Waldvogel et al. \(1979\)](#); [Foote et al. \(2005\)](#)) that indicates a probability of a hailstorm occurring at a certain location, and Maximum Expected Severe Hail Size (MESHS, [Treloar \(1998\)](#); [Joe et al. \(2004\)](#)) that estimates expected severe hail size at the ground over the Alpine region.

An additional challenge in understanding hail processes is the limited number of high-resolution modeling studies of hailstorms. With increasing computational power, it has become possible to run simulations at convection-permitting scales (horizontal grid spacing < 4 km). Several studies reported the benefits of using models at kilometer scales for more realistic representations of convective processes ([Leutwyler et al., 2017](#)), mean diurnal cycles of precipitation ([Ban et al., 2014](#)), spatial precipitation patterns and associated extreme values ([Prein et al., 2013](#); [Brisson et al., 2016, 2018](#); [Pichelli et al., 2021](#)), better representation of convective clouds ([Keller et al., 2016](#); [Brisson et al., 2016](#); [Hentgen et al., 2019](#)), short-term heavy precipitation events ([Vergara-Temprado et al., 2021](#)), local wind systems like sea breeze ([Belušić et al., 2017](#)), and complex terrain winds ([Horvath et al., 2012](#)). Since models, when run at km scales, can produce a more realistic representation of convective processes, [Adams-Selin and Ziegler \(2016\)](#) integrated a physically improved 1D hail growth scheme — called HAILCAST ([Poolman, 1992](#); [Brimelow et al., 2002](#); [Jewell and Brimelow, 2009](#)) — with the km-scale WRF model. When HAILCAST is coupled with WRF, the model simulates the maximum expected hail size at the ground using the profiles of cloud liquid and ice water, vertical velocity, temperature, water vapor and pressure fields from a given model timestep. Several recent studies employed HAILCAST embedded in high-resolution numerical models, such as WRF or COSMO, to study hailstorms occurring over the United States and Europe. The studies found that the models can reproduce the atmospheric conditions and triggering mechanisms responsible for hailstorm formation, resulting in simulating comparable hailstorms to those observed over the complex terrain of the United States ([Adams-Selin and Ziegler, 2016](#); [Adams-Selin et al., 2019](#)), Switzerland ([Trefalt et al., 2018](#); [Raupach et al., 2021](#); [Cui et al., 2023](#)), Italy ([Manzato et al., 2020](#); [Tiesi et al., 2022](#)), and Croatia ([Malečić et al., 2022](#)).

Similar to hail, lightning poses a serious threat to human lives ([Curran et al., 2000](#); [Holle et al., 2005](#)), wind turbines ([Rachidi et al., 2008](#)) and transportation ([Kanata et al., 2012](#); [Lee and Collins, 2017](#); [Thornton et al., 2017](#)). Moreover, lightning is a major cause of wildfires ([Latham and Williams, 2001](#); [Abatzoglou and Williams, 2016](#); [Dowdy et al., 2017](#)). Considering the hazards associated with lightning occurrence, the lightning potential index (LPI) was developed as a tool for diagnosing areas prone to lightning discharges ([Lynn and Yair, 2010](#); [Yair et al., 2010](#)). With a better representation of convective processes km-scale simulations, LPI offers the possibility to use the parameterizations of lightning that describe the non-inductive process occurring inside a thundercloud ([Yair et al., 2010](#); [Brisson et al., 2021](#)). It is defined as a potential for charge formation and separation inside a thundercloud and it relies on the presence of both solid and liquid hydrometeors. Even though LPI is not directly connected to the observed number of lightning flashes, several studies found that LPI could be a valuable tool for implicit

lightning forecasting in the COSMO (Sokol and Minářová, 2020; Cui et al., 2023) and WRF (Yair et al., 2010; Lagasio et al., 2017; Malečić et al., 2022) models. Recently, LPI was used in the climatological assessment of lightning over Germany (Brisson et al., 2021) and proved to be a better indicator of lightning occurrence than the commonly used convective available potential energy times precipitation ($\text{CAPE} \times \text{PREC}$) parameterization (Romps et al., 2014).

Recently, an effort was made to utilize both HAILCAST and LPI to study hailstorms occurring in Croatia using WRF (Malečić et al., 2022) and over the broader Alpine-Adriatic region using COSMO (Cui et al., 2023) models. More specifically, Cui et al. (2023) selected 8 days with severe convection over the Alpine-Adriatic region based on the observed impacts and underlying synoptic forcing to study the mechanisms responsible for severe weather effects. Adopting the process-oriented approach, the authors found that both HAILCAST and LPI successfully reproduced observed hail and lightning characteristics over a broad range of synoptic situations.

Motivated by the promising results, this study aims to complement the valuable previous research on hailstorm simulation over the topographically complex Alpine-Adriatic region (Fig. 2.1a). More specifically, we employ these two diagnostic tools in km-scale models (COSMO and WRF) to simulate hailstorms analyzed by Cui et al. (2023), with a geographical focus on Croatia and Switzerland. By analyzing eight hail cases using two models, we aim (a) to conduct a systematic and quantitative evaluation of the model's performance for hail and lightning, and (b) to identify the robustness of HAILCAST and LPI results produced by two intrinsically different modeling systems. The outcome of this study reveals information about model biases and the origins of disagreements between the two models in simulating severe storms associated with hail and lightning over the complex Alpine-Adriatic region. Moreover, this study benefits from two valuable but intrinsically different data sets of hail observations, namely spatially discrete in-situ hail measurements from the hailpad network (and two hailpad polygons) in Croatia, and spatially continuous remote-sensing radar estimates on hail occurrence in Switzerland. Therefore, the objectives of this paper can be summarized as follows:

- To what extent can HAILCAST and LPI credibly diagnose the occurrence of hail and lightning?
- How do simulations with two distinct models but the same diagnostic hail and lightning modules differ from each other?

This chapter is organized as follows: Section 3.2 describes the selected hail events and observational data used to evaluate COSMO and WRF models. An overview of the model setups and evaluation approach is indicated in Section 3.3. The results are presented and discussed in Section 3.6. The conclusions and remarks are given in Section 3.7.

3.2 Selected hailstorms and observational data

Eight days with severe convection occurring over the Alpine-Adriatic region already analyzed in Cui et al. (2023) are selected for the analysis. Out of eight selected days, hailstorms were observed in Croatia and/or Switzerland during seven of these days. During the day without observed hail in the central and eastern Alps, intense precipitation over the Alps leading to severe flooding is reported. Hailstorms are selected based on their intensity, measured by their impact or the kinetic energy recorded with hailpads. Besides that, an attempt was made to select hailstorms occurring over a set of synoptic and mesoscale situations to assess the abilities of both models to reproduce the observed convection during a variety of driving conditions. Moreover, by selecting a day where no hail is observed, the ability of both models to distinguish between convective days with and without hail is assessed. The type of observations available for eight selected events along with a brief description of their impacts are listed in Table 2.1.

To assess the model's ability to reproduce the observed severe weather events, several datasets are used. To validate simulated precipitation over the Alpine-Adriatic region, the Final Run of Integrated Multi-satellitE Retrievals for Global Precipitation Measurement (IMERG) mission (Huffman et al., 2019) data set is used. IMERG is a globally gridded precipitation product that estimates surface precipitation rates at 0.1° spatial and 30 min temporal resolution. IMERG incorporates satellite microwave precipitation estimates, microwave-calibrated infrared satellite estimates and rain gauge observations. Combining remote sensing and in-situ observations, IMERG provides spatially and temporally continuous and homogeneous precipitation estimates over the whole Alpine-Adriatic region.

Further, to assess the ability of LPI to reproduce the observed lightning activity, lightning data from the Lightning Detection Network (LINET, Betz et al. (2009)) is used. With 190 sensors in 31 countries that are up to 250 km away, LINET successfully detects cloud-to-ground and intracloud lightning flashes and differentiates between positive and negative discharges across Europe. Moreover, the LINET network can detect weaker stroke signals with a current amplitude lower than 1 kA. With continuous improvements of the LINET network, the median values of detected current amplitude values had decreased by half from 2009 (Franc et al., 2016), showing significant improvement in the sensitivity detection toward smaller stroke current amplitudes. For most of the European region (Franc et al., 2016; Jelić et al., 2021), the average minimum detectable signal is 0.7 kA, and the median location accuracy error is ± 84 m. Here, we considered total lightning information, that is, we did not differentiate between types or polarities of lightning flashes as LPI presents the overall potential for lightning activity without preferences to the type or polarity of lightning discharges. The total lightning for the examined cases was taken from the 2D database of lightning flashes at a $3 \text{ km} \times 3 \text{ km}$ horizontal and 2 min temporal resolution (developed by Jelić et al. (2021)) over the domain shown in Figure 2.1b.

Next, hail detection products from the Swiss radar network (Willemse and Furger, 2016; Germann et al., 2022) operated by MeteoSwiss are used to assess the HAILCAST

results. Namely, the operationally computed POH product is used. POH indicates the grid-based probability of hail reaching the ground. It is computed following Waldvogel et al. (1979) and Foote et al. (2005) from the difference in height between the altitude of the center of the highest radar bin at which 45 dBZ echo (i.e., Echo Top of 45 dBZ) is found and the height of the freezing level retrieved from the forecasts of the operational numerical prediction model COSMO. POH has been verified using insurance loss data (Morel, 2014; Nisi et al., 2016) and a good agreement between hail damage and $\text{POH} \geq 80\%$ was found. The area in which this product is available is indicated in Fig. 2.1b.

Finally, HAILCAST results are assessed against in-situ hail measurements from the Croatian hailpad network. It consists of (a) hail suppression stations in the continental region of Croatia, (b) a specially designed hailpad polygon in northwestern Croatia, and (c) hailpad stations in the northeastern (NE) Adriatic region (Fig. 2.1c). Overall, 590 hailpads on hail suppression stations, and 150 hailpads on the polygon, with average spacing between hailpads of ~ 5.5 km and ~ 2 km, respectively, have been installed and maintained by the Croatian Meteorological and Hydrological Service (Počakal et al., 2009; Počakal, 2011). Moreover, during the VITCLIC project (<https://www.pmf.unizg.hr/geof/en/research/climatology/vitclic>) 65 hailpads were installed in Istria (NE Adriatic) in the vicinity of an agricultural area with vineyards. Notably, the Istrian region is not a part of the hail suppression network; therefore, hail observations from these hailpads are not under the potential influence of hail suppression activities.

3.3 Modeling setup and evaluation approach

3.4 COSMO and WRF setups

Selected hailstorms were simulated using an Advanced Research Weather Research and Forecasting (WRF, version 4.1.5) model (Skamarock et al., 2019), and the climate version of the Consortium for Small Scale Modeling (COSMO-crCLIM based on COSMO 5.0) model (Baldauf et al., 2011; Leutwyler et al., 2017; Schär et al., 2020) alongside HAILCAST and LPI. An attempt was made to make a setup of both models as similar as possible. Additionally, one of the hailstorms is simulated using the newest version of COSMO v6.0 model.

The modeling setup consisted of two one-way nested domains with horizontal grid spacing of approximately 12 km (0.11°) and 2.2 km (0.02°) (Figure 2.1a). The model setup consists of 65 vertical levels in WRF and 60 vertical levels in COSMO. WRF uses a hybrid sigma-pressure vertical coordinate (Park et al., 2013) while COSMO uses a generalized Gal-Chen coordinate. WRF's time step is set to 20 and 4 s, while COSMO's time step is set to 90 and 20 s for 12 and 2.2 km simulations, respectively. The simulations were initialized and driven at the lateral boundaries using ERA5 reanalysis (Hersbach et al., 2020) at 12 UTC the day before severe convection was observed. ERA5 surface and pressure levels are used for WRF while COSMO uses three-dimensional ERA5 information. It should be noted that unlike for WRF, soil moisture for COSMO was not initialized from ERA5 reanalysis. Instead, each case simulation was initialized 7 days before

the event using the equilibrated monthly mean soil profiles from a 10-year (1999–2008) 12 km COSMO climate simulation (Vergara-Temprado et al., 2020) and let run for 7-day. Then, the model integration started at 12 UTC the day before severe convection was observed using the new soil moisture conditions from the 7 days run. This approach allows for an adjustment of the top soil layers to the conditions of each event. Physics setups of the models are summarized in Table 3.1. For the simulation of hail and lightning, HAILCAST (Adams-Selin and Ziegler, 2016) and LPI (Lynn and Yair, 2010; Yair et al., 2010) are used in both models. HAILCAST is a time-dependent hail growth model that provides the forecast of the maximum hailstone diameter at the ground. In our setup, HAILCAST is activated every 5 min on the inner 2.2 km convection-permitting domain if the updraft in a particular grid point exceeds 10 m s^{-1} for more than 15 min. Similarly, we adopt the same formulation of LPI in both WRF and COSMO models. More details on LPI formulation adopted can be found in Brisson et al. (2021). In this study, LPI is computed every 15 and 15 min fields are stored for both models.

Table 3.1: Modeling setups of COSMO and WRF models used in this study.

	COSMO	WRF
Domain	12 km (361×361 grid points) 2 km (800×600 grid points)	12 km (361×361 grid points) 2 km (800×600 grid points)
Vertical levels	60 Gal-Chen	65 hybrid sigma pressure
Time step	90 s, 20 s	20 s, 4 s
Soil moisture spin up	Yes	No
Cumulus parameterization	12 km Tiedtke (Tiedtke, 1989) 2.2 km no cumulus scheme	12 km Kain-Frisch (Kain, 2004) 2.2 km no cumulus scheme
PBL scheme	Prognostic TKE scheme (Raschendorfer, 2001)	MYNN 2.5 (Nakanishi and Niino, 2006)
Microphysics scheme	Single moment (Reinhardt and Seifert, 2006)	WSM6 (Hong and Lim, 2006)
Radiation	δ -two-stream approach (Ritter and Geleyn, 1992)	RRTM and Dudhia scheme (Mlawer et al., 1997)
Hail	HAILCAST activates every 5 min	HAILCAST activates every 5 min
Lightning	LPI activates every 15 min	LPI activates every 15 min

3.5 Evaluation approach

When evaluating the results of diagnostic tools such as HAILCAST and LPI against observations, it should be considered that their performance relies on the skill of the convection-permitting model to represent the convection properly. For this reason, the results are evaluated in three sequential phases. First, the model’s skill to represent the

observed precipitation is evaluated. Second, simulated LPI is assessed against LINET lightning data using the minimum coverage neighborhood verification method (Ebert, 2008). Third, HAILCAST results are evaluated against radar estimates on hail occurrence from Switzerland and direct hail measurements from the Croatian hailpad. Moreover, to account for possible time shifts between simulated and observed convection, only daily aggregated fields are evaluated.

Simulated precipitation is assessed against precipitation estimated by IMERG. Given the discrepancy in horizontal grid spacing between IMERG (0.1°) and simulated precipitation (2.2 km), both IMERG and simulated precipitation are interpolated to a common 12 km grid (Table 3.1). The evaluation is performed by using Taylor diagrams (Taylor, 2001) which compare spatial distribution of simulated and observed fields and summarize the results using statistical metrics. Evaluation is done by determining standardized deviations, correlation coefficients and root mean square errors between observed and simulated fields.

LPI is assessed against lightning observations from the LINET network. First, to account for the differences in horizontal grid spacing between LINET (3 km) and LPI (2.2 km), simulated fields are interpolated to a common 3 km grid as indicated in Table 3.1. However, considering that a high-resolution simulation cannot perfectly match the observation in space and/or time, but can still be useful (Ebert, 2008), we are using a minimum coverage neighborhood method. In that approach, a useful forecast is defined as the one where lightning is simulated anywhere in the neighborhood of the point where it is observed. Based on this method, a contingency table is built and a symmetric extremal dependence index (SEDI, Ferro and Stephenson (2011)) is computed. Additionally, verification window size as well as threshold for the number of lightning flashes is varied to examine the scale-intensity combination at which high-resolution simulation is useful.

HAILCAST results are assessed against radar products POH and MESHS from Switzerland and hail measurements from the Croatian hailpad network. To evaluate HAILCAST results against radar products, a minimum coverage verification method with varying verification windows sizes is utilized and categorical skill score such as probability of detection (POD), false alarm ratio (FAR) and extremal dependence index (EDI, Ferro and Stephenson (2011)) are determined. Next, HAILCAST results are assessed against hailpad observation from Croatian hailpad network. To overcome challenges associated with the limited spatial information from hailpad networks and to limit the effect of double penalty that occurs when verifying slightly offset high-resolution forecasts of extremely rare events (Ebert, 2008), an upscaled neighborhood verification method is used (Malečić et al., 2022). This verification methodology is composed of the elements of point to point, upscaling and a minimum coverage verification method (as described by Ebert (2008) and Malečić et al. (2022)). Based on this method, a contingency table is built and categorical skill scores are determined (POD, FAR, EDI).

Table 3.2: Validation procedures when using fields of different spatial resolutions. The interpolation method as well as the common grids used are indicated.

Observational dataset	Observations horizontal grid spacing (km)	Model horizontal grid spacing (km)	Common grid	Interpolation method
LINET	3	2.2	3 km×3 km	Distance-weighted
IMERG	11	2.2	12 km×12 km	Cumulative

3.6 Results and discussion

3.6.1 Precipitation

The first step considers the comparison between simulated and observed precipitation. The comparison refers to the period from 00 UTC to 24 UTC on the day when severe convection was observed. When comparing the daily accumulated fields, a generally good agreement between observed and simulated fields is found (Figure 3.1). Both models reproduce the observed precipitation patterns fairly well, even though there are slight local variations. Moreover, the areas with more intense precipitation correspond well between simulated and observed fields. However, a tendency of both models to produce more peaked and more scattered precipitation objects data is found for all analyzed cases except for 8 July 2017 and 18 June 2013. This tendency could partially be attributed to the differences in horizontal resolution between simulated and observed fields (2.2 and 11 km horizontal grid spacing, respectively). On the other hand, for 18 June 2013 and 8 July 2017, both models produced mostly smaller and less peaked objects than observed. In addition, comparison of COSMO-crCLIM and WRF fields, reveals that WRF tends to produce slightly less peaked precipitation objects than COSMO-crCLIM.

To further expand and complement this analysis, hourly accumulated precipitation averaged over the whole inner domain (Fig. 2.1b) is compared between the observations and the models (Fig. 3.2). To account for discrepancies in the horizontal resolutions between observations and simulated fields, interpolated fields are analyzed, as discussed in Table 3.2. The comparison reveals that both models reproduce the temporal evolution of precipitation fairly well in all cases, except for 25 June 2017 although some discrepancies exist, depending on the case. For the case of 25 June 2017, both models fail to represent the two local maximums of precipitation observed in the early morning and evening hours. During most cases, both models simulate comparable or slightly larger amounts of precipitation compared to the observations. An underestimation of precipitation is present only for 18 June 2013 and 8 July 2017 cases as already noted above.

The daily accumulated precipitation results are further compared quantitatively using Taylor diagrams (Taylor, 2001). As shown in Fig. 3.3, both models perform similarly, although larger differences in standardized deviations are found for the cases of 18 June

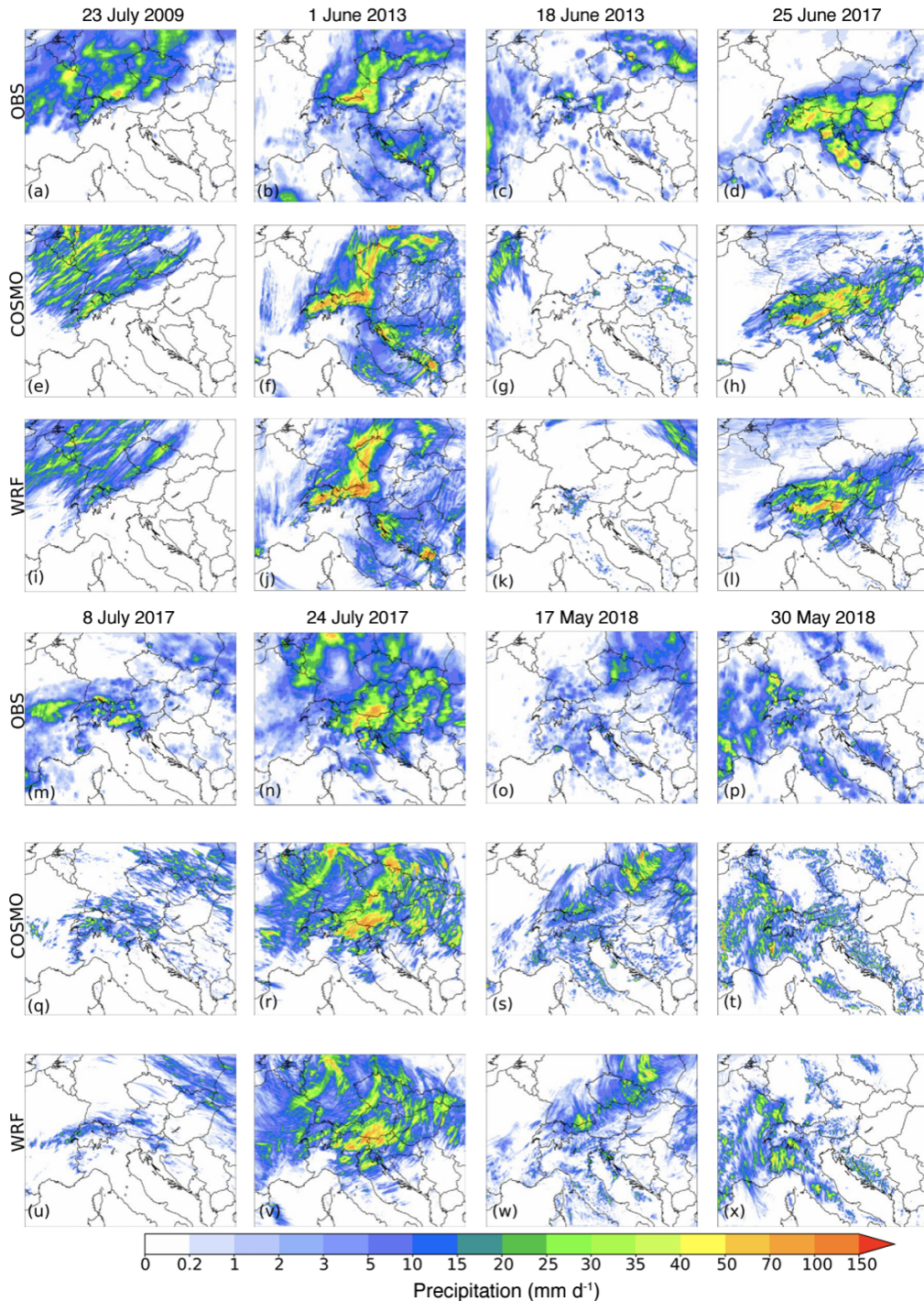


Figure 3.1: Accumulated precipitation for the period between 00 and 24 UTC on the day severe convection was observed for the eight case studies. The results are presented for (a–d; m–p) IMERG observations, (e–h; q–t) COSMO-crCLIM and (i–l; u–x) WRF simulations.

2013 and 8 July 2017. Both models show similar correlation coefficients between simulated and observed fields. Looking at the median performance for all cases together,

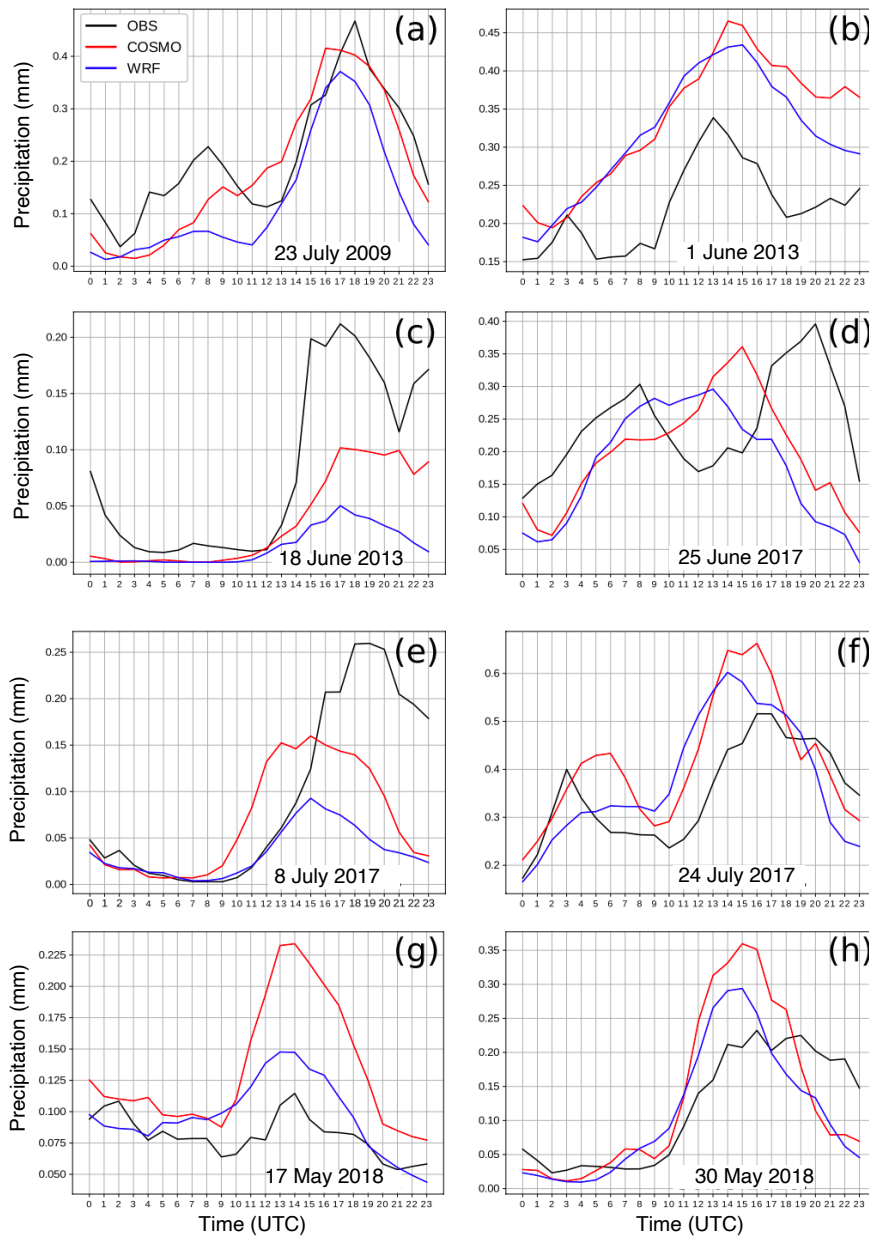


Figure 3.2: Hourly accumulated precipitation obtained from IMERG (black) observations and simulated by COSMO-crCLIM (red) and WRF (blue) for all eight cases (a–h). The observed and simulated hourly precipitation amounts are interpolated to a 12 km grid and then averaged over the 2.2 km domain.

we can see that both models perform similarly in simulating the observed precipitation with standardized deviations of 1.14 and 1, correlation coefficients of 0.48 and 0.46 and root mean square errors of 1.14 and 1.04 for COSMO-crCLIM and WRF, respectively.

Overall, we can see that both models successfully represent the observed precipitation, and that WRF tends to simulate less precipitation than COSMO-crCLIM.

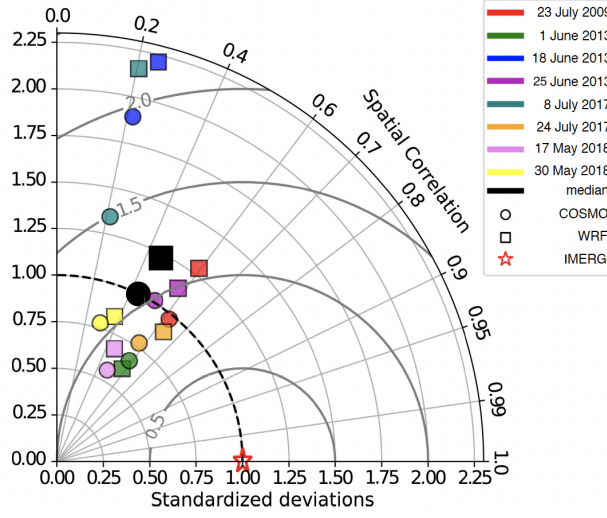


Figure 3.3: Taylor diagram showing the performance of COSMO-crCLIM (circles) and WRF (squares) when simulating daily accumulated precipitation observed by IMERG (red star). The performance for each case is indicated by colored markers, while the black markers indicate the corresponding median values.

3.6.2 Lightning potential index results

The second step of the evaluation considers the assessment of LPI (J kg^{-1}) against the observed number of lightning flashes from the LINET network. LPI indicates the potential for lightning activity, and as such, it is not directly connected to the observed number of lightning flashes. To make a direct comparison between LPI and the observed number of lightning flashes, a conversion of LPI to the number of lightning flashes following [Brisson et al. \(2021\)](#) and [Malečić et al. \(2022\)](#) is done considering LPI and LINET measurements on a common grid (Table 3.2). Conversion assumes a linear relationship between the LPI and the observed number of lightning flashes as well as the existence of the threshold value of LPI for which a lightning flash is produced, such that:

$$LPI_{\text{adj}} = \begin{cases} 0 & LPI \leq t \\ k \cdot LPI + l & LPI > t \end{cases} \quad (3.1)$$

where LPI_{adj} ($\text{km}^{-2} \text{h}^{-1}$) denotes the adjusted LPI, that is, LPI converted to the number of lightning flashes, parameter t denotes the minimum value of LPI for which a lightning flash is produced, k and l represent the parameters of a straight line. The parameters t , k and l are iterated across $[0, 20]$, $[0, 10]$, $[-20, 20]$, intervals, respectively. For every combination of parameters t , k , and l , hourly means of LPI_{adj} are calculated. Then, a distribution function of both simulated and observed hourly means of lightning flashes during all cases is determined. Further, a root mean square error (RMSE) between the two discussed distributions is calculated. The optimal combination of parameters is the one that minimizes the RMSE. Here, a conversion is done by using $t = 0.045$, $k = 3.3$ and $l = 0.1$ for COSMO-crCLIM and $t = 0.65$, $k = 0.65$ and $l = -0.2$ for WRF for all cases. The discrepancy in optimal parameter values between WRF and COSMO highlights the discrepancies between LPI produced by COSMO-crCLIM and

WRF. Namely, higher values of t and lower values of k associated with WRF indicate that WRF produces higher LPI, contrary to the results obtained for precipitation where WRF produced slightly lower precipitation amounts compared to COSMO.

The daily sums of both LPI_{adj} produced by COSMO-crCLIM and WRF and the observed number of lightning flashes for each case analyzed are presented in Figure 3.4. Overall, it seems that the general spatial pattern of the observed lightning activity is well reproduced by both models although the simulated fields appear to be more scattered than the observed. This could be partially attributed to the fact that LPI is calculated every 15 min, while the LINET network detects lightning flashes continuously. Moreover, considering all cases, it is noted that the conversion of LPI to lightning flashes is better fitted toward less intense lightning activity. This is explained by the fact that the fit is performed on all grid points: as there are more grid points with low flash counts than intense lightning activity, the fit is intrinsically better for lower flash counts. The discrepancy in fit between lower and higher flash counts is more pronounced during the cases with more intense and widespread lightning activity, that is, 25 June 2017 and 24 July 2017. Nonetheless, in general, the spatial distribution of lightning, that is, the distribution of the areas with more and less intense lightning activity, corresponds well between simulated and observed fields, although local discrepancies could be present, depending on the case and model analyzed. Looking at the differences between fields produced by COSMO-crCLIM and WRF, a tendency of COSMO-crCLIM to produce more scattered and less peaked fields can be found.

Furthermore, to quantitatively evaluate the capabilities of COSMO-crCLIM and WRF to simulate the observed lightning activity, a minimum coverage method is utilized. To get more robust results, the evaluation is done by aggregating all analyzed cases together (Fig. 3.5). Both models show similar performance which is better for the lower thresholds of lightning flashes. Moreover, we get good performance ($SEDI > 0.6$) even for more intense thresholds if we consider larger verification window sizes. WRF tends to have higher SEDI values than COSMO-crCLIM toward higher and more localized lightning flashes (bottom right side of diagrams), which confirms the previous findings that COSMO-crCLIM tends to produce more scattered lightning activity.

3.6.3 HAILCAST results

HAILCAST results are assessed against remote-sensing and ground observations for a period from 00 UTC to 24 UTC on the day severe convection was observed. First, we perform a qualitative comparison between hail swaths produced by the two models. Figure 3.6 suggests that both models produce generally similar hail swaths over the same area, although some local discrepancies between simulated hail swaths exist. Despite the overall similarity of the results, a tendency of COSMO-crCLIM to produce more hail in all analyzed cases is apparent. Both models correctly reproduce heavy precipitation without hail over the Alps for 1 June 2013, which suggests that both models are able to distinguish intense precipitation events from hail events. However, it should be noted that both models still produce hail over only a few grid points over the Alps.

Figure 3.7 shows the simulated and observed hail swaths over the Alpine region. Since POH indicates the probability of hail, and HAILCAST the simulated maximum

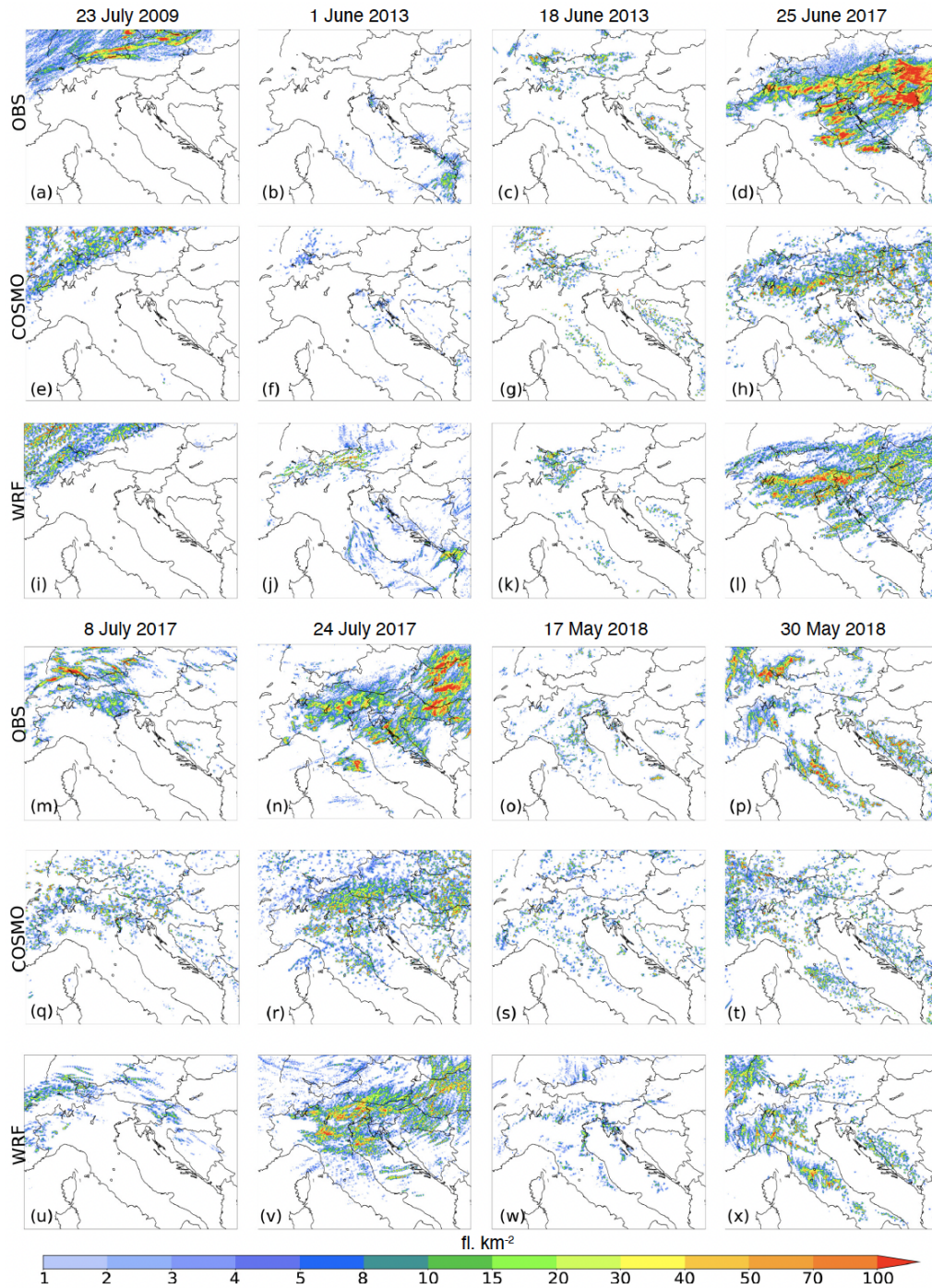


Figure 3.4: Simulated and observed lightning flash accumulation in the time window from 00 to 24 UTC on the day with severe convection. Columns denote cases, while rows denote measurements from the (a–d; m–p) LINET network, and fields produced by (e–h; q–t) COSMO-crCLIM and (i–l; u–x) WRF models.

hailstone diameter, only the spatial distribution of hail as observed by POH and simulated by HAILCAST is compared. It is clear that both models can produce hail swaths

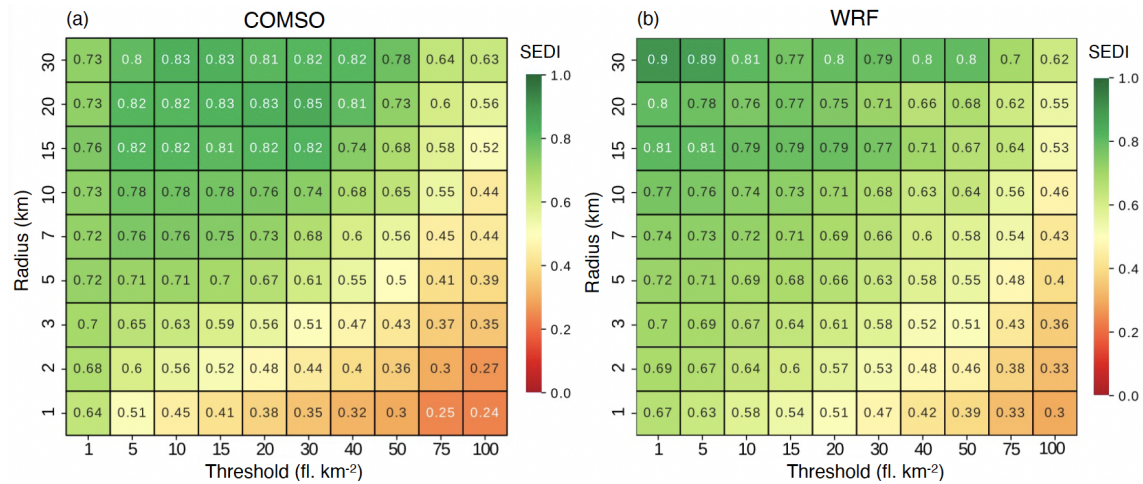


Figure 3.5: Performance of (a) COSMO-crCLIM and (b) WRF in simulating the observed lightning flashes. Performance depending on the threshold for the number of lightning flashes and verification window sizes (radius) is indicated in terms of SEDI skill score (shading). The higher/lower SEDI score means better/worse performance of the model, as reflected by the green/red colors.

comparable to those observed, both in the context of the area affected by hail and the shapes of the observed hail swaths. Notably there is not an exact match between simulated and observed fields, as, some deviations are present. For most cases, WRF produces smaller hail swaths than COSMO-crCLIM, while on the other hand, WRF simulates more grid points having maximum hailstone diameters greater than 35 mm.

Next, we assess simulated fields against another source of hail observations—hailpad observations from the Croatian hailpad network. Out of eight cases with severe convection over the Alpine-Adriatic region, hailpads in Croatia recorded hail on only three of those days (25 June 2017, 24 July 2017, 17 May 2018). For these days, simulated hail swaths with indicated impacted hailpads are presented in Figure 3.8. There is a generally good agreement between observed and simulated hail produced by both models. Most of impacted hailpads are within the area of simulated hail. However, both models exhibit a certain number of false alarms, that is, hail is not observed, but the model simulates hail. Notably, some of these false alarms could be attributed to the limited spatial information on hail occurrence provided by the hailpad network. Unlike radars, the hailpad network provides information on hail occurrence only at the exact position where the hailpad is installed. In theory, hail could easily occur anywhere between the two hailpads and be left unrecorded. Nonetheless, the greatest number of false alarms is present for the 24 July 2017 case with WRF producing more false alarms than COSMO-crCLIM. Surprisingly, both models successfully reproduce even a highly localized hailstorm occurring on 17 May 2018 with a flat surface pressure distribution over the north-eastern Adriatic, although it should be noted that, unlike WRF, COSMO-crCLIM produces a few spurious false signals in the continental part of Croatia. Moreover, two of the analyzed cases, namely 25 June 2017 and 24 July 2017, previously analyzed in [Malečić et al. \(2022\)](#) but simulated with different modeling settings (i.e.,

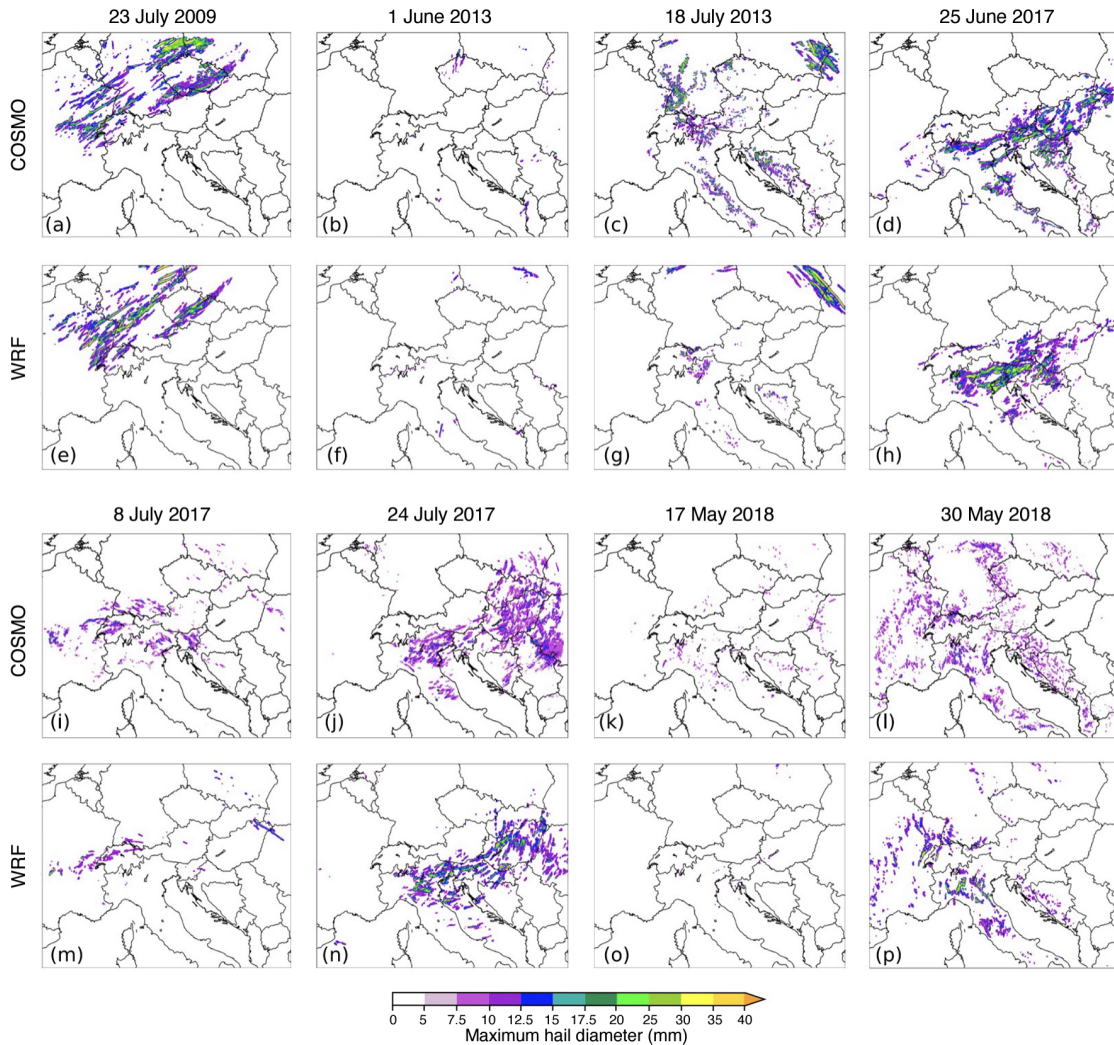


Figure 3.6: Maximum hailstone diameters in the time window from 00 UTC to 24 UTC on the day with severe convection simulated by COSMO-crCLIM (a–d); (i–l), and WRF (e–h); (m–p).

different domains, horizontal resolutions, input data or HAILCAST activation time), show similar hail swaths in both studies produced by WRF. Notably, in the future, other indices commonly used for estimating hail size such as hail size index, large hail parameter, significant hail parameter could also be investigated and added to the analysis (Czernecki et al., 2019).

The fields presented in Figure 3.7 are assessed against $\text{POH} \geq 80\%$ signals, as the region corresponding to $\text{POH} \geq 80\%$ is highly probable to have hail on the ground (Nisi et al., 2016). Obtained performance diagrams for all 8 cases together presented in Figures 3.9a and 3.9b reveal that COSMO-crCLIM performs better in terms of POD and EDI skill scores for all considered verification window sizes. On the other hand, WRF performs better in terms of FAR for all verification window sizes except the one corresponding to 30 grid points. These findings could be attributed to the fact that COSMO-crCLIM

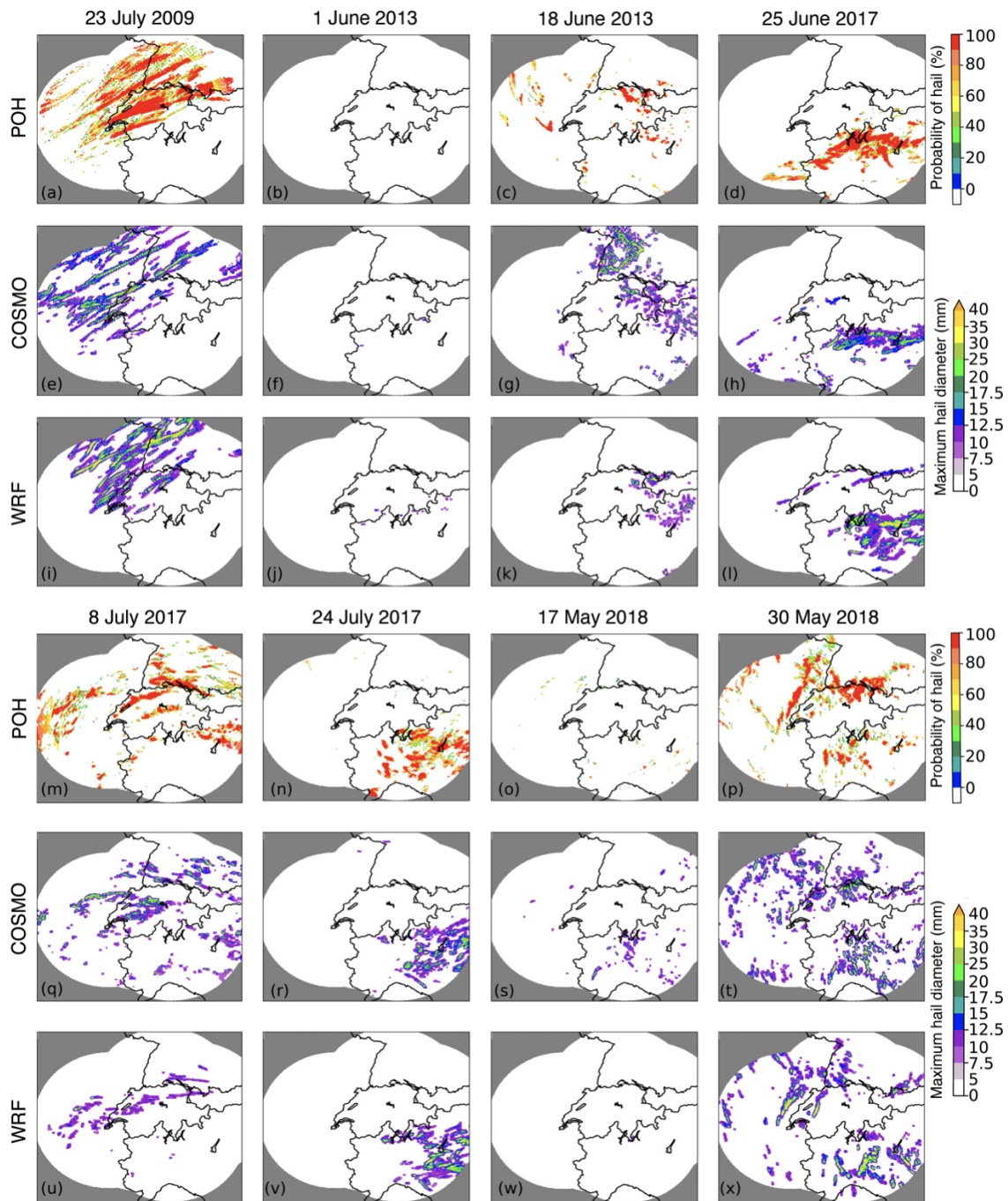


Figure 3.7: Daily maximums of the hailstone diameter simulated by (e–h); (q–t) COSMO-crCLIM and (i–l); (u–x) WRF and daily maximums of (a–d); (m–p) POH radar product.

produces more hail compared to WRF, which leads to higher POD and FAR values. According to the insights obtained in Figures 3.7, 3.9a and 3.9b, COSMO-crCLIM tends to produce hail swaths more similar to those observed than WRF over the Alpine region.

Next, simulated fields are evaluated against observations from the hailpad network in Croatia. The obtained performance diagrams for all three cases together (Figures

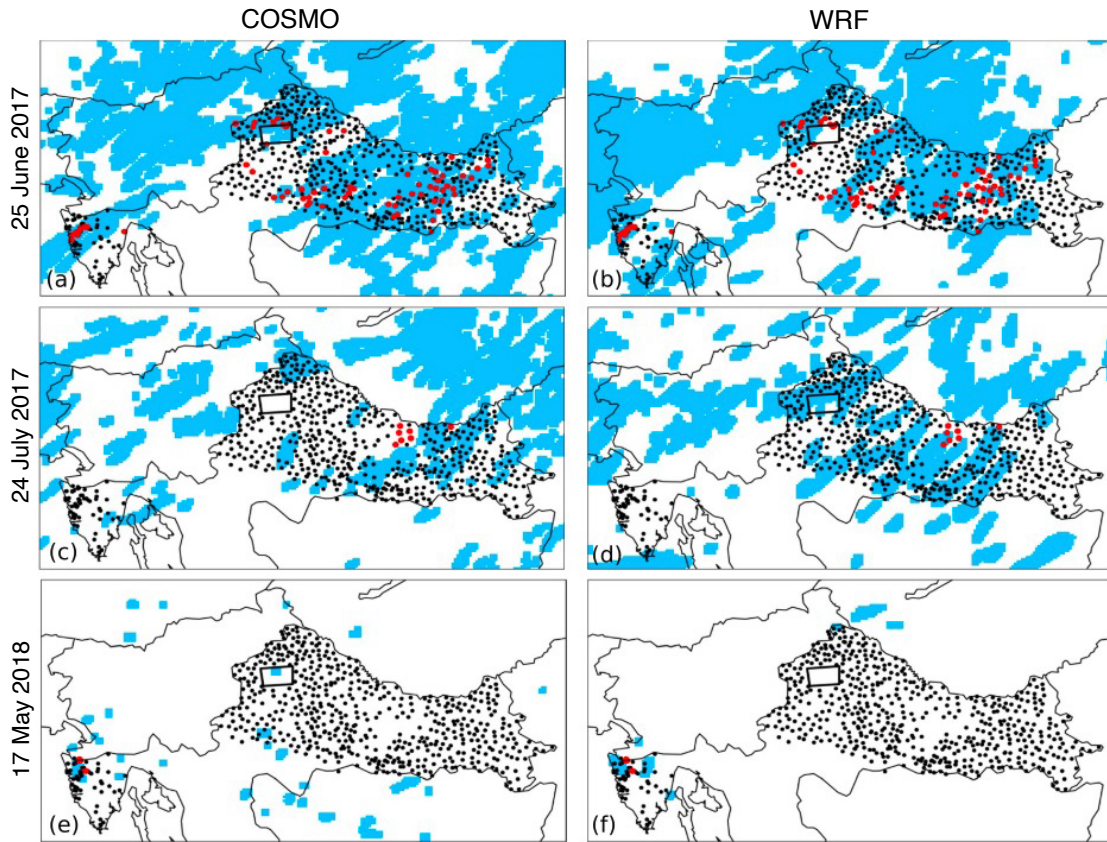


Figure 3.8: Simulated and recorded hail during the three cases with hail in Croatia. The shaded blue area represents simulated hail swaths (maximum hailstone diameter larger of equal to 5 mm) from 00 to 24 UTC on the day hail was observed. The position of hailpads is indicated with black dots. Impacted hailpads are marked with red circles. The position of a densely populated hailpad polygon is marked with a black rectangle and the stations within the polygon are colored only if the hail was observed at that specific station. Fields produced by (a,c,e) COSMO-crCLIM and (b,d,f) WRF are presented.

3.9c-d) show similar performance between the models. High POD values for larger verification window sizes indicate that models simulated hail where it was observed. However, unlike the results connected with radars (Figures 3.9a and 3.9b), FAR values associated with the hailpad network are much higher. That could be connected to the potential tendency of the model to overestimate the area affected by hail, if not also to the lack of spatially continuous information on hail occurrence in Croatia. Notably, there is a great contribution to the FAR values from the case on 24 July 2017 where both models produce a lot of false alarms. Interestingly, the same case, 24 July 2017, was also poorly represented in Malečić et al. (2022) using different modeling setups with a lot of false alarms indicating a low predictability of the atmospheric conditions leading to the initiation and evolution of the observed convection.

Hailpad networks, besides delivering information on hail occurrence, also provide information on hailstone sizes on the ground. Based on this information, a comparison

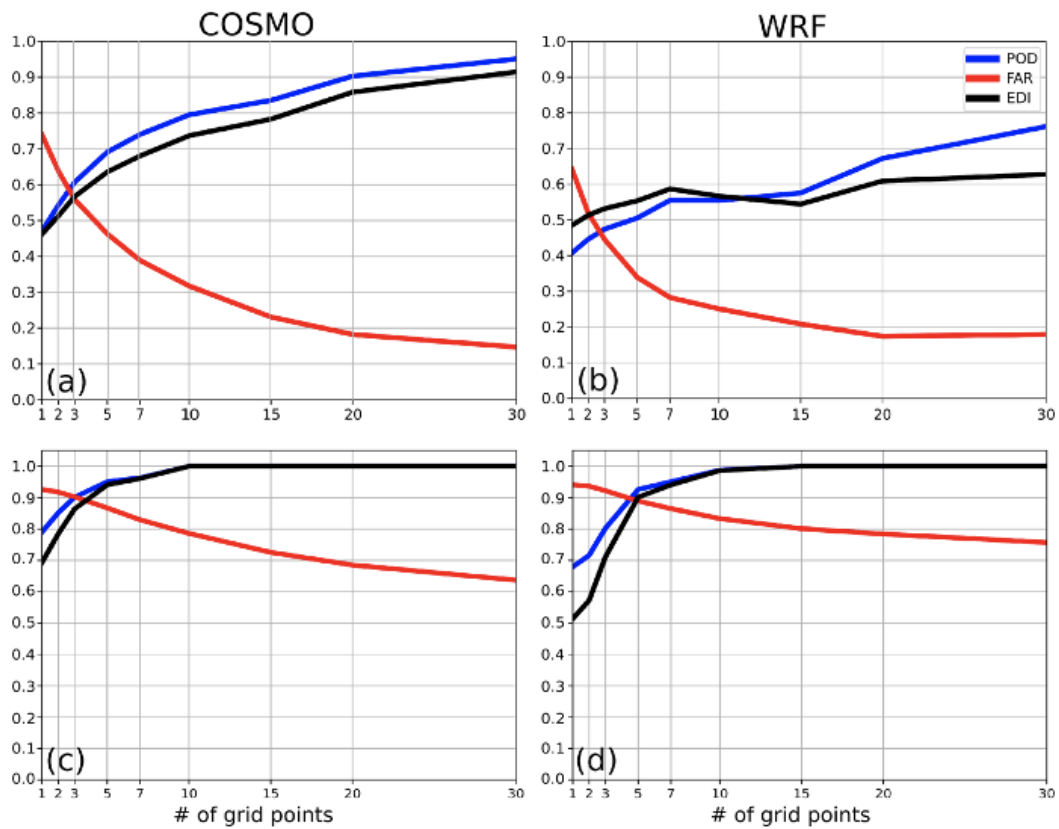


Figure 3.9: Performance of (a) COSMO-crCLIM and (b) WRF to simulate hail swaths as observed by the probability of hail (POH) radar product, and performance of (c) COSMO-crCLIM and (d) WRF in simulating hail as observed by the Croatian hailpad network in terms of probability of detection (POD, blue), false-alarm rate (FAR, red) and extremal dependence index (EDI, black) skill scores. Performance depending on the verification window size is presented.

of simulated and observed maximum hailstone diameters is performed. To account for possible spatial shifts between observed and simulated fields, a neighborhood inside a radius of 5 grid points (roughly corresponding to 12 km) of each impacted hailpad is scanned. The maximum simulated hailstone diameter inside this area is compared to the observed maximum hailstone diameter (Figure 3.10a). Both models underestimate the occurrence of smaller hailstones (diameters of 5–10 mm and 10–20 mm) and overestimate the occurrence of larger hailstones (diameters larger than 20 mm). However, when analyzing such results, one should proceed with caution, as it has been known from previous studies that hailpads are unlikely to record the largest hailstones given that they cover only 0.25 m² (Smith and Waldvogel, 1989). Indeed, to obtain a more realistic comparison between simulated and observed maximum hailstone diameter, it would be better to use the information on hailstone size observed by an observer—data that was not available for this study. Nonetheless, some tendencies could be extrapolated from the present comparison. Namely, COSMO-crCLIM mostly simulates hailstones in the 20–30 mm category, while WRF mostly simulates hailstones in the 30–50 mm category.

Additionally, WRF was able to reproduce an observed hailstone larger than 50 mm. Those differences between the two models are further confirmed if we compare the distribution of maximum hailstone sizes over the whole domain and all cases (Figure 11b). Here, it is clear that COSMO-crCLIM produces more hailstones in the 5–10 mm category than WRF, while WRF tends to produce more larger hailstones.

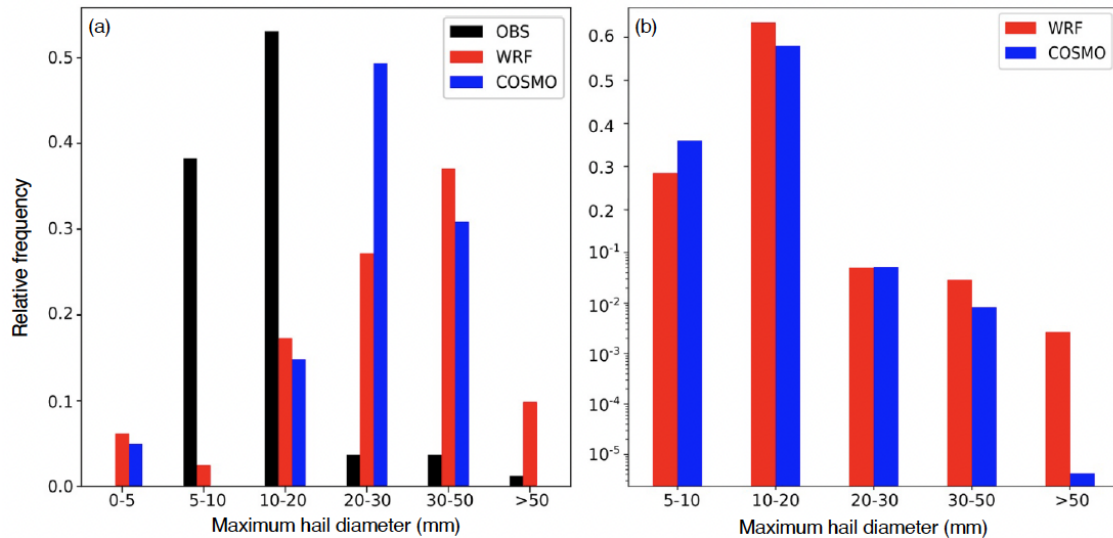


Figure 3.10: (a) Relative frequency of maximum recorded hailstone size from hailpads (black) and simulated maximum hailstone size by COSMO-crCLIM (blue) and WRF (red), and (b) the relative frequency of simulated maximum hailstone sizes over the whole domain for COSMO-crCLIM (blue) and WRF (red). Histograms are normalized by dividing the count of hailstone sizes in each category with the total observed number of hailstones. To better depict differences between models and runs, the y-axis in (b) is partly linear and partly logarithmic.

3.6.4 Differences between models and model internal variability

The analysis reveals that WRF tends to produce less precipitation, smaller hail swaths but higher values of LPI and more large hailstones compared to COSMO-crCLIM. Here, we study the potential origins of these differences, and consider the role of model internal variability in our results. For this reason, we form an ensemble of simulations with different initialization times for one of the cases with widespread hail and lightning across the Alpine-Adriatic region, namely the 30 May 2018. Both models were initialized at 06, 12 and 18 UTC the day before hail was observed (29 May 2018). Additionally, we utilize a simulation of the newest version of COSMO, namely COSMO 6.0, to further increase the ensemble size and to increase the robustness of our conclusions. The simulation using COSMO 6.0 is initialized at 12 UTC the day before hail was observed.

First, we analyze simulated daily precipitation fields between ensemble members (Figure 3.11) and see that all ensemble members produce precipitation patterns similar to the observed. Moreover, there is a greater difference in the fields produced by COSMO and WRF than between the members of the same model. This finding sug-

gests that the differences in results are rather linked to systematic differences between models than to the model’s internal variability. However, it should be noted that differences between model members exist. Both versions of COSMO produce comparable fields, although local differences are present that may be relevant for forecasting applications. For instance, the observed heavy precipitation along the French-German border is largely or completely missed in two of the COSMO ensemble members but present in the member initialized at 06 UTC. This highlights the need for using ensemble techniques in numerical weather prediction (NWP) applications (Klasa et al., 2018).

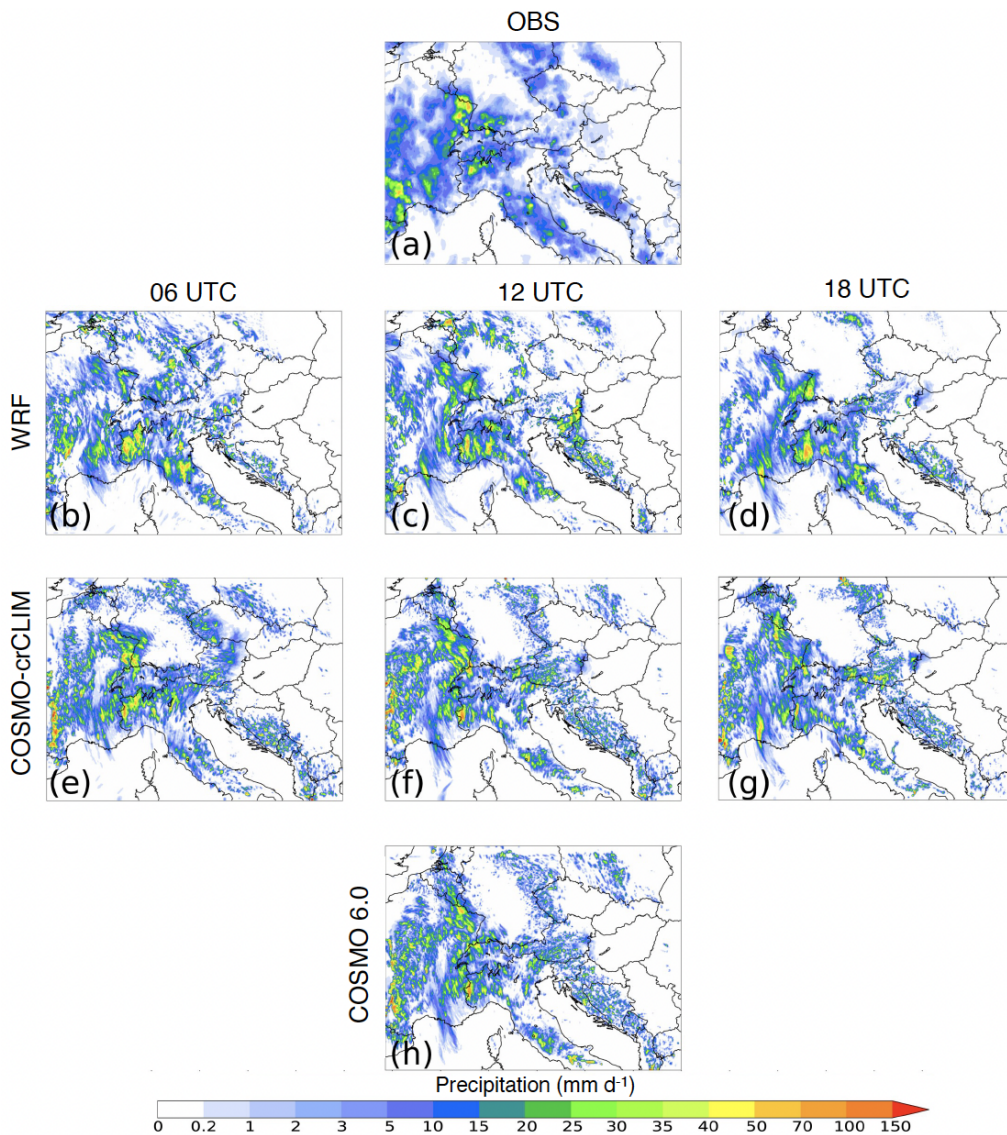


Figure 3.11: Accumulated precipitation for the period between 00 and 24 UTC on 30 May 2018. From top to bottom rows are (a) IMERG observation and simulated fields using (b–d) WRF, (e–g) COSMO-crCLIM, (h) COSMO 6.0. The columns from left to right represent the simulations initialized at 06, 12 and 18 UTC on the day before the event, respectively.

Similarly, daily maximums of LPI produced by each of the ensemble members are

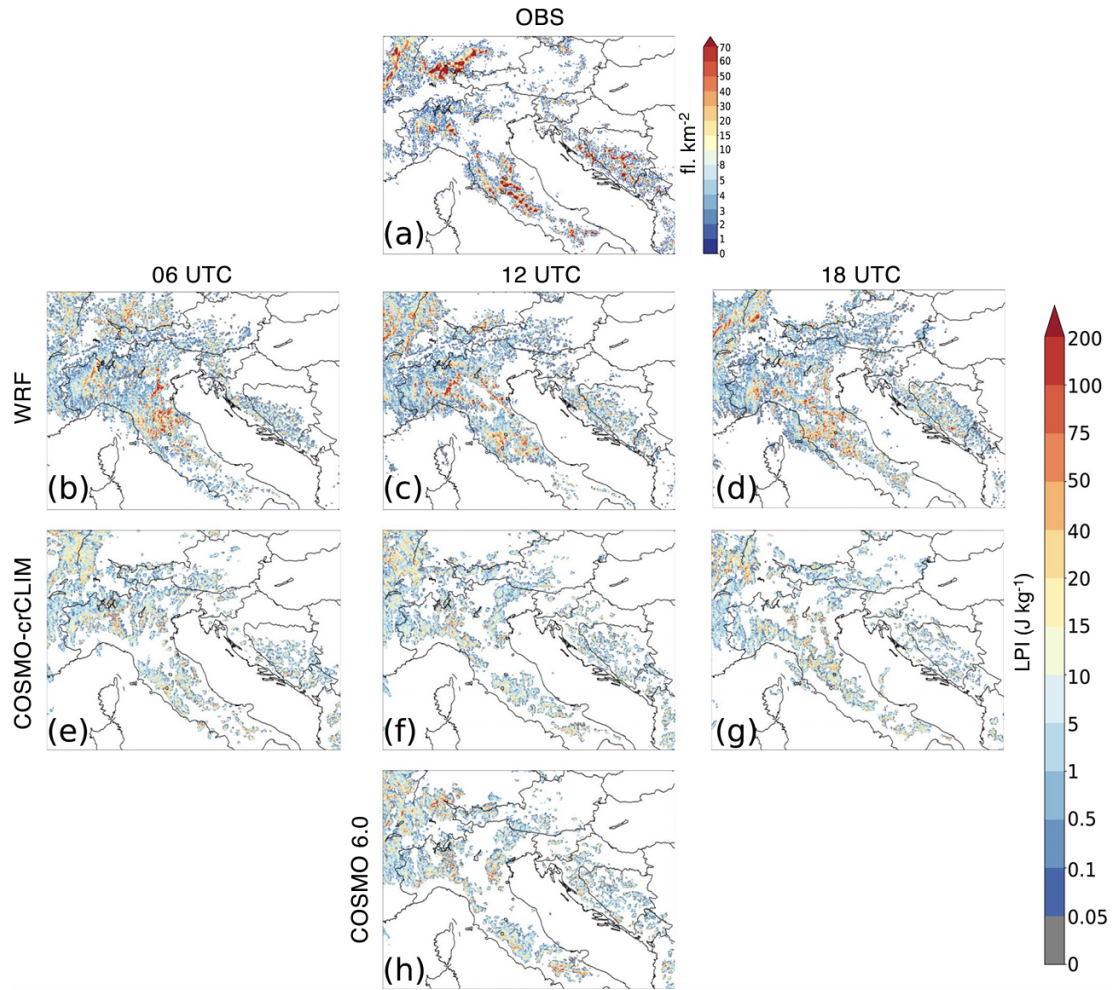


Figure 3.12: (a) Daily sum of the observed lightning flashes by the LINET network for the period between 00 and 24 UTC on 30 May 2018. Daily maximum of LPI produced by (b–d) WRF, (e–g) COSMO-crCLIM, and (h) COSMO 6.0. The columns represent simulations initialized at with 06, 12 and 18 UTC on the day before the event.

compared against daily sums of the number of lightning flashes from the LINET network (Figure 3.12). Here we use the raw LPI instead of the adjusted LPI because we want to avoid filtering the signals to have a direct comparison. It is clear that both models reproduced the area affected by lightning fairly well, although WRF produces higher values of LPI. This finding is consistent with the above results, for which we applied a higher threshold for WRF to convert LPI to the observed number of lightning flashes. Although there are differences in LPI between the model members, there are larger differences in LPI produced by the two different models. COSMO 6.0 produced LPI in agreement with COSMO-crCLIM, although with slightly higher values.

By comparing daily maximums of the hailstone diameters produced by ensemble members for both spatial (Figure 3.13) and cumulative distribution (Figure 3.14), similar conclusions are found. Figure 3.13 shows that the simulated fields are overall similar, although WRF produces less hail compared to COSMO regardless of the initialization

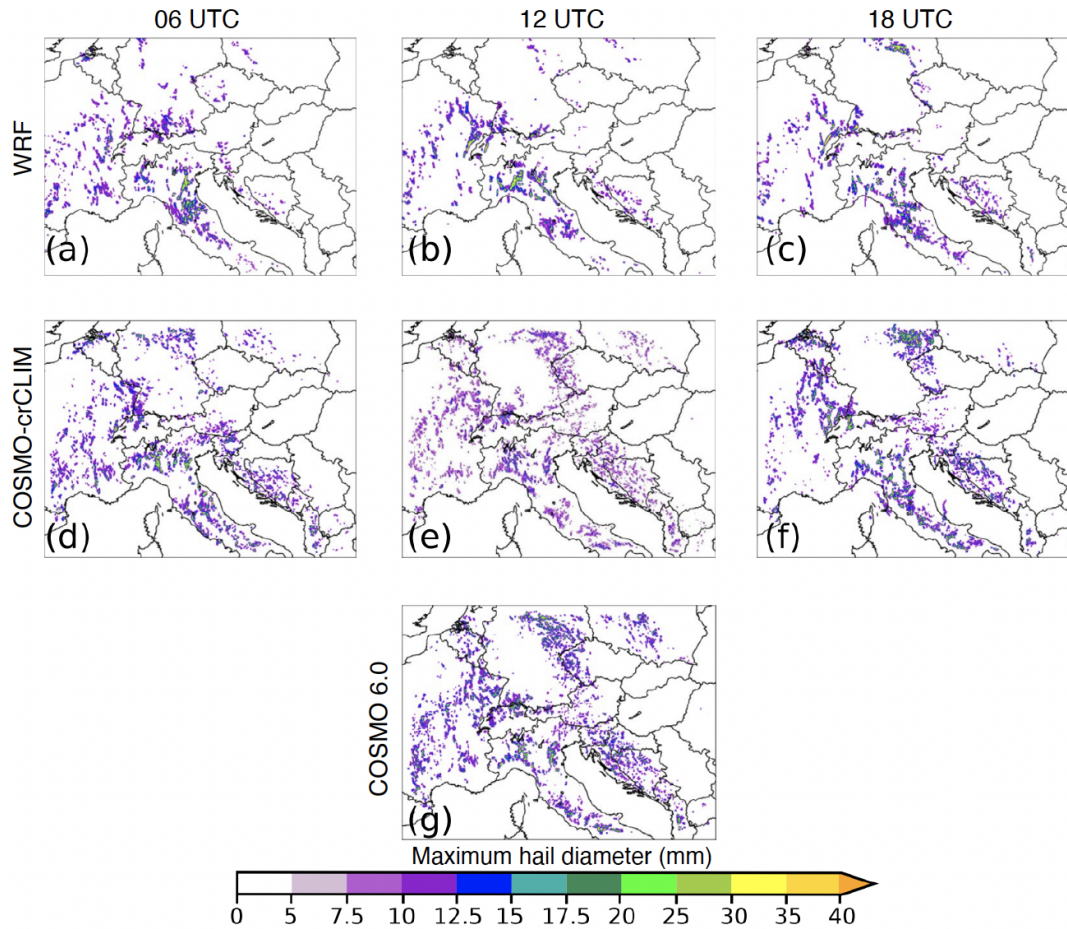


Figure 3.13: Daily maximum of hailstone diameter for the period between 00 and 24 UTC on 30 May 2018 simulated by (a–c) WRF, (d–f) COSMO-crCLIM, and (g) COSMO 6.0. The columns represent the simulations initialized at 06, 12 and 18 UTC on the day before the event.

time. Hail produced by the same model but different initialization times (06, 12 and 18 UTC) and different model versions (COSMO-crCLIM and COSMO 6.0) is more similar than hail produced by different modeling systems (WRF vs. COSMO). When comparing simulated maximum hailstone diameters (Figure 3.14), we notice that, for hailstones smaller than 30 mm, the differences between COSMO and WRF are within each model’s internal variability. However, for hailstones larger than 30 mm, not only the differences between models become larger than model internal variability, but also it is clear that, out of all ensemble members, only WRF produced hailstones larger than 50 mm.

It should be noted that these findings are valid for one case only, and since the magnitude of the internal variability depends on the synoptic situation, model configuration, region and season (Lavin-Gullon et al., 2020) more cases should be analyzed to get more robust conclusions.

Further, considering the importance of the updrafts, as well as solid and liquid hydrometeors in the LPI and HAILCAST formulations, vertical profiles of these variables

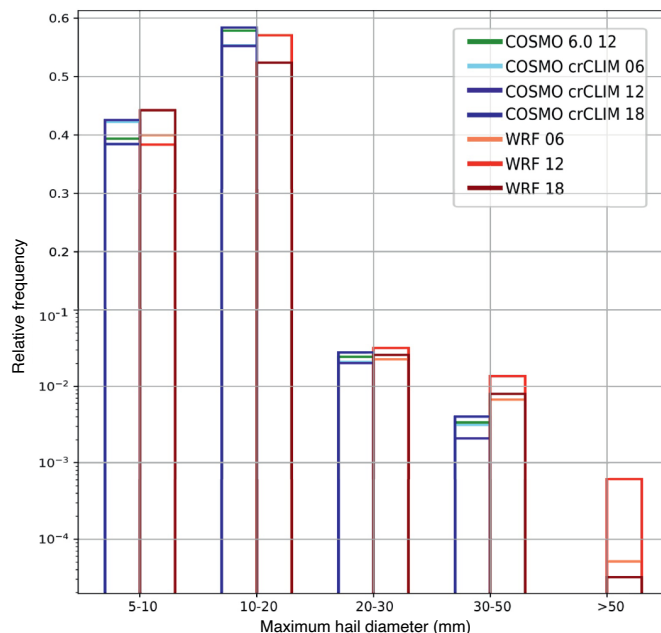


Figure 3.14: Relative frequency of the simulated maximum hailstone diameter over the whole domain for COSMO-crCLIM initialized at 06, 12 and 18 UTC (shades of blue), WRF initialized at 06, 12 and 18 UTC (shades of red) and COSMO 6.0 initialized at 12 UTC (green). The histograms are normalized by dividing the count of hailstone sizes in each category by the total number of grid points where hail occurs. To better depict differences between models and members, the y-axis is partly linear and partly logarithmic.

are compared among the models. Figure 3.15 presents vertical profiles averaged over time and grid points that have LPI greater than 0 during the 30 May 2018 case. The models produced different distributions of solid and liquid hydrometeors inside thunderclouds. Namely, WRF produces higher cloud water mixing ratios compared to both versions of COSMO and higher rain water mixing ratios compared to COSMO-crCLIM, but lower rain water mixing ratios compared to COSMO 6.0. Similarly, both versions of COSMO produce higher ice and graupel water mixing ratios, but lower snow water mixing ratios. Since in the LPI formulation, the ratio between solid and liquid hydrometeors inside a thundercloud is more important than their exact values, total liquid water and ice fractional liquid ratio terms from the LPI formulation (q_L and q_F terms from Equations 2.3 and 2.4) are computed alongside a dimensionless parameter ε representing the scaling factor for the updraft in the LPI formulation (Equation 2.2). ε obtains maximum values when total liquid water and ice fractional mixing ratios are equal (Equation 2.2). Surprisingly, analysis of ε shows no apparent discrepancies between the models even though there are some differences in q_L and q_F parameters. However, there is a difference in the simulated updrafts, that is, both COSMO versions simulate, on average, weaker and higher updraft cores compared to WRF. WRF simulates stronger updrafts with the updraft core exactly at the position of the maximum value of ε , coinciding with the region with nearly equal amounts of solid and liquid hydrometeors. Since

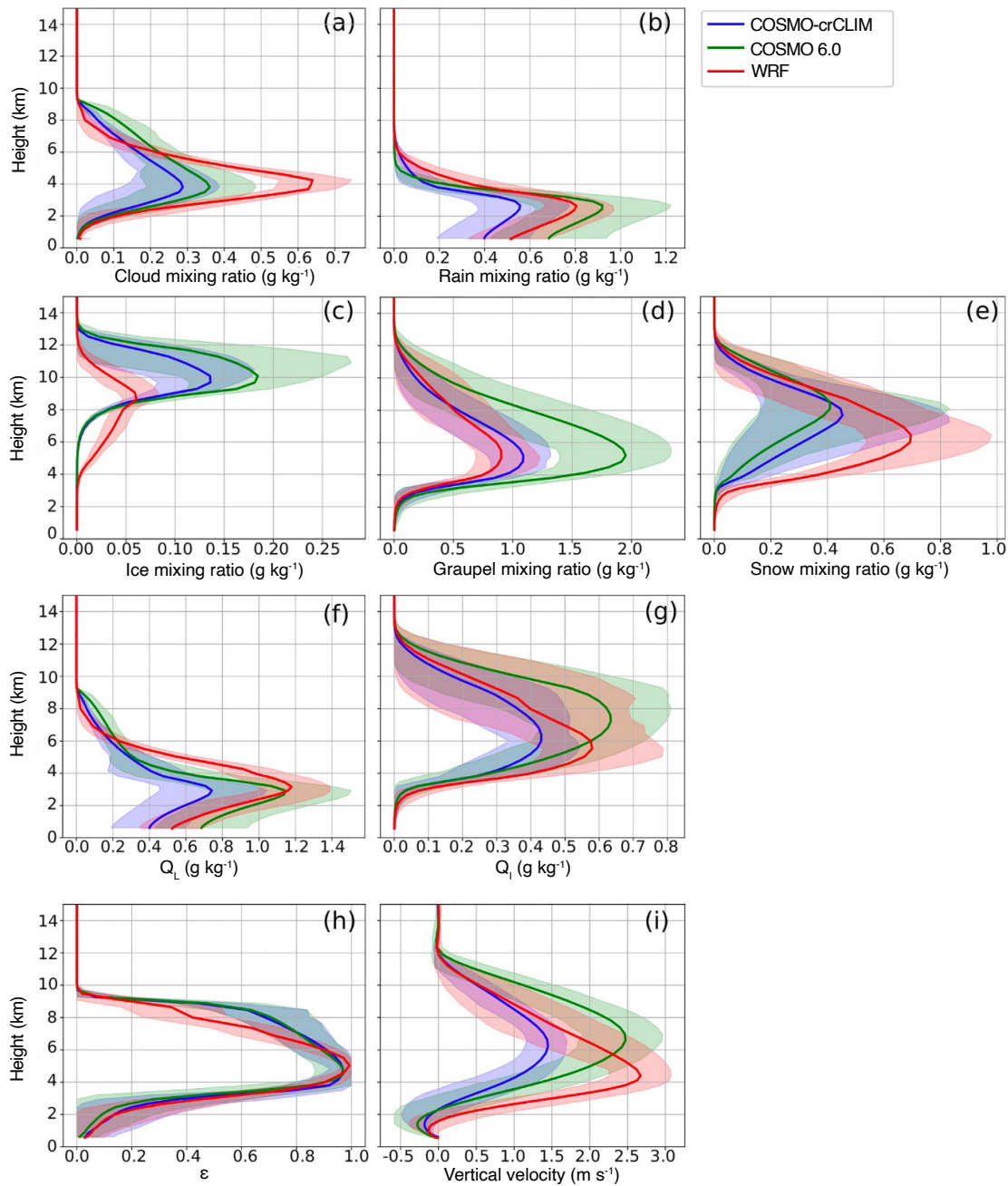


Figure 3.15: Vertical profiles of (a) cloud, and (b) rain mixing ratio; (c) ice, (d) graupel, (e) snow, (f) total liquid water, and (g) ice fractional mixing ratio; (h) updraft scaling parameter; and (i) vertical velocity as simulated by COSMO-crCLIM (blue), COSMO 6.0 (green) and WRF (red) models. The lines indicate the mean values across all grid points with $LPI > 0$, while the shading indicates the range between 5th and 95th percentile.

the presence of both solid and liquid hydrometeors is important for lightning and hail growth processes, it is not surprising that WRF simulates higher LPI and more large hailstones compared to COSMO. On the other hand, the updraft core in both versions of COSMO is in the region with much more solid than liquid hydrometeors which is

not as favorable for lightning or hail growth processes. This could be the reason why COSMO simulates lower LPI values and higher amounts of smaller hailstones. COSMO 6.0 simulates stronger updraft cores compared to COSMO-crCLIM which could explain why COSMO 6.0 produces higher LPI values than COSMO-crCLIM (Figure 3.12) and larger hailstones compared to COSMO-crCLIM (Figure 3.14a).

Several studies reported a sensitivity of hail and lightning-related variables such as updrafts and graupel mixing ratios on the choice of microphysics (Lagasio et al., 2017; Trefalt et al., 2018; Manzato et al., 2020; Sokol and Minářová, 2020; Raupach et al., 2021) a combination of microphysics and planetary boundary layer parameterization scheme (Malečić et al., 2022) and large-scale forcing and initialization time (Manzato et al., 2020). Thus, different models with different configurations can produce large variability for different cases.

Likewise, differences in updrafts strength and structure strongly depend upon the dynamical core of the models. Such differences can objectively be assessed using kinetic energy spectra (Skamarock, 2004). While both models considered here have similar dynamical cores using the split-explicit approach, there are significant differences in terms of advection schemes. The role of model formulation for heavy summer convection over Europe has recently been investigated in an intercomparison of the COSMO and the ECMWF-IFS models (Zeman et al., 2021). Results revealed a strong sensitivity with respect to the dynamical core (split-explicit vs. spectral) but also with respect to time-step size as well as (explicit or implicit) numerical diffusion.

3.7 Conclusions

Hail and lightning, which are damaging and relatively frequent phenomena over the Alpine-Adriatic region, still remain difficult to model. Thus, this study employed two km-scale models, namely COSMO and WRF, with hail (HAILCAST) and lightning (LPI) diagnostic tools to simulate eight severe convective events occurring over the Alpine-Adriatic region. The main aim was to analyze the robustness of HAILCAST and LPI results produced by the two different modeling systems, to explore their differences and to systematically and quantitatively evaluate the performance of each model. The main conclusions from this analysis can be summarized as follows:

- Both models reproduced the observed spatiotemporal precipitation characteristics, with WRF producing slightly lower amounts.
- Both models showed good performance in reproducing the observed lightning activity despite WRF's tendency to simulate higher LPI values.
- Simulated hail swaths are overall similar, with COSMO tendency to produce more hail. Both models showed a good performance in reproducing hail observed by radar estimates over Switzerland and in-situ measurements over Croatia, although COSMO performed slightly better than WRF. Both models, on average, overestimated observed maximum hailstone diameters, with WRF tendency to produce larger hailstones.
- Differences between the models are present regardless of their initialization time

and can be linked to different distributions of updrafts and hydrometeors inside thunderclouds.

In conclusion, we show that atmospheric conditions leading to hailstorm formation and evolution are well simulated using state-of-the-art km-scale modeling systems. Moreover, HAILCAST and LPI have great potential for real-time forecasting and climatological assessment of hail and lightning in current and future climates. However, the variability of the results depending on the modeling system used encourages the use of a multi-model and/or multi-physics ensemble when modeling such events. Despite the promising results, it should be noted that this study is based on a small number of cases. To get statistically more robust conclusions a larger number of hailstorms needs to be analyzed. Moreover, this study would highly benefit from employing other data sources of hail observations covering the whole Alpine-Adriatic region. Nonetheless, given all limitations, this study represents the first attempt to systematically analyze and evaluate the performance of two intrinsically different km-scale modeling systems to reproduce the main characteristics of multiple hailstorms occurring over the Alpine-Adriatic region.

Author contributions. BM, RC and PV run the WRF, COSMO-crCLIM and COSMO 6.0 simulations, respectively. BM drafted the paper, with all co-authors contributing with scientific and writing input.

Chapter 4

Evaluation of decade-long hail and lightning simulation over the Alpine-Adriatic region using a km-scale climate model

Ruoyi Cui¹, Nikolina Ban², Marie-Estelle Demory^{1,3,4,5}, Lucija Blašković⁶, Damjan Jelić⁶, Maja Telišman Prtenjak⁶, Christoph Schär¹

This chapter is a manuscript in preparation

Abstract Severe convective storms accompanied by hail and lightning can lead to significant property, infrastructure, and life damage. Despite the catastrophic nature, our understanding of the characteristics of such events has been limited due to observational and modeling challenges. Although limited in space and time, newly emerging observations of hail and lightning provide valuable information and support the evaluation of newly emerging kilometer-scale climate models which are able to explicitly represent deep convective processes.

In this study, we perform a decade-long simulation with the Consortium for Small-scale Modeling (COSMO) model at 2.2 km horizontal grid spacing over the Alpine-Adriatic region. The simulation is driven by ERA5 reanalysis that covers the 2009–2018 period and consists of the extended summer season (April–September). The model is run with hail and lightning diagnostics - the one-dimensional hail growth model (HAIL-CAST) and lightning potential index (LPI) - based on model physics, i.e., updrafts and

¹Institute for Atmospheric and Climate Science, ETH Zurich, Zurich, Switzerland

²Department of Atmospheric and Cryospheric Sciences (ACINN), University of Innsbruck, Innsbruck, Austria

³Wyss Academy for Nature, University of Bern, Bern, Switzerland

⁴Climate and Environmental Physics, Physics Institute, University of Bern, Bern, Switzerland

⁵Oeschger Centre for Climate Change Research, University of Bern, Bern, Switzerland

⁶Department of Geophysics, Faculty of Science, University of Zagreb, Zagreb, Croatia

microphysical profiles.

One part of the study focuses on the evaluation of hail and lightning climatology produced by the model against available Croatian station observations, Swiss radar-based estimates, and LINET lightning observations. The modeled and observed seasonal cycle, diurnal cycle, and frequency of hailstones sizes are discussed. Overall, they show similar patterns. The diurnal cycle of hail and lightning is more pronounced in mountainous regions than in coastal regions. A higher frequency of severe events in summer is found over higher elevated topography. The second part of the study focuses on the comparison of the results obtained by HAILCAST and LPI against widely used hail and lightning proxies based on environmental variables. The results show that HAILCAST and LPI diagnostics are closer to observations than simpler proxies. These promising results reveal that both HAILCAST and LPI can provide valuable information on hail and lightning, and are good candidates for future climate change studies.

4.1 Introduction

Severe convective storms accompanied by hail and lightning can lead to significant socioeconomic impact. Therefore, it is of utmost importance to understand the spatiotemporal variability of hail and lightning and the processes that lead to these events. The progress in these areas has been slow due to several challenges related to observing and modeling such events.

The primary challenge has been the lack of long-term high-quality observations (Punge and Kunz, 2016). In recent years, several developments have been made by developing new tools and algorithms to collect and construct the data. For example, thunderstorm climatology can be constructed using lightning detection networks (Poelman et al., 2016; Galanaki et al., 2018; Enno et al., 2020) or satellite-based sensors (Punge et al., 2017). However, constructing hail climatology is more difficult since the spatial coverage of direct observations is too dispersed to capture the scale of hail events (Taszarek et al., 2019). Instead, one can use radar-based algorithms as done over the Alpine region (Nisi et al., 2016, 2018), France, Germany, Belgium, and Luxembourg (Fluck et al., 2021). Hail information can also be obtained from crowd-sourced observations, such as MeteoSwiss application (Barras et al., 2019) or European Severe Weather Database (ESWD) (Dotzek et al., 2009; Púčík et al., 2019), insurance reports (Vinet, 2001), hailpad networks and newspaper archives (Kahraman et al., 2015; Punge et al., 2014). While some of those provide information on a country scale, the other suffers from a strong bias towards densely populated areas.

Another challenge is related to the modeling hail and lightning. This requires a physical understanding of the hail growth process or cloud electrification and discharge mechanisms. At the same time, it also requires high-resolution models that can explicitly represent convective processes associated with hail and lightning, which come with high computational costs.

In the last decade, kilometer-scale models have been increasingly used for climate simulations. These models are characterized by reducing the model grid spacing to less

than 4 km (Schär et al., 2020). At such scales, convection parameterization schemes can be switched off as deep convection starts to be resolved explicitly (Ban et al., 2014; Prein et al., 2015). Such an approach leads to improvements in the simulations of precipitation, especially heavy precipitation and convective processes (Ban et al., 2014; Leutwyler et al., 2017; Ban et al., 2021). With this progress in modeling, new diagnostics tools have started to emerge. For example, hail and lightning diagnostics can be embedded within high-resolution models, using information at each model level, grid point, and timestep. As such, they can provide a better estimation of hail and lightning occurrence. For example, the one-dimensional hail growth model HAILCAST (Adams-Selin and Ziegler, 2016) tracks the prescribed embryos as they rise, grow, and fall within the grid columns. Lightning potential index (LPI, Yair et al. (2010); Lynn and Yair (2010)) considers the non-inductive mechanism by collisions of ice and graupel in the presence of supercooled water within the main charging zone. Recent studies show that when the convection is well represented in the model, HAILCAST serves as a good indicator of hailstone sizes at the ground (Adams-Selin et al., 2019), and LPI is highly correlated with the observed lightning flashes (Yair et al., 2010). Moreover, applications of the HAILCAST and LPI over the Alpine-Adriatic region for various case studies have demonstrated good performance in comparison to observations, although the results can differ between different modeling systems (Malečić et al., 2023; Cui et al., 2023).

Due to the limitations in both observations and modeling, the use of environmental proxies has been used extensively to study hail and lightning and to understand the change in severe convective storms under global warming (Romps et al., 2014; Seeley and Romps, 2015). These proxies use environmental variables from the reanalysis or output from coarse resolution models (REF), such as CAPE and CIN, precipitation, temperature, and wind, available as average or instantaneous values over 1-, 3- or 6-hour periods. In recent years, the use of statistical model (Rädler et al., 2019) and machine learning (Czernecki et al., 2019; Torralba et al., 2023) has also gained some attention. However, hail and lightning proxies suffer from several drawbacks. They are mainly derived empirically using limited observations and provide “prone” or “not prone” environments (Raupach et al., 2023). Thus, their applicability to other regions can be limited by different storm environments (Taszarek et al., 2020b; Raupach et al., 2023). The use of reanalysis, even as the latest as ERA5, still suffers from too coarse horizontal resolution and from biases in the lower atmosphere that impact the estimation of temperature, moisture, and instability (Taszarek et al., 2020b). Brisson et al. (2021) has conducted a regional climate simulation over central Germany and has found that LPI outperforms the CAPE×PREC parameterization (Romps et al., 2014) used in climate models with a coarser-grid spacing which relies on deep convection parameterization. One of the main shortcomings of the CAPE×PREC parameterization is a poor diurnal cycle of lightning, which can be related to poor representation of precipitation and CAPE in these REFs. These findings underscore the promise of diagnostics such as HAILCAST and LPI as prospective candidates for climate studies of hail and lightning.

The third challenge is related to the uncertainty of future projections of hail and lightning. An increase in convective instability does not guarantee more frequent and severe hailstorms or thunderstorms, as the accompanying rise in melting level height may reduce surface hail (Brimelow et al., 2017; Raupach et al., 2023). The impact of

climate change on lightning is even more uncertain, as previous studies have shown that different regions have contrasting stories using different proxies and schemes (Clark et al., 2017; Finney et al., 2018; Romps, 2019; Gordillo-Vázquez et al., 2019; Brisson et al., 2021; Charn and Parishani, 2021; Kahraman et al., 2022). The best way to simulate lightning and lightning projection in climate models remains an open question (Clark et al., 2017). Thus, there is a clear need to enhance our comprehension of hail and lightning processes and explore diverse approaches for generating information on such events.

Motivated by the promising results from previous high-resolution modeling studies, here we aim to evaluate the climate simulation of hail and lightning using a km-scale climate model. We present a 10-year-long km-scale simulation over the Alpine-Adriatic region, employing the COSMO-crCLIM model (Schär et al., 2020) driven by ERA5 re-analysis. This simulation presents one of the first km-scale climate simulations using both hail and lightning diagnostics over such a large domain and for such a long time period. Our analysis is focused on the extended convective season from April to September, which is the main hail and lightning season over the Alpine-Adriatic region (e.g., Nisi et al. (2018); Simon et al. (2023)). The evaluation is conducted against different types of observations available from different sources due to the lack of more consistent and uniform observations across the entire simulated domain. Furthermore, we compare the results obtained by HAILCAST and LPI with different hail and lightning proxies derived from environmental variables. The objectives of this study are the following:

- What are the main characteristics of hail and lightning over the Alpine-Adriatic region?
- How does the COSMO model at km-scale resolution reproduce those characteristics of hail and lightning over different topographical regions?
- What are the reasons behind these (if any) differences over different topographical regions?
- How do the results of hail and lightning differ between different diagnostic tools (i.e., HAILCAST and LPI versus proxies)?

The chapter is structured as follows. Section 4.2 introduces the model setup, hail and lightning proxies, and the observations used for evaluation. Section 4.3.1 discusses the evaluation of temperature and precipitation. Section 4.3.2 evaluates the seasonal and diurnal variations of hail and lightning over different topographical regions against available observations. Section 4.3.3 covers the intercomparison of hail and lightning proxies. Finally, Section 4.4 summarizes the main findings.

4.2 Data and methods

4.2.1 Model setup

A 10-year long (2009–2018) extended convective season (April–September) simulations are conducted using the climate version of the non-hydrostatic Consortium for Small-Scale Modeling (COSMO) model, which is able to run on hybrid CPU-GPU archi-

tures (Leutwyler et al., 2017; Schär et al., 2020). The simulations are driven by ERA5 reanalysis (Hersbach et al., 2020) with a 3-hourly update interval of the boundary conditions. The model was run using a one-way two-step nesting approach. The outer nest (CTRL12) ran continuously throughout the entire year with a horizontal grid spacing of 12 km and covering almost the entire Europe. The inner nest (CTRL2), featuring a finer horizontal grid spacing of 2.2 km, covers the Alpine-Adriatic region (Fig. 4.1), and is initiated in February each year. With the analysis period starting from April, this leaves a two-month soil spin-up period to ensure the equilibrium of surface physics for climate analysis.

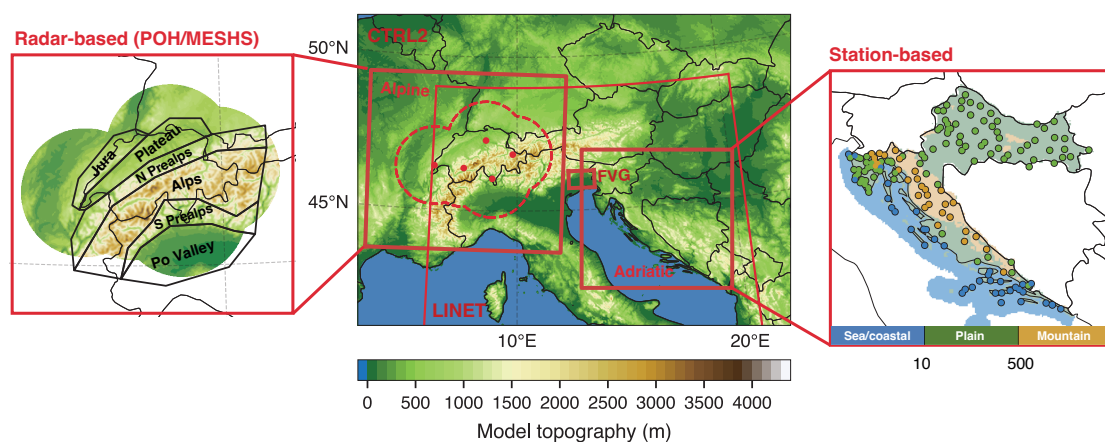


Figure 4.1: COSMO 2.2 km domain and regions covered by different observational data sets used in this study. (Middle panel) COSMO 2.2 km analysis domain and LINET lightning observations shown by red polygon covering the largest region. The polygons indicate the area of radar observation over Switzerland (left), hailpad observations over FVG, and station observations over Croatia (right). (Left panel) Radar-based POH/MESHS observations with the area within a 140 km radius of 5 Swiss radar stations which are indicated as red dots. This domain is split into 6 subdomains, as delineated in black lines for evaluation. (Right panel) Hail observations recorded on Croatia stations. This domain is split into 3 topographical subdomains: sea/coastal, plains, and mountainous areas defined by the height thresholds shown in the color bar. Details regarding the subdomains can be found in Table 4.1.

Both simulations are configured to have 60 terrain-following hybrid vertical levels, where vertical spacing ranges from 20 m above the surface to 1.2 km at the model top located at 23.5 km above mean sea level. In the CTRL12 domain, the Tiedtke scheme (Tiedtke, 1989) is turned on for shallow convection and switched off for deep and mid-level convection following recent findings of Vergara-Temprado et al. (2020). In the CTRL2 domain, the Tiedtke scheme is switched off entirely to resolve the convection processes explicitly. Furthermore, we use a single-moment microphysics scheme with prognostic cloud water, cloud ice, graupel, rain, and snow (Reinhardt and Seifert, 2006), and a radiation scheme with a δ -two-stream approach (Ritter and Geleyn, 1992). The soil properties are modeled using a 10-layer soil model, TERRA_ML (Heise et al., 2006), with the subgrid-scale treatment of orography following Schlemmer et al. (2018). To

Table 4.1: Description of subdomains over the Alpine and Adriatic region used in the analysis. The number of stations that recorded hail within the subdomains of Croatia from 1989 to 2018 is provided in the brackets.

Region	Subdomains	Spatial coverage (km ²)	Mean model elevation (m)
Alpine	Jura	8426	791.4
	Plateau	14460	562.5
	N Prealps	19903	1077.2
	Alps	42033	2028.4
	S Prealps	13591	1022.7
	Po Valley	24678	195.8
Adriatic	Sea/coastal	28465 (37)	0.5
	Plain	47702 (93)	169.5
	Mountains	11977 (31)	777.5

ensure the soil moisture and the atmosphere are well equilibrated at the beginning of the simulations, the soil moisture profiles for the CTRL12 simulation are taken from a recently conducted 10-year long ERA-Interim driven COSMO climate simulation by Vergara-Temprado et al. (2020) and runs with the above settings for a period of 5 years (2004–2009) prior to the simulation period analyzed in this study.

4.2.2 Hail and lightning diagnostics

For the simulation of hail and lightning, we utilize the COSMO model with embedded HAILCAST and LPI, both of which are physically based diagnostic tools and use more detailed model information than the simpler proxies described later. These proxies are calculated using COSMO model output fields (Glahn and Lowry, 1972) and serve to identify the environment favorable for the development of hail and lightning.

In each of the following sections, dedicated to hail and lightning, we first start by describing physically based diagnostics and then continue with proxies used in this study for the purpose of conducting a comprehensive intercomparison.

Hail

1D hail growth model — HAILCAST. HAILCAST (Adams-Selin and Ziegler, 2016) is a one-dimensional, time-dependent hail growth model that was developed to simulate the maximum expected hail size at the ground. HAILCAST uses the profiles of cloud liquid and ice water, vertical velocity, temperature, water vapor, and pressure fields from a given model timestep within the CTRL2 domain. The evolution of 5 hail embryos is calculated based on microphysics – two embryos of 5 and 7.5 mm in diameter are initialized at -8°C level, and three embryos of 5, 7.5, and 10 mm in diameter are initialized at -13°C . The HAILCAST is activated every 5 min if the updraft velocity is larger than 10 m s^{-1} for more than 15 minutes, and the output is saved as the hourly maximum. More details on the description and settings can be found in Cui et al. (2023), where COSMO HAILCAST was evaluated for eight severe convective cases.

Updraft helicity — UH25. Updraft helicity (UH, $\text{m}^2 \text{s}^{-2}$) is one of the proxies used to indicate hail (Brooks et al., 1994). It is a diagnostic variable that represents the strong rotating updrafts and is always used as an indication of supercell thunderstorms and even tornadoes (Kain et al., 2008; Ashley et al., 2023). It was developed for model runs at high resolution and is computed as the vertical integral of vertical vorticity (ζ) times the vertical velocity (w), usually within 2–5 km above ground level:

$$UH25 = \int_{2\text{km}}^{5\text{km}} w\zeta dz \quad (4.1)$$

hereafter referred to as UH25. This range, 2–5 km, encompasses the layer where mesocyclones occur (Kain et al., 2008), which are generated when horizontal vorticity is tilted into the vertical by vertical wind shear. UH25 is calculated every 15 min from CTRL2 output and used the hourly maximum of the wind field for analysis.

Column-integrated graupel — GRPL. As a second hail proxy, we apply a heuristic estimation of hail occurrence based on the hourly maximum of column-integrated graupel (GRPL, kg m^{-2}) (similar to Trapp et al. (2019)). The testing presented in the Supporting Information, shows similar results as in (ESSL, 2015; Trapp et al., 2019), where $\text{GRPL} \geq 10 \text{ kg m}^{-2}$ corresponds approximately to hail diameters $\geq 20 \text{ mm}$. In this study, we computed the GRPL every 15 min from CTRL2 output and used the hourly maximum field for analysis.

Significant hail parameter — SHIP. Another hail proxy, a significant hail parameter (SHIP; https://www.spc.noaa.gov/exper/mesoanalysis/help/help_sigh.html) is defined by NOAA Storm Prediction Center and is used for large hail prediction and in many studies in the US (Prein and Holland, 2018; Tang et al., 2019; Taszarek et al., 2021). The parameter is calculated at each grid point according to the following equation:

$$SHIP = \frac{MUCAPE \times MR \times LR \times (-T_{500\text{hPa}}) \times S06}{42,000,000} \quad (4.2)$$

where MUCAPE is the most unstable CAPE calculated in the lowest 300 hPa of the atmosphere, MR is the mixing ratio of the most unstable parcel and confined to 11–13.6 g kg^{-1} , S06 is wind shear calculated in the lowest 6 km of the atmosphere confined to 7–27 m s^{-1} , and LR is the 500–700 hPa temperature lapse rate. We should note that the 500 hPa temperature is set to -5.5 when any warmer values than that occur. In addition, the SHIP will be adjusted under three conditions: (1) if $MUCAPE < 1300 \text{ J kg}^{-1}$, then $SHIP = SHIP \times (MUCAPE/1300)$; (2) if $LR < 5.8 \text{ K km}^{-1}$, then $SHIP = SHIP \times (LR/5.8)$; and (3) if $H0 < 2400 \text{ m}$, then $SHIP = SHIP \times (H0/2400)$. The SHIP parameter is calculated based on hourly output fields.

Lightning

Lightning potential index — LPI. Lightning potential index (LPI, J kg^{-1}) (Yair et al., 2010; Lynn and Yair, 2010) is a measure of lightning charge potential. It considers the main charging zone (0°C to -20°C), where the non-inductive mechanism is most efficient. The same as in our previous study (Cui et al., 2023), we use the LPI version

modified by [Brisson et al. \(2021\)](#) to prevent spurious signals due to deep orographic wave clouds. The LPI is thus calculated as follows:

$$LPI = f_1 f_2 \frac{1}{H_{-20^\circ\text{C}} - H_{0^\circ\text{C}}} \int_{H_{0^\circ\text{C}}}^{H_{-20^\circ\text{C}}} \varepsilon w^2 g_{(w)} dz \quad (4.3)$$

where $q_L = q_c + q_r$ and $q_F = q_g \left(\frac{\sqrt{q_i q_g}}{q_i + q_g} + \frac{\sqrt{q_s q_g}}{q_s + q_g} \right)$ refers to the sum of the liquid species and frozen hydrometeors, respectively. The dimensionless scaling factor for the cloud draft $\varepsilon = \frac{2(q_L q_F)^{0.5}}{q_L + q_F}$ has a value between 0 and 1, and reaches the maximum when q_L and q_F are equal. LPI is activated every 15 min, and the output is saved as the hourly maximum. More detailed information on LPI can be found in [Brisson et al. \(2021\)](#), and more information on the settings used here in [Cui et al. \(2023\)](#).

Cloud top height — CTH. One of the lightning proxies used in this study for inter-comparison with LPI is based on cloud top height. It is a commonly used proxy for the calculation of total lightning flashes and considers the relationship between the intensity of updraft velocity and cloud top height. Since continental and maritime thunderstorms are different, two equations are used for the calculation ([Price and Rind, 1992](#)). Thus, the flash frequency over land (F_{land}) and sea (F_{ocean}) is calculated following equations:

$$F_{\text{land}} = 3.44 \times 10^{-5} H^{4.9} \quad (4.4)$$

$$F_{\text{ocean}} = 6.2 \times 10^{-4} H^{1.73}. \quad (4.5)$$

H refers to the cloud top height (km) and it is defined as the simulated 20 dBZ reflectivity top used in WRF ([Wong et al., 2013](#)). The CTH is calculated based on 15-min model output and saved as the hourly maximum.

Convective precipitation — PRECON. The cloud-to-ground flashes can be calculated as a polynomial function of convective precipitation following [Allen and Pickering \(2002\)](#):

$$F_{\text{CG}} = \frac{\Delta x \Delta y}{A} (a + bP + cP^2 + dP^3 + eP^4) \quad (4.6)$$

where P is the grid cell convective precipitation. The polynomial coefficients $a - e$ are different over land and ocean and are as follows: for land 3.75×10^{-2} , -4.76×10^{-2} , 5.41×10^{-3} , 3.21×10^{-4} and -2.93×10^{-6} , while the corresponding coefficients for the ocean are 5.23×10^{-2} , -4.80×10^{-2} , 5.45×10^{-3} , 3.68×10^{-5} and -2.42×10^{-7} , respectively. Land points are defined as grid points where the land fraction is greater or equal to 0.25. Since the current function by default predicts cloud-to-ground lightning flash rate, we apply the [Price and Rind \(1993\)](#) partitioning scheme based on the cold cloud depth to get the total lightning flash rate.

4.2.3 Observations

Meteorological observations

Besides the 0.25° ERA5 ([Hersbach et al., 2020](#)) reanalysis, we use several observational datasets for validation. We use the 0.1° E-OBS data (version 28.0, [Cornes et al. \(2018\)](#)) for the evaluation of daily mean, minimum, and maximum temperature, and

precipitation. The E-OBS data is daily gridded data that covers the entire European continent (land only) and is obtained through interpolation of station data.

Precipitation observations

To account for observational uncertainty, we use the high-resolution Pan-Alpine EURO4M-APGD precipitation data (Isotta et al., 2014) in addition to ERA5 and E-OBS. APGD is obtained from rain-gauge stations across the greater Alpine region with daily temporal and 5 km spatial resolution. The APGD data covers the period of 1971–2008, so here for the evaluation we consider the more recent 10-year period of 1999–2008.

In addition, the Final Run of Integrated Multi-satellite Retrievals for Global Precipitation Measurement (IMERG V07, Huffman et al. (2023)) dataset is used to validate the simulated sub-daily precipitation. This dataset has a spatial grid spacing of 0.1° and is available at half-hourly (30 min) time-frequency with the unit of mm h^{-1} . Hourly estimates are derived by accumulate precipitation at 30 min intervals and deviding the result by 2. The IMERG data covers the entire analysis domain and simulation period (2009–2018), including oceans that lack in-situ precipitation-measuring instruments.

Hail observations

Two radar-based hail algorithms (Nisi et al., 2016) are used to analyze hail characteristics over the Alpine region (Fig. 4.1): probability of hail (POH) and maximum expected severe hail size (MESHS). Both products rely on the third-generation C-band radars (in operation since 2009) and the fourth-generation dual-polarization radars (in operation since 2012). The algorithms require information on the freezing-level height (H0) provided by the MeteoSwiss weather forecasts using COSMO. POH considers the vertical distance between the highest radar reflectivity of at least 45 dBZ and H0 (Waldvogel et al., 1979; Foote et al., 2005), while MESHS considers the vertical distance between 50 dBZ and H0 (Treloar, 1998; Joe et al., 2004). Both products have a spatial resolution of 1 km on the Cartesian grid and a temporal resolution of 5 min. As validated against insurance claims (Nisi et al., 2016), a hail day is defined when $\text{POH} > 80\%$ between 06 UTC and 06 UTC of the following day. Using crowdsourced reports collected by MeteoSwiss, Barras et al. (2019) found POH/MESHS are defined too restrictively, therefore some hail events might be missed by the algorithms. The POH and MESH data are available during the entire simulation period and are as such taken into the analysis.

For the evaluation of hail over the eastern coast of the Adriatic Sea and Croatia, we use unique station-based hail observation (Fig. 4.1 right) collected and digitalized from 199 stations across Croatia by the Croatian Meteorological and Hydrological Service (DHMZ) (Blašković et al., 2023). Hail occurrence was observed by professional and trained personnel and subjected to quality control during the digitalization process.

Additionally, we use a hailpad dataset over the plain of Friuli Venezia Giulia (FVG), situated over the north-easternmost part of Italy with the Alps to the north and the Adriatic Sea to the south (Fig. 4.1). This network is coordinated by the regional meteorological service Osservatorio Meteorologico Regionale (OSMER) and Restione Rischì Naturali (GRN)–Agenzia Regionale per la Protezione dell’Ambiente (ARPA) FVG and in

operation since 1988 (Giaiotti et al. (2003), <https://www.meteo.fvg.it/grandine.php>). The volunteers from 360 hailpad stations have reported the number of total panels, average median diameter, maximum diameter, average densities, and accumulated kinetic energy flux of all hit panels (Manzato et al., 2022a). We use the daily hail database (0-24 UTC) of four macro-areas from April–September 1988–2016 as described in Manzato et al. (2022a). Followed by Giaiotti et al. (2003), a hail day on the FVG plain is defined as a day in which at least one hailpad is hit by a hailstone.

Lightning observations

LPI and lightning proxies are evaluated against lightning detection network data (LINET), which covers large parts of Europe (see Fig. 4.1 and Betz et al. (2009)). LINET has an average location accuracy of approximately 150 m, and it has the capability to detect the total number and location of lightning strikes, where cloud-to-ground strokes, in-cloud, and cloud-to-cloud discharges are included (Betz et al., 2009). The LINET lightning data is taken from Jelić et al. (2021), where it has been aggregated to hourly temporal resolution and a spatial grid spacing of 3 km. For the evaluation against simulations with a different resolution, we employ the lightning flash density (fl. $\text{km}^{-2} \text{h}^{-1}$), which is calculated as the total lightning divided by the area of each grid box.

4.2.4 Analysis methods

We analyze the spatial distribution of precipitation through the following indices: mean precipitation, wet day frequency, mean wet day intensity, and 99th percentiles of daily precipitation with all events (wet and dry, following Schär et al. (2016)). A wet day (hour) is defined as a day (hour) with precipitation larger than 1 mm/day (0.1 mm/h) (see e.g., Ban et al. (2014)).

In order to compare the number of hail days from HAILCAST and proxies with observations, we define a threshold of a hail day for each proxy. As shown in Fig. 4.2, the calculation of the threshold includes the calculation of the root-mean-square error (RMSE) between the model data and station observations in Croatia. From the model data, we take the nearest corresponding model grid point for each station. The threshold is then chosen as the one with the smallest RMSE, such that the number of hail days in the model is close to the station-based observations. The term hail day used hereafter in this study refers to the exceedance of that threshold on a given day. The results for different thresholds for HAILCAST, UH25, GRPL, and SHIP are provided in the Supporting Information, where the green color indicates the chosen threshold for each of the indicators. The POH dataset is not utilized since it provides probability estimation. Nevertheless, we applied different thresholds over the Alpine region, and compared them against POH. The results are similar compared to the thresholds gained from station-based observations (see Supporting Information).

For lightning, to account for different resolutions from the model and observations and resolution-dependent proxies, we first convert them to the lightning flash density (fl. $\text{km}^{-2} \text{h}^{-1}$) as in observations. As illustrated in Fig. 4.2, we apply the empirical quantile mapping (EQM, Panofsky and Brier (1968); Gudmundsson et al. (2012)), such

that the simulated lightning potential is matched to the observed counterparts using a transfer function. To do so, first, we conservatively remap the lightning proxies in CTRL2 from the original 2.2 km grid to the 3 km grid of the LINET observations. We define a lightning day (hour) when at least 2 flashes in a grid cell within a given day (hour) have occurred.

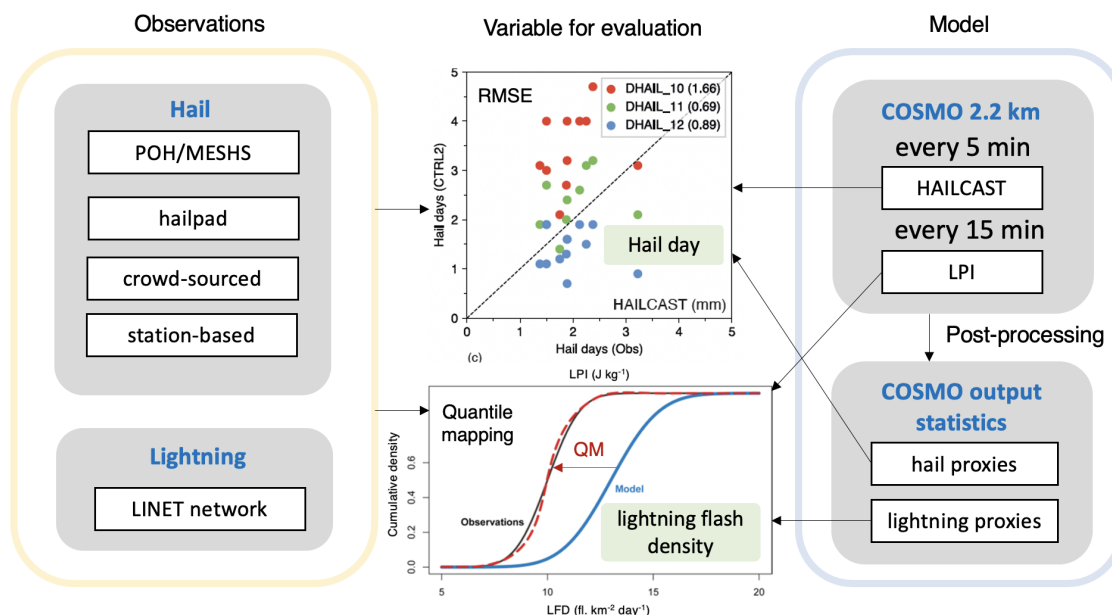


Figure 4.2: The workflow to get the number of hail days and lightning flash density for the evaluation of hail and lightning. For hail, we test different thresholds from COSMO HAILCAST and hail proxies, and select the number with the minimum RMSE. For lightning, we apply the quantile mapping to get the lightning flash density from LPI and lightning proxies.

For validation of diurnal cycles, we apply time smoothing with 3-hour moving windows ($x^t = \frac{1}{4}[x^{t-1} + 2x^t + x^{t+1}]$). The peak day of the year and the peak hour of the day for hail and lightning events are determined from the running mean with circular statistics (Taszarek et al., 2020a). The evaluation is confined to the radar domain with a 140 km radius for each radar site, enabling a comprehensive coverage of the domain with both hail and lightning observations. Furthermore, to conduct a further analysis across diverse topographic regions, we use subdomains over the Alpine region as delineated by the polygons defined in Raupach et al. (2021) and Feldmann et al. (2023). Over the Adriatic region, we consider sea/coastal, plains, and low mountains based on elevations following Manzato et al. (2022b). Detailed information is provided in the Table 4.1.

4.3 Results

4.3.1 Evaluation of temperature and precipitation

In this section, we first evaluate the surface temperature and precipitation against available observations. Multi-seasonal (April–September) mean daily, minimum and

maximum 2 m temperature from E-OBS, ERA5, CTRL12 and CTRL2, and their biases compared to E-OBS are shown in Fig. 4.3. Overall, a small cold bias in the mean temperature compared to E-OBS for both CTRL12 and CTRL2 simulations is found over the entire domain except for the Po Valley. This warm bias in summer over the Po Valley is not as large as with the previous version of the COSMO model (Ban et al., 2014). Montesarchio et al. (2014) relates it to possible underestimation of temperature in the E-OBS data and models' overestimation of summer temperature over this region. A small cold bias over the entire domain for the mean temperature is also the opposite of warm bias, which is enhanced in a higher resolution model simulated with a previous version of the COSMO model (Ban et al., 2014). Those differences might be due to the modified land surface scheme after Schlemmer et al. (2018) used in simulations here. The second and third rows in Fig. 4.3 display the multi-seasonal mean daily minimum and maximum 2 m temperature. Large parts of the domain show a warm bias of the daily minimum and a cold bias of the daily maximum. These results show that the model has a systematic bias in cold and warm extremes, and the diurnal temperature range in these simulations is underestimated.

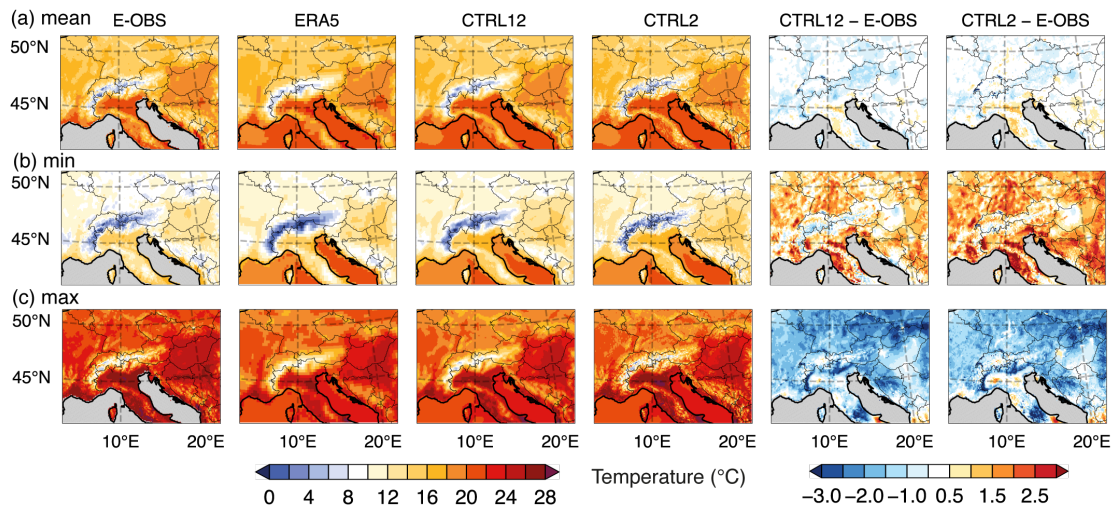


Figure 4.3: Evaluation of 2-meter temperature for the average of (a) daily mean, (b) daily minimum, and (c) daily maximum temperature from April to September in the period of 2009–2018. From left to right: E-OBS, ERA5, and COSMO 12 km and 2.2 km simulated and bias of two simulations compared to E-OBS. To account for elevation differences between the model and observations, the height correction was applied assuming a lapse rate of 0.65 K/100 m.

Last but not least, we should note that there is no big or systematic difference in the biases between CTRL12 and CTRL2 simulations. Even though it has been shown that the added value of higher resolution models for the simulation of the temperature is small (see e.g., Soares et al. (2022)). Small differences here between CTRL12 and CTRL2 simulations can also be explained by similarities in the setup, of which the most important would be the explicit treatment of deep convection.

The evaluation of daily precipitation is presented in Fig. 4.4, and it shows the daily

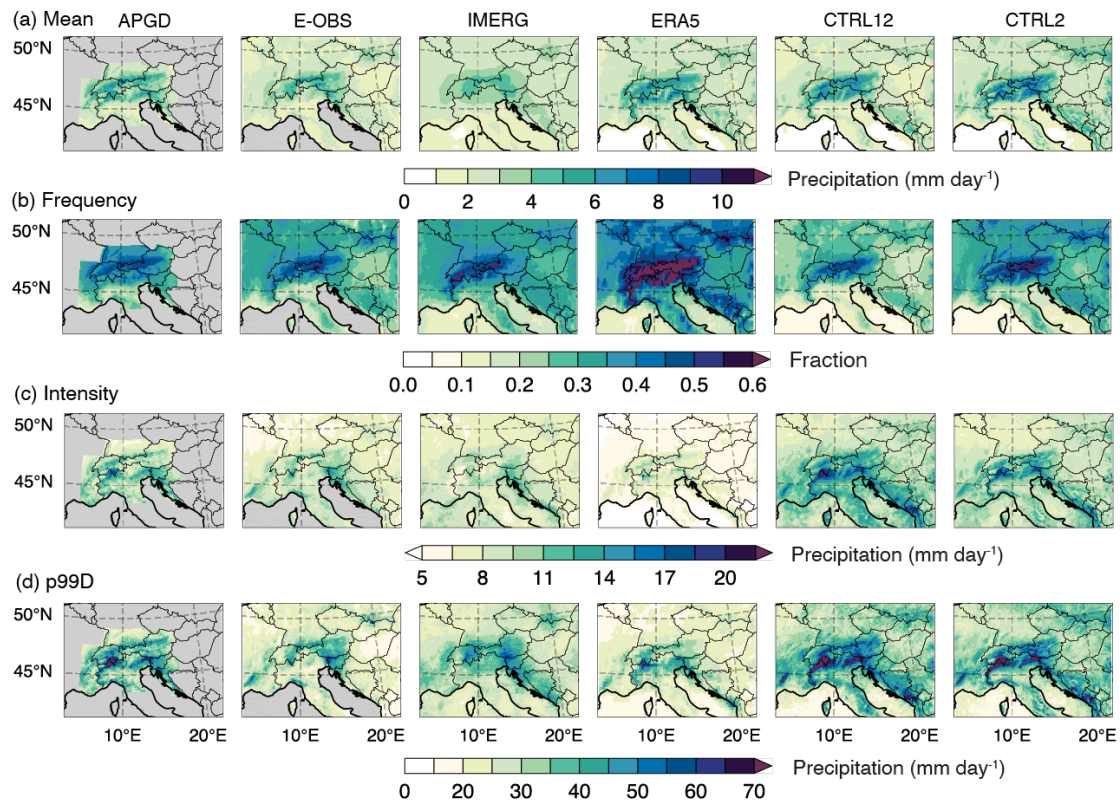


Figure 4.4: Evaluation of daily precipitation for (a) daily mean, (b) wet-day frequency, (c) wet-day intensity, and (d) heavy precipitation (p99D) in the period from April to September. From left to right: APGD (1999–2008), E-OBS, and IMERG observations, ERA5 reanalysis, and COSMO 12 km and 2.2 km simulations.

statistics of multi-seasonal precipitation, including mean precipitation, frequency, intensity, and heavy precipitation defined as the 99th percentile. The results show big differences in the observational datasets, especially for the heavy precipitation, where EOBS underestimates the intensity of it in comparison to APGD and IMERG. The reanalysis and driving ERA5 data tends to have higher wet-day frequency with lower intensity compared to observations, as also found by [Bandhauer et al. \(2021\)](#). In addition, it also underestimates the intensity of heavy precipitation. The two simulations, CTRL2 and CTRL12, represent the observed precipitation quite well, although some small differences exist. The most notable added value in comparison to the reanalysis data is a reduction of wet-day overestimation and heavy precipitation underestimation.

Even though we do not show it here, we should note that our high-resolution simulations also show benefits in representing hourly precipitation features, as already shown by many previous studies ([Ban et al., 2014, 2021](#); [Adinolfi et al., 2023](#)). As such, in the remaining part of the manuscript we focus on CTRL2 simulation and the evaluation of hail and lightning produced by proxies that rely on variables such as updrafts and which are better represented by high-resolution models ([Zeman et al., 2021](#)).

4.3.2 Evaluation of hail and lightning

4.3.2.1 Seasonal variations

Hail

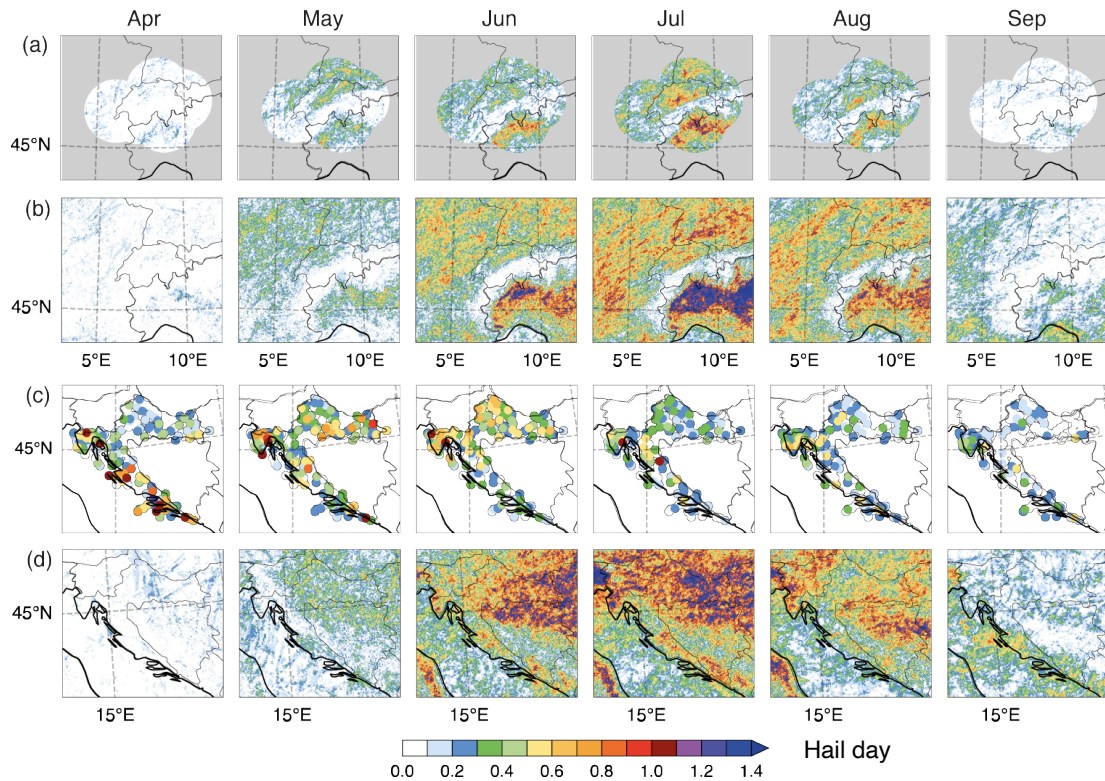


Figure 4.5: Monthly mean hail days obtained from (a) Swiss radar-based and (c) Croatian station-based observations, and COSMO HAILCAST over the (b) Alpine region and (d) over the Adriatic region. The radar observations cover the same period of 2009–2018 as COSMO simulations, while station observations in Croatia cover the period of 1989–2018.

The multi-seasonal cycle (April–September) of simulated hail days is compared against radar-derived observations over the Alpine region (Fig. 4.5a,b) and station-based records in Croatia (Fig. 4.5c,d). Over the Alpine region, the observed and simulated hail days are very small in April and September. The peak month for hail occurrence is in July, with relatively higher hail days in the Po Valley and the Swabian Jura. In August, the hail days decreased compared to July. In September, hail days significantly decrease in the Po Valley, while it is simulated near the coastlines of the Gulf of Genoa and the southern edge of the Massif Central in France. This is likely associated with the warmer sea and cooler air masses in autumn, providing favorable conditions for convection (Manzato, 2007).

Figure 4.6a,b shows the seasonal cycles across 6 different topographical subdomains over the Alpine region. The number of hail days over the south of the Alps is higher compared to the north, especially in June, July, and August. There is a significant in-

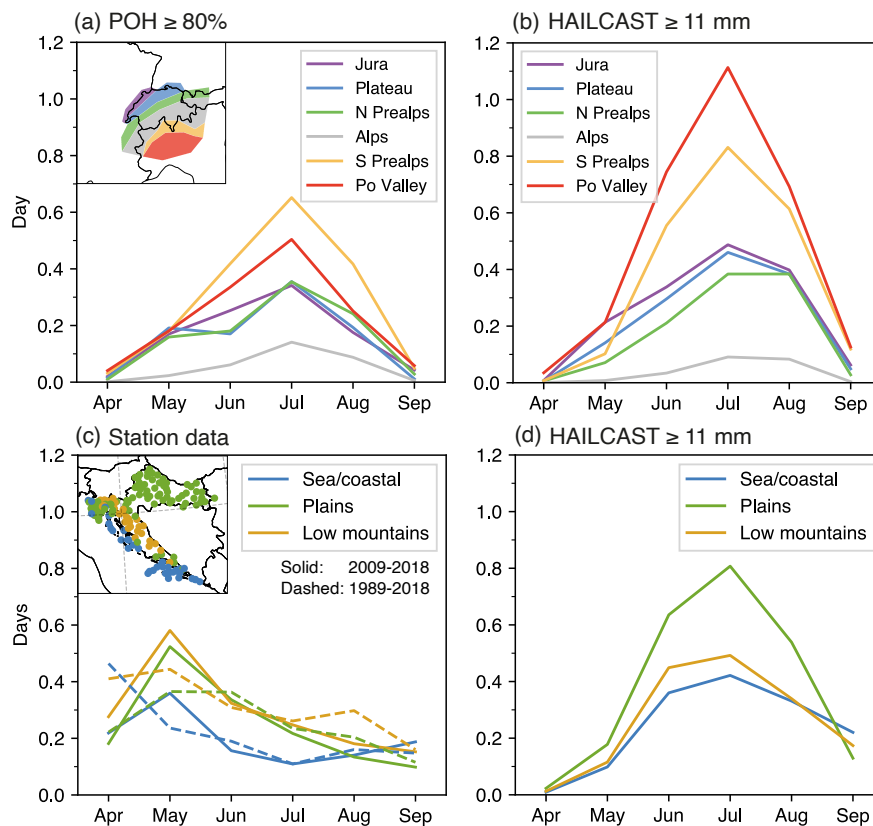


Figure 4.6: Seasonal cycle of hail day from (a) radar-based estimates and (b) HAILCAST over the Alpine region. (c) Station observations and (d) HAILCAST over the Adriatic region.

crease in hail days in June in the south of the Alps compared to the north. This can be attributed to the warm and moist conditions near the Mediterranean Sea, providing favorable conditions for severe storms to the south of the Alps (Nisi et al., 2016). The number of hail days over the Alpine ridge (gray) is the lowest among different subdomains, because lower moisture prevents the formation and organization of the storms over the Alpine main ridge. It is important to note that radar can only detect hail at higher altitudes (Nisi et al., 2016), and the melting process can impact the estimation of hail, especially in summer. Even so, HAILCAST overestimates the hail days in July and August over the south of the Alps compared to radar-based observations.

Over the eastern coast of the Adriatic Sea (Fig. 4.5c,d), we utilized the station observations in Croatia spanning the period of 2009–2018 (solid lines) and the extended time period of 1989–2018 (dashed lines) to have a time series long enough for climatological analysis. From the collected observations, the mean number of hail days is higher in the months of April, May and June. However, HAILCAST underestimates the number of hail days in April, where the coast was not well simulated. In July, HAILCAST overestimated the number of hail days over northeastern Croatia compared to the observations. In September, HAILCAST is able to simulate hail activities near the coast. To further illustrate the variations across different topography, we use 3 subdomains for analysis:

sea/coastal, plains, and low mountains based on elevation as outlined in [Manzato et al. \(2022b\)](#). Analyzing the station observations (Fig. 4.6c,d), the number of hail days over the sea/coastal exhibits a bimodal behavior from April to September, where the first peak in late spring is higher than the second peak in the early autumn. Over plains and lower mountain regions, the number of hail days is higher in May. Given the considerable computational resources required, it is crucial to note that the 10-year simulation period might not be representative of the average hail frequency over a much longer timeframe and severe convective storms exhibit spatial and temporal variabilities ([Piper et al., 2019](#)). Additionally, it is also important to acknowledge the uncertainties arising from observers and gaps in time series for some stations ([Jelić et al., 2020](#)). These factors need to be carefully considered when interpreting the simulation results and their real-world implications. In general, we conclude the HAILCAST failed to simulate hail in late spring and overestimated the number of hail days in July and August.

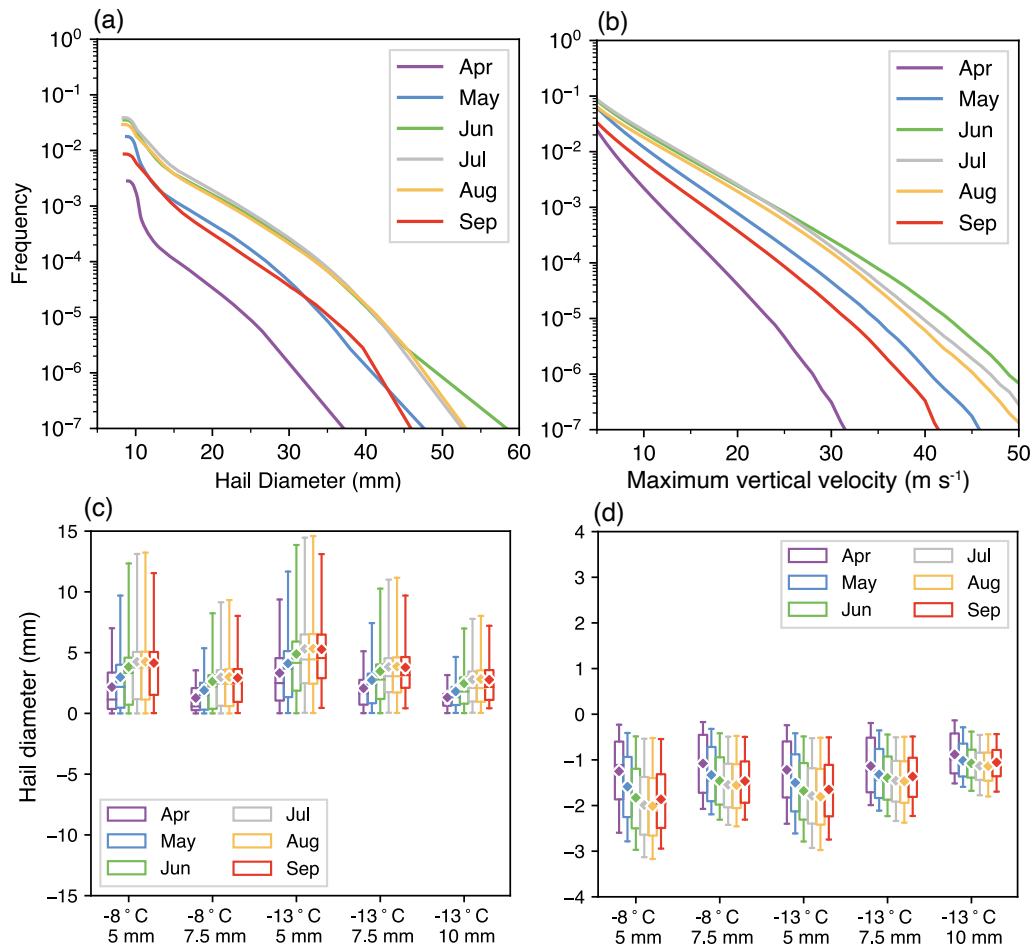


Figure 4.7: Cumulative distribution of (a) HAILCAST simulated daily maximum hail diameter, and (b) daily maximum vertical velocity from April to September. (c) Increase in hail size before hailstone leaves the cloud, and (d) decrease in hail size due to the melting process for 5 different hail embryos from April to September.

Although the model cannot be expected to produce accurate hail sizes, especially

for very large hailstones (Adams-Selin et al., 2019). It is interesting to point out that, the simulated hail frequency over the whole analysis domain in April is the smallest, followed by May and September, and higher in June, July and August (Fig. 4.7a). These monthly distributions align with earlier hailpad observations in FVG (see Fig. 2 in Girotti et al. (2001)). In June, HAILCAST simulates a higher frequency of very large hailstones (e.g., >50 mm), and this is also noted by observational studies (e.g., Kahraman et al. (2015) and Blašković et al. (2023)). Higher maximum vertical velocity in summer seasons could potentially lead to a higher increase in hailstone size (Fig. 4.7b,c). In April, the maximum vertical velocity is the smallest, therefore a smaller frequency of large hailstones. However, the melting process could contribute to the decrease in hail size. As shown in Fig. 4.7d, the melting size is determined by calculating the difference once a hailstone exits the cloud and when it reaches the ground. The melting is stronger in July and August, consequently resulting in a lower frequency of very large hailstones.

Lightning

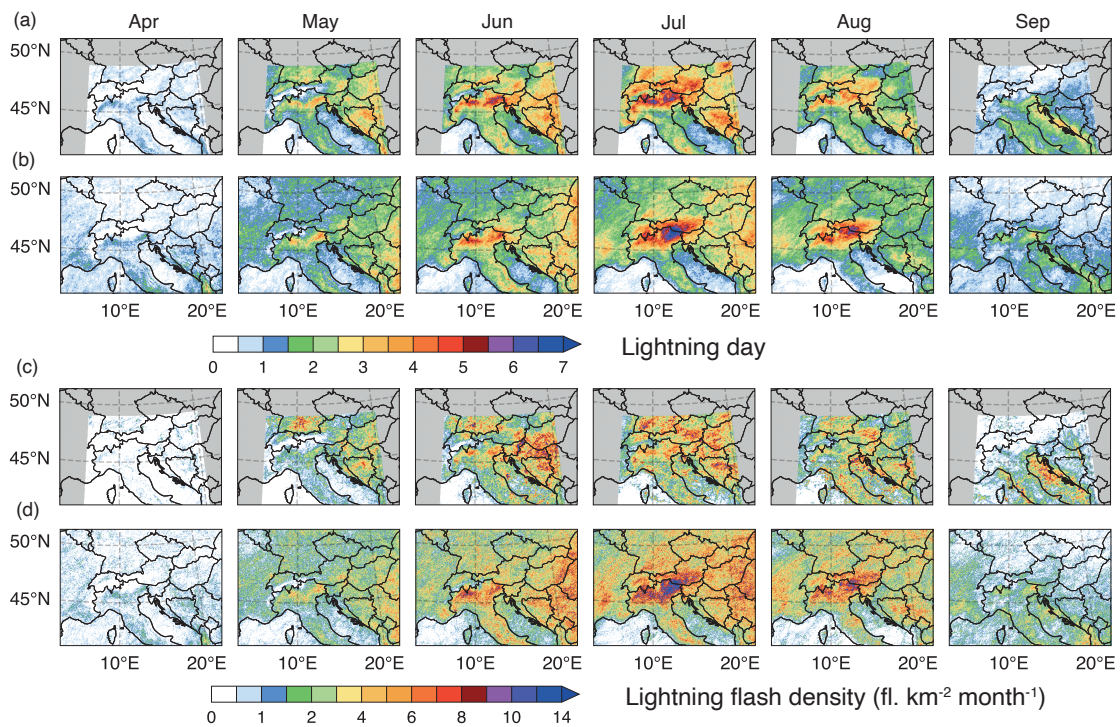


Figure 4.8: (a,b) Mean lightning day and (c,d) lightning flash density over the analysis domain from April to September (2009–2018) from (a,c) LINET observations and (b,d) LPI.

Simulated lightning days (Fig. 4.8a,b) and lightning flash density (Fig. 4.8c,d) are compared against LINET observations. There are a higher number of days with lightning compared to hail. Both observed and simulated lightning frequency and density in April are relatively low. The lightning days and density increased significantly in May and June, reaching the maximum in July. In September, lightning activity appears

along the coastlines. Overall, LPI is able to reproduce the seasonal cycle of lightning days. However, LPI overestimates the number of lightning days and lightning density over the FVG region in northeastern Italy, especially in July and August. The FVG region exhibits the highest lightning density as a result of mature storms initiated from the west or developing under the prevailing upper-level flow that propagated into this region (Manzato et al., 2022b).

Figure 4.9a,b depicts the multi-seasonal mean lightning flash density across different subdomains over the Alpine region. The peak lightning activity is observed and simulated in July for all subdomains. The highest lightning flash density is to the south Prealps, which is the local maximum of convection initiation as demonstrated by Manzato et al. (2022b). The south of the Alps displays an earlier commencement of intense lightning activity in June compared to the north of the Alps. Moreover, the Alpine ridge shows the latest onset of intense lightning activity compared to other subdomains. Notably, unlike hail, the Alps exhibit a comparable lightning flash density to that of the Jura subdomain during the peak month in July.

Over the Adriatic region (Fig. 4.9c,d), the observed peak month of lightning flash density is in June over the plain, and August over the mountain. While over the sea/-coastal region, the lightning activity gradually increased from late spring, though with a slight decrease in summer, attained the highest intensity in September over the simulated period of April to September. In September, the lightning activity near the coast surpasses the plain and mountain regions. The simulated decrease in August could be attributed to the high air temperatures with less instability, which in turn hinders the development of severe convective storms. It should be noted that this does not imply September is the peak month of lightning throughout the year. In fact, the summer season constitutes the period of reduced lightning activity near the coast, while lightning becomes more frequent during winter months (Kotroni and Lagouvardos, 2008), which is beyond the scope of this study.

4.3.3.2 Diurnal variations

Hail

We use radar-based and station records to evaluate the diurnal cycle. Over the Alpine region (Fig. 4.10a,b), the peak hour is around 16 UTC in the afternoon, and the minimum appears in the early morning. The Swabian Jura observes the earliest peak among other subdomains. The reason is that many hailstorms over the Alpine region are associated with cold fronts, and typically approach this region from the northwest (Schemm et al., 2016). To the south of the Alps, the hail frequency is higher during the late afternoon and evening hours compared to the subdomains to the north of the Alps. In the south Prealps, there is a second peak between 00 and 04 UTC. This nighttime peak to the south of the Alps can be attributed to the thermally driven orographic circulation called “Alpine pumping” (e.g., Langhans et al. (2013); Heim et al. (2020)). The mountain-plain wind system evolves during the day – from the plains to the Alps during daytime, and conversely, from the Alps to the valleys during nighttime (Weissmann et al., 2005). It can produce local convergences that promote convection. The Alps subdomain with the

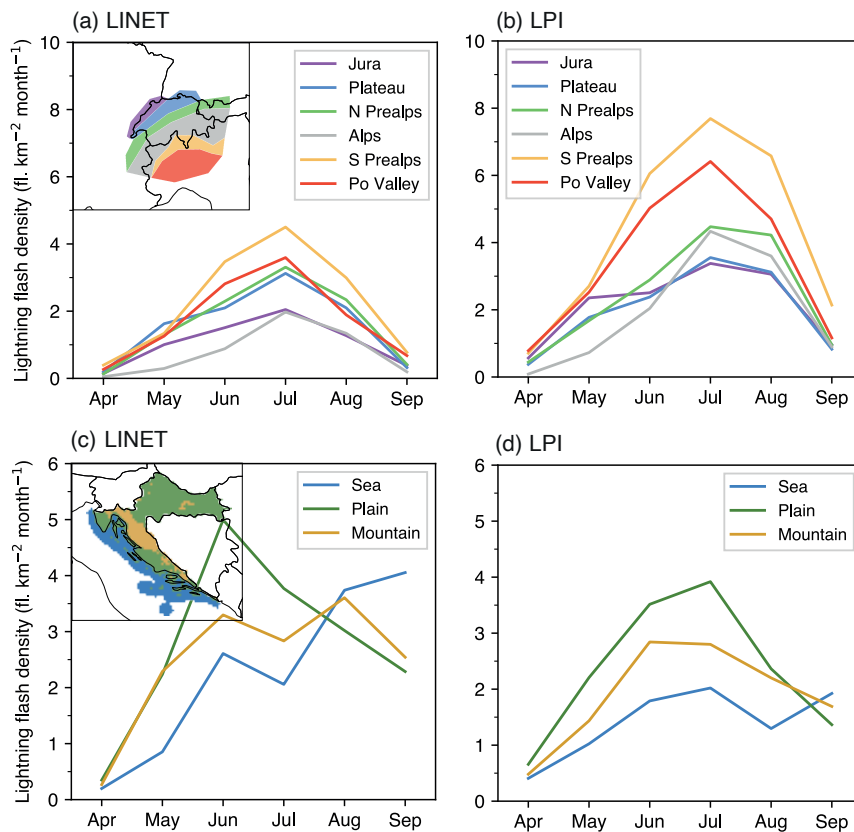


Figure 4.9: Mean lightning flash density over the Alpine (upper panels) and Adriatic (bottom panels) region from April to September (2009–2018) from LINET observations and LPI.

highest elevation experiences a less pronounced peak in the afternoon and has relatively low occurrences of hail. Overall, HAILCAST is able to reproduce the characteristics of the diurnal cycle over the Alpine region, however, it tends to overestimate the hail frequency over the Po Valley.

Over the Adriatic region (Fig. 4.10c,d), the diurnal cycle of hail frequency exhibits variations across the coastal, plains and mountainous regions. In the continental region, the hail frequency peaks around midday over the low mountains and in the afternoon over the plains. Near the coast, the observed diurnal cycle is characterized by a first peak occurring in the early morning hours between 04 to 08 UTC, followed by the second and third peaks at approximately 12 and 18 UTC. Compared to the station observations, HAILCAST is able to reproduce the diurnal cycle over the plain and low mountains. The first and third peaks near the coast are captured by HAILCAST, although it simulates a lower frequency during midday.

Lightning

Figure 4.11a,b shows the diurnal cycle of mean lightning flash density over the Alpine region, characterized by a peak in the afternoon and a minimum in the early

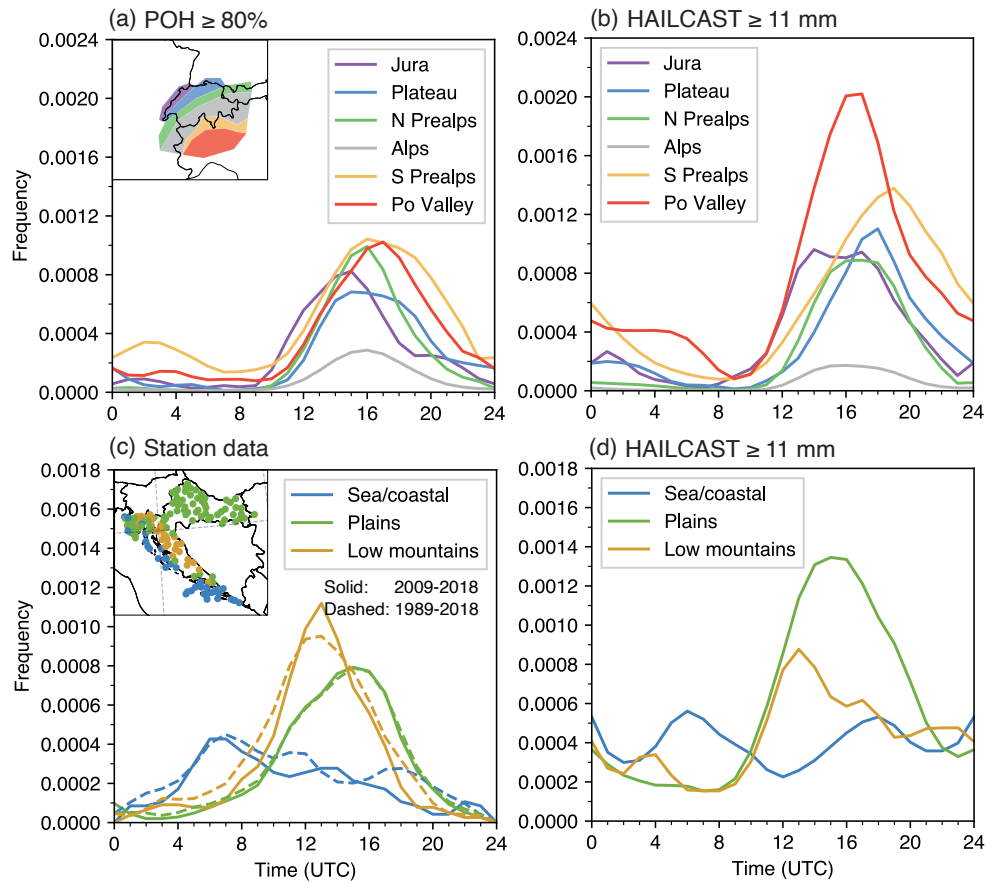


Figure 4.10: Diurnal cycle of hail hour frequency using (a,b) radar-based and (c,d) station observations from April to September.

morning. Over the Alps and Jura mountain, the lightning flash density is lower in the late afternoon compared to other subdomains. The mountain-to-plain winds transport moisture from elevated regions to the surrounding plains and can be favorable for evening and nighttime convection [Rampanelli et al. \(2004\)](#). Overall, LPI is able to reproduce the diurnal cycle, though it tends to overestimate the lightning flash density over the south of the Alps, especially at midnight.

Over the Adriatic region (Fig. 4.11c,d), the lightning flash density shows a similar diurnal cycle compared to hail frequency (Fig. 4.10c,d). Overall, LPI is able to reproduce the diurnal cycle compared to LINET observations. Nevertheless, it tends to underestimate the first peak in the early morning near the coastal region as well as the midday peak over the mountains.

4.3.3 Comparison of different proxies

Hail

We first compare the spatial distribution of hail days using HAILCAST and hail surrogate proxies. Figure 4.12 presents the mean number of hail days, the peak month,

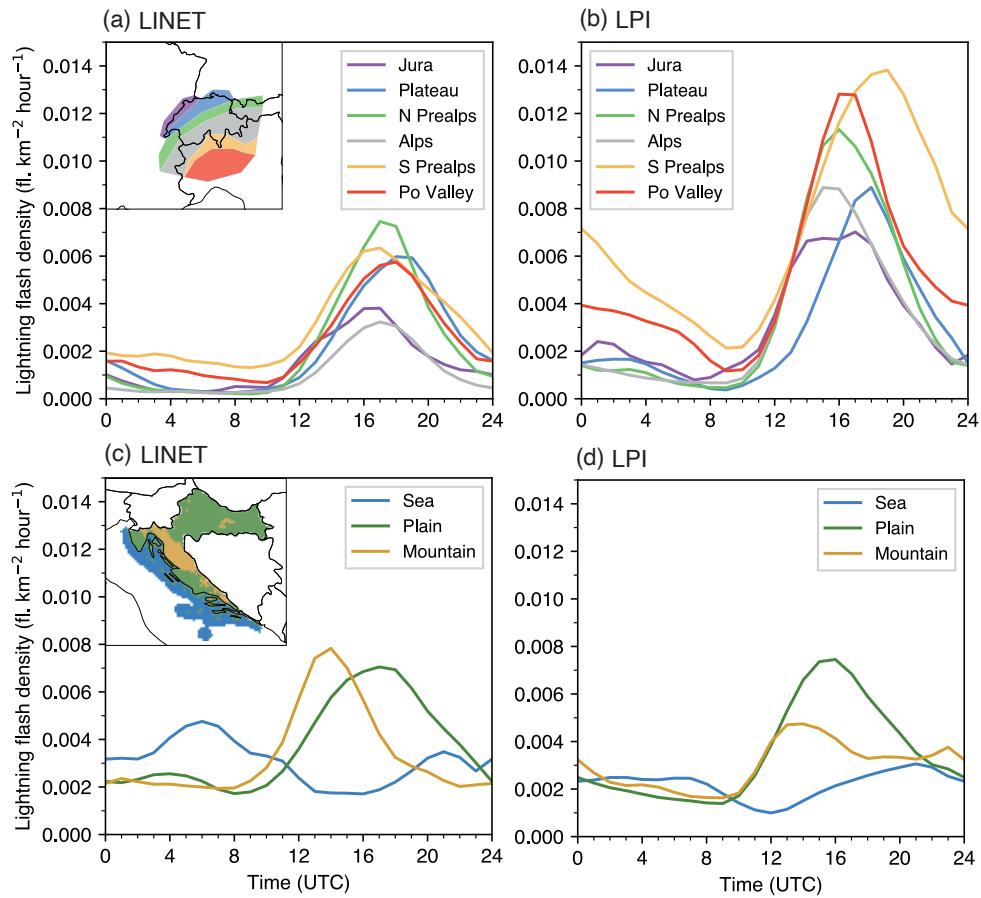


Figure 4.11: Diurnal cycle of lightning flash density over the Alpine (upper panels) and Adriatic region (bottom panels) from LINET (left) and LPI (right) from April to September.

and the peak hour of hail frequency from April to September. The highest number of hail days, up to 4 days per convective season, is found to the south of the Alps, with the exception of SHIP. Conversely, the lowest frequency of hail days is observed over the crest of the Alps and the Mediterranean Sea. It should be noted that SHIP, an environmental proxy derived for the US, is likely unsuitable for Europe. The number of hail days can be unrealistically high if we adopt the suggested threshold $SHIP > 1$, especially over the Adriatic Sea. When comparing the results of UH25 and GRPL to HAILCAST, we find that they yield similar outcomes. However, these surrogate proxies display a lower occurrence of hail days over the Apennines and eastern Europe. Additionally, UH25 exhibits a higher number of hail days over northeastern Italy.

The peak hour over the south of the Alpine region is around an hour later compared to the north. Over the eastern coast of the Adriatic Sea, the peak occurs in the middle of the day (with several exceptions during the night hours), while over the continental part, it occurs later in the afternoon. Overall, these patterns of hail are well reproduced by HAILCAST, especially for the patterns of hail days and peak hours, while some differences exist for the peak month. For example, the majority of the stations in Croatia

indicated May as a peak month, while the model produces the peak around June/July.

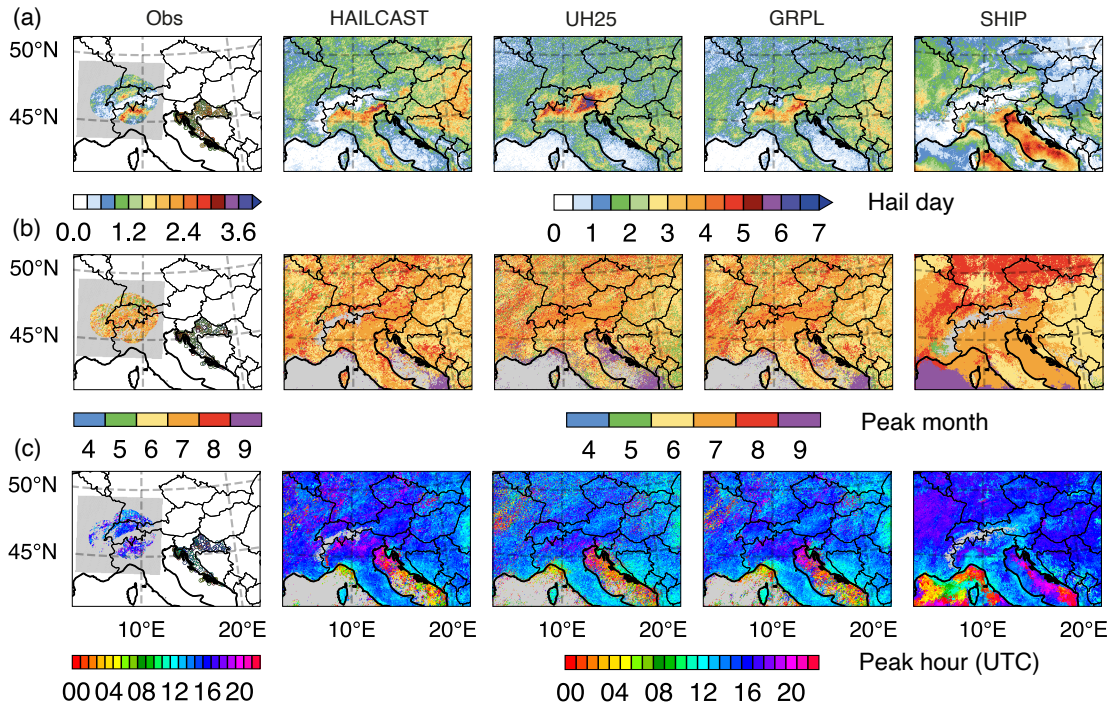


Figure 4.12: Evaluation of hail for (a) the mean number of hail days, (b) the peak month, and (c) the peak hour as an average in the period from April to September during all 10 simulated years (2009–2018). Shown are (from left to right) POH from Alpine radar-based observations, COSMO-HAILCAST results, and UH25, GRPL, and SHIP proxies calculated using CTRL2 data. Mean hail day/hour smaller than 1 is not taken into account.

Lightning

Figure 4.13a illustrates the spatial distribution of lightning days, comparing the results obtained from LPI and several lightning parameterizations against LINET observations. The south of the Alps exhibits the highest frequency of above 20 lightning days from April to September, which is well captured in all considered lightning parameterizations. While discrepancies arise over eastern Europe, particularly over the Carpathians in the Panonian Basin. In this area, CTH tends to overestimate the lightning days while PRECON underestimates them. Also, CTH underestimates the lightning days over the sea, which could be due to the inconsistent assumptions in the lightning parameterization (Boccippio, 2002).

When we compared the spatial distribution of peak hours (Fig. 4.13c), it became evident that the LPI produces the best results. While LPI and CTH accurately represent the nighttime peak near the coastal region, nevertheless, during daytime over the continental regions, the peak hour in CTH appears to be slightly earlier, especially over eastern Europe. The cluttered pattern shown in PRECON is due to heavy precipitation,

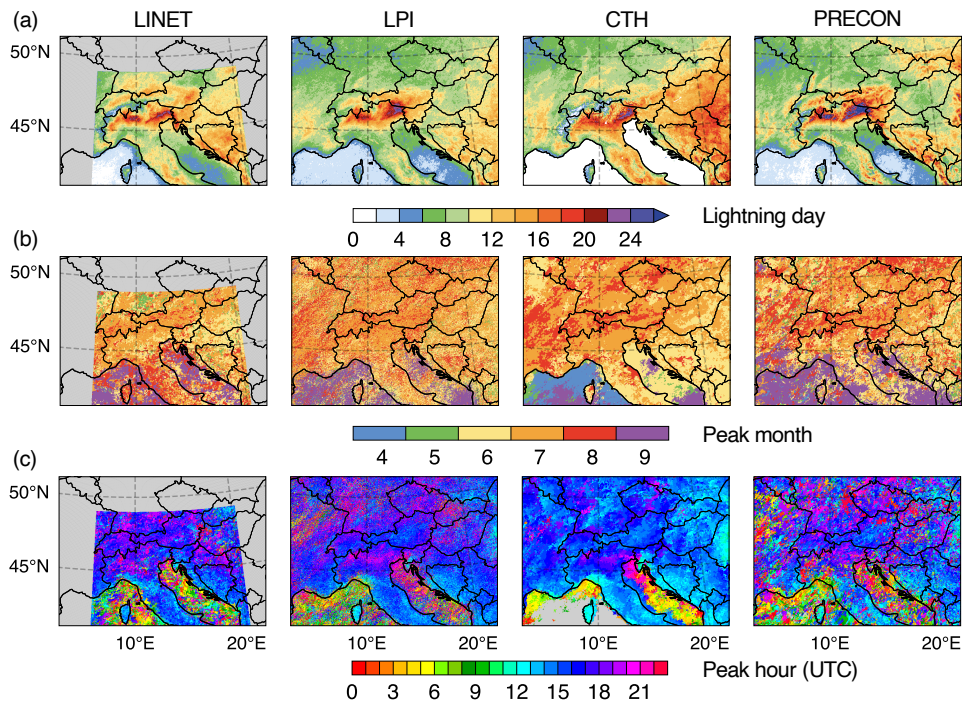


Figure 4.13: Evaluation of lightning through (a) mean number of lightning days, (b) peak month, and (c) peak hour of lightning flash density from April to September during all 10 simulated years (2009–2018). Shown are (from left to right) LINET observations, COSMO-LPI results, and CTH and PRECON proxies calculated using CTRL2 data.

which does not necessarily accompany lightning activity. In summary, LPI demonstrates the closest results compared to the LINET observations.

Skill assessment and discussions

To quantitatively evaluate the performance of hail and lightning proxies, we employ the performance diagram commonly applied for rare events, as introduced by Roebber (2009). It considers the probability of detection (POD), false alarm ratio (FAR), critical success index (CSI), and frequency bias:

$$POD = a/(a + c) \quad (4.7)$$

$$FAR = b/(a + b) \quad (4.8)$$

$$bias = (a + b)/(a + c) = POD/(1 - FAR) \quad (4.9)$$

$$CSI = a/(a + b + c) \quad (4.10)$$

where a, b, c , and d are the number of hits, false alarms, misses, and correct negatives. The performance is the best with a CSI equal to 1, when the POD is large and the FAR is small. As shown in Fig. 4.14, the combination of POD, FAR and CSI for hail and lightning over the radar-covered domain and LINET-covered domain are evaluated during 2009–2018. Days without matched pairs are excluded to prevent penalizing where

the model failed to predict convection, for example, hail simulated where no hail was observed, resulting in a POD of 0 and FAR of 1. From the diagram, HAILCAST achieves the highest CSI, while UH25 and GRPL show lower POD and higher FAR. On the other hand, LPI and CTH show similar skills, whereas CTH shows slightly better results.

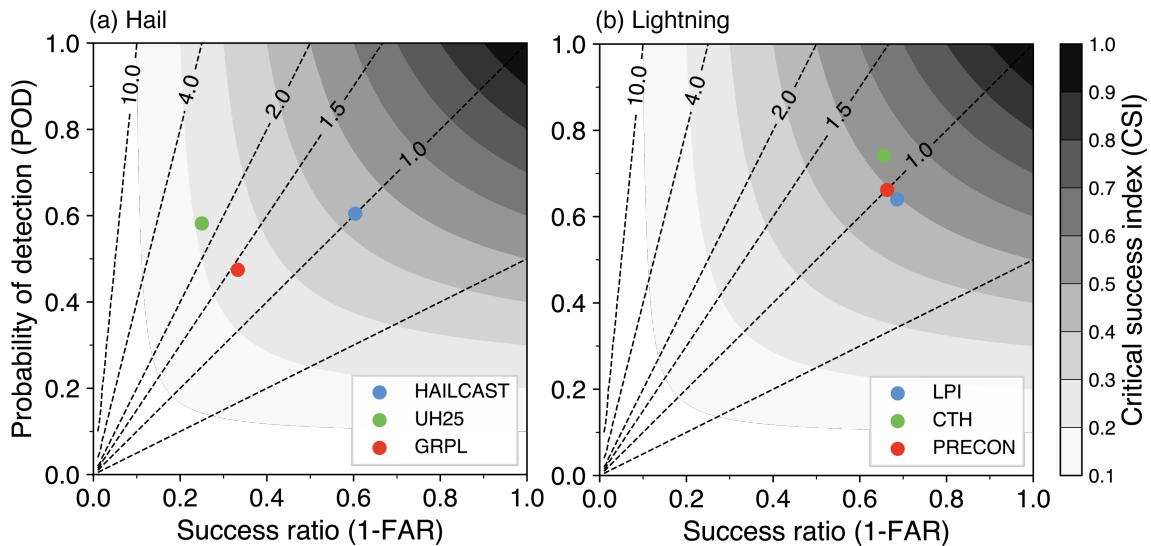


Figure 4.14: Performance diagram of daily (a) hail and (b) lightning that evaluated over the radar-covered domain and LINET-covered domain. Different colors indicate different proxies, where different distances are considered when evaluated against observations. The shaded gray contours indicate the CSI, and the dashed lines are the frequency bias.

To provide a more comprehensive depiction of the storm environment related to hail and lightning and understand the behavior of different proxies, we have selected several predictor variables, and conducted an analysis of their conditional probabilities with respect to hail sizes and LPI (Fig. 4.15). The hail size and lightning intensity are larger with increasing vertical velocity by design. However, for 0-6km vertical shear, they both show similar behavior as climatology, meaning no significant preference for larger hailstones under a strong shear environment. This outcome may be attributed to a couple of factors. Firstly, it's possible that neither of these diagnostics accounts for wind shear effects. Secondly, it's worth noting that Europe exhibits a weaker shear regime in comparison to the United States (Taszarek et al., 2020b). Consequently, SHIP appears to yield less accurate results in Europe. In such instances, e.g., Mohr et al. (2015) proposed a hail logistic hail model, taking daily minimum temperature into account. From our analysis, larger hailstones tend to be associated with higher daily minimum temperature (Fig. 4.15e). These findings underscore that variables that are considered as environmental proxies can be important when accessing hail and lightning phenomena in different regions. In such sense, HAILCAST and LPI can be more beneficial, as they are embedded in high-resolution models based on a more realistic physical environment.

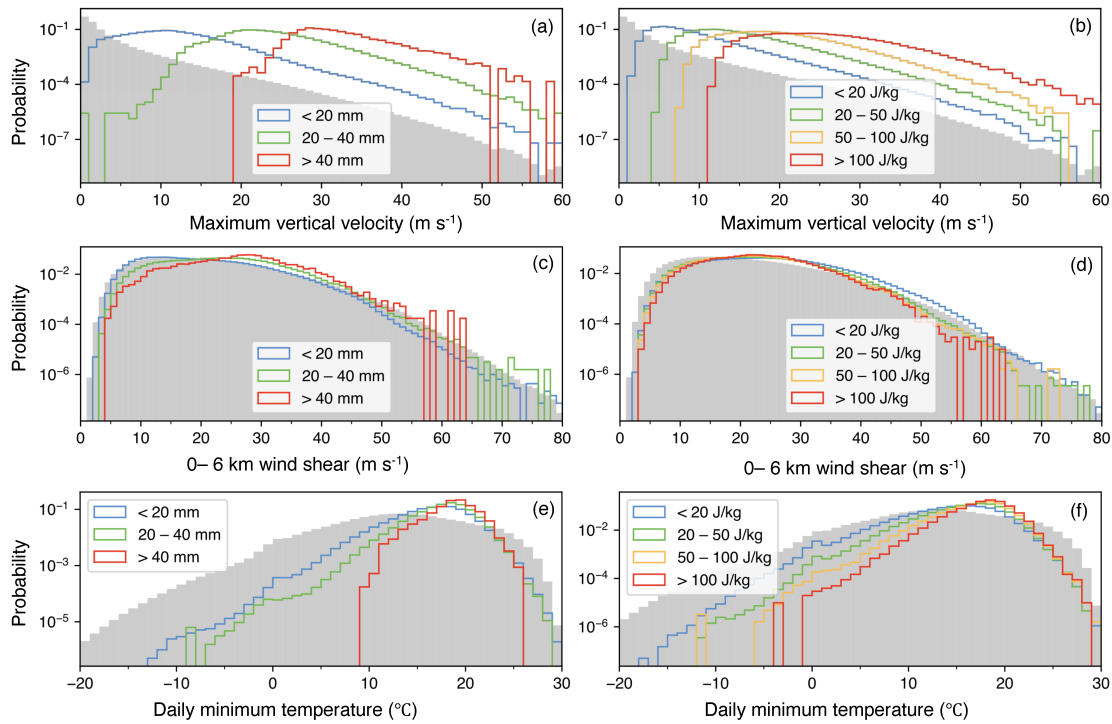


Figure 4.15: Environmental conditions for hail (left panels) and lightning (right panels). The daily climatological probability distribution for each variable from 2009 to 2018 is indicated in shaded gray. The conditional probability for different hail sizes and LPI are indicated in different colors.

4.4 Conclusions

In this study, we conducted decade-long (2009–2018) multi-seasonal (April–September) km-scale simulations over the Alpine-Adriatic region. In addition to the HAILCAST and LPI diagnostics, we compared several widely used hail and lightning proxies against available observations. This enables us not only to assess their performance but also to examine the climatologies over different topographic regions.

The first part of the paper focuses on the evaluation of simulated hail and lightning characteristics against observations over different topographic subdomains over the Alpine and Adriatic regions. From observations and simulations, the south of the Alps shows an earlier onset of hail season and extended diurnal cycle to the late evening compared to the north. Also, the south Prealps exhibits the highest lightning flash density in comparison to other subdomains. Over the Adriatic region, the seasonal and diurnal cycle behave differently across the coastal, plains and mountains. This is due to the temperature contrast of land and sea near the coastal region. Furthermore, the simulated hail sizes have a higher frequency in June. This could be attributed to the stronger simulated updrafts in June and stronger melting in summer. This result is in line with previous hailpad observations (e.g., Blašković et al. (2023)).

Furthermore, to illustrate the added value of physically based diagnostics, we com-

pare HAILCAST and LPI against several widely used surrogate proxies calculated from the model output. They are able to reproduce the spatial distributions except for SHIP. Nonetheless, it is important to acknowledge that HAILCAST and radar-based observations both have some shortcomings in accurately reproducing hail days. For lightning, LPI and lightning proxies need to be carefully calibrated against lightning observations when the model grid and physics change. Overall, HAILCAST and LPI show good results, especially for the diurnal cycles.

In summary, this study is one of the first to present the simulation of both hail and lightning using a km-scale climate model over a decade-long period. It demonstrates promising and encouraging results, and a step towards climate change simulations of hail and lightning. On the other hand, the importance of reliable observations has been accentuated during this study. There is a pressing need for enhanced high-quality observations (e.g., including improved radar-based/satellite detection algorithms, quality-controlled crowd-sourced reports, and denser coverage) that improve our comprehension of severe convective storms, ultimately leading to refinements of modeling hail and lightning in weather and climate models, and implications for risk assessment.

Author contributions. RC performed the simulations and analysed the model output and observations. RC and NB wrote the manuscript. LB and DJ digitized the station-based observations. NB, MED, MTP, and CS provided scientific advice throughout the project.

Acknowledgements. The work presented here has been conducted within the SWALDRIC (IZHRZ0-180587) project of the Croatian-Swiss Research Program co-funded by the Swiss National Science Foundation and Croatian Science Foundation. The authors acknowledge the Partnership for Advanced Computing in Europe (PRACE) for awarding us access to Piz Daint at ETH Zurich/Swiss National Supercomputing Centre (CSCS, Switzerland) for climate simulations. The authors thank Rebecca Adams-Selin for providing the HAILCAST code as well as the support from MeteoSwiss for porting the GPU version of HAILCAST and LPI in COSMO. Special thanks to the Croatian Meteorological and Hydrological Service and ARPA FVG-OSMER for providing the hailpad observations and the observers who devotedly maintained the hailpad observations.

Chapter 5

Conclusions and outlook

5.1 Conclusions

The present thesis investigates severe convective storms with a focus on hail and lightning over the Alpine-Adriatic region using kilometer-scale simulations. In this section, the main findings and conclusions are summarized.

Kilometer-scale simulations of eight observed cases were analyzed in Chapter 2. Overall, COSMO is generally able to credibly replicate key processes of severe convective storms. We identified storm environments that contribute to severe convection, including a capping layer that serves to accumulate humidity and energy below this layer, a "back building process" that contributes to convective cells remaining quasi-stationary near the elevated terrains. These factors explain the hail and lightning hotspots south of the Alps and identify the role of moisture over the Po Valley. Also, the role of the upper-level trough and an approaching cold front in promoting ascent over this region was investigated.

To further investigate the ability of different modeling systems in reproducing such convective extremes and the uncertainties associated with simulating such localized phenomena, a model intercomparison of COSMO and WRF is present in Chapter 3. An attempt is made to make a setup for both models as similar as possible. Ensemble simulations are conducted with different initialization times for case studies to consider the role of model internal variability. The ratio between solid and liquid hydrometeors between COSMO and WRF is similar, while the discrepancies come from the location of the updraft core. Compared to COSMO, WRF simulates stronger updrafts, and the updraft cores are located exactly at the position coinciding with the region with a nearly equal amount of solid and liquid hydrometeors. Therefore, WRF shows a higher LPI in comparison with COSMO. The results highlight not only the strength of the updraft but also the role of the location of the updraft cores and hydrometeors can contribute to the differences in lightning.

The evaluation of hail and lightning characteristics using 10 years of multi-seasonal simulations is presented in Chapter 4. Overall, the hotspots can be reproduced using LPI compared to lightning climatologies using ground-based lightning detection net-

works. The climate simulation of hail over the Alps is for the first time produced using HAILCAST in kilometer-scale simulations. The south of the Alps experiences an earlier onset of the hail season and extended diurnal cycle towards the late evening, compared to the north of the Alps. Also, the highest lightning flash density is found to the south of the Alps. Over the Adriatic region, the seasonal and diurnal cycle behave differently across the coastal, plains and mountains.

Describing hail and lightning in GCMs is challenging, alternatively, using environmental proxies could help. HAILCAST and LPI in kilometer-scale models have the potential to provide more information, as these models are able to explicitly resolve convection and represent the higher velocities that support the hail growth processes. Also, explicit convection will represent CAPE-removal. The use of CAPE-based hail and lightning indicators in kilometer-scale models is thus potentially problematic and might not be suitable to reproduce the hail climatology over Europe.

5.2 Outlook

There are a series of research questions that may be addressed by further studies. They include the following aspects:

- **Severe convective storms — from climatology to climate change**

The encouraging outcomes from the endeavors detailed in Chapter 4 are not limited to the analysis under the current climate. A step forward is to unravel the potential changes in severe convective storms due to global warming, with regard to the knowledge of their characteristics under current climate conditions. This could be achieved through additional climate simulations with hail and lightning diagnostics under future climate scenarios (e.g., CH2018 (2018)) using the pseudo-global warming (PGW) approach (Schär et al., 1996). This kind of work over the European domain is currently underway within the scClim project (<https://scclim.ethz.ch/>).

- **Storyline approach to understanding hail and lightning projections**

As stated before, the conventional approach to representing uncertainty is based on ensembles of simulations. An alternative method called the “storyline approach” is emerging, which is an event-oriented method (Shepherd et al., 2018). A step further to investigate the climate change signals through the framework of different synoptic regimes could be beneficial. Potentially, ensemble simulations for frontal (e.g., 23 July 2009) and “fair weather situation” triggered near topography (e.g., 30 May 2018) cases as shown in Chapter 2 could be done. This approach could increase confidence in understanding the predictability of severe convective storms and improve the understanding of future projections of hail and lightning.

- **Added values of more high-quality observations**

Throughout the course of this project, the importance of reliable observations has been accentuated, particularly when considering extreme events. The improvement of observational records of hail and lightning can be beneficial for future

research. Encouragingly, recent advancements have been made in various aspects. For example, a newly set-up Swiss hail network of automatic hail sensors can report hail sizes and kinetic energy of individual hailstones with very high temporal and size resolution (Kopp et al., 2023). Furthermore, research has emerged in the realm of improving methodologies for hail detection in dual-polarization radar (e.g., Aregger et al. (2023)). The potential of harnessing a more extensive pool of observational data (e.g., crowd-sourced hail reports with the MeteoSwiss App (Barras et al., 2019), drone-based aerial photogrammetry hail detection model (Soderholm et al., 2020; Lainer et al., 2023)) could greatly enhance our comprehension of severe events, ultimately leading to refinements of modeling hail and lightning in weather and climate models.

- **Towards more sophisticated parameterization in higher resolution simulations**

Given the numerous time-varying and looping nature of the hail growth process, we employed the 1D HAILCAST model (Adams-Selin and Ziegler, 2016) to estimate hail size on the ground. Recent advancements in hail trajectory modeling, as demonstrated by Kumjian and Lombardo (2020) and Adams-Selin (2023), have explored 3D hailstone pathways. On the other hand, explicitly simulating lightning activity can be achieved using electrification physics (e.g., Fierro et al. (2013)) instead of diagnostics based on kinematic and microphysical variables (e.g., Lynn and Yair (2010)). This requires the use of a double-moment microphysics scheme. More sophisticated parameterizations can be integrated within large-eddy simulations (LES) with horizontal resolutions less than 100 m (e.g., Heinze et al. (2017)). This, in turn, facilitates understanding the dynamics and microphysics of severe convective storms, and can be potentially used for climatological research.

- **Hail loss estimation, damage prevention, and mitigation strategies**

The outcomes from high-resolution climate simulations could be further used for estimating economic and insured losses caused by hail and lightning. One illustrative example is incorporating the spatiotemporal characteristics of hail size information in conjunction with vulnerability and exposure information, into the natural catastrophe databases and platforms like NatCatSERVICE (Kron et al., 2012) and CLIMADA (Aznar-Siguan and Bresch, 2019)). This input provides better risk estimation on various objects, such as buildings, vineyards, vehicles, and crops. Development of this approach is in progress within the scClim project, engaging with the stakeholders, agricultural and viticulture sectors to make better-informed decisions regarding insurance coverage and risk mitigation strategies.

Appendix A

Simulation documentation

The following tables provide information of output variables that are used for the SWALDRIC project. The simulations are done using the climate version of COSMO with HAILCAST and LPI diagnostics (https://github.com/C2SM-RCM/cosmo-pompa/tree/crclim_hailcast). The variables that are marked in blue color are new variables added compared to Vergara-Temprado et al. (2020), and marked using ‘-’ are removed variables. The red color is variables that are specifically used for the analysis of severe convective events. The domain size is $800 \times 600 \times 60$ for 2.2 km simulations that cover the Alpine-Adriatic region.

A.1 Output frequency: 10 min

Table A.1: Precipitation (33 G/month)

Name	Long name	Units
1. TOT_PREC	total precipitation	kg m^{-2}
2. TOT_SNOW	total snow fall amount	kg m^{-2}

A.2 Output frequency: 1 h

Table A.2: Variables near the surface (17 G/month)

Name	Long name	Units
1. U_10M	U-component of 10m wind	m s^{-1}
2. V_10M	V-component of 10m wind	m s^{-1}
3. VMAX_10M	maximum 10m wind speed	m s^{-1}
4. VABSMX_10M	maximum 10m wind speed (without gust)	m s^{-1}
5. T_G	surface temperature	K
6. T_2M	2m temperature	K
7. RELHUM_2M	2m relative humidity	%
8. TD_2M	2m dew point temperature	K

9. PS	sureface pressure	Pa
10. PSML	mean sea level pressure	Pa
-. QV_2M	2m specific humidity	kg kg ⁻¹

Table A.3: Precipitation, hail and lightning (19 G/month)

Name	Long name	Units
1. RUNOFF_S	surface runoff	kg m ⁻²
2. RUNOFF_G	subsurface runoff	kg m ⁻²
3. DHAIL_MX	maximum hail diameter	mm
4. DHAIL_AV	average hail diameter	mm
5. DHAIL_SD	standard deviation of hail diameter	mm
6. DHAIL_8A	maximum hail diameter (-8 °C, 5 mm)	mm
7. DHAIL_8B	maximum hail diameter (-8 °C, 7.5 mm)	mm
8. DHAIL_13A	maximum hail diameter (-13 °C, 5 mm)	mm
9. DHAIL_13B	maximum hail diameter (-13 °C, 7.5 mm)	mm
10. DHAIL_13C	maximum hail diameter (-13 °C, 10 mm)	mm
11. LPI_MAX	lightning potential index	J kg ⁻¹
12. LPI_BUO	lightning potential index buoyancy	
-. TOT_PR	precipitation rate	kg m ⁻² s ⁻¹
-. QCVG_CON	moisture convergence in the air for kuo type closure	s ⁻¹

Table A.4: Radiation (21 G/month)

Name	Long name	Units
1. ASHFL_S	surface sensible heat flux	W m ⁻²
2. ALHFL_S	surface latent heat flux	W m ⁻²
3. ASWDIR_S	averaged direct downward SW at the surface	W m ⁻²
4. ASWDIFD_S	averaged diffuse downward SW at the surface	W m ⁻²
5. ASWDIFU_S	averaged diffuse upward SW at the surface	W m ⁻²
6. ATHD_S	averaged downward LW radiation at the surface	W m ⁻²
7. ATHU_S	averaged upward LW radiation at the surface	W m ⁻²
8. ASOB_S	averaged surface net downward SW radiation	W m ⁻²
9. ATHB_S	averaged surface net downward LW radiation	W m ⁻²
10. ASOB_T	averaged TOA net downward SW radiation	W m ⁻²
11. ATHB_T	averaged TOA outgoing LW radiation	W m ⁻²
12. ASOD_T	averaged solar downward radiation at top	W m ⁻²
13. ALB_RAD	surface albedo	1
-. ASWD_S	total downward SW radiation at the surface	W m ⁻²
-. LWU_S	upward LW radiation at the surface	W m ⁻²
-. AEVAP_S ¹	surface evaporation	W m ⁻²

¹ Cause the warning AEVAP_S is not allocated and is removed from the list.

Table A.5: Instability (13 G/month)

Name	Long name	Units
1. CAPE_ML	atmosphere convective available potential energy	J kg^{-1}
2. CIN_ML	convection inhibition	J kg^{-1}
3. LFC_ML	level of free convection	m
4. LCL_ML	lifting condensation level	m
5. SLI	surface lifted index	K
6. W_CTMAX	updraft maximum over last output interval	m s^{-1}
7. HZEROCL	height of freezing level	m
8. HPBL	height of boundary layer	m
-. MCONV ¹	horizontal low-level moisture convergence (0-1km)	$\text{kg kg}^{-1} \text{s}^{-1}$

¹ MCONV is not updated in the model output process, so that it produces the same field as the previous variable in the namelist. Current code in COSMO only consider positive updrafts, the new update can choose whether only consider the cyclonically rotating updrafts or positive updrafts.

Table A.6: Cloud and moisture (17 G/month)

Name	Long name	Units
1. CLCT	total cloud cover	1
2. CLCH	high cloud cover	1
3. CLCM	medium cloud cover	1
4. CLCL	low cloud cover	1
5. TQV	precipitable water	kg m^{-2}
6. TQC	vertical integrated cloud water	kg m^{-2}
7. TQI	vertical integrated cloud ice	kg m^{-2}
8. TQG	vertical integrated graupel	kg m^{-2}
9. TQR	vertical integrated rain water	kg m^{-2}
10. TQS	vertical integrated snow	kg m^{-2}

A.3 Output frequency: 3 h

Table A.7: Water fluxes (2 G/month)

Name	Long name	Units
1. TWATFLXU	total zonal water flux	$\text{kg m}^{-1} \text{s}^{-1}$
2. TWATFLXV	total meridional water flux	$\text{kg m}^{-1} \text{s}^{-1}$
-. TWATER	total water content	$\text{kg}^2 \text{m}^{-1}$

Table A.8: Variables at pressure levels: 200, 500, 700, 850, 925, 1000 hPa (17 G/month)

Name	Long name	Units
1. U	U-component of wind	m s^{-1}
2. V	V-component of wind	m s^{-1}
3. W	vertical wind velocity	m s^{-1}
4. T	temperature	K
5. FI	geopotential	$\text{m}^2 \text{s}^{-2}$
6. RELHUM	relative humidity	%
-. QV	specific humidity	kg kg^{-1}

A.4 Output frequency: 24 h

Table A.9: Soil and runoff (1.5 G/month)

Name	Long name	Units
1. T_SO	soil temperature	K
2. W_SO	soil water content	m
3. H_SNOW	surface snow thickness	m
4. W_SNOW	surface snow amount	m
5. TMIN_2M	2m minimum temperature	K
6. TMAX_2M	2m maximum temperature	K

A.5 Post-processing fields

The scripts for the following variables can be found on GitLab: <https://gitlab.ethz.ch/hymet/swaldric/-/tree/main/post-processing>.

Name	Long name	Units
1. S01	0-1 km wind shear	m s^{-1}
2. S03	0-3 km wind shear	m s^{-1}
3. S06	0-6 km wind shear	m s^{-1}
4. S08	0-8 km wind shear	m s^{-1}
5. KI	K index	$^{\circ}\text{C}$
6. UH	updraft helicity (2-5 km)	$\text{m}^2 \text{s}^{-2}$
7. DBZ_CMAX	composite radar reflectivity	–
8. MCONV	0-1 km moisture convergence	$\text{kg kg}^{-1} \text{s}^{-1}$

Appendix B

Supporting information for Chapter 4

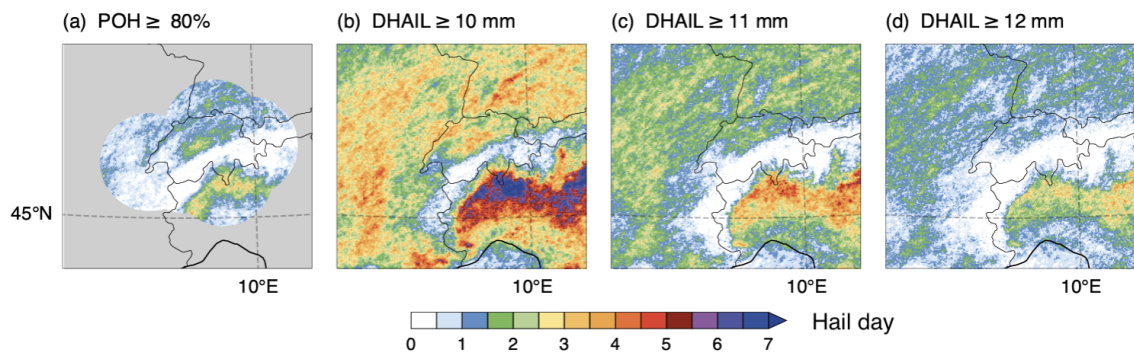


Figure B.1: Mean number of hail days of different hail diameter thresholds from COSMO HAILCAST in comparison with POH observations from April to September during the 2009–2018 period.

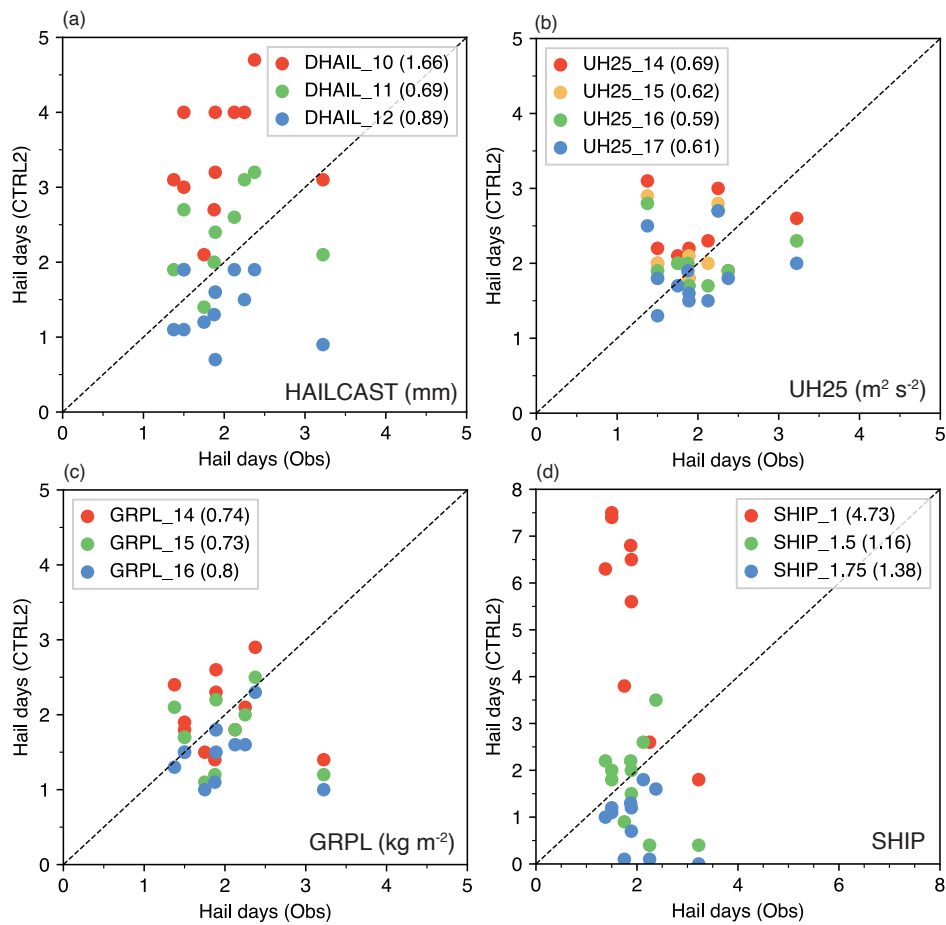


Figure B.2: Scatter plots of mean hail days obtained from station observations in Croatia and from CTRL2 during the 2009–2018 period using different thresholds for (a) HAILCAST, (b) UH25, (c) GRPL, and (d) SHIP. The root mean square error (RMSE) corresponding to each threshold is indicated in the parentheses in the legend. Observations from stations with less than 7 years of data are excluded from the analysis.

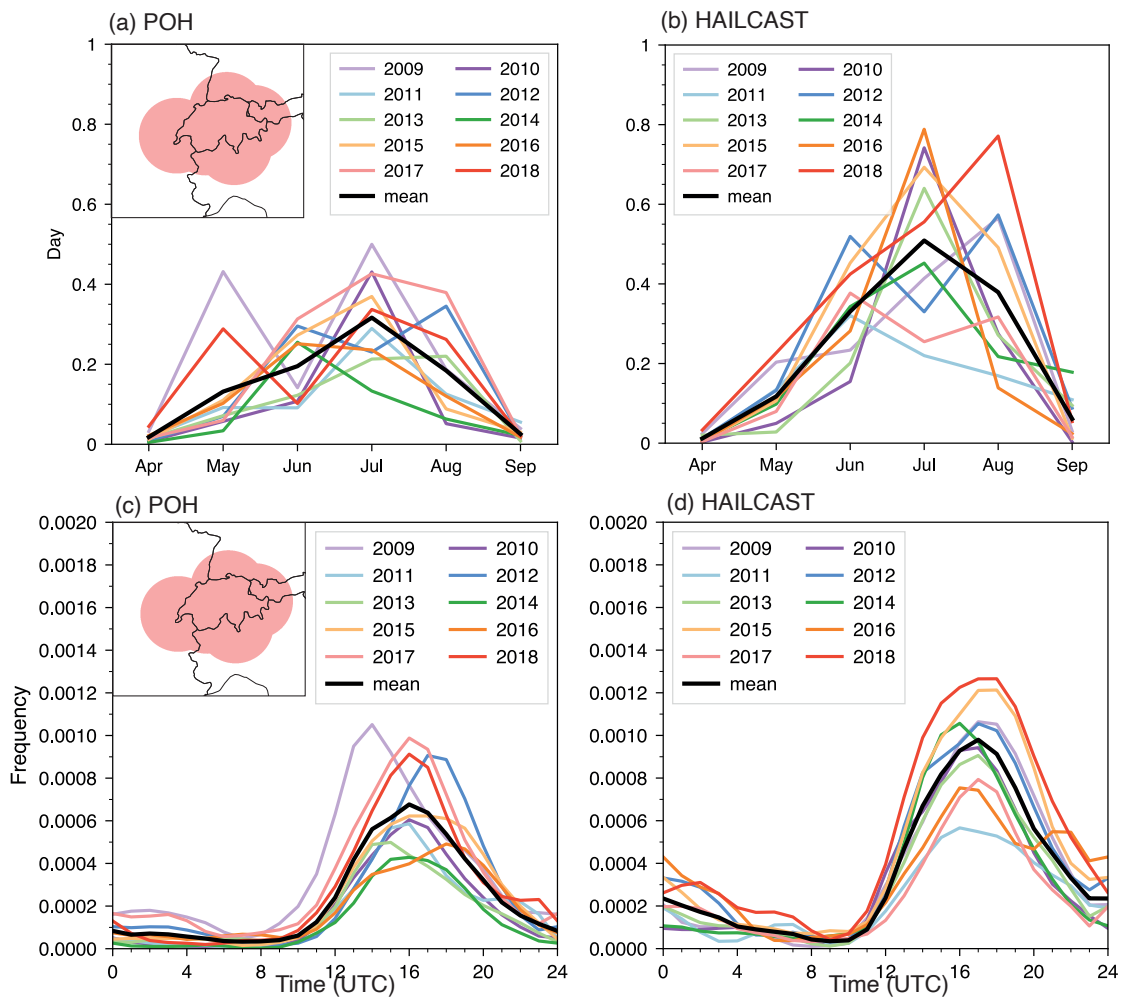


Figure B.3: (a-b) Seasonal and (c-d) diurnal cycle of hail hour from April to September (2009–2018) over the radar-covered domain from POH (left panels) and HAILCAST (right panels).

Acknowledgements

First and foremost, BIG THANKS to Christoph Schär for giving me the opportunity to carry out my master and PhD thesis in your group. Your knack for tackling big problems from a bird's eye view has been invaluable in shaping my research.

Thanks to my supervisors, Nikolina and Marie-Estelle, for taking time for our weekly discussions. Your support in not only honing my writing skills but also helping me master the art of presenting one's work. I couldn't have asked for better mentors!

Also, thanks to my Croatia colleagues, Barbara and Damjan, for not only sharing the amazing new results and the cookbook during COVID, but also for creating unforgettable memories of our time together in Zagreb's coffee shops. Cheers to our wonderful experiences that worked as PhD students in the SWALDRIC project. Thanks to Lucija, Branimir, Maja, and many people involved in this project for the great collaboration that has facilitated my research.

I would like to express my gratitude to H el ene for your help with the crowd-sourced data, and Olivia for your invaluable and constructive comments and for being on my PhD committee. Thanks to Rebecca Adams-Selin for sharing your experience with HAILCAST. Thanks to the people from MeteoSwiss for providing radar observations, as well as Oliver and Xavier for your efforts in porting the GPU version of HAILCAST and LPI to COSMO.

I extend my gratitude to the Hymet people on L floor, who make it a nice working environment. Thanks to the support from Jesus, Laureline, and Martin during my master's thesis, as well as Roman, Raffael and Jonas for their help at the beginning of my PhD. Thanks to Christoph Heim for being a lifesaver with technical problems with PGW. Thanks to my awesome officemates, Doria, Daniel, Patricio, and Luna, for making our office a welcoming place with positive vibes. Thanks to Ruolan, Shuchang, Shuping, Lukas, Borianana, Abraham, Praveen, Brigitta, Alberto, Pascalle, Christian S., Jacopo, and Christian Z. for making the round table on the L floor the most interesting place in the whole workspace. Thanks to Hans-Heini and Matthieu for their technical support. Last but not least, thanks to the administrative staff Rahel and Adelheid for their excellent assistance.

I'm so lucky to have my parents and dear friends during this journey.

References

- Abatzoglou, J. T., and A. P. Williams, 2016: Impact of anthropogenic climate change on wildfire across western US forests. *Proc. Natl. Acad. Sci. (USA)*, **113** (42), 11 770–11 775, doi: 10.1073/pnas.1607171113.
- Adams-Selin, R. D., 2023: A three-dimensional hail trajectory clustering technique. *Mon. Wea. Rev.*, doi: 10.1175/mwr-d-22-0345.1.
- Adams-Selin, R. D., A. J. Clark, C. J. Melick, S. R. Dembek, I. L. Jirak, and C. L. Ziegler, 2019: Evolution of WRF-HAILCAST during the 2014–16 NOAA/hazardous weather testbed spring forecasting experiments. *Wea. Forecasting*, **34** (1), 61–79, doi: 10.1175/waf-d-18-0024.1.
- Adams-Selin, R. D., and C. L. Ziegler, 2016: Forecasting Hail Using a One-Dimensional Hail Growth Model within WRF. *Mon. Wea. Rev.*, **144** (12), 4919–4939, doi: 10.1175/MWR-D-16-0027.1.
- Adinolfi, M., M. Raffa, A. Reder, and P. Mercogliano, 2023: Investigation on potential and limitations of ERA5 reanalysis downscaled on Italy by a convection-permitting model. *Climate Dyn.*, doi: 10.1007/s00382-023-06803-w.
- Allen, D. J., and K. E. Pickering, 2002: Evaluation of lightning flash rate parameterizations for use in a global chemical transport model. *J. Geophys. Res. Atmos.*, **107** (D23), ACH 15–1–ACH 15–21, doi: 10.1029/2002jd002066.
- Allen, J. T., I. M. Giammanco, M. R. Kumjian, H. J. Punge, Q. Zhang, P. Groenemeijer, M. Kunz, and K. Ortega, 2020: Understanding hail in the earth system. *Rev. Geophys.*, **58** (1), doi: 10.1029/2019rg000665.
- Allen, M. R., and W. J. Ingram, 2002: Constraints on future changes in climate and the hydrologic cycle. *Nature*, **419** (6903), 224–232, doi: 10.1038/nature01092.
- Anderson, G., and D. Klugmann, 2014: A European lightning density analysis using 5 years of ATDnet data. *Nat. Hazards Earth Syst. Sci.*, **14** (4), 815–829, doi: 10.5194/nhess-14-815-2014.
- Aran, M., J. Pena, and M. Torà, 2011: Atmospheric circulation patterns associated with hail events in Lleida (Catalonia). *Atmos. Res.*, **100** (4), 428–438, doi: 10.1016/j.atmosres.2010.10.029.
- Aregger, M., O. Martius, A. Hering, and U. Germann, 2023: Detection of differential reflectivity columns using operational C-band radar and their relation to hail prob-

- ability and size in switzerland. 11th European Conference on Severe Storms, doi: 10.5194/ecss2023-58.
- Ashley, W. S., A. M. Haberlie, and V. A. Gensini, 2023: The future of supercells in the united states. *Bull. Amer. Meteor. Soc.*, **104** (1), E1–E21, doi: 10.1175/bams-d-22-0027.1.
- Aznar-Siguan, G., and D. N. Bresch, 2019: CLIMADA v1: a global weather and climate risk assessment platform. *Geosci. Model Dev.*, **12** (7), 3085–3097, doi: 10.5194/gmd-12-3085-2019.
- Baldauf, M., A. Seifert, J. Förstner, D. Majewski, M. Raschendorfer, and T. Reinhardt, 2011: Operational Convective-Scale Numerical Weather Prediction with the COSMO Model: Description and Sensitivities. *Mon. Wea. Rev.*, **139** (12), 3887–3905, doi: 10.1175/MWR-D-10-05013.1.
- Ban, N., J. Schmidli, and C. Schär, 2014: Evaluation of the convection-resolving regional climate modeling approach in decade-long simulations. *J. Geophys. Res. Atmos.*, **119** (13), 7889–7907, doi: 10.1002/2014jd021478.
- Ban, N., J. Schmidli, and C. Schär, 2015: Heavy precipitation in a changing climate: Does short-term summer precipitation increase faster? *Geophys. Res. Lett.*, **42** (4), 1165–1172, doi: 10.1002/2014gl062588.
- Ban, N., and Coauthors, 2021: The first multi-model ensemble of regional climate simulations at kilometer-scale resolution, part i: evaluation of precipitation. *Climate Dyn.*, **57** (1-2), 275–302, doi: 10.1007/s00382-021-05708-w.
- Bandhauer, M., and Coauthors, 2021: Evaluation of daily precipitation analyses in E-OBS (v19.0e) and ERA5 by comparison to regional high-resolution datasets in european regions. *Int. J. Climatol.*, **42** (2), 727–747, doi: 10.1002/joc.7269.
- Banerjee, A., A. T. Archibald, A. C. Maycock, P. Telford, N. L. Abraham, X. Yang, P. Braesicke, and J. A. Pyle, 2014: Lightning NO_x, a key chemistry–climate interaction: impacts of future climate change and consequences for tropospheric oxidising capacity. *Atmos. Chem. Phys.*, **14** (18), 9871–9881, doi: 10.5194/acp-14-9871-2014.
- Barnes, E. A., and L. Polvani, 2013: Response of the midlatitude jets, and of their variability, to increased greenhouse gases in the CMIP5 models. *J. Climate*, **26** (18), 7117–7135, doi: 10.1175/jcli-d-12-00536.1.
- Barras, H., A. Hering, A. Martynov, P. A. Noti, U. Germann, and O. Martius, 2019: Experiences with >50,000 crowdsourced hail reports in Switzerland. *Bull. Amer. Meteor. Soc.*, **100** (8), 1429–1440, doi: 10.1175/BAMS-D-18-0090.1.
- Barras, H., O. Martius, L. Nisi, K. Schroer, A. Hering, and U. Germann, 2021: Multi-day hail clusters and isolated hail days in switzerland – large-scale flow conditions and precursors. *Weather Clim. Dyn.*, **2** (4), 1167–1185, doi: 10.5194/wcd-2-1167-2021.
- Bedka, K. M., 2011: Overshooting cloud top detections using MSG SEVIRI infrared brightness temperatures and their relationship to severe weather over europe. *Atmos. Res.*, **99** (2), 175–189, doi: 10.1016/j.atmosres.2010.10.001.

- Belušić, A., M. T. Prtenjak, I. Güttler, N. Ban, D. Leutwyler, and C. Schär, 2017: Near-surface wind variability over the broader adriatic region: insights from an ensemble of regional climate models. *Climate Dyn.*, **50 (11-12)**, 4455–4480, doi: 10.1007/s00382-017-3885-5.
- Berthet, C., J. Dessens, and J. Sanchez, 2011: Regional and yearly variations of hail frequency and intensity in france. *Atmos. Res.*, **100 (4)**, 391–400, doi: 10.1016/j.atmosres.2010.10.008.
- Berthet, C., E. Wesolek, J. Dessens, and J. Sanchez, 2013: Extreme hail day climatology in southwestern france. *Atmos. Res.*, **123**, 139–150, doi: 10.1016/j.atmosres.2012.10.007.
- Betz, H. D., K. Schmidt, P. Laroche, P. Blanchet, W. P. Oettinger, E. Defer, Z. Dziewit, and J. Konarski, 2009: LINET-An international lightning detection network in Europe. *Atmos. Res.*, **91 (2-4)**, 564–573, doi: 10.1016/j.atmosres.2008.06.012.
- Blašković, L., D. Jelić, B. Malečić, B. Omazić, I. Güttler, and M. T. Prtenjak, 2023: Trend analysis and climatology of hail in croatia. *Atmos. Res.*, 106927, doi: 10.1016/j.atmosres.2023.106927.
- Boccippio, D. J., 2002: Lightning scaling relations revisited. *J. Atmos. Sci.*, **59 (6)**, 1086–1104, doi: 10.1175/1520-0469(2002)059<1086:lsrr>2.0.co;2.
- Brimelow, J. C., W. R. Burrows, and J. M. Hanesiak, 2017: The changing hail threat over north america in response to anthropogenic climate change. *Nat. Climate Change*, **7 (7)**, 516–522, doi: 10.1038/nclimate3321.
- Brimelow, J. C., G. W. Reuter, and E. R. Poolman, 2002: Modeling Maximum Hail Size in Alberta Thunderstorms. *Wea. Forecasting*, **17 (5)**, 1048–1062, doi: 10.1175/1520-0434(2002)017<1048:MMHSIA>2.0.CO;2.
- Brisson, E., U. Blahak, P. Lucas-Picher, C. Purr, and B. Ahrens, 2021: Contrasting lightning projection using the lightning potential index adapted in a convection-permitting regional climate model. *Climate Dyn.*, **57 (7-8)**, 2037–2051, doi: 10.1007/s00382-021-05791-z.
- Brisson, E., C. Brendel, S. Herzog, and B. Ahrens, 2018: Lagrangian evaluation of convective shower characteristics in a convection-permitting model. *Meteor. Z.*, **27 (1)**, 59–66, doi: 10.1127/metz/2017/0817.
- Brisson, E., K. V. Weverberg, M. Demuzere, A. Devis, S. Saeed, M. Stengel, and N. P. M. van Lipzig, 2016: How well can a convection-permitting climate model reproduce decadal statistics of precipitation, temperature and cloud characteristics? *Climate Dyn.*, **47 (9-10)**, 3043–3061, doi: 10.1007/s00382-016-3012-z.
- Brogli, R., N. Kröner, S. L. Sørland, D. Lüthi, and C. Schär, 2019: The Role of Hadley Circulation and Lapse-Rate Changes for the Future European Summer Climate. *J. Climate*, **32 (2)**, 385–404, doi: 10.1175/JCLI-D-18-0431.1.
- Brooks, H. E., C. A. Doswell, and J. Cooper, 1994: On the environments of tornadic and nontornadic mesocyclones. **9 (4)**, 606–618, doi: 10.1175/1520-0434(1994)009<0606:oteota>2.0.co;2.

- Brown, T. M., W. H. Pogorzelski, and I. M. Giammanco, 2015: Evaluating hail damage using property insurance claims data. *Weather Clim. Soc.*, **7** (3), 197–210, doi: 10.1175/wcas-d-15-0011.1.
- Browning, K. A., 1977: The structure and mechanisms of hailstorms. *Hail: A Review of Hail Science and Hail Suppression*, American Meteorological Society, 1–47, doi: 10.1007/978-1-935704-30-0_1.
- Burcea, S., R. Cică, and R. Bojariu, 2016: Hail climatology and trends in romania: 1961–2014. *Mon. Wea. Rev.*, **144** (11), 4289–4299, doi: 10.1175/mwr-d-16-0126.1.
- Byers, H. R., and R. R. Braham, 1949: *The thunderstorm*. U.S. Government Printing Office.
- Carlson, T. N., S. G. Benjamin, G. S. Forbes, and Y.-F. Li, 1983: Elevated mixed layers in the regional severe storm environment: Conceptual model and case studies. *Mon. Wea. Rev.*, **111** (7), 1453–1474, doi: 10.1175/1520-0493(1983)111<1453:emlitr>2.0.co;2.
- Cecil, D. J., D. E. Buechler, and R. J. Blakeslee, 2014: Gridded lightning climatology from TRMM-LIS and OTD: Dataset description. *Atmos. Res.*, **135–136**, 404–414, doi: 10.1016/j.atmosres.2012.06.028.
- CH2018, 2018: Climate scenarios for switzerland. National Centre for Climate Services, Zurich, URL <http://www.climate-scenarios.ch>.
- Changnon, S. A., 2009: Increasing major hail losses in the u.s. *Climatic Change*, **96** (1-2), 161–166, doi: 10.1007/s10584-009-9597-z.
- Charn, A. B., and H. Parishani, 2021: Predictive proxies of present and future lightning in a superparameterized model. *J. Geophys. Res. Atmos.*, **126** (17), doi: 10.1029/2021jd035461.
- Christian, H. J., 2003: Global frequency and distribution of lightning as observed from space by the optical transient detector. *J. Geophys. Res.*, **108** (D1), doi: 10.1029/2002jd002347.
- Cintineo, J. L., T. M. Smith, V. Lakshmanan, H. E. Brooks, and K. L. Ortega, 2012: An objective high-resolution hail climatology of the contiguous United States. *Wea. Forecasting*, **27** (5), 1235–1248, doi: 10.1175/WAF-D-11-00151.1.
- Clark, S. K., D. S. Ward, and N. M. Mahowald, 2017: Parameterization-based uncertainty in future lightning flash density. *Geophys. Res. Lett.*, **44** (6), 2893–2901, doi: 10.1002/2017gl073017.
- Cornes, R. C., G. van der Schrier, E. J. M. van den Besselaar, and P. D. Jones, 2018: An ensemble version of the e-OBS temperature and precipitation data sets. *J. Geophys. Res. Atmos.*, **123** (17), 9391–9409, doi: 10.1029/2017jd028200.
- Cui, R., N. Ban, M.-E. Demory, R. Aellig, O. Fuhrer, J. Jucker, X. Lapillonne, and C. Schär, 2023: Exploring hail and lightning diagnostics over the alpine-adriatic region in a km-scale climate model. *Weather Clim. Dyn.*, **4** (4), 905–926, doi: 10.5194/wcd-4-905-2023.
- Ćurić, M., and D. Janc, 2015: Hail climatology in serbia. *Int. J. Climatol.*, **36** (9), 3270–3279, doi: 10.1002/joc.4554.

- Curran, E. B., R. L. Holle, and R. E. López, 2000: Lightning casualties and damages in the united states from 1959 to 1994. *J. Climate*, **13** (19), 3448–3464, doi: 10.1175/1520-0442(2000)013<3448:lcadit>2.0.co;2.
- Czernecki, B., M. Taszarek, M. Marosz, M. Pórolniczak, L. Kolendowicz, A. Wyszogrodzki, and J. Szturc, 2019: Application of machine learning to large hail prediction - the importance of radar reflectivity, lightning occurrence and convective parameters derived from ERA5. *Atmos. Res.*, **227**, 249–262, doi: 10.1016/j.atmosres.2019.05.010.
- Deierling, W., and W. A. Petersen, 2008: Total lightning activity as an indicator of updraft characteristics. *J. Geophys. Res. Atmos.*, **113** (D16), doi: 10.1029/2007jd009598.
- Dennis, E. J., and M. R. Kumjian, 2017: The impact of vertical wind shear on hail growth in simulated supercells. *J. Atmos. Sci.*, **74** (3), 641–663, doi: 10.1175/jas-d-16-0066.1.
- Dessens, J., 1998: A physical evaluation of a hail suppression project with silver iodide ground burners in southwestern france. *J. Appl. Meteor.*, **37** (12), 1588–1599, doi: 10.1175/1520-0450(1998)037<1588:apeoah>2.0.co;2.
- Dessens, J., C. Berthet, and J. Sanchez, 2015: Change in hailstone size distributions with an increase in the melting level height. *Atmos. Res.*, **158-159**, 245–253, doi: 10.1016/j.atmosres.2014.07.004.
- Diffenbaugh, N. S., M. Scherer, and R. J. Trapp, 2013: Robust increases in severe thunderstorm environments in response to greenhouse forcing. *Proc. Natl. Acad. Sci. (USA)*, **110** (41), 16 361–16 366, doi: 10.1073/pnas.1307758110.
- Doblas-Reyes, F., and Coauthors, 2021: Linking global to regional climate change. *Climate Change 2021: The Physical Science Basis. Contribution of Working Group I to the Sixth Assessment Report of the Intergovernmental Panel on Climate Change*, Cambridge University Press, Cambridge, United Kingdom and New York, NY, USA, book section 10, URL https://www.ipcc.ch/report/ar6/wg1/downloads/report/IPCC_AR6_WGI_Chapter10.pdf.
- Dotzek, N., P. Groenemeijer, B. Feuerstein, and A. M. Holzer, 2009: Overview of ESSL's severe convective storms research using the european severe weather database ESWD. *Atmos. Res.*, **93** (1-3), 575–586, doi: 10.1016/j.atmosres.2008.10.020.
- Dowdy, A. J., M. D. Fromm, and N. McCarthy, 2017: Pyrocumulonimbus lightning and fire ignition on black saturday in southeast australia. *J. Geophys. Res. Atmos.*, **122** (14), 7342–7354, doi: 10.1002/2017jd026577.
- Ebert, E. E., 2008: Fuzzy verification of high-resolution gridded forecasts: a review and proposed framework. *Meteorol. Appl.*, **15** (1), 51–64, doi: 10.1002/met.25.
- Eccel, E., P. Cau, K. Riemann-Campe, and F. Biasioli, 2011: Quantitative hail monitoring in an alpine area: 35-year climatology and links with atmospheric variables. *Int. J. Climatol.*, **32** (4), 503–517, doi: 10.1002/joc.2291.
- Enno, S.-E., J. Sugier, R. Alber, and M. Seltzer, 2020: Lightning flash density in europe based on 10 years of ATDnet data. *Atmos. Res.*, **235**, 104 769, doi: 10.1016/j.atmosres.2019.104769.

- ESSL, 2015: Summary of the evaluation of cosmo and icon model products at the essl testbed 2015. ESSL, URL <https://www.essl.org/media/publications/essl-report-2015-02.pdf>, (last access: 8 May 2023).
- Federer, B., W. Schmid, and A. Waldvogel, 1978: The design of grossversuch IV, a randomized hail suppression experiment in switzerland. *Atmos.–Ocean*, **16** (1), 6–16, doi: 10.1080/07055900.1978.9649009.
- Federer, B., and Coauthors, 1986: Main results of grossversuch IV. *J. Appl. Meteor. Climatol.*, **25** (7), 917–957, doi: 10.1175/1520-0450(1986)025<0917:mrogi>2.0.co;2.
- Feldmann, M., U. Germann, M. Gabella, and A. Berne, 2021: A characterisation of alpine mesocyclone occurrence. *Weather Clim. Dyn.*, **2** (4), 1225–1244, doi: 10.5194/wcd-2-1225-2021.
- Feldmann, M., A. Hering, M. Gabella, and A. Berne, 2023: Hailstorms and rainstorms versus supercells—a regional analysis of convective storm types in the alpine region. *npj Climate Atmos. Sci.*, **6** (1), doi: 10.1038/s41612-023-00352-z.
- FEON, 2013: Hydrological yearbook of switzerland 2013. Federal Office for the Environment, MeteoSwiss, URL <https://www.bafu.admin.ch/bafu/de/home/themen/wasser/publikationen-studien/publikationen-wasser/hydrologisches-jahrbuch-der-schweiz.html>, (last access: 16 Mar 2023).
- Ferro, C. A. T., and D. B. Stephenson, 2011: Extremal dependence indices: Improved verification measures for deterministic forecasts of rare binary events. *Wea. Forecasting*, **26** (5), 699–713, doi: 10.1175/waf-d-10-05030.1.
- Fierro, A. O., E. R. Mansell, D. R. MacGorman, and C. L. Ziegler, 2013: The implementation of an explicit charging and discharge lightning scheme within the WRF-ARW model: Benchmark simulations of a continental squall line, a tropical cyclone, and a winter storm. *Mon. Wea. Rev.*, **141** (7), 2390–2415, doi: 10.1175/mwr-d-12-00278.1.
- Finney, D. L., R. M. Doherty, O. Wild, H. Huntrieser, H. C. Pumphrey, and A. M. Blyth, 2014: Using cloud ice flux to parametrise large-scale lightning. *Atmos. Chem. Phys.*, **14** (23), 12 665–12 682, doi: 10.5194/acp-14-12665-2014.
- Finney, D. L., R. M. Doherty, O. Wild, D. S. Stevenson, I. A. MacKenzie, and A. M. Blyth, 2018: A projected decrease in lightning under climate change. *Nat. Climate Change*, **8** (3), 210–213, doi: 10.1038/s41558-018-0072-6.
- Fischer, E. M., and R. Knutti, 2016: Observed heavy precipitation increase confirms theory and early models. *Nat. Climate Change*, **6** (11), 986–991, doi: 10.1038/nclimate3110.
- Fluck, E., M. Kunz, P. Geissbuehler, and S. P. Ritz, 2021: Radar-based assessment of hail frequency in europe. *Nat. Hazards Earth Syst. Sci.*, **21** (2), 683–701, doi: 10.5194/nhess-21-683-2021.
- Foote, B., T. W. Krauss, and V. Makitov, 2005: Hail matrices using convectional radar. *Proceedings of 16th Conference on Planned and Inadvertent Weather Modification*, American Meteorological Society, San Diego, CA.

- Fowler, H. J., and Coauthors, 2021: Anthropogenic intensification of short-duration rainfall extremes. *Nat. Rev. Earth Environ.*, **2** (2), 107–122, doi: 10.1038/s43017-020-00128-6.
- Franc, B., B. Filipović-Grčić, and V. Milardić, 2016: Lightning overvoltage performance of 110kv air-insulated substation. *Electr. Power Syst. Res.*, **138**, 78–84, doi: 10.1016/j.epsr.2015.12.002.
- Fujita, T. T., 1978: Manual of downburst identification for project nimrod.
- Galanaki, E., K. Lagouvardos, V. Kotroni, E. Flaounas, and A. Argiriou, 2018: Thunderstorm climatology in the mediterranean using cloud-to-ground lightning observations. *Atmos. Res.*, **207**, 136–144, doi: 10.1016/j.atmosres.2018.03.004.
- Genio, A. D. D., M.-S. Yao, and J. Jonas, 2007: Will moist convection be stronger in a warmer climate? *Geophys. Res. Lett.*, **34** (16), doi: 10.1029/2007gl030525.
- Germann, U., M. Boscacci, L. Clementi, M. Gabella, A. Hering, M. Sartori, I. V. Sideris, and B. Calpini, 2022: Weather radar in complex orography. *Remote Sens.*, **14** (3), 503, doi: 10.3390/rs14030503.
- Germann, U., G. Galli, M. Boscacci, and M. Bolliger, 2006: Radar precipitation measurement in a mountainous region. *Quart. J. Roy. Meteor. Soc.*, **132** (618), 1669–1692, doi: 10.1256/qj.05.190.
- Giaiotti, D., E. Gianesini, and F. Stel, 2001: Heuristic considerations pertaining to hailstone size distributions in the plain of friuli-venezia giulia. *Atmos. Res.*, **57** (4), 269–288, doi: 10.1016/s0169-8095(01)00080-1.
- Giaiotti, D., S. Nordio, and F. Stel, 2003: The climatology of hail in the plain of friuli venezia giulia. *Atmos. Res.*, **67-68**, 247–259, doi: 10.1016/s0169-8095(03)00084-x.
- Giorgi, F., 2006: Climate change hot-spots. *Geophys. Res. Lett.*, **33** (8), doi: 10.1029/2006gl025734.
- Glahn, H. R., and D. A. Lowry, 1972: The use of model output statistics (MOS) in objective weather forecasting. *J. Appl. Meteor.*, **11** (8), 1203–1211, doi: 10.1175/1520-0450(1972)011<1203:tuomos>2.0.co;2.
- Gordillo-Vázquez, F. J., F. J. Pérez-Invernón, H. Huntrieser, and A. K. Smith, 2019: Comparison of six lightning parameterizations in CAM5 and the impact on global atmospheric chemistry. *Earth Space Sci.*, **6** (12), 2317–2346, doi: 10.1029/2019ea000873.
- Grams, C. M., H. Binder, S. Pfahl, N. Piaget, and H. Wernli, 2014: Atmospheric processes triggering the central european floods in june 2013. *Nat. Hazards Earth Syst. Sci.*, **14** (7), 1691–1702, doi: 10.5194/nhess-14-1691-2014.
- Groenemeijer, P., and Coauthors, 2017: Severe convective storms in europe: Ten years of research and education at the european severe storms laboratory. *Bull. Amer. Meteor. Soc.*, **98** (12), 2641–2651, doi: 10.1175/bams-d-16-0067.1.
- Gudmundsson, L., J. B. Bremnes, J. E. Haugen, and T. Engen-Skaugen, 2012: Technical note: Downscaling RCM precipitation to the station scale using statistical transfor-

- mations – a comparison of methods. *Hydrol. Earth Syst. Sci.*, **16** (9), 3383–3390, doi: 10.5194/hess-16-3383-2012.
- GVZ, 2013: Geschäftsbericht 2013. Gebäudeversicherung Kanton Zürich, URL https://www.gvz.ch/_file/146/gvz-geschaeftsbericht-2013.pdf, (last access: 25 Feb 2023).
- Haberlie, A. M., W. S. Ashley, C. M. Battisto, and V. A. Gensini, 2022: Thunderstorm activity under intermediate and extreme climate change scenarios. *Geophys. Res. Lett.*, **49** (14), doi: 10.1029/2022gl098779.
- Heim, C., D. Panosetti, L. Schlemmer, D. Leuenberger, and C. Schär, 2020: The influence of the resolution of orography on the simulation of orographic moist convection. *Mon. Wea. Rev.*, **148** (6), 2391–2410, doi: 10.1175/mwr-d-19-0247.1.
- Heinze, R., and Coauthors, 2017: Large-eddy simulations over germany using ICON: a comprehensive evaluation. *Quart. J. Roy. Meteor. Soc.*, **143** (702), 69–100, doi: 10.1002/qj.2947.
- Heise, E., M. Lange, B. Ritter, and R. Schrodin, 2006: Improvement and validation of the multi-layer soil mode. *COMSO Newsletter*, **3**, 198–203.
- Hentgen, L., N. Ban, N. Kröner, D. Leutwyler, and C. Schär, 2019: Clouds in Convection-Resolving Climate Simulations Over Europe. *J. Geophys. Res. Atmos.*, **124** (7), 3849–3870, doi: 10.1029/2018JD030150.
- Hersbach, H., and Coauthors, 2020: The ERA5 global reanalysis. *Quart. J. Roy. Meteor. Soc.*, **146** (730), 1999–2049, doi: 10.1002/qj.3803.
- Holle, R. L., R. E. López, and B. C. Navarro, 2005: Deaths, injuries, and damages from lightning in the united states in the 1890s in comparison with the 1990s. *J. Appl. Meteor.*, **44** (10), 1563–1573, doi: 10.1175/jam2287.1.
- Hong, S.-Y., and J.-O. J. Lim, 2006: The WRF single-moment 6-class microphysics scheme (WSM6). *Journal of Korean Meteorological Society*, **42**, 129–151.
- Horvath, K., D. Koracin, R. Vellore, J. Jiang, and R. Belu, 2012: Sub-kilometer dynamical downscaling of near-surface winds in complex terrain using WRF and MM5 mesoscale models. *J. Geophys. Res. Atmos.*, **117** (D11), doi: 10.1029/2012jd017432.
- Houze, R. A., W. Schmid, R. G. Fovell, and H.-H. Schiesser, 1993: Hailstorms in switzerland: Left movers, right movers, and false hooks. *Mon. Wea. Rev.*, **121** (12), 3345–3370, doi: 10.1175/1520-0493(1993)121<3345:hislmr>2.0.co;2.
- Houze, R. A., Jr, 2014: *Cloud Dynamics*. 2nd ed., Academic Press.
- Huffman, G., E. Stocker, D. Bolvin, E. Nelkin, and J. Tan, 2019: Gpm imerg final precipitation l3 half hourly 0.1 degree x 0.1 degree v06. doi: 10.5067/GPM/IMERG/3B-HH/06.
- Huffman, G., E. Stocker, D. Bolvin, E. Nelkin, and J. Tan, 2023: Gpm imerg final precipitation l3 half hourly 0.1 degree x 0.1 degree v07. doi: 10.5067/GPM/IMERG/3B-HH/07.

- Huntrieser, H., H. H. Schiesser, W. Schmid, and A. Waldvogel, 1997: Comparison of traditional and newly developed thunderstorm indices for Switzerland. *J. Appl. Meteor.*, **36** (1), 108–125, doi: 10.1175/1520-0434(1997)012<0108:cotand>2.0.co;2.
- Isotta, F. A., and Coauthors, 2014: The climate of daily precipitation in the Alps: Development and analysis of a high-resolution grid dataset from pan-Alpine rain-gauge data. *Int. J. Climatol.*, **34** (5), 1657–1675, doi: 10.1002/joc.3794.
- James, R. P., and P. M. Markowski, 2010: A numerical investigation of the effects of dry air aloft on deep convection. *Mon. Wea. Rev.*, **138** (1), 140–161, doi: 10.1175/2009mwr3018.1.
- Jelić, D., O. A. Megyeri, B. Malečić, A. Belušić Vozila, N. Strelec Mahović, and M. Telišman Prtenjak, 2020: Hail Climatology Along the Northeastern Adriatic. *J. Geophys. Res. Atmos.*, **125** (23), doi: 10.1029/2020JD032749.
- Jelić, D., M. T. Prtenjak, B. Malečić, A. B. Vozila, O. A. Megyeri, and T. Renko, 2021: A new approach for the analysis of deep convective events: Thunderstorm intensity index. *Atmosphere*, **12** (7), doi: 10.3390/atmos12070908.
- Jewell, R., and J. Brimelow, 2009: Evaluation of Alberta hail growth model using severe hail proximity soundings from the United States. *Wea. Forecasting*, **24** (6), 1592–1609, doi: 10.1175/2009waf2222230.1.
- Joe, P., D. Burgess, R. Potts, T. Keenan, G. Stumpf, and A. Treloar, 2004: The S2K severe weather detection algorithms and their performance. *Wea. Forecasting*, **19** (1), 43–63, doi: 10.1175/1520-0434(2004)019<0043:tsswda>2.0.co;2.
- Johns, R. H., and C. A. Doswell, 1992: Severe Local Storms Forecasting. *Wea. Forecasting*, **7** (4), 588–612, doi: 10.1175/1520-0434(1992)007<0588:SLSF>2.0.CO;2.
- Kahraman, A., E. J. Kendon, H. J. Fowler, and J. M. Wilkinson, 2022: Contrasting future lightning stories across Europe. *Environ. Res. Lett.*, **17** (11), 114023, doi: 10.1088/1748-9326/ac9b78.
- Kahraman, A., Ş. Tilev-Tanriover, M. Kadioglu, D. M. Schultz, and P. M. Markowski, 2015: Severe hail climatology of Turkey. *Mon. Wea. Rev.*, **144** (1), 337–346, doi: 10.1175/mwr-d-15-0337.1.
- Kain, J. S., 2004: The Kain–Fritsch convective parameterization: An update. *J. Appl. Meteor.*, **43** (1), 170–181, doi: 10.1175/1520-0450(2004)043<0170:tkcpau>2.0.co;2.
- Kain, J. S., and Coauthors, 2008: Some practical considerations regarding horizontal resolution in the first generation of operational convection-allowing NWP. *J. Appl. Meteor.*, **47** (5), 931–952, doi: 10.1175/waf2007106.1.
- Kalthoff, N., and Coauthors, 2009: The impact of convergence zones on the initiation of deep convection: A case study from COPS. *Atmos. Res.*, **93** (4), 680–694, doi: 10.1016/j.atmosres.2009.02.010.
- Kanata, J., A. Ametani, and K. Yamamoto, 2012: Threats of lightning current through an

- electric vehicle. *2012 International Conference on Lightning Protection (ICLP)*, IEEE, doi: 10.1109/iclp.2012.6344299.
- Keil, C., F. Heinlein, and G. C. Craig, 2013: The convective adjustment time-scale as indicator of predictability of convective precipitation. *Quart. J. Roy. Meteor. Soc.*, **140 (679)**, 480–490, doi: 10.1002/qj.2143.
- Keller, M., O. Fuhrer, J. Schmidli, M. Stengel, R. Stöckli, and C. Schär, 2016: Evaluation of convection-resolving models using satellite data: The diurnal cycle of summer convection over the alps. *Meteor. Z.*, **25 (2)**, 165–179, doi: 10.1127/metz/2015/0715.
- Klasa, C., M. Arpagaus, A. Walser, and H. Wernli, 2018: An evaluation of the convection-permitting ensemble COSMO-e for three contrasting precipitation events in switzerland. *Quart. J. Roy. Meteor. Soc.*, **144 (712)**, 744–764, doi: 10.1002/qj.3245.
- Kopp, J., A. Manzato, A. Hering, U. Germann, and O. Martius, 2023: How observations from automatic hail sensors in switzerland shed light on local hailfall duration and compare with hailpad measurements. *Atmos. Meas. Tech.*, **16 (14)**, 3487–3503, doi: 10.5194/amt-16-3487-2023.
- Kotroni, V., and K. Lagouvardos, 2008: Lightning occurrence in relation with elevation, terrain slope, and vegetation cover in the mediterranean. *J. Geophys. Res.*, **113 (D21)**, doi: 10.1029/2008jd010605.
- Kotroni, V., and K. Lagouvardos, 2016: Lightning in the mediterranean and its relation with sea-surface temperature. *Environ. Res. Lett.*, **11 (3)**, 034006, doi: 10.1088/1748-9326/11/3/034006.
- Krause, A., S. Kloster, S. Wilkenskjeld, and H. Paeth, 2014: The sensitivity of global wildfires to simulated past, present, and future lightning frequency. *J. Geophys. Res. Biogeosci.*, **119 (3)**, 312–322, doi: 10.1002/2013jg002502.
- Kron, W., M. Steuer, P. Löw, and A. Wirtz, 2012: How to deal properly with a natural catastrophe database – analysis of flood losses. *Nat. Hazards Earth Syst. Sci.*, **12 (3)**, 535–550, doi: 10.5194/nhess-12-535-2012.
- Kumjian, M. R., and K. Lombardo, 2020: A hail growth trajectory model for exploring the environmental controls on hail size: Model physics and idealized tests. *J. Atmos. Sci.*, **77 (8)**, 2765–2791, doi: 10.1175/jas-d-20-0016.1.
- Kunz, M., U. Blahak, J. Handwerker, M. Schmidberger, H. J. Punge, S. Mohr, E. Fluck, and K. M. Bedka, 2017: The severe hailstorm in southwest germany on 28 july 2013: characteristics, impacts and meteorological conditions. *Quart. J. Roy. Meteor. Soc.*, **144 (710)**, 231–250, doi: 10.1002/qj.3197.
- Kunz, M., J. Sander, and C. Kottmeier, 2009: Recent trends of thunderstorm and hailstorm frequency and their relation to atmospheric characteristics in southwest germany. *Int. J. Climatol.*, **29 (15)**, 2283–2297, doi: 10.1002/joc.1865.
- Lac, C., and Coauthors, 2018: Overview of the meso-NH model version 5.4 and its applications. *Geosci. Model Dev.*, **11 (5)**, 1929–1969, doi: 10.5194/gmd-11-1929-2018.

- Lagasio, M., A. Parodi, R. Procopio, F. Rachidi, and E. Fiori, 2017: Lightning potential index performances in multimicrophysical cloud-resolving simulations of a back-building mesoscale convective system: The genoa 2014 event. *J. Geophys. Res. Atmos.*, **122** (8), 4238–4257, doi: 10.1002/2016jd026115.
- Lainer, M., K. P. Brennan, A. Hering, J. Kopp, S. Monhart, D. Wolfensberger, and U. Germann, 2023: Drone-based photogrammetry combined with deep-learning to estimate hail size distributions and melting of hail on the ground. doi: 10.5194/amt-2023-89.
- Langhans, W., J. Schmidli, O. Fuhrer, S. Bieri, and C. Schär, 2013: Long-term simulations of thermally driven flows and orographic convection at convection-parameterizing and cloud-resolving resolutions. *J. Appl. Meteor. Climatol.*, **52** (6), 1490–1510, doi: 10.1175/jamc-d-12-0167.1.
- Lanucci, J. M., and T. T. Warner, 1991: A Synoptic Climatology of the Elevated Mixed-Layer Inversion over the Southern Great Plains in Spring. Part I: Structure, Dynamics, and Seasonal Evolution. *Wea. Forecasting*, **6** (2), 181–197, doi: 10.1175/1520-0434(1991)006<0181:ASCOTE>2.0.CO;2.
- Latham, D., and E. Williams, 2001: Lightning and forest fires. *Forest Fires*, Elsevier, 375–418, doi: 10.1016/b978-012386660-8/50013-1.
- Lavin-Gullon, A., and Coauthors, 2020: Internal variability versus multi-physics uncertainty in a regional climate model. *Int. J. Climatol.*, **41** (S1), doi: 10.1002/joc.6717.
- Lee, J. Y., and G. J. Collins, 2017: Risk analysis of lightning effects in aircraft systems. *2017 IEEE Aerospace Conference*, IEEE, doi: 10.1109/aero.2017.7943671.
- Leutwyler, D., O. Fuhrer, X. Lapillonne, D. Lüthi, and C. Schär, 2016: Towards European-scale convection-resolving climate simulations with GPUs: a study with COSMO 4.19. *Geosci. Model Dev.*, **9** (9), 3393–3412, doi: 10.5194/gmd-9-3393-2016.
- Leutwyler, D., D. Lüthi, N. Ban, O. Fuhrer, and C. Schär, 2017: Evaluation of the convection-resolving climate modeling approach on continental scales. *J. Geophys. Res. Atmos.*, **122** (10), 5237–5258, doi: 10.1002/2016JD026013.
- Li, M., Q. Zhang, and F. Zhang, 2016: Hail day frequency trends and associated atmospheric circulation patterns over china during 1960–2012. *J. Climate*, **29** (19), 7027–7044, doi: 10.1175/jcli-d-15-0500.1.
- Lock, N. A., and A. L. Houston, 2014: Empirical examination of the factors regulating thunderstorm initiation. *Mon. Wea. Rev.*, **142** (1), 240–258, doi: 10.1175/MWR-D-13-00082.1.
- Lohmann, U., F. Lüönd, and F. Mahrt, 2016: *An introduction to clouds*. Cambridge University Press, Cambridge, England.
- Luo, L., M. Xue, and K. Zhu, 2020: The Initiation and Organization of a Severe Hail-Producing Mesoscale Convective System in East China: A Numerical Study. *J. Geophys. Res. Atmos.*, **125** (17), 1–23, doi: 10.1029/2020JD032606.
- Lüthi, S., N. Ban, S. Kotlarski, C. R. Steger, T. Jonas, and C. Schär, 2019: Projections of

- alpine snow-cover in a high-resolution climate simulation. *Atmosphere*, **10** (8), 463, doi: 10.3390/atmos10080463.
- Lynn, B., and Y. Yair, 2010: Prediction of lightning flash density with the WRF model. *Adv. Geosci.*, **23** (8), 11–16, doi: 10.5194/adgeo-23-11-2010.
- Mahoney, K., M. A. Alexander, G. Thompson, J. J. Barsugli, and J. D. Scott, 2012: Changes in hail and flood risk in high-resolution simulations over Colorado's mountains. *Nat. Climate Change*, **2** (2), 125–131, doi: 10.1038/nclimate1344.
- Malečić, B., M. T. Prtenjak, K. Horvath, D. Jelić, P. M. Jurković, K. Čorko, and N. S. Mahović, 2022: Performance of HAILCAST and the lightning potential index in simulating hailstorms in croatia in a mesoscale model – sensitivity to the PBL and microphysics parameterization schemes. *Atmos. Res.*, **272**, 106143, doi: 10.1016/j.atmosres.2022.106143.
- Malečić, B., and Coauthors, 2023: Simulating hail and lightning over the alpine adriatic region—a model intercomparison study. *J. Geophys. Res. Atmos.*, **128** (13), doi: 10.1029/2022jd037989.
- Manzato, A., 2007: The 6 h climatology of thunderstorms and rainfalls in the friuli venezia giulia plain. *Atmos. Res.*, **83** (2-4), 336–348, doi: 10.1016/j.atmosres.2005.08.013.
- Manzato, A., A. Cicogna, M. Centore, P. Battistutta, and M. Trevisan, 2022a: Hailstone characteristics in northeast italy from 29 years of hailpad data. *J. Appl. Meteor. Climatol.*, **61** (11), 1779–1795, doi: 10.1175/jamc-d-21-0251.1.
- Manzato, A., V. Riva, A. Tiesi, and M. M. Miglietta, 2020: Observational analysis and simulations of a severe hailstorm in northeastern italy. *Quart. J. Roy. Meteor. Soc.*, **146** (732), 3587–3611, doi: 10.1002/qj.3886.
- Manzato, A., S. Serafin, M. M. Miglietta, D. Kirshbaum, and W. Schulz, 2022b: A pan-alpine climatology of lightning and convective initiation. *Mon. Wea. Rev.*, **150** (9), 2213–2230.
- Markowski, P., and Y. Richardson, 2010: *Mesoscale Meteorology in Midlatitudes*. Wiley, doi: 10.1002/9780470682104.
- Marwitz, J. D., 1972: The structure and motion of severe hailstorms. part II: Multi-cell storms. *J. Appl. Meteor.*, **11** (1), 180–188, doi: 10.1175/1520-0450(1972)011<0180:tsamos>2.0.co;2.
- McCaul, E. W., S. J. Goodman, K. M. LaCasse, and D. J. Cecil, 2009: Forecasting lightning threat using cloud-resolving model simulations. **24** (3), 709–729, doi: 10.1175/2008waf2222152.1.
- MeteoSwiss, 2017: Klimabulletin juni 2017. National Centre for Climate Services, Zurich, URL <https://www.meteoswiss.admin.ch/services-and-publications/publications/reports-and-bulletins/2017/klimabulletin-juni-2017.html>, (last access: 13 Sep 2023).
- Mlawer, E. J., S. J. Taubman, P. D. Brown, M. J. Iacono, and S. A. Clough, 1997: Radiative

- transfer for inhomogeneous atmospheres: RRTM, a validated correlated-k model for the longwave. *J. Geophys. Res. Atmos.*, **102 (D14)**, 16 663–16 682, doi: 10.1029/97jd00237.
- Mohr, S., M. Kunz, and B. Geyer, 2015: Hail potential in europe based on a regional climate model hindcast. *Geophys. Res. Lett.*, **42 (24)**, 10,904–10,912, doi: 10.1002/2015gl067118.
- Montesarchio, M., A. L. Zollo, E. Bucchignani, P. Mercogliano, and S. Castellari, 2014: Performance evaluation of high-resolution regional climate simulations in the alpine space and analysis of extreme events. *J. Geophys. Res. Atmos.*, **119 (6)**, 3222–3237, doi: 10.1002/2013jd021105.
- Morel, S., 2014: Verification of radar-based hail detection algorithms with insurance loss data in switzerland. M.S. thesis, University of Bern.
- Mortelmans, J., M. Bechtold, E. Brisson, B. Lynn, S. Kumar, and G. D. Lannoy, 2022: Lightning over central canada: Skill assessment for various land-atmosphere model configurations and lightning indices over a boreal study area. *J. Geophys. Res. Atmos.*, **128 (1)**, doi: 10.1029/2022jd037236.
- Nakanishi, M., and H. Niino, 2006: An improved mellor–yamada level-3 model: Its numerical stability and application to a regional prediction of advection fog. *Bound.-Layer Meteorol.*, **119 (2)**, 397–407, doi: 10.1007/s10546-005-9030-8.
- NCCS, 2021: Hail climate switzerland – national hail hazard maps. National Centre for Climate Services, Zurich.
- Ni, X., A. Muehlbauer, J. T. Allen, Q. Zhang, and J. Fan, 2020: A climatology and extreme value analysis of large hail in china. *Mon. Wea. Rev.*, **148 (4)**, 1431–1447, doi: 10.1175/mwr-d-19-0276.1.
- Nisi, L., A. Hering, U. Germann, and O. Martius, 2018: A 15-year hail streak climatology for the Alpine region. *Quart. J. Roy. Meteor. Soc.*, **144 (714)**, 1429–1449, doi: 10.1002/qj.3286.
- Nisi, L., O. Martius, A. Hering, M. Kunz, and U. Germann, 2016: Spatial and temporal distribution of hailstorms in the Alpine region: A long-term, high resolution, radar-based analysis. *Quart. J. Roy. Meteor. Soc.*, **142 (697)**, 1590–1604, doi: 10.1002/qj.2771.
- Orville, R. E., and G. R. Huffines, 2001: Cloud-to-ground lightning in the united states: NLDN results in the first decade, 1989–98. *Mon. Wea. Rev.*, **129 (5)**, 1179–1193, doi: 10.1175/1520-0493(2001)129<1179:ctglit>2.0.co;2.
- Panofsky, H. A., and G. W. Brier, 1968: *Some Applications of Statistics to Meteorology*. The Pennsylvania State University Press.
- Panosetti, D., L. Schlemmer, and C. Schär, 2018: Convergence behavior of idealized convection-resolving simulations of summertime deep moist convection over land. *Climate Dyn.*, **55 (1–2)**, 215–234, doi: 10.1007/s00382-018-4229-9.
- Park, S.-H., W. C. Skamarock, J. B. Klemp, L. D. Fowler, and M. G. Duda, 2013: Evaluation of global atmospheric solvers using extensions of the jablonowski and

- williamson baroclinic wave test case. *Mon. Wea. Rev.*, **141** (9), 3116–3129, doi: 10.1175/mwr-d-12-00096.1.
- Piani, F., A. Crisci, G. D. Chiara, G. Maracchi, and F. Meneguzzo, 2005: Recent trends and climatic perspectives of hailstorms frequency and intensity in tuscany and central italy. *Nat. Hazards Earth Syst. Sci.*, **5** (2), 217–224, doi: 10.5194/nhess-5-217-2005.
- Pichelli, E., and Coauthors, 2021: The first multi-model ensemble of regional climate simulations at kilometer-scale resolution part 2: historical and future simulations of precipitation. *Climate Dyn.*, **56** (11–12), 3581–3602, doi: 10.1007/s00382-021-05657-4.
- Piper, D. A., M. Kunz, J. T. Allen, and S. Mohr, 2019: Investigation of the temporal variability of thunderstorms in central and western europe and the relation to large-scale flow and teleconnection patterns. *Quart. J. Roy. Meteor. Soc.*, **145** (725), 3644–3666, doi: 10.1002/qj.3647.
- Počakal, D., 2011: Hailpad data analysis for the continental part of croatia. *Meteor. Z.*, **20** (4), 441–447, doi: 10.1127/0941-2948/2011/0263.
- Počakal, D., Ž. Večenaj, P. M. Jurković, and B. Grisogono, 2018: Analysis of orographic influence on hail parameters in NW croatia. *Int. J. Climatol.*, **38** (15), 5646–5658, doi: 10.1002/joc.5769.
- Počakal, D., Ž. Večenaj, and J. Štalec, 2009: Hail characteristics of different regions in continental part of croatia based on influence of orography. *Atmos. Res.*, **93** (1–3), 516–525, doi: 10.1016/j.atmosres.2008.10.017.
- Poelman, D. R., W. Schulz, G. Diendorfer, and M. Bernardi, 2016: The european lightning location system EUCLID – part 2: Observations. *Nat. Hazards Earth Syst. Sci.*, **16** (2), 607–616, doi: 10.5194/nhess-16-607-2016.
- Poolman, E., 1992: Die voorspelling van haelkorrelgroei in suid- afrika (the forecasting of hail growth in south africa). Master’s thesis, University of Pretoria, 113 pp.
- Prein, A. F., and A. J. Heymsfield, 2020: Increased melting level height impacts surface precipitation phase and intensity. *Nat. Climate Change*, **10** (8), 771–776, doi: 10.1038/s41558-020-0825-x.
- Prein, A. F., and G. J. Holland, 2018: Global estimates of damaging hail hazard. *Weather Clim. Extremes*, **22**, 10–23, doi: 10.1016/j.wace.2018.10.004.
- Prein, A. F., G. J. Holland, R. M. Rasmussen, J. Done, K. Ikeda, M. P. Clark, and C. H. Liu, 2013: Importance of regional climate model grid spacing for the simulation of heavy precipitation in the colorado headwaters. *J. Climate*, **26** (13), 4848–4857, doi: 10.1175/jcli-d-12-00727.1.
- Prein, A. F., and Coauthors, 2015: A review on regional convection-permitting climate modeling: Demonstrations, prospects, and challenges. *Rev. Geophys.*, **53** (2), 323–361, doi: 10.1002/2014RG000475.
- Price, C., and D. Rind, 1992: A simple lightning parameterization for calculat-

- ing global lightning distributions. *J. Geophys. Res. Atmos.*, **97 (D9)**, 9919–9933, doi: 10.1029/92jd00719.
- Price, C., and D. Rind, 1993: What determines the cloud-to-ground lightning fraction in thunderstorms? *Geophys. Res. Lett.*, **20 (6)**, 463–466, doi: 10.1029/93gl00226.
- Púčik, T., C. Castellano, P. Groenemeijer, T. Kühne, A. T. Rädler, B. Antonescu, and E. Faust, 2019: Large Hail Incidence and Its Economic and Societal Impacts across Europe. *Mon. Wea. Rev.*, **147 (11)**, 3901–3916, doi: 10.1175/MWR-D-19-0204.1.
- Punge, H., K. Bedka, M. Kunz, and A. Reinbold, 2017: Hail frequency estimation across europe based on a combination of overshooting top detections and the ERA-INTERIM reanalysis. *Atmos. Res.*, **198**, 34–43, doi: 10.1016/j.atmosres.2017.07.025.
- Punge, H. J., K. M. Bedka, M. Kunz, and A. Werner, 2014: A new physically based stochastic event catalog for hail in europe. *Nat. Hazards*, **73 (3)**, 1625–1645, doi: 10.1007/s11069-014-1161-0.
- Punge, H. J., and M. Kunz, 2016: Hail observations and hailstorm characteristics in Europe: A review. *Atmos. Res.*, **176–177**, 159–184, doi: 10.1016/j.atmosres.2016.02.012.
- Rachidi, F., M. Rubinstein, J. Montanya, J.-L. Bermudez, R. R. Sola, G. Sola, and N. Korovkin, 2008: A review of current issues in lightning protection of new-generation wind-turbine blades. *IEEE Transactions on Industrial Electronics*, **55 (6)**, 2489–2496, doi: 10.1109/tie.2007.896443.
- Rädler, A. T., P. H. Groenemeijer, E. Faust, R. Sausen, and T. Púčik, 2019: Frequency of severe thunderstorms across europe expected to increase in the 21st century due to rising instability. *npj Climate Atmos. Sci.*, **2 (1)**, doi: 10.1038/s41612-019-0083-7.
- Rampanelli, G., D. Zardi, and R. Rotunno, 2004: Mechanisms of up-valley winds. *J. Atmos. Sci.*, **61 (24)**, 3097–3111, doi: 10.1175/jas-3354.1.
- Raschendorfer, M., 2001: The new turbulence parameterization of lm. *COMSO Newsletter*, **1**, 89–97.
- Raupach, T. H., J. Soderholm, A. Protat, and S. C. Sherwood, 2022: An improved instability–shear hail proxy for Australia. *Mon. Wea. Rev.*, 545–567, doi: 10.1175/mwr-d-22-0127.1.
- Raupach, T. H., J. Soderholm, A. Protat, and S. C. Sherwood, 2023: An improved instability–shear hail proxy for australia. *Mon. Wea. Rev.*, **151 (2)**, 545–567, doi: 10.1175/mwr-d-22-0127.1.
- Raupach, T. H., and Coauthors, 2021: The effects of climate change on hailstorms. *Nat. Rev. Earth Environ.*, **2 (3)**, 213–226, doi: 10.1038/s43017-020-00133-9.
- Reinhardt, T., and A. Seifert, 2006: A three-category ice scheme for lmk. *COMSO Newsletter*, **6**, 115–120.
- Reynolds, S. E., M. Brook, and M. F. Gourley, 1957: THUNDERSTORM CHARGE SEPARATION. *J. Meteor.*, **14 (5)**, 426–436, doi: 10.1175/1520-0469(1957)014<0426:tcs>2.0.co;2.

- Rison, W., R. J. Thomas, P. R. Krehbiel, T. Hamlin, and J. Harlin, 1999: A GPS-based three-dimensional lightning mapping system: Initial observations in central new mexico. *Geophys. Res. Lett.*, **26 (23)**, 3573–3576, doi: 10.1029/1999gl010856.
- Ritter, B., and J.-F. Geleyn, 1992: A comprehensive radiation scheme for numerical weather prediction models with potential applications in climate simulations. *Mon. Wea. Rev.*, **120 (2)**, 303–325, doi: 10.1175/1520-0493(1992)120<0303:acrsfn>2.0.co;2.
- Rodger, C. J., S. Werner, J. B. Brundell, E. H. Lay, N. R. Thomson, R. H. Holzworth, and R. L. Dowden, 2006: Detection efficiency of the VLF world-wide lightning location network (WWLLN): initial case study. *Ann. Geophys.*, **24 (12)**, 3197–3214, doi: 10.5194/angeo-24-3197-2006.
- Roebber, P. J., 2009: Visualizing multiple measures of forecast quality. **24 (2)**, 601–608, doi: 10.1175/2008waf2222159.1.
- Romps, D. M., 2019: Evaluating the future of lightning in cloud-resolving models. *Geophys. Res. Lett.*, **46 (24)**, 14 863–14 871, doi: 10.1029/2019gl085748.
- Romps, D. M., J. T. Seeley, D. Vollaro, and J. Molinari, 2014: Projected increase in lightning strikes in the united states due to global warming. *Science*, **346 (6211)**, 851–854, doi: 10.1126/science.1259100.
- Said, R. K., U. S. Inan, and K. L. Cummins, 2010: Long-range lightning geolocation using a VLF radio atmospheric waveform bank. *J. Geophys. Res.*, **115 (D23)**, doi: 10.1029/2010jd013863.
- Schär, C., C. Frei, D. Lüthi, and H. C. Davies, 1996: Surrogate climate-change scenarios for regional climate models. *Geophys. Res. Lett.*, **23 (6)**, 669–672, doi: 10.1029/96GL00265.
- Schär, C., and Coauthors, 2016: Percentile indices for assessing changes in heavy precipitation events. *Climatic Change*, **137 (1-2)**, 201–216, doi: 10.1007/s10584-016-1669-2.
- Schär, C., and Coauthors, 2020: Kilometer-Scale Climate Models: Prospects and Challenges. *Bull. Amer. Meteor. Soc.*, **101 (5)**, E567–E587, doi: 10.1175/BAMS-D-18-0167.1.
- Schemm, S., L. Nisi, A. Martinov, D. Leuenberger, and O. Martius, 2016: On the link between cold fronts and hail in Switzerland. *Atmos. Sci. Lett.*, **17 (5)**, 315–325, doi: 10.1002/asl.660.
- Schlemmer, L., C. Schär, D. Lüthi, and L. Strebel, 2018: A Groundwater and Runoff Formulation for Weather and Climate Models. *J. Adv. Model. Earth Syst.*, **10 (8)**, 1809–1832, doi: 10.1029/2017MS001260.
- Schmid, W., H. H. Schiesser, and A. Waldvogel, 1992: The kinetic energy of hailfalls. part IV: Patterns of hailpad and radar data. *J. Appl. Meteor.*, **31 (10)**, 1165–1178, doi: 10.1175/1520-0450(1992)031<1165:tkeohp>2.0.co;2.
- Schumann, U., 1987: Influence of mesoscale orography on idealized cold fronts. *J. Atmos. Sci.*, **44 (23)**, 3423–3441, doi: 10.1175/1520-0469(1987)044<3423:iomooi>2.0.co;2.

- Schumann, U., and H. Huntrieser, 2007: The global lightning-induced nitrogen oxides source. *Atmos. Chem. Phys.*, **7** (14), 3823–3907, doi: 10.5194/acp-7-3823-2007.
- Schuster, S. S., R. J. Blong, R. J. Leigh, and K. J. McAneney, 2005: Characteristics of the 14 april 1999 sydney hailstorm based on ground observations, weather radar, insurance data and emergency calls. *Nat. Hazards Earth Syst. Sci.*, **5** (5), 613–620, doi: 10.5194/nhess-5-613-2005.
- Seeley, J. T., and D. M. Romps, 2015: The effect of global warming on severe thunderstorms in the united states. *J. Climate*, **28** (6), 2443–2458, doi: 10.1175/jcli-d-14-00382.1.
- Seneviratne, S., and Coauthors, 2021: Weather and climate extreme events in a changing climate. *Climate Change 2021: The Physical Science Basis. Contribution of Working Group I to the Sixth Assessment Report of the Intergovernmental Panel on Climate Change*, V. Masson-Delmotte, P. Zhai, A. Pirani, S. L. Connors, C. Péan, S. Berger, N. Caud, Y. Chen, L. Goldfarb, M. I. Gomis, M. Huang, K. Leitzell, E. Lonnoy, J. B. R. Matthews, T. K. Maycock, T. Waterfield, O. Yelekçi, R. Yu, and B. Zhou, Eds., Cambridge University Press, Cambridge, United Kingdom and New York, NY, USA, book section 11, URL https://www.ipcc.ch/report/ar6/wg1/downloads/report/IPCC_AR6_WGI_Chapter11.pdf.
- Shaw, T. A., and Coauthors, 2016: Storm track processes and the opposing influences of climate change. *Nat. Geosci.*, **9** (9), 656–664, doi: 10.1038/ngeo2783.
- Shedd, L., M. R. Kumjian, I. Giammanco, T. Brown-Giammanco, and B. R. Maiden, 2021: Hailstone shapes. *J. Atmos. Sci.*, **78** (2), 639–652, doi: 10.1175/jas-d-20-0250.1.
- Shepherd, T. G., and Coauthors, 2018: Storylines: an alternative approach to representing uncertainty in physical aspects of climate change. *Climatic Change*, **151** (3-4), 555–571, doi: 10.1007/s10584-018-2317-9.
- Simon, T., G. J. Mayr, D. Morgenstern, N. Umlauf, and A. Zeileis, 2023: Amplification of annual and diurnal cycles of alpine lightning. *Climate Dyn.*, doi: 10.1007/s00382-023-06786-8.
- Singh, M. S., and P. A. O’Gorman, 2014: Influence of microphysics on the scaling of precipitation extremes with temperature. *Geophys. Res. Lett.*, **41** (16), 6037–6044, doi: 10.1002/2014gl061222.
- Sioutas, M., T. Meaden, and J. D. Webb, 2009: Hail frequency, distribution and intensity in northern greece. *Atmos. Res.*, **93** (1-3), 526–533, doi: 10.1016/j.atmosres.2008.09.023.
- Skamarock, W. C., 2004: Evaluating mesoscale NWP models using kinetic energy spectra. *Mon. Wea. Rev.*, **132** (12), 3019–3032, doi: 10.1175/mwr2830.1.
- Skamarock, W. C., and Coauthors, 2019: A description of the advanced research wrf model version 4. doi: 10.5065/1DFH-6P97.
- Smith, P. L., and A. Waldvogel, 1989: On determinations of maximum hailstone sizes from hallpad observations. *J. Appl. Meteor.*, **28** (1), 71–76, doi: 10.1175/1520-0450(1989)028<0071:odomhs>2.0.co;2.

- Soares, P. M. M., and Coauthors, 2022: The added value of km-scale simulations to describe temperature over complex orography: the CORDEX FPS-convection multi-model ensemble runs over the alps. *Climate Dyn.*, doi: 10.1007/s00382-022-06593-7.
- Soderholm, J. S., M. R. Kumjian, N. McCarthy, P. Maldonado, and M. Wang, 2020: Quantifying hail size distributions from the sky – application of drone aerial photogrammetry. *Atmos. Meas. Tech.*, **13** (2), 747–754, doi: 10.5194/amt-13-747-2020.
- Sokol, Z., and J. Minářová, 2020: Impact of 1- and 2-moment cloud microphysics and horizontal resolution on lightning potential index within COSMO NWP model. *Atmos. Res.*, **237**, 104862, doi: 10.1016/j.atmosres.2020.104862.
- Svabik, O., 1989: Review of meteorological aspects on hail defense activities in austria. *Theor. Appl. Climatol.*, **40** (4), 247–254, doi: 10.1007/bf00865975.
- SwissRe, 2021: Sigma: Natural catastrophes in 2020. SwissRe, URL <https://www.swissre.com/institute/research/sigma-research/sigma-2021-01.html>.
- SwissRe, 2023: Sigma: Natural catastrophes and inflation in 2022. SwissRe, URL <https://www.swissre.com/institute/research/sigma-research/sigma-2023-01.html>.
- Takahashi, T., 1978: Electrical properties of oceanic tropical clouds at ponape, micronesia. *Mon. Wea. Rev.*, **106** (11), 1598–1612, doi: 10.1175/1520-0493(1978)106<1598:epootc>2.0.co;2.
- Tang, B. H., V. A. Gensini, and C. R. Homeyer, 2019: Trends in united states large hail environments and observations. *npj Climate Atmos. Sci.*, **2** (1), doi: 10.1038/s41612-019-0103-7.
- Taszarek, M., J. T. Allen, H. E. Brooks, N. Pilguy, and B. Czernecki, 2021: Differing trends in united states and european severe thunderstorm environments in a warming climate. *Bull. Amer. Meteor. Soc.*, **102** (2), E296–E322, doi: 10.1175/bams-d-20-0004.1.
- Taszarek, M., J. T. Allen, P. Groenemeijer, R. Edwards, H. E. Brooks, V. Chmielewski, and S.-E. Enno, 2020a: Severe convective storms across europe and the united states. part I: Climatology of lightning, large hail, severe wind, and tornadoes. *J. Climate*, **33** (23), 10239–10261, doi: 10.1175/jcli-d-20-0345.1.
- Taszarek, M., J. T. Allen, T. Púčik, K. A. Hoogewind, and H. E. Brooks, 2020b: Severe convective storms across europe and the united states. part II: ERA5 environments associated with lightning, large hail, severe wind, and tornadoes. *J. Climate*, **33** (23), 10263–10286, doi: 10.1175/jcli-d-20-0346.1.
- Taszarek, M., and Coauthors, 2019: A climatology of thunderstorms across europe from a synthesis of multiple data sources. *J. Climate*, **32** (6), 1813–1837, doi: 10.1175/jcli-d-18-0372.1.
- Taylor, K. E., 2001: Summarizing multiple aspects of model performance in a single diagram. *J. Geophys. Res. Atmos.*, **106** (D7), 7183–7192, doi: 10.1029/2000jd900719.
- Thompson, R. L., B. T. Smith, J. S. Grams, A. R. Dean, and C. Broyles, 2012: Convective modes for significant severe thunderstorms in the contiguous united states.

- part II: Supercell and QLCS tornado environments. *27* (5), 1136–1154, doi: 10.1175/waf-d-11-00116.1.
- Thornton, J. A., K. S. Virts, R. H. Holzworth, and T. P. Mitchell, 2017: Lightning enhancement over major oceanic shipping lanes. *Geophys. Res. Lett.*, **44** (17), 9102–9111, doi: 10.1002/2017gl074982.
- Tiedtke, M., 1989: A Comprehensive Mass Flux Scheme for Cumulus Parameterization in Large-Scale Models. *Mon. Wea. Rev.*, **117** (8), 1779–1800, doi: 10.1175/1520-0493(1989)117<1779:ACMFSF>2.0.CO;2.
- Tiesi, A., and Coauthors, 2022: Numerical simulation of a giant-hail-bearing mediterranean supercell in the adriatic sea. *Atmosphere*, **13** (8), 1219, doi: 10.3390/atmos13081219.
- Torralba, V., R. Hénin, A. Cantelli, E. Scoccimarro, S. Materia, A. Manzato, and S. Gualdi, 2023: Modelling hail hazard over italy with era5 large-scale variables. *Weather Clim. Extremes*, **39**, 100535, doi: 10.1016/j.wace.2022.100535.
- Trapp, R. J., N. S. Diffenbaugh, H. E. Brooks, M. E. Baldwin, E. D. Robinson, and J. S. Pal, 2007: Changes in severe thunderstorm environment frequency during the 21st century caused by anthropogenically enhanced global radiative forcing. *Proc. Natl. Acad. Sci. (USA)*, **104** (50), 19719–19723, doi: 10.1073/pnas.0705494104.
- Trapp, R. J., N. S. Diffenbaugh, and A. Gluhovsky, 2009: Transient response of severe thunderstorm forcing to elevated greenhouse gas concentrations. *Geophys. Res. Lett.*, **36** (1), doi: 10.1029/2008gl036203.
- Trapp, R. J., K. A. Hoogewind, and S. Lasher-Trapp, 2019: Future changes in hail occurrence in the united states determined through convection-permitting dynamical downscaling. *J. Climate*, **32** (17), 5493–5509, doi: 10.1175/jcli-d-18-0740.1.
- Trefalt, S., and Coauthors, 2018: A severe hail storm in complex topography in switzerland - observations and processes. *Atmos. Res.*, **209**, 76–94, doi: 10.1016/j.atmosres.2018.03.007.
- Treloar, A., 1998: Vertically integrated radar reflectivity as an indicator of hail size in the greater sydney region of australia. *Proceedings of 19th Conference on Severe Local Storms*, American Meteorological Society, Minneapolis, MN.
- Vergara-Temprado, J., N. Ban, D. Panosetti, L. Schlemmer, and C. Schär, 2020: Climate models permit convection at much coarser resolutions than previously considered. *J. Climate*, **33** (5), 1915–1933, doi: 10.1175/JCLI-D-19-0286.1.
- Vergara-Temprado, J., N. Ban, and C. Schär, 2021: Extreme sub-hourly precipitation intensities scale close to the clausius-clapeyron rate over europe. *Geophys. Res. Lett.*, **48** (3), doi: 10.1029/2020gl089506.
- Vinet, F., 2001: Climatology of hail in france. *Atmos. Res.*, **56** (1-4), 309–323, doi: 10.1016/S0169-8095(00)00082-X.
- Waldvogel, A., B. Federer, and P. Grimm, 1979: Criteria for the detection of hail cells.

- J. Appl. Meteor.*, **18** (12), 1521–1525, doi: 10.1175/1520-0450(1979)018<1521:cftdoh>2.0.co;2.
- Wang, P. K., 2013: *Physics and Dynamics of Clouds and Precipitation*. Cambridge University Press, doi: 10.1017/cbo9780511794285.
- Weisman, M. L., and J. B. Klemp, 1982: The dependence of numerically simulated convective storms on vertical wind shear and buoyancy. *Mon. Wea. Rev.*, **110** (6), 504–520, doi: 10.1175/1520-0493(1982)110<0504:tdonsc>2.0.co;2.
- Weissmann, M., F. J. Braun, L. Gantner, G. J. Mayr, S. Rahm, and O. Reitebuch, 2005: The alpine mountain–plain circulation: Airborne doppler lidar measurements and numerical simulations. *Mon. Wea. Rev.*, **133** (11), 3095–3109, doi: 10.1175/mwr3012.1.
- Wernli, H., M. Paulat, M. Hagen, and C. Frei, 2008: SAL - A novel quality measure for the verification of quantitative precipitation forecasts. *Mon. Wea. Rev.*, **136** (11), 4470–4487, doi: 10.1175/2008MWR2415.1.
- Willemse, S., 1995: A statistical analysis and climatological interpretation of hailstorms in switzerland. Ph.D. thesis, ETH Zurich, doi: 10.3929/ethz-a-001486581.
- Willemse, S., and M. Furger, Eds., 2016: *From weather observations to atmospheric and climate sciences in Switzerland*. 1st ed., vdf Hochschulverlag, Zürich, Switzerland.
- Williams, E., 2005: Lightning and climate: A review. *Atmos. Res.*, **76** (1-4), 272–287, doi: 10.1016/j.atmosres.2004.11.014.
- Williams, E. R., 1989: The tripole structure of thunderstorms. *J. Geophys. Res.*, **94** (D11), doi: 10.1029/jd094id11p13151.
- Wilson, C. T. R., 1921: III. investigations on lightning discharges and on the electric field of thunderstorms. *Philos. Trans. Roy. Soc. London*, **221** (582-593), 73–115, doi: 10.1098/rsta.1921.0003.
- Witt, A., M. D. Eilts, G. J. Stumpf, J. T. Johnson, E. D. W. Mitchell, and K. W. Thomas, 1998: An enhanced hail detection algorithm for the WSR-88d. *Wea. Forecasting*, **13** (2), 286–303, doi: 10.1175/1520-0434(1998)013<0286:aehdaf>2.0.co;2.
- Wong, J., M. C. Barth, and D. Noone, 2013: Evaluating a lightning parameterization based on cloud-top height for mesoscale numerical model simulations. *Geosci. Model Dev.*, **6** (2), 429–443, doi: 10.5194/gmd-6-429-2013.
- Wüest, M., C. Frei, A. Altenhoff, M. Hagen, M. Litschi, and C. Schär, 2009: A gridded hourly precipitation dataset for switzerland using rain-gauge analysis and radar-based disaggregation. *Int. J. Climatol.*, **30** (12), 1764–1775, doi: 10.1002/joc.2025.
- Yair, Y., B. Lynn, C. Price, V. Kotroni, K. Lagouvardos, E. Morin, A. Mugnai, and M. d. C. Llasat, 2010: Predicting the potential for lightning activity in Mediterranean storms based on the Weather Research and Forecasting (WRF) model dynamic and microphysical fields. *J. Geophys. Res.*, **115** (D4), D04205, doi: 10.1029/2008JD010868.
- Zeman, C., N. P. Wedi, P. D. Dueben, N. Ban, and C. Schär, 2021: Model intercomparison

- of COSMO 5.0 and IFS 45r1 at kilometer-scale grid spacing. *Geosci. Model Dev.*, **14** (7), 4617–4639, doi: 10.5194/gmd-14-4617-2021.
- Ziegler, C. L., P. S. Ray, and N. C. Knight, 1983: Hail growth in an oklahoma multicell storm. *J. Atmos. Sci.*, **40** (7), 1768–1791, doi: 10.1175/1520-0469(1983)040<1768:hgiaom>2.0.co;2.
- Zimmer, M., G. C. Craig, C. Keil, and H. Wernli, 2011: Classification of precipitation events with a convective response timescale and their forecasting characteristics. *Geophys. Res. Lett.*, **38** (5), doi: 10.1029/2010gl046199.

Curriculum Vitae

Ruoi Cui 

Personal information

Universitätstrasse 16
8092 Zurich
Tel.: (+41) 78 732 34 77
E-Mail: ruoyi.cui@env.ethz.ch
born in 7 Oct. 1994
Beijing, China

Education

2019–2023 PhD Institute for Atmospheric and Climate Science, *ETH Zurich, Zurich, Switzerland*
2017–2019 M.Sc. in Atmospheric and Climate Science, *ETH Zurich, Zurich, Switzerland*
2013–2017 B.Sc. Atmospheric Science, Minor in French, *Sun Yat-sen University, Guangzhou, China*

Supervision

2022 Maximilian Forberg: Ability of COSMO-crCLIM convection-resolving climate model to simulate the remarkable July 13, 2021 hail storm over Switzerland, *master project, ETH Zurich*

Publications

Cui, R., Ban, N., Demory, M. E., Aellig, R., Fuhrer, O., Jucker, J., Lapillonne, X., and Schär, C., 2023: Exploring hail and lightning diagnostics over the alpine-adriatic region in a km-scale climate model. *Weather Clim. Dyn.*, 4 (4), 905–926, <https://doi.org/10.5194/wcd-4-905-2023>.

Malečić, B., **Cui, R.**, Demory, M. E., Horvath, K., Jelić, D., Schär, C., Prtenjak, M. T., Velasquez, P., and Ban, N., 2023: Simulating Hail and Lightning Over the Alpine Adriatic Region – A Model Intercomparison Study, *J. Geophys. Res. Atmos.*, 128(13), <https://doi.org/10.1029/2022jd037989>.

Cui, R., Ban, N., Demory, M. E., Blašković, L., Jelić, D., Prtenjak, M. T., and Schär, C., 2023: Evaluation of decade-long hail and lightning simulation over the Alpine-Adriatic region using km-scale climate model, in prep.

Oral presentations

Cui, R., et al., 2023: Evaluation of hail and lightning climatology using km-scale climate model over the Alpine region. 36th International Conference on Alpine Meteorology. St. Gallen, Switzerland, June 2023.

Cui, R., et al., 2022: Exploring the hail and lightning associated convective events in km-resolution simulations over the Alpine-Adriatic region (online). 2022 North American Workshop on Hail & Hailstorms. Boulder, USA, September 2022.

Cui, R., et al., 2022: Exploring the potential of HAILCAST and LPI in km-resolution simulations over the Alpine-Adriatic region. EGU General Assembly 2022, Vienna, Austria, May 2022.

Cui, R., et al., 2021: Exploring hail and lightning mechanisms over the Alpine-Adriatic region using HAILCAST and LPI in a convection-resolving model. 3rd European Hail Workshop, Online, March 2021.

Cui, R., et al., 2021: Exploring hail and lightning mechanisms over the Alpine-Adriatic region using HAILCAST and LPI in a convection-resolving model. ICCARUS (ICON/COSMO/CLM/ART User Seminar) 2021, Online, March 2021.